The Dissertation Committee for Onur Kacar Certifies that this is the approved version of the following dissertation:

BUILDING A FRAMEWORK FOR PREDICTING THE SETTLEMENTS OF SHALLOW FOUNDATIONS ON GRANULAR SOILS USING DYNAMICALLY MEASURED SOIL PROPERTIES

Committee:

Kenneth H. Stokoe,II, Supervisor

Loukas F. Kallivokas

Robert B. Gilbert

Ellen M. Rathje

Clark R. Wilson

Michael R. Lewis

BUILDING A FRAMEWORK FOR PREDICTING THE SETTLEMENTS OF SHALLOW FOUNDATIONS ON GRANULAR SOILS USING DYNAMICALLY MEASURED SOIL PROPERTIES

by

Onur Kacar, B.S.; M.S.

Dissertation

Presented to the Faculty of the Graduate School of

The University of Texas at Austin

in Partial Fulfillment

of the Requirements

for the Degree of

Doctor of Philosophy

The University of Texas at Austin

May, 2014

Dedication

To my parents, Melahat and Nusret Kacar, whose efforts changed lives for me and my family for generations to come.

Acknowledgements

I would like to thank every individual that stood by me patiently when the only thing that mattered to me was this dissertation. Without the continuous support from my family and friends, this work could not be accomplished.

First of all, I would like to express my heartfelt gratitude to my supervising professor, Dr. Kenneth Stokoe, II, for his enthusiasm and guidance throughout my studies. I would like to sincerely thank him for being always on his students' side and supporting them to the fullest extent.

I would like to extend my thanks to Dr. Loukas F. Kallivokas for his guidance and help with the numerical application part of my dissertation. I would also like to give special thanks to my committee members, Dr. Ellen M. Rathje, Dr. Robert B. Gilbert, Dr. Clark R. Wilson and Mr. Michael R. Lewis, for their valuable comments. My sincere appreciation is extended to Dr. Roy E. Olson, who broadened my knowledge both in technical and non-technical areas through our conversations.

I would also give my sincerest thanks to other geotechnical engineering faculty members, Dr. Jorge Zornberg, Dr. Brady Cox and Dr. Chadi El-Mohtar for their endless efforts in teaching and research. I am also deeply grateful to Dr. Thomas Benz for his help and guidance in implementing the subroutine in PLAXIS.

Thanks are extended to the administrative and technical staff at UT Austin who helped me in every step of this study, especially Ms. Melinda Jakobovits.

There are many fellow graduate students that I would like to thank for their help, motivation and friendship; Dr. Kwangsoo Park, Dr. Changyoung Kim, Dr. Rachelle Howell, Dr. Matthew LeBlanc, Mr. Oscar Suncar, Ms. Julia Roberts, Mr. Jung Su Lee, Mr. Osman Okuyucu and Mr. Marcelo Azevedo.

I would like to extend my sincerest thanks to my friends with whom I shared many years both in and outside of school; Dr. Menzer Pehlivan, and Ms. Hande Gerkus who reminded me often times that there is a life outside the university.

Sincere thanks and deepest appreciation are extended to my friends Dr. Ahmet Oncel and Mr. Sertan Kutal Gokce. All the years I have spent in Austin, they proved to me that there are people who share similar values with me and they will be lifelong friends. All the coffee breaks, political discussions, and all the silly jokes kept me alive. Thanks for the good times brothers.

One of my greatest pleasures in Austin was to have met people who brought joy to my life. I lived under the same roof with Dr. Julio Zambrano and with Mr. Yiorgos Zalachoris and shared many memories with them. They are now “kardes” to me. I know I will have many opportunities to thank them personally my entire life, but I want to emphasize here how much their friendship meant to me.

I would like to give my sincerest thanks to my dear Emel Guldogan for her existence in my life. All the love, laughter, and strength she has given me made this journey possible.

Last but not least, I would like to express my deepest gratitude to my sister Arzu, and my brothers Alaattin, Gokturk and Alper. I cannot imagine a life without their continuous love and support. There is no day passing without me appreciating their help.

Building a Framework for Predicting the Settlements of Shallow Foundations on Granular Soils Using Dynamically Measured Soil Properties

Onur Kacar, Ph.D.

The University of Texas at Austin, 2014

Supervisor: Kenneth H. Stokoe, II

In this dissertation, the framework is being developed for a new method to predict the settlements of shallow foundations on granular soil based on field seismic and laboratory dynamic tests. The new method combines small-strain seismic measurements in the field with nonlinear measurements in the field and/or in the laboratory. The small-strain shear modulus (G_{max}) of granular soil and the stress dependency of G_{max} is determined from the shear wave velocity measurements in the field. Normalized shear modulus (G/G_{max}) versus log shear strain($\log\gamma$) curves are determined from field or laboratory measurements or from empirical relationships. The $G/G_{max} - \log\gamma$ curves and G_{max} values are combined to determine the shear stress-shear strain response of granular soil starting from strains of 0.0001% up to 0.2-0.5%. The shear stress-shear strain responses at strains beyond 1.0-2.0 % are evaluated by adjusting the normalized shear modulus curves to larger-strain triaxial test data. A user defined soil model (MoDaMP) combines these relationships and incorporates the effect of increasing confining pressure during foundation loading. The MoDaMP is implemented in a finite element program, PLAXIS, via a subroutine.

Measured settlements from load-settlement tests at three different sites where field seismic and laboratory dynamic measurements are available, are compared with the predicted settlements using MoDaMP. Predictions with MoDaMP are also compared with predictions with two commonly used methods based on Standard Penetration and Cone Penetration tests.

The comparison of the predicted settlements with the measured settlements show that the new method developed in this research works well in working stress ranges. The capability of the new method has significant benefits in hard-to-sample soils such as in large-grained soils with cobbles and cemented soils where conventional penetration test methods fail to capture the behavior of the soil. The new method is an effective-stress analysis which has applicability to slower-draining soils such as plastic silts and clays.

Table of Contents

Table of Contents iix

List of Tables xiv

List of Figures xv

Chapter 1: Introduction 1

1.1 Introduction 1

1.2 research Objectives 3

1.3 Organization of Dissertation 4

Chapter 2: Methods Used to Predict Settlements 7

2.1 INTRODUCTION 7

2.1 CONSTANT ELASTIC MODULI METHODS 8

2.1.1 Terzaghi and Peck's Method (1948) 8

2.1.2 Meyerhof's Method (1965) 9

2.1.3 Schmertmann's Method (1970) and Schmertmann et al. Method (1978) 9

2.1.4 Burland and Burbidge Method (1985) 12

2.1.5 Mayne and Poulos Method (1999) 14

2.1.6 Briaud Method (2007) 17

3.2 VARYING ELASTIC MODULI METHODS 21

3.2.1 Berardi and Lancelotta Method (1991) 21

2.2.2 Mayne Method (2000) 24

2.2.3 Lehane and Fahey Method (2002) 27

2.2.4 Elhakim Method (2005) 29

2.3 SUMMARY 31

Chapter 3: Dynamic Soil Properties 33

3.1 INTRODUCTION 33

3.2 SMALL-STRAIN BEHAVIOR OF GRANULAR SOILS 34

3.2.1 Parameters Affecting the Small-Strain Shear Modulus of Granular Soil 35

3.2.1.1 Effect of Mean Effective Confining Pressure and Void Ratio on G_{max} of Granular Soil....37

3.2.1.2 Effect of Soil Gradation Characteristics on G_{max} of Nonplastic Granular Soil....40

3.2.1.3 Effects of Sample Disturbance....43

3.3 NONLINEAR BEHAVIOR OF GRANULAR SOILS....44

3.3.1 Comparison of Field and Laboratory G/G_{max}-$log\ \gamma$ Relationships....46

3.3.2 Parameters Affecting the Nonlinear Shear Modulus of Granular Soil....52

3.3.2 Empirical Relationships for Nonlinear Shear Modulus of Granular Soil....54

3.3.3 Empirical Relationships for Nonlinear Shear Modulus of Nonplastic Granular Soil Proposed by Menq (2003)....56

3.4 SUMMARY....65

Chapter 4: Development of the Model of Dynamically Measured Properties (MoDaMP)....66

4.1 INTRODUCTION....66

4.2 STRESSES AND STRAINS....68

4.3 POISSON'S RATIO, BULK MODULUS AND CONSTRAINED MODULUS....72

4.4 DERIVATION OF THE STIFFNESS MATRIX....89

4.5 USER DEFINED SOIL MODELS....92

4.5.1 Existing Soil Models in PLAXIS....92

4.5.2 General Procedures in Implementing User Defined Soil Models in PLAXIS....93

4.5.2.1 IDTask 1 (Initilization of State Variables)....94

4.5.2.2 IDTask 4 (Return the Number of State Variables)....95

4.5.2.3 IDTask 3 (Creation of the Effective Stiffness Matrix)....95

4.5.2.4 IDTask 2 (Stress Calculation based on the Constitutive Model)....96

4.5.2.5 IDTask 5 (Return Matrix Attributes)....96

4.5.2.6 IDTask 6 (Creation of the Elastic Stiffness Matrix)....97

4.5.3 Implementation of the User Defined Soil Model, MoDaMP, into PLAXIS....97
4.5.4 Verification of the User Defined Soil Model, MoDaMP....103
4.6 SUMMARY....108

Chapter 5: Development of the Model of Dynamically Measured Properties Combined with Perfect Plasticity (MoDaMP-P)....110
5.1 INTRODUCTION....110
5.2 YIELD FUNCTION....111
5.3 FLOW RULE AND PLASTIC POTENTIAL....117
5.4 FORMULATION OF THE ELASTO-PLASTIC STIFFNESS MATRIX....118
5.5 IMPLEMENTATION OF MODAMP-P INTO PLAXIS....120
5.6 VERIFICATION OF THE NONLINEAR ELASTO-PLASTIC MODEL....122
5.6.1 Element Tests....122
5.6.1.1 Nonlinear-Elastic Range of MoDaMP-P....123
5.6.1.2 Perfectly-Plastic Range of MoDaMP-P....123
5.7 SUMMARY....125

Chapter 6: Load-Settlement Tests at the NGES Test Site....127
6.1 INTRODUCTION....127
6.2 SOIL PROPERTIES AT THE NGES TEST SITE....128
6.3 SPT,CPT AND TRIAXIAL TEST RESULTS....130
6.4 SEISMIC IN-SITU AND DYNAMIC LABORATORY MEASUREMENTS....132
6.4.1 SASW Tests....132
6.4.2 RCTS Tests....132
6.5 REPRESENTATIVE SHEAR WAVE VELOCITY PROFILE AT THE FOOTING LOCATIONS....147
6.6 LOAD-SETTLEMENT TESTS....149
6.7 LOAD-SETTLEMENT PREDICTIONS....152
6.7.1 Load-Settlement Predictions with MoDaMP....152
6.7.1.1 PLAXIS Model for the Footings....154
6.7.1.2 Predicted Settlements....156

6.7.2 Modification of $G/Gmax - \log\gamma$ Relationships in MoDaMP .161

6.7.2.1 Settlement Predictions with modified $G/G_{max} - log\gamma$ Relationships implemented in MoDaMP 164

6.7.4 Load-Settlement Predictions with varying Poisson's Ratio.....171

6.7 SUMMARY 174

Chapter 7: Load-Settlement Tests at the Hornsby Bend Test Site.....176

7.1 INTRODUCTION.....176

7.2 LABORATORY TESTS AND GENERAL SOIL PROPERTIES 176

7.3 IN-SITU TESTS 180

7.3.1 CPT Tests.....181

7.3.2 SASW Tests.....182

7.3.3 Crosshole Tests 183

7.4 REPRESENTATIVE SHEAR WAVE VELOCITY PROFILE AT THE FOOTING LOCATIONS 186

7.5 G/G_{max} $-\log\gamma$ RELATIONSHIPS FOR HORNSBY BEND SITE.....190

7.6 LOAD-SETTLEMENT TESTS AT THE HORNSBY BEND SITE 191

7.7 LOAD-SETTLEMENT PREDICTIONS 198

7.7.1 Load-Settlement Predictions with MoDaMP.....199

7.7.1.1 PLAXIS model for the Footings 200

7.7.1.2 Predicted Settlements.....202

7.7.2 Modification of $G/Gmax - \log\gamma$ Relationships in MoDaMP .203

7.7.2.1 Settlement Predictions with modified $G/G_{max} - log\gamma$ Relationships implemented in MoDaMP 204

7.7.3 Load-Settlement Predictions with CPT and SPT Based Methods 210

7.7.4 Load-Settlement Predictions with varying Poisson's Ratio.....213

7.8 SUMMARY 216

Chapter 8: Loading Tests at the Yucca Mountain Test Site 218

8.1 INTRODUCTION.....218

8.2 SOIL PROPERTIES AT THE YUCCA MOUNTAIN TEST SITE 219

8.3 LINEAR SEISMIC AND DYNAMIC TESTS AT THE YUCCA MOUNTAIN TEST SITE 220
8.3.1 Downhole Test Results 221
8.3.2 SASW Test Results....230
8.4 NONLINEAR SEISMIC AND DYNAMIC TESTS AT THE YUCCA MOUNTAIN TEST SITE 235
8.4.1 Steady-State Dynamic Tests 235
8.5 LOAD-SETTLEMENT TESTS....240
8.6 LOAD-SETTLEMENT PREDICTIONS 243
8.6.1 Load-Settlement Predictions with MoDaMP....243
8.6.1.1 PLAXIS Model for the Footings....244
8.6.1.2 Predicted Settlements....244
8.6.2 Modification of $G/Gmax - \log\gamma$ Relationships in MoDaMP .247
8.6.2.1 Settlement Predictions with modified $G/G_{max} - log\gamma$ Relationships....249
8.6.3 Load-Settlement Predictions with varying Poisson's Ratio....251
8.7 SUMMARY 254
Chapter 9: Summary, Conclusions, and Recommendations....256
9.1 SUMMARY 256
9.1.1 Development of Soil Model using Dynamically Measured Properties (MoDaMP)....257
9.1.2 Implementation of Soil Model using Dynamically Measured Properties (MoDaMP) into PLAXIS 259
9.1.3 Load-Settlement Predictions....260
9.2 CONCLUSIONS 263
9.3 RECOMMENDATIONS FOR FUTURE RESEARCH....264
References....266

List of Tables

Table 2.1: Limiting values for maximum settlements and limiting maximum distortions in buildings (after Skempton and MacDonald, 1956).....1

Table 2.2: Influence factor I_s for settlement evaluation (from Berardi and Lancelotta, 1991) 21

Table 3.1 Values of A_G and n_G for sandy and gravelly soils (taken from Menq, 2003) 38

Table 3.2 $K2_{max}$ values for sandy and gravelly soils (from Seed et al., 1986)39

Table 3.3 Parameters affecting the nonlinear soil behavior and their relative importance (from Hardin and Drnevich, 1972) 53

Table 6.1 Input parameters used in the settlement analysis with MoDaMP for NGES test site 154

Table 7.1: Input parameters used in the settlement analysis with MoDaMP for the Hornsby Bend site 200

Table 8.1: Input parameters used in MoDaMP analyses for: (a) TP6 and (b) TP7 243

List of Figures

Figure 2.1: Strain Influence Factors, I_z, proposed by Schmertmann (1970) and Schmertmann et al. (1978)..... 12

Figure 2.2: Model for a foundation resting on elastic medium (from Das and Sivakugan (2007) showing the nomenclature used by Mayne and Poulos ,1999) 15

Figure 2.3: Variation of IG with E_0/kB' and H_s/B' (from Mayne and Poulos, 1999) 17

Figure 2.4: Recommended Γ values for different SB ratios (from Briaud, 2007) 19

Figure 2.5: Variation of $K_{E(s/B=0.1\%)}$ with D_r(from Berardi and Lancelotta, 1991) 23

Figure 2.6: Variation of $K_E/\ K_{E(s/B=0.1\%)}$with relative settlement, S/B representing the strain level(from Berardi and Lancelotta, 1991).....23

Figure 2.7: Modulus reduction for Pisa clay (LoPresti et al. 1995) 26

Figure 2.7: Measured and predicted settlements of 3-meter square foundation on sand at College Station, Texas 27

Figure 3.1: Idealized $G/G_{max} - \log\gamma$ curve with the linear, nonlinear elastic, moderately nonlinear and highly nonlinear and nonlinear ranges 34

Figure 3.2: Variation in small-strain shear modulus with effective confining pressure of sandy and gravelly soils with a constant C_u of about 1.2 (from Menq, 2003) 40

Figure 3.3: (a) Log C_{G1}- log e relationships for a constant C_u and (b) log C_{G1}- log e relationships for a constant D_{50} (from Menq, 2003).....42

Figure 3.4: (a) Log n_G - e relationships and (b) log n_G - log C_u relationships sand and gravelly soils (from Menq, 2003).....42

Figure 3.5: Effects of coefficient of uniformity, median grain size and mean effective confining pressure on G_{max} based on Menq's (2003) formulations.....43

Figure 3.6: Comparison of small-strain shear modulus between in-situ and laboratory (from Kokusho and Tanaka, 1994).....44

Figure 3.7: Variation of sampling disturbance expressed in terms of $V_{s,lab}, V_{s,field}$ and $G_{max,lab}, G_{max,field}$ with the in-situ shear wave velocity (from Darendeli, 2001).....45

Figure 3.8: Idealized $G/G_{max} - log\,\gamma$ curve with the linear, nonlinear elastic, moderately nonlinear and highly nonlinear ranges.....47

Figure 3.9: Typical $\tau - \gamma$ curve acquired using $G/G_{max} - log\,\gamma$ relationship and the linear, nonlinear and highly nonlinear ranges on $\tau - \gamma$ curve.....47

Figure 3.10: Comparison of Shear Modulus Reduction Curves in the Field and in the Laboratory (from Kurtulus and Stokoe, 2008).....49

Figure 3.11: Comparison of Field Data with Empirical Curves for Silts from Darendeli (2001) (from Kurtulus and Stokoe, 2008).....49

Figure 3.12: The $G/G_{max} - log\,\gamma$ relationships developed from the linear and nonlinear dynamic tests at Fitzpatrick Ranch (from Park, 2010).....50

Figure 3.13: Comparison of the $G/G_{max} - log\,\gamma$ relationships of the cemented alluvium from field dynamic tests at LMY and TP7 and laboratory RC measurements.....51

Figure 3.14: Effect of confining pressure on normalized modulus reduction curves (from Kokusho, 1980).....54

Figure 3.15: Normalized Modulus Reduction Curves Proposed by Seed et al. (1986) (Note: $\sigma_0' \sim$ 1 atm) 54

Figure 3.16: Variation of reference strain with (a) void ratio where C_u is constant, (b) void ratio where D_{50} is constant, (c) D_{50} and (d) C_u (from Menq, 2003) 57

Figure 3.17: Variation of curvature coefficient "a" with (a) void ratio where Cu is constant, (b) void ratio where D_{50} is constant, (c) D_{50} and (d) C_u (from Menq, 2003).....58

Figure 3.18: Variation of (a) reference strain with effective confining pressure (b) curvature coefficient "a" with effective confining pressure.....60

Figure 3.19: Effects of (a) mean effective confining pressure and (b) coefficient of uniformity on$G/G_{max} - \log\gamma$ curves based Menq's (2003) formulation 61

Figure 3.20: Effects of (a) mean effective confining pressure and (b) coefficient of uniformity on $G - \log\gamma$ curves based Menq's (2003) formulation ..62

Figure 3.21: Effects of (a) mean effective confining pressure and (b) coefficient of uniformity on $\tau - \gamma$ curves based Menq's (2003) formulation 62

Figure 3.22: Effects of (a) reference shear strain, γ_r and (b) curvature coefficient, "a" on $G/G_{max} - \log\gamma$ curves based on Menq's (2003) formulation 64

Figure 3.23: Effects of (a) reference shear strain, γ_r and (b) curvature coefficient, "a" on $\tau - \gamma$ curves based on Menq's (2003) formulation 64

Figure 4.1: Shear modulus reduction with increasing shear strain and typical shear strain levels associated with different field and laboratory tests (from Mayne, 2001) 67

Figure 4.2: Presentation of (a) stresses (b) strains acting at a point in the Cartesian coordinate system.....71

Figure 4.3: Change in Poisson's ratio with increasing vertical strain (from Lehane and Cosgrove, 2000) 73

Figure 4.4: Examples of (a) volumetric and (b) constrained compressive strains in a soil mass in 3-dimensional space 75

Figure 4.5: Change in Poisson's ratio of a SW soil with increasing shear strain if K is assumed to be constant at all strain levels (using Equation 4.11) .77

Figure 4.6: Change in Poisson's ratio with increasing shear strain for different values of (a) "a" and (b) γ_r in the $G/G_{max} - \log\gamma$ relationships if K is assumed to be constant at all strain levels 78

Figure 4.7: Change in E/E_{max} and $M/M_{max}$with increasing γ obtained using $G/G_{max} - \log\gamma$ relationships and assuming a constant K.....80

Figure 4.8: Generalized $M/M_{max} - \log\varepsilon$ relationships by Axtell, (2002) and LeBlanc, (2013) with proposed constant $M/M_{max} - \log\varepsilon$ relationship 83

Figure 4.9: Generalized $M/M_{max} - \log\varepsilon$ and $G/G_{max} - \log\gamma$ relationships for Site 2 (LeBlanc, 2013) and the calculated Poisson's ratios 84

Figure 4.10: Change in Poisson's ratio of a SW soil with increasing shear strain if M is assumed to be constant at all strain levels (Equation 4.15).....86

Figure 4.11: Change in Poisson's ratio with increasing shear strain for different values of (a) "a" and (b) γ_r in the $G/G_{max} - \log\gamma$ relationships if M is assumed to be constant at all strain levels 87

Figure 4.12: Change in E/E_{max} and K/K_{max} with increasing γ obtained using $G/G_{max} - \log\gamma$ relationships and assuming a constant M 88

Figure 4.13: Definition of (a) G_s and $G_t$and (b) incremental formulation of shear stress-shear strain curve based on G_t 91

Figure 4.14: Illustration of the updating procedure of G_{max}, $G/G_{max} - log\,\gamma_{oct}$ relationships and G with increasing load levels.....102

Figure 4.15: Verification of MoDaMP in pure shear loading by comparing $\tau - \gamma$ curves obtained numerically and analytically for different values of $\sigma 0'$ 106

Figure 4.16: Verification of MoDaMP in pure shear loading by comparing $\tau - \gamma$ curves during loading and unloading/reloading obtained numerically and analytically.....107

Figure 4.17: Verification of MoDaMP by comparing the settlements of a rigid footing on an elastic half space with theoretical approach with the predicted settlements obtained using MoDaMP as a linear elastic model.....108

Figure 5.1: Illustration of $\tau - \gamma$ responses of strain softening, strain hardening and perfectly plastic soils.....111

Figure 5.2: Definition of Yield and Flow Conditions for an Elasto-Plastic Material 114

Figure 5.3: Drucker-Prager (a) and Mohr-Coulomb (b) yield surfaces in the π -plane 115

Figure 5.4: Drucker-Prager and Mohr-Coulomb yield surfaces matched at the major and minor vertices.....115

Figure 5.5: Comparison of shear stress-shear strain curves obtained numerically with MoDaMP-P and obtained analytically based on the $G/G_{max} - \log\gamma$ curves determined from Menq (2003) model 124

Figure 5.6: Comparison of shear stress-shear strain curves obtained numerically with MoDaMP-P and Mohr-Coulomb to verify MoDaMP-P in the plastic range 126

Figure 6.1: Location of the NGES Test Site at College Station, Texas.....128

Figure 6.2: Soil types and layer depths at the NGES test site at Texas A & M University (after Briaud and Gibbens, 1994).....129

Figure 6.3: Grain size analysis (from Briaud and Gibbens, 1994) 129

Figure 6.4: SPT profiles at the NGES sand site (from Briaud and Gibbens,1994) 131

Figure 6.5: CPT profiles at the NGES sand site (from Briaud and Gibbens,1994). 131

Figure 6.6: Shear wave velocity profiles at the NGES sand site (a) to a depth of 49 ft (15 m) and (b) expanded to show the top 10 ft (3 m) (from Park et al., 2009) 133

Figure 6.7: Log Vs-log σ_0' relationships for the NGES test site obtained from RCTS tests 135

Figure 6.8: $G - \log\gamma$ relationships determined from RCTS tests at $\sigma o' = 6$ psi of two intact specimen from the NGES test site 137

Figure 6.9: $G - \log\gamma$ relationships determined from RCTS tests at $\sigma o' = 24$ psi of two intact specimen from the NGES test site 138

Figure 6.10: $G - \log\gamma$ relationships determined from RCTS tests at $\sigma o' = 48$ psi of one intact specimen from the NGES test site.....139

Figure 6.11: $G/G_{max} - \log\gamma$ relationships for the NGES test site obtained from RCTS tests at $\sigma_0' = 6$ psi.....141

Figure 6.12: $G/G_{max} - log\gamma$ relationships for the NGES test site obtained from RCTS tests at $\sigma_0' = 24$ psi 142

Figure 6.13: $G/G_{max} - log\gamma$ relationships for the NGES test site obtained from RCTS tests at $\sigma_0' = 48$ psi 143

Figure 6.14: $G/G_{max} - log\gamma$ relationships for the NGES test site obtained from RCTS tests at all σ_0' values and the best-estimate curves fit to the RCTS data based on the Darendeli (2001) model 144

Figure 6.15: $\gamma_r - \log \sigma_0'$ relationship based on the best-estimate curves to the RCTS test data using the Darendeli (2001) model 145

Figure 6.16: Comparison of best-estimate $G/G_{max} - log\gamma$ relationships for the NGES test site with the $G/G_{max} - log\gamma$ relationships proposed by Menq (2003).....146

Figure 6.17: Log Vs log σ_0' relationships for the NGES test site obtained from the average SASW testing results.....148

Figure 6.18: Idealized, two-layer shear wave velocity profile from the logVs-log σ_0' relationships compared with the average shear wave velocity profile from SASW tests.....150

Figure 6.19: Cross-sectional view of 3.0-ft (0.91-m) diameter footing at the NGES test site (from Park et al., 2009).....151

Figure 6.20: Load-settlement tests at the NGES sand site: (a) T-Rex loading the 3.0-ft (0.91-m) diameter footing, and (b) set-up of the instrumentation to load and measure the settlement of the 1.5-ft (0.46-m) diameter footing (from Park et al. 2009).....151

Figure 6.21: Load-unload-reload settlement results for the 3.0-ft (0.91-m) diameter footing (a) and for the 1.5-ft (0.46-m) diameter footing (b) with backbone curves fitted to approximate simple continuous loading (from Park et. al, 2009) 153

Figure 6.22: Variation of G/G_{max} in the soil mass with increased applied pressure levels for analysis NG-3.0-CP-mdf2.....157

Figure 6.23: Variation of G (psf) in the soil mass with increased applied pressure levels for analysis NG-3.0-CP-mdf2.....158

Figure 6.24: Illustration showing how the modulus-strain relationships and secant shear moduli change in the numerical model during loading at three reference points beneath the 3.0-ft (0.91-m) diameter footing for NG-3.0-CP-mdf2.....159

Figure 6.25: Predicted footing settlements for the 3.0-ft (0.91-m) diameter footing at the NGES site using MoDaMP assuming constant Poisson's ratio during loading.....160

Figure 6.26: Comparison of shear stress-shear strain curves from triaxial tests and from $G/G_{max} - \log\gamma$ relationships.....162

Figure 6.27: Comparison of unmodified and modified (1st modification) $G/Gmax - \log\gamma$ relationships.....163

Figure 6.28 Comparison of shear stress-shear strain responses from triaxial tests and from the modified (1st modification) $G/G_{max} - \log\gamma$ relationships164

Figure 6.29: Predicted footing settlements using MoDaMP-1 with a constant Poisson's ratio and modified (1st modification) $G/G_{max} - \log\gamma$ relationships for (a) 3.0-ft (0.91-m) diameter and (b) 1.5-ft (0.46-m) diameter footings at the NGES Site 165

Figure 6.30: Comparison of unmodified and modified (2nd modification) $G/G_{max} - \log\gamma$ relationships.....167

Figure 6.31: Comparison of shear stress-shear strain responses from triaxial tests and from the 2nd modification of the $G/G_{max} - \log\gamma$ relationships to account for increases in the horizontal stresses during footing loading 167

Figure 6.32: Predicted footing settlements using MoDaMP-2 with a constant Poisson's ratio and the second modification of the $G/G_{max} - \log\gamma$ relationships for (a) 3.0-ft (0.91-m) diameter and (b) 1.5-ft (0.46-m) diameter footings at the NGES Site 169

Figure 6.33: Comparison of settlements predicted using the CPT-based and SPT-based methods of Schmertmann et al. (1978) and Burland and Burbidge (1985), respectively with the measured settlements for the (a) 3.0-ft (0.91-m) and (b) 1.5-ft (0.46-m) diameter footings at the NGES test site 170

Figure 6.34 Predicted footing settlements using MoDaMP with a varying Poisson's ratio (a) $M =$ constant and (b) $K =$ constant and modified $G/G_{max} - \log\gamma$ relationships for 3.0-ft (0.91-m) diameter footing at the NGES test site 172

Figure 6.35 Predicted footing settlements using MoDaMP with a varying Poisson's ratio (a) $M =$ constant and (b) $K =$ constant and modified $G/G_{max} - \log\gamma$ relationships for 1.5-ft (0.46-m) diameter footing at the NGES test site 173

Figure 7.1: Location of the Hornsby Bend Test Site at Austin, Texas 177

Figure 7.2: Plan view of the layout of the project site (from Van Pelt, 2010).....178

Figure 7.3: Grain size distribution of the soil at the Hornsby Bend Site (from Jeff Van Pelt, 2010) 178

Figure 7.4: Deviatoric stress-axial strain curves from CD Triaxial tests (from Van Pelt, 2010) 179

Figure 7.5: Total-stress envelope from CD Triaxial tests (from Van Pelt, 2010) 180

Figure 7.6: Tip resistance and side friction profiles from CPT testing at the Hornsby Bend Site (after Van Pelt, 2010) 182

Figure 7.7: Tip resistance and side friction profiles from CPT testing at the Hornsby Bend Site up to 15 ft below the ground surface (after Van Pelt, 2010)182

Figure 7.8: Shear wave velocity profiles near the 3.0-ft (0.91-m). diameter footing at the Hornsby Bend site (after Van Pelt, 2010) 184

Figure 7.9: Shear wave velocity profiles near the 1.5-ft (0.46-m) diameter footing at the Hornsby Bend site (after Van Pelt, 2010) 185

Figure 7.10: Comparison of compression and shear wave velocities measured with crosshole seismic testing beneath the small-scale footings along with the average shear wave velocity profile obtained with SASW testing (after Van Pelt, 2010) 187

Figure 7.11: Log Vs-log σ_0' relationships for the Hornsby test site obtained from the average SASW testing results near the 3.0-ft (0.91-m) diameter footing 188

Figure 7.12: Log Vs-log σ_0' relationships for the Hornsby test site obtained from the average SASW testing results near the 1.5-ft (0.46-m) diameter footing 189

Figure 7.13: Representative Vs profiles obtained from log Vs-log σ_0' relationships compared with the average Vs profiles obtained from SASW testing beneath the 1.5-ft (0.46-m). diameter footing.....192

Figure 7.14: Representative Vs profiles obtained from log Vs-log σ_0' relationships compared with the average Vs profiles obtained from SASW testing beneath the 3.0-ft (0.91-m) diameter footing.....193

Figure 7.15: G/G_{max} $-\log\gamma$ relationships based on Darendeli (2001) and Menq (2003) relationships evaluated for the Hornsby Bend site.....194

Figure 7.16: Cross-sectional view of (a) the 3.0-ft (0.91-m) diameter footing, and (b) the 1.5-ft (0.46-m) diameter footing and (c) tell-tales beneath the 3.0-ft (0.91-m) diameter footing (from Van Pelt, 2010).....196

Figure 7.17: Load-transfer system and the lay-out of the linear potentiometers for the (a) 3.0-ft (0.91-m) diameter and (b) for the 1.5-ft (0.46-m) diameter footings (from Van Pelt, 2010) 197

Figure 7.18: T-Rex in position during loading, with the operator constantly monitoring the applied load (after Van Pelt, 2010) 198

Figure 7.19: Measured settlements for the 3.0-ft (0.91-m) and 1.5-ft (0.46-m) diameter footings at the Hornsby Bend site (after Van Pelt, 2010) 199

Figure 7.20: PLAXIS model geometry and mesh used in the settlement analysis with MoDaMP.....202

Figure 7.21: Illustration showing how the modulus-strain relationships and secant shear moduli change in the numerical model during loading at three reference points beneath the 3.0-ft diameter footing at the Hornsby Bend site for HB-3.0-CP-mdf1 205

Figure 7.22: Predicted footing settlements using MoDaMP with an assumption of constant Poisson's ratio for (a) 3.0-ft (0.91-m) diameter footing and (b) 1.5-ft (0.46-m) diameter footing at the Hornsby Bend Site.....206

Figure 7.23: Comparison of shear stress-shear strain responses from the triaxial tests and from the $G/G_{max} - \log\gamma$ relationships.....207

Figure 7.24: Comparison of unmodified and modified $G/G_{max} - \log\gamma$ relationships 207

Figure 7.25: Comparison of shear stress-shear strain responses from the triaxial tests and from the modified $G/G_{max} - \log\gamma$ relationships.....208

Figure 7.26:Predicted footing settlements using modified $G/G_{max} - \log\gamma$ relationships (MoDaMP-1) with a constant Poisson's ratio for (a) the 3.0-ft (0.91-m) diameter footing and (b) the 1.5-ft (0.46-m) diameter footing at the Hornsby Bend Site.....209

Figure 7.27: Predicted and measured vertical strains beneath the 3.0-ft diameter footing at the Hornsby Bend site 211

Figure 7.28: Settlements predicted using the Schmertmann et al. (1978) and Burland and Burbidge (1985) methods and their comparison with the measured settlements for (a) the 3.0-ft (0.91-m) diameter footing and, (b)1.5-ft (0.46-m) diameter footing at the Hornsby Bend site 212

Figure 7.29: Predicted footing settlements with modified $G/G_{max} - \log\gamma$ relationships (MoDaMP-1) and a varying Poisson's ratio ($M =$ constant) for (a) the 3.0-ft (0.91-m) diameter footing and (b) the 1.5-ft (0.46-m) diameter footing at the Hornsby Bend Site.....214

Figure 7.30: Predicted footing settlements with modified $G/G_{max} - \log\gamma$ relationships (MoDaMP-1) and a varying Poisson's ratio (K = constant) for (a) the 3.0-ft (0.91-m) diameter footing and (b) the 1.5-ft (0.46-m) diameter footing at the Hornsby Bend Site.....215

Figure 8.1: Location of Yucca Mountain, Nevada (from Park, 2010).....219

Figure 8.2: Plan view of Test Pit 6 (not to scale) (from Park, 2010).....221

Figure 8.3: $\mathrm{Log}Vs - \log\sigma_0$ relationships for Test Pit 6 obtained from small-scale downhole tests (after Park, 2010) 223

Figure 8.4: $\mathrm{Log}Vp - \log\sigma_0$ relationships for Test Pit 6 obtained from small-scale downhole tests (after Park, 2010) 224

Figure 8.5: $\mathrm{Log}Vs - \log\sigma_0$ relationships for Test Pit 7 obtained from small-scale downhole tests (after Park, 2010) 225

Figure 8.6: $\mathrm{Log}Vp - \log\sigma_0$ relationships for Test Pit 7 obtained from small-scale downhole tests (after Park, 2010) 226

Figure 8.7: $\mathrm{Log}Vs - \log\sigma_v$ relationships for Test Pit 7 obtained from small-scale downhole tests (after Park, 2010) 228

Figure 8.8: $\mathrm{Log}Vp - \log\sigma_v$ relationships for Test Pit 7 obtained from small-scale downhole tests (after Park, 2010) 229

Figure 8.9: $\mathrm{Log}Vs - \log\sigma_v$ relationships measured with the RC tests on 11 intact alluvium specimens (from Park, 2010, modified from Schuhen, 2009) 231

Figure 8.10: Vs profiles determined from SASW measurements at TP 6 and TP 7 sites (after Park, 2010) 232

Figure 8.11: Comparison of Vs profiles determined from SASW measurements at TP 6 and with Vs profiles determined from the small-scale downhole measurements beneath the 3.0-ft (0.91-m) diameter footing.....233

Figure 8.12: Comparison of Vs profiles determined from SASW measurements at TP 7 and with Vs profiles determined from the small-scale downhole measurements beneath the 3.0-ft (0.91-m) diameter footing.....234

Figure 8.13: $G/G_{max} - \log\gamma$ relationships obtained from steady-state dynamic tests at Lower Muck Yard and Test Pit 7 and the best fit curves to the data with Darendeli (2001) model (from Schuhen, 2009).....237

Figure 8.14: $G/G_{max} - \log\gamma$ relationships obtained from steady-state dynamic tests at Lower Muck Yard and Test Pit 7 and from RC tests (Park, 2010 and Schuhen, 2009) 238

Figure 8.15: Best-estimate $G/G_{max} - \log\gamma$ curves determined by combining the steady-state dynamic tests in the field at Lower Muck Yard and Test Pit 7 with the results from laboratory RC tests on intact alluvial specimens 239

Figure 8.16: Reference strain-log confining pressure relationship based on the best-estimate $G/G_{max} - \log\gamma$ curves shown in Figure 8.15 240

Figure 8.17: Cross-sectional view of the 3-ft diameter footing at the TP 7 and TP 6 sites (from Park, 2010).....241

Figure 8.18: Load-unload-reload settlement results for the 3.0-ft (0.91-m) diameter footings with backbone curves fitted to approximate simple continuous loading at: (a) Test Pit 6 and (b) at Test Pit 7 242

Figure 8.19: Geometry of the soil-footing model and the undeformed mesh for Test Pit 7 245

Figure 8.20: Predicted footing settlements using MoDaMP with a constant value of Poisson's ratio (see Table 8.1) for: (a) TP 6 and (b) TP 7 246

Figure 8.21: Comparison of shear stress-shear strain responses from quasi-static tests and from the $G/G_{max} - \log\gamma$ relationships (quasi-static test results are from Schuhen, 2009).....247

Figure 8.22: Comparison of unmodified (MoDaMP) and modified (MoDaMP-1) $G/G_{max} - \log\gamma$ relationships 248
249

Figure 8.23: Comparison of shear stress-shear strain responses from quasi-static tests and from modified $G/G_{max} - \log\gamma$ relationships (used in MoDaMP-1) 249

Figure 8.24: Comparison of predicted footing settlements using MoDaMP-1 with a constant Poisson's ratio value assumption and measured settlements for the 3.0-ft (0.91-m) diameter footing at: (a) TP6 and (b) TP7 250

Figure 8.25: Comparison of predicted footing settlements using MoDaMP-1 with a constant compression modulus (M) assumption and measured settlements for the 3.0-ft (0.91-m) diameter footing at: (a) TP6 and (b) TP7.....252

Figure 8.26: Comparison of predicted footing settlements using MoDaMP-1 with a constant bulk modulus (K) assumption and measured settlements for the 3.0-ft (0.91-m) diameter footing at: (a) TP6 and (b) TP7.....253

Chapter 1: Introduction

1.1 INTRODUCTION

When designing shallow foundations, permissible settlement and bearing capacity are the two main criteria considered. Permissible settlement generally becomes the governing factor for foundations on granular soil since the bearing capacities are relatively high for foundations on granular soil. An important aspect in evaluating settlements on granular soils is that it is difficult and/or expensive to obtain undisturbed samples of granular soil. Hence, the stress-strain behavior of undisturbed granular soil is generally not measured in the laboratory. Therefore, settlements of footings on granular soil are estimated from empirical correlations. Foundation settlements are predicted using empirical correlations that relate in-situ penetration test results with load-settlement tests or case histories. It is worth noting that penetration test results incorporated in these correlations represent an indirect evaluation of soil stiffness.

In most settlement predictions methods, an average representative stiffness of the granular soil is estimated based on the in-situ penetration tests. This average stiffness is expressed in terms of either the Young's modulus estimated from Cone Penetration Test (CPT) data (Schmertmann et al., 1978) or directly expressed in terms blow counts in Standard Penetration Test (SPT) (Burland and Burbidge, 1985). However, it is widely known that the shear modulus, G, which is the most commonly stiffness parameter used in geotechnical engineering, is a stress and strain dependent parameter (Hardin and Drnevich, 1972). Based on the strain range, the soil response can be divided into the following four regions:

(1) Linear range (small-strain range) where the shear modulus is not strain dependent up to some strain level, typically denoted as the elastic threshold strain, γ_t^e. In this range the shear modulus is called G_{max}.

(2) Beyond γ_t^e, the shear modulus is strain dependent and this range is called nonlinear elastic range up to a strain range, γ_t^c, which is the cyclic threshold strain.

(3) The soil response becomes moderately nonlinear beyond γ_t^c up to a strain level of about 0.2 %.

(4) Beyond this moderately nonlinear range, the soil response is highly nonlinear and the soil properties in this range are evaluated by cyclic and/or static measurements.

In a deformation based analysis, the shear modulus should be compatible with the shear strain range in the analysis. During loading of foundations, the soil is strained from the linear elastic range to the highly nonlinear range. The shear modulus of granular soil can be measured with a combination of field seismic and laboratory dynamic tests up to strain levels of 0.1-0.2%. Beyond this strain level, the response of the soil is evaluated with static or cyclic triaxial or simple shear test. Combining the results from seismic and dynamic measurements with the triaxial test data, a complete shear stress-shear strain response of the soil can be evaluated to be used in a settlement prediction analysis of shallow foundations.

In addition to the strain dependency, shear moduli of granular soils at all strains are also stress dependent. The shear modulus increases as the confining pressures increases. Therefore, during loading of a shallow foundation, the soil mass beneath the foundation experiences increasing confining pressures. The effect of the increased

confining pressure due to loading is not taken into account in conventional settlement prediction methods that utilize an average soil stiffness.

Therefore, a method that accounts for the stress and strain dependency of shear modulus of granular soil in all strain ranges is essential in predicting the nonlinear load-settlement curve of shallow foundations. Such a method does not exist today.

1.2 RESEARCH OBJECTIVES

Due to the lack of a comprehensive deformation-based method for predicting the settlements of shallow foundations that includes the stress and strain dependency of shear modulus of granular soil, a generalized framework is proposed in this research. This framework combines small-strain field seismic measurements, larger-strain strain field and laboratory dynamic measurements and large-strain triaxial test data to estimate the shear modulus over the wide strain range involved in settlement analyses.

This research was undertaken to develop a soil model incorporating the aforementioned stress and strain dependencies of granular soil and to apply this model in predicting settlements of shallow foundations. The main objectives of this research are:

(1) to create a data set of load-settlement tests where field seismic, field and/or laboratory dynamic and triaxial test data are available. All the load-settlement test results included in this research come from studies completed at the University of Texas at Austin.

(2) to characterize the dynamic properties of the soils at the load-settlement test sites based on the field seismic and laboratory dynamic measurements conducted at these sites. It is worth noting that there are very few load-settlement tests reported in the literature where field seismic and laboratory dynamic tests are available (Smith, 2005).

(3) to write a user defined soil model in FORTRAN that incorporates the dynamically measured soil properties combined with the larger-strain measurements in the laboratory (MoDaMP).

(4) to implement this user define soil model in a commercially available finite element program, PLAXIS and to verify that the developed soil model is working correctly by comparing the soil model with known analytical solutions.

(5) and to predict the settlements of shallow foundations from load-settlement tests using MoDaMP and comparing them with the measured settlements. Also, to compare the predicted settlements using MoDaMP with the predicted settlements obtained using two widely known settlement prediction methods; Schmertmann et al., 1978 and Burland and Burbidge, 1985.

1.3 ORGANIZATION OF DISSERTATION

The objectives of this research are described in the previous section and are addressed in nine chapters. The content and the organization of these chapters are discussed as follows.

In Chapter 1, the scope of the dissertation is introduced by addressing the importance and the need of a new method based on dynamically measured soil properties. The main objectives of the dissertation and the dissertation organization are discussed.

Previous studies dealing with settlement prediction methods for shallow foundations on granular soil are presented in Chapter 2. The main characteristics of these methods and the differences between these methods are discussed. The shortcomings of these methods are discussed to emphasize the need of this research.

In Chapter 3, dynamic soil properties of granular soils in the linear and nonlinear ranges are discussed. Field and laboratory testing methods and the results of these tests

on granular soils are presented in this chapter. Empirical relationships and comparison of these relationships with test results are also introduced in Chapter 3.

In Chapter 4, the general procedure followed in creating user-defined soil models for PLAXIS is discussed. The conceptual and numerical issues in creating the user-defined soil model, MoDaMP, are explained herein. The implementation and verification of the MoDaMP model are also presented in this chapter.

The nonlinear elastic-perfectly plastic model, designated as MoDaMP-P, is presented in Chapter 5. A general description of the yield and flow rules for soils is given. The yield and flow rules incorporated in MoDaMP-P and the implementation of this model into PLAXIS are presented in the remainder of Chapter 5.

With the user-defined soil model, MoDaMP, three case studies were undertaken. These case studies are described below. The user-defined soil model, MoDaMP-P, needs further research to be used in settlement predictions. Therefore, it was not included in these three case studies.

The first case study is presented in Chapter 6. This case study involved comparisons with load-settlement tests performed at the National Geotechnical Experimentation (NGES) test site (Park et al., 2009). The field and laboratory test results are presented. Development of representative shear wave velocity profiles at the NGES site and determination of soil parameters used in MoDaMP are discussed. The PLAXIS model and the analysis details are also given. Comparison of predicted settlements with the measured settlements is presented. Modification of the normalized shear modulus-shear strain relationship at larger strains and predicted settlements with this modified relationship are then presented. The effect of varying Poisson's ratio is also discussed.

The second case study is presented in Chapter 7. This case study involved load-settlement tests at the Hornsby Bend site conducted by Van Pelt (2010). The procedures followed to develop the shear wave velocity profiles, to obtain the soil parameters to be used in MoDaMP and to run the analyses are discussed. The predicted settlements are then compared with the measured settlements.

The third case study is presented in Chapter 8. This case study involved load-settlement tests at the Yucca Mountain site. The linear and nonlinear field and laboratory test results are presented. As discussed in Chapters 6 and 7, development of representative shear wave velocity profiles and the soil parameters used in MoDaMP are discussed. Predicted settlements are compared with measured settlements. The effect of varying Poisson's ratio is also presented.

Chapter 9 presents the conclusions of this research and it also provides a summary of the findings in this research. The advantages and the applicability of the proposed method are discussed. Recommendations for future research are also presented.

Chapter 2: Methods Used to Predict Settlements

2.1 INTRODUCTION

Calculation of settlements of shallow foundations is one of the fundamental topics in foundation engineering. The deformational behavior usually governs the design of shallow foundations on granular soil. Granular soils have higher limit loads compared to cohesive soils, thus the bearing capacity, which is a limit equilibrium phenomenon, is higher for granular soil. Hence, the design of shallow foundations is usually based on allowable settlement. Table 2.1 shows the maximum allowable settlement and maximum allowable distortion recommended by Skempton and MacDonald (1956) for foundations on sand and clay.

Table 2.1: Limiting values for maximum settlements and limiting maximum distortions in buildings (after Skempton and MacDonald, 1956)

Maximum Total Settlement	In Sand	32 mm
	In Clay	45 mm
Maximum Differential Settlement	Isolated Foundations in Sand	51 mm
	Isolated Foundations in Clay	76 mm
	Raft in Sand	51-76 mm
	Raft in Clay	76-127 mm
Maximum Distortion	Maximum Angular Distortion	1/300

One of the key difficulties in dealing with granular soils is that it is difficult and/or expensive to obtain undisturbed sample. Hence, the stress-strain behavior of undisturbed granular soil cannot be readily determined in the laboratory. Therefore, settlements of shallow foundations on such soil have traditionally been predicted based on correlations with in-situ penetration tests. Most in-situ tests results are incorporated in settlement prediction formulations either as an indirect or direct measure of soil stiffness

to be used in an equivalent elastic analysis or as a direct parameter to be used in an empirical analysis.

There are various methods to predict the settlements of shallow foundations. Most of these methods are based on in-situ results from tests such as the cone penetrometer test (CPT), standard penetration test (SPT) or pressuremeter test (PMT). These results are then used to obtain a soil stiffness parameter which is utilized in equivalent, elasticity-based predictions or they are incorporated into empirical formulations. In most of these methods, major parameters controlling the settlements of shallow foundations are: (1) applied pressure, (2) soil stiffness, (3) footing dimensions and shape (4) embedment depth and (5) soil layer thickness. In these methods, the soil stiffness is assumed as constant at a given depth. These methods are denoted as "constant elastic moduli methods" herein.

In a few studies, the nonlinearity in the soil response, e.g., the strain dependency of the elastic moduli is also included in the formulations. These methods are denoted as "varying elastic moduli methods" herein. The most commonly used methods in practice are summarized in the following sections. These methods are discussed in chronologic order. It should also be noted that there are many more methods that were not included herein because they have received much less use in the profession.

2.1 CONSTANT ELASTIC MODULI METHODS

2.1.1 Terzaghi and Peck's Method (1948)

One of the first methods to predict the settlements of foundations on granular soils was proposed by Terzaghi and Peck (1948). They used results from plate-load test with 300-mm square plates on sand. The sand had a wide range in standard penetration test

(SPT) blow count (N). They related the observed settlements from the load tests to the expected settlements on actual foundations. The correlation they proposed is:

$$S_{footing} = S_{plate}\left(\frac{2B}{B+0.3}\right)^2\left(\frac{1-D_f}{4B}\right) \tag{2.1}$$

where $S_{footing}$ is the footing settlement, S_{plate} is the plate settlement, B is the foundation width and D_f is the embedment depth.

2.1.2 Meyerhof's Method (1965)

Meyerhof (1965) proposed an approach to estimate the settlements of shallow foundations based on standard penetration test (SPT) blow count (N_{60}). In this approach, the effects of applied pressure, foundation width and embedment depth is taken into account. Also, a distinction is made between foundations with widths larger and smaller than 1.22 m. The expression formulated by Meyerhof (1965) is as follows:

$$S_{footing}\ (mm) = \frac{1.33q\ (kPa)}{N_{60}}\left(\frac{1-D_f}{4B}\right)\ for\ B \leq 1.22\ m \tag{2.2}$$

$$\mathrm{S_{footing}\ (mm)} = \frac{0.53\mathrm{q\ (kPa)}}{\mathrm{N_{60}}}\left(\frac{2\mathrm{B}}{\mathrm{B}+0.3}\right)^2\left(\frac{1-\mathrm{D_f}}{4\mathrm{B}}\right)\ \mathrm{for\ B} \geq 1.22\ \mathrm{m} \tag{2.3}$$

where $S_{footing}$ is the footing settlement, B is the foundation width and D_f is the embedment depth.

2.1.3 Schmertmann's Method (1970) and Schmertmann et al. Method (1978)

Schmertmann (1970) presented a semi-empirical approach to predict the settlements on granular soils which has been widely used in practice. The approach is

based on elastic theory and is supported by experiments and numerical solutions. Schmertmann assumed a circular, rigid foundation resting on an elastic half space. Using the well-known expression of strain distribution developed by Ahlvin and Ulery (1962) given in Equation 2.4, Schmertmann defined a strain influence factor, I_z, that is presented in Equation 2.5.

$$\varepsilon_z = \frac{q}{E}(1+\nu)[(1-2\nu)A + F] \tag{2.4}$$

$$I_z = (1+\nu)[(1-2\nu)A + F] \tag{2.5}$$

In Equations 2.4 and 2.5, q is the applied uniform pressure, E is Young's modulus, ν is the Poisson's ratio and A and F are dimensionless factors depending on the location of the point considered. In Figure 2.1, the distribution of the simplified strain influence factor, I_z, with depth beneath the footing that was proposed by Schmertmann (1970) is shown. To find the total settlement of the shallow foundation, Equation 2.4 should be integrated over the depth of influence which is taken as $2B$ (B = foundation width) by Schmertmann. The final form of the expression is given as:

$$S = C_1 C_2 \Delta q \sum_{0}^{2B} \left(\frac{I_z}{E}\right) \Delta z \tag{2.6}$$

where S is the settlement, Δq is the net applied uniform pressure and Δz is the thickness of the considered layer. The Young's modulus, E, is determined from the cone tip resistance, q_c, from CPT measurements. The value of E is obtained with $E = 2q_c$. In addition, C_1 and C_2

in Equation 2.6 are correction factors for depth of embedment and creep, respectively, as presented below:

$$C_1 = 1 - 0.5\frac{\sigma_v'}{\Delta q} \quad \geq 0.5 \tag{2.7}$$

$$C_2 = 1 + 0.2log\left(\frac{t\ (yr)}{0.1}\right) \tag{2.8}$$

where σ_v' is the initial vertical effective stress at the bottom of the footing, Δq is the increase in vertical pressure due to loading, and "t" is the time after construction of the foundation in years.

Schmertmann et al. (1978) improved Schmertmann's (1970) method further by numerical modeling and model tests. Additionally, the effects of width-to-length ratio, B/L, of the foundations were also considered in this formulation. The main difference in these two models is the consideration of the effects of the foundation type, square or strip, i.e., axisymmetric or plane strain case. The modified strain influence factors are shown in Figure 2.1 and the peak values, $I_{z,peak}$, are given by:

$$I_{z,peak} = 0.5 + 0.1\left(\frac{\Delta q}{\sigma_z'}\right)^{0.5} \tag{2.9}$$

where σ_z' is the effective vertical stress computed at depth "z" where $I_{z,peak}$ occurs. In the Schmertmann et al. (1978) method, the correlation between modulus of elasticity and the CPT tip resistance is also modified by considering the effects of axisymmetric and plane strain cases. The modified correlations are $E = 2.5q_c$ for the axisymmetric ($B/L = 1$) case and $E = 3.5q_c$ for plane strain ($B/L = 0$) case.

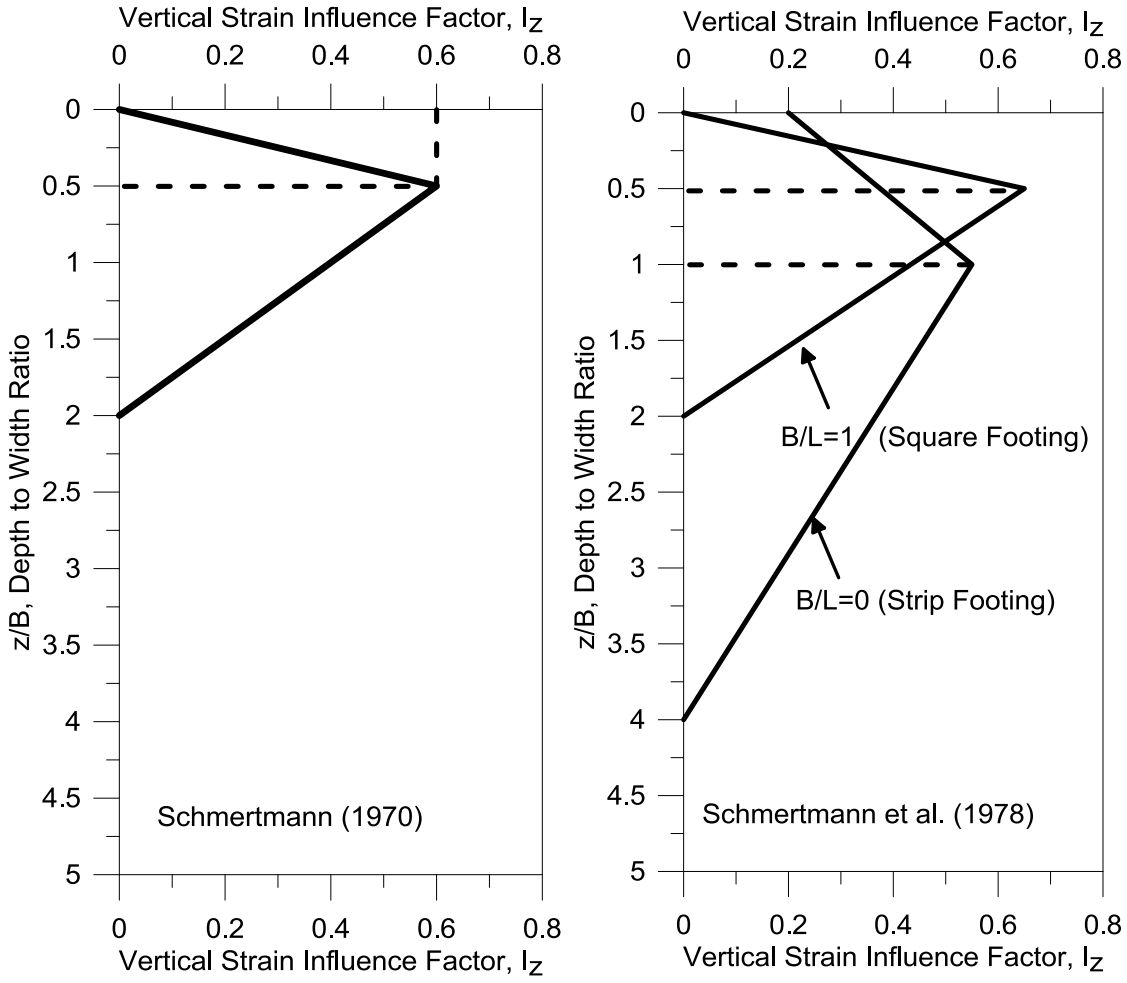

Figure 2.1: Strain Influence Factors, I_z, proposed by Schmertmann (1970) and Schmertmann et al. (1978)

2.1.4 Burland and Burbidge Method (1985)

Burland and Burbidge analyzed over 200 cases of settlements of foundations, tanks and embankments on sand and gravels. From their analysis, they developed a simple expression correlating the settlements with applied pressure, foundation width and blow count from SPT tests, N_{60}, as follows. First, they defined a term that accounted for subgrade compressibility, a_f, which is the ratio of increase in settlement (ΔS) to increase in applied pressure (Δq) , $\Delta S/\Delta q = a_f$. It was noted that the depth of influence, z_I, which

is the depth at which 75% of the total settlement took place, could be estimated by $z_I = B^{0.7}$, where B is the footing width and both z_I and B are in meters. Next, they plotted the values of $a_f/B^{0.7}$, denoted as I_c, against the average SPT value over the depth of influence, denoted as $\bar{N}$. The following relationship was found:

$$I_c = \frac{1.71}{\bar{N}^{1.4}} \tag{2.10}$$

They proposed correcting the SPT blow counts as $N'_{60} = 15 + 0.5(N_{60} - 15)$ if N_{60} is greater than 15 for very fine sand and silty sand below the water table. They also corrected the N_{60} value if the soil is gravel or sandy gravel as $N'_{60} = 1.25N$. Their proposed equation to estimate settlements is:

$$S = q \cdot B^{0.7} \cdot I_c \tag{2.11}$$

where S is the settlement in mm, q is the pressure in kN/m^2 and B is in meters. For overconsolidated soils with a preconsolidation pressure of σ'_{v0}, Equation 2.11 becomes:

$$S = \frac{1}{3} q \cdot B^{0.7} \cdot I_c \quad for \;\; q \leq \sigma'_{v0} \tag{2.12}$$

If σ'_{v0} is greater than q, than the settlement prediction expression becomes:

$$S = \left(q - \frac{2}{3}\sigma'_{v0}\right) \cdot B^{0.7} \cdot I_c \quad for \;\; q > \sigma'_{v0} \tag{2.13}$$

Burland and Burbidge (1985) applied correction factors for the shape of the footing, for the depth of the granular soil layer and for creep. These correction factors are presented below in Equations 2.14 through 2.16.

$$f_s = \left(\frac{1.25L/B}{0.25 + L/B}\right)^2 \tag{2.14}$$

where L is the foundation length. If the foundation is not square shaped, the settlement given in Equation 2.11 should be multiplied with the shape correction factor in Equation 2.14. If the depth of granular soil layer, H_s, is less than the depth of influence, z_I, than the correction factor given in Equation 2.15 should be applied.

$$f_I = \frac{H_s}{z_I}\left(2 - \frac{H_s}{z_I}\right) \tag{2.15}$$

Upon investigating the data set, Burland and Burbidge realized that time is another factor in settlements of shallow foundations and they proposed the following correction factor:

$$f_t = 1 + R_3 + R_t log\frac{t'}{3} \tag{2.16}$$

where R_t is a term accounting the time effects in the first three years, and R_3 is a term that accounts for the time effects starting after three years of completion of the construction. If the foundation is not square, the settlement given in Equation 2.9 should be multiplied with the shape correction factor.

2.1.5 Mayne and Poulos Method (1999)

Mayne and Poulos (1999) proposed a method to estimate the settlements of shallow foundations using the general form of settlement analysis derived from elasticity theory and applied several correction factors. They considered an axially loaded circular flexible foundation resting on elastic medium. The foundation they considered is shown in Figure 2.2 with the parameters used in their method. The Young's modulus is assumed

to be increasing linearly with depth, with a value of E_0 at foundation level. It should be noted that the Young's modulus is constant a given depth and it doesn't change with increasing stress. The settlements are calculated as:

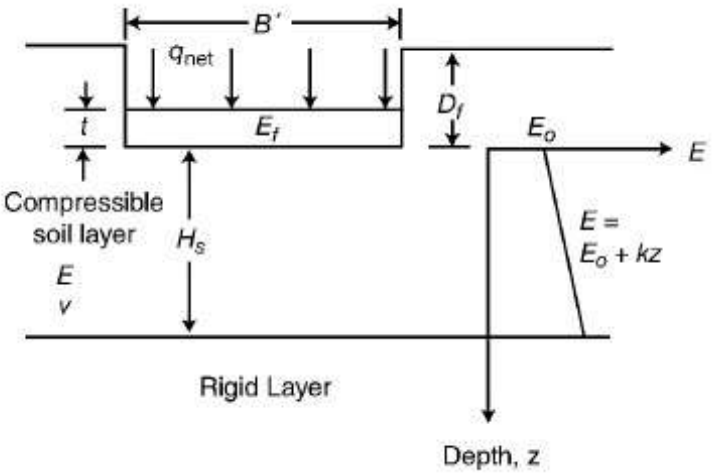

Figure 2.2: Model for a foundation resting on elastic medium (from Das and Sivakugan (2007) showing the nomenclature used by Mayne and Poulos ,1999)

$$S = \frac{qB'I_G I_F I_E(1-\nu^2)}{E_0} \tag{2.17}$$

where q is the pressure, I_G is the displacement influence factor, I_F is the rigidity coefficient factor, I_E is depth of embedment factor and B' is the equivalent diameter of a rectangular footing that is calculated based on equal areas as $B' = (4BL/\pi)^{0.5}$.

The effect of the foundation rigidity on stress distribution and therefore on strains beneath the foundation is considered by introducing a rigidity coefficient factor:

$$I_F = \frac{\pi}{4} + \frac{1}{4.6 + 10\left(\frac{E_f}{E_0 + \frac{B'}{2}k}\right)\left(\frac{2t}{B'}\right)^3} \tag{2.18}$$

where E_f = the modulus of elasticity of foundation material, t = foundation thickness and k = increase in soil stiffness per unit depth.

The depth of embedment is another factor that affects the settlements of shallow foundations; however the importance of this factor is evaluated differently among researchers. The embedment depth correction coefficient proposed by Mayne and Poulos (1999) is:

$$I_E = 1 - \frac{1}{3.5\ exp(1.22\nu - 0.4)\left[\left(\frac{B'}{D_f}\right) + 1.6\right]} \tag{2.19}$$

where B' is the equivalent diameter and D_f is the depth of embedment as shown in Figure 2.2.

The soil stiffness is one of the key parameters in the settlement analysis of Mayne and Poulos (1999). Figure 2.2 shows that Mayne and Poulos considered a soil profile where the soil stiffness E increases linearly with increasing depth (Gibson-type soil profile). The rate of the increase in E per unit depth, k, and the thickness of the soil layer from the bottom of the foundation to the incompressible layer, H_s, affect the settlements. They proposed a correction factor, I_G, to account for these parameters. The variation of I_G with $\mathrm{E_0}/kB'$ and $\mathrm{H_s}/B'$ is presented in Figure 2.3.

The settlements can be calculated utilizing Equation 2.17. In this case, values for I_F and I_E are calculated using Equations 2.18 and 2.19, respectively, and the value for I_G is taken from Figure 2.3.

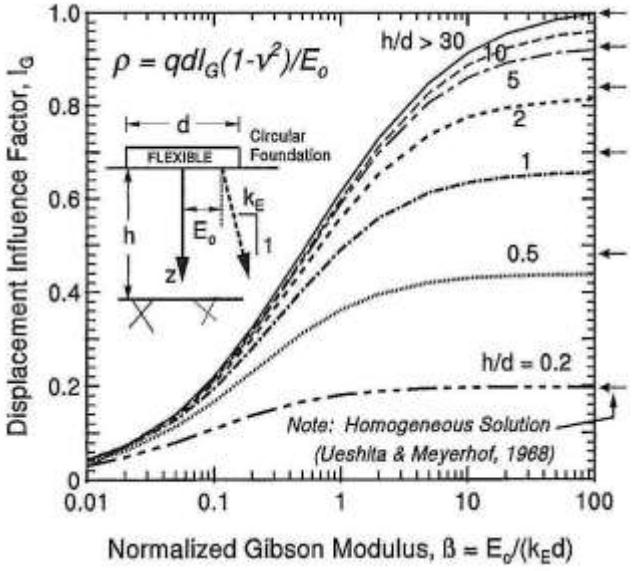

Figure 2.3: Variation of I_G with E_0/kB' and H_s/B' (from Mayne and Poulos, 1999)

2.1.6 Briaud Method (2007)

Briaud (2007) proposed a method based on a pressuremeter curve representative of the soil beneath the foundation to obtain a continuous load-settlement curve.

According to Briaud, the reason to choose the pressuremeter test is the similarity of the deformation pattern during the pressuremeter test and during loading of the foundation. Briaud used 24 load-settlement tests, 15 three-dimensional numerical analyses, the elastic settlement calculation theory and the bearing capacity theory to develop his method.

Briaud normalized the load-settlement curves by plotting the foundation pressure, q, divided by a measure of the soil strength (N, q_c or p_L depending on the availability of field data for a particular test site) versus the settlement divided by the foundation width, S/B. Based on these normalized curves, he concluded that the load-

settlement curves are independent of scale and embedment. Therefore, he decided to obtain the load-settlement curve for a reference foundation from a soil test alone and the effects of the shape, load eccentricity and proximity to a slope could be incorporated via correction factors.

The load-settlement curves and the pressuremeter test results are correlated by: (1) matching them at their ultimate strain levels and (2) transforming the pressures at the various strain levels. The ultimate strain level used in this transformation is $S/B = 0.1$ for the foundation and $\Delta R/R_o = 0.414$ for pressuremeter test where ΔR is the increase in cavity radius and R_o is the initial cavity radius. This transformation procedure is given by the following equations:

$$S/B = 0.24\Delta R/R \tag{2.20}$$

$$p_f = \Gamma p_p \tag{2.21}$$

where p_f is the mean stress under the foundation, $p_p$is the pressure in the PMT and Γ is a function linking these two pressures. The recommended values for Γ are presented in Figure 2.4. It should be noted that these values are for the case of a square footing that is loaded vertically and concentrically and is also resting on a level ground surface. Briaud proposed using correction factors that he obtained by running nonlinear numerical analyses for more general cases. The correction factor for the shape of the foundation is expressed as:

$$f_{L/B} = 0.8 + 0.2\,B/L \tag{2.22}$$

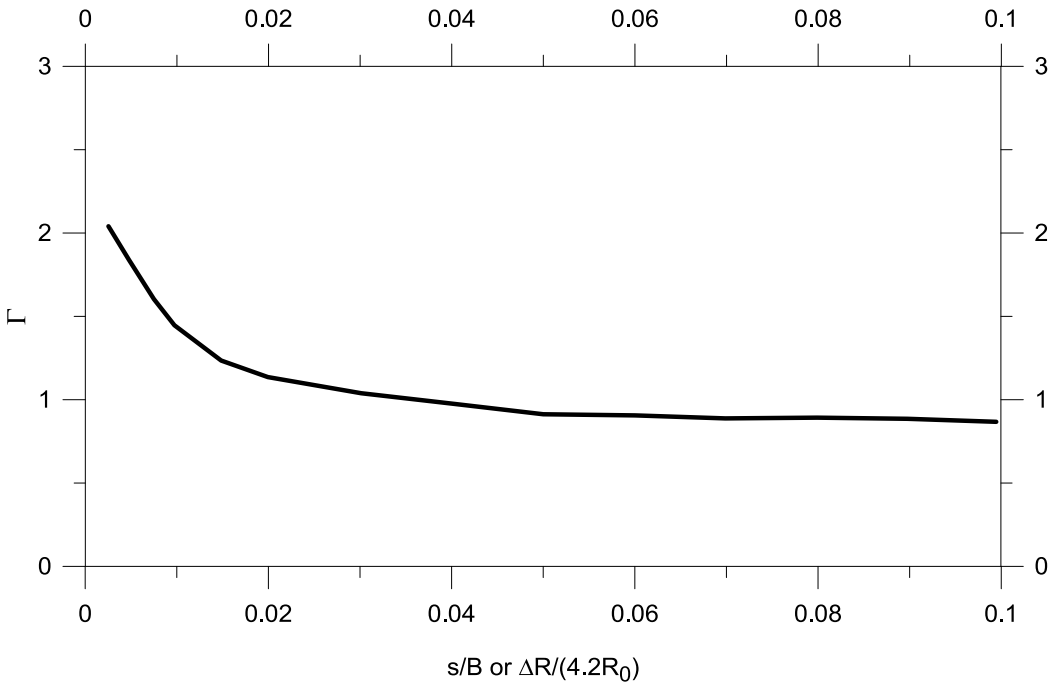

Figure 2.4: Recommended Γ values for different S/B ratios (from Briaud, 2007)

where B is the footing width and L is the footing length. Another correction factor, f_e, accounts for the eccentricity of the applied load and is calculated by:

$$f_e = 1.0 - (e/B)^{0.5} \quad at\ the\ critical\ edge \tag{2.23}$$

$$f_e = 1.0 - 0.33(e/B) \quad at\ the\ center \tag{2.24}$$

where e is the eccentricity of the load. A distinction between the center and the edge of the footing is made since the settlements under eccentric loading are not equal at these two locations. A similar distinction is also made for the inclined load correction factor, f_δ, as presented by:

$$f_\delta = 1.0 - (\delta/360)^{0.5} \quad at\ the\ critical\ edge \tag{2.25}$$

$$f_\delta = 1.0 - (\delta/90)^{\,2} \quad at\ the\ center \tag{2.26}$$

In Equations 2.25 and 2.26, δ, is the inclination of the load from the vertical in degrees.

The last correction factor in Briaud's method accounts for the proximity of the foundation to sloping ground. Correction factors for 3 to 1 and for 2 to 1 slopes are provided as :

$$f_\beta = 0.8(1.0 + d/B)^{0.1} \quad for\ a\ 3\ to\ 1\ slope \tag{2.27}$$

$$f_\beta = 0.7(1.0 + d/B)^{0.15} \quad for\ a\ 2\ to\ 1\ slope \tag{2.28}$$

where d/B is the ratio of the distance of the slope to the foundation width.

The proposed procedure to obtain the load-settlement curve can be summarized as follows:

a) Plot p_p versus $\Delta R/R$ curves from the PMT results. Correct these curves for the initial expansion.
b) Using the influence charts (Schmertmann, 1970), determine the mean pressuremeter curve within the depth of influence.
c) Transform the pressuremeter curve into a short-term, load-settlement curve by finding the Γ function from Figure 2.4 and apply the correction factors for shape, inclination, eccentricity and slope at every increment of load.

3.2 VARYING ELASTIC MODULI METHODS

3.2.1 Berardi and Lancelotta Method (1991)

Berardi and Lancelotta (1991) investigated the cases reported by Burland and Burbidge (1985) and they proposed a new settlement prediction method on granular soil. The proposed method takes the effect of strain level on Young's modulus into account by modifying the modulus according to settlement to foundation width ratio (relative settlement) which is defined as S/B. The proposed expression to evaluate the settlements is given as:

$$S = I_s \frac{qB}{E} \tag{2.29}$$

where I_s is the influence factor for a rigid footing. The value of I_s determined from Table 2.2. For simplicity, they assumed the depth of influence, z_I, equal to B. Berardi and Lancelotta back-calculated the Young's modulus values according to Equation 2.29 for

Table 2.2: Influence factor I_s for settlement evaluation (from Berardi and Lancelotta, 1991)

z_I/B	*L/B*					
	1	2	3	5	10	Circle
0.5	0.35	0.39	0.40	0.41	0.42	0.34
1.0	0.56	0.65	0.67	0.68	0.71	0.52
1.5	0.63	0.76	0.81	0.84	0.89	0.59
2.0	0.69	0.88	0.96	0.99	1.06	0.63

over a hundred cases. To account for the effects of overburden pressure, they found a nondimensional modulus number,K_E, using Janbu's (1963) expression:

$$E = K_E P_a \left(\frac{\sigma_v' + 0.5\Delta q}{P_a} \right)^{0.5} \tag{2.30}$$

where σ_v' =effective overburden pressure, Δq = pressure increase due to foundation loading and P_a =atmospheric pressure. They corrected the average SPT blow count for the overburden pressure according to:

$$(N_1)_{60} = N_{60} \left(\frac{2}{1 + \sigma_v'} \right) \tag{2.31}$$

They used the corrected SPT blow count over the depth of influence to obtain an average value, $\bar{N}$. They then evaluated the relative density of the soil according to the formulation:

$$D_r = \left(\frac{\bar{N}}{60} \right)^{0.5} \tag{2.32}$$

They plotted K_E values at a relative settlement of $S/B = 0.1\%$, ($K_{E(S/B=0.1\%)}$), as a function of D_r. Figure 2.5 presents this relationship. As a final step, they analyzed all available data for the stiffness reduction with increasing relative settlement by normalizing K_E with $K_{E(S/B=0.1\%)}$ which is shown in Figure 2.6.

The procedure proposed by Berardi and Lancelotta (1991) to evaluate the settlements of shallow foundations can be summarized as follows.

(a) Determine the average SPT blow count, N_{60}, throughout the depth of influence which is assumed to be equal to foundation width. Apply an overburden pressure correction to N_{60} value according to Equation 2.31.

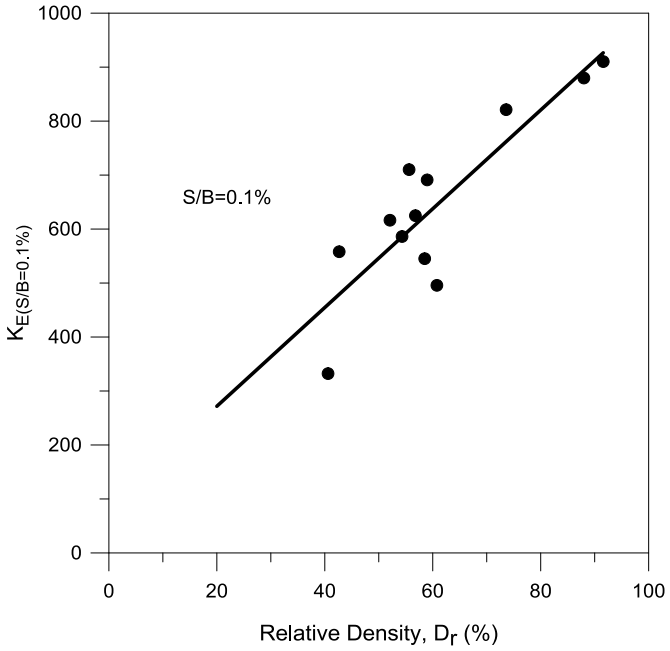

Figure 2.5: Variation of $K_{E(S/B=0.1\%)}$ with D_r (from Berardi and Lancelotta, 1991)

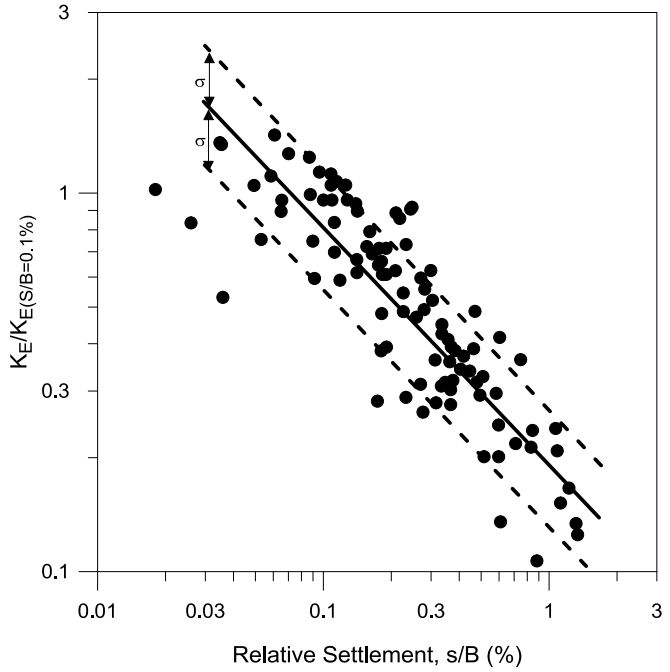

Figure 2.6: Variation of $K_E/\ K_{E(S/B=0.1\%)}$ with relative settlement, S/B representing the strain level (from Berardi and Lancelotta, 1991)

(b) Using the average corrected SPT blow count, $\bar{N}$, evaluate D_r from the expression given in Equation 2.32.

(c) Use the D_r value to determine $K_{E(S/B=0.1\%)}$ from Figure 2.5.

(d) Find E from Equation 2.30 and using the value of K_E

(e) Evaluate the settlement, S, using Equation 2.29

(f) If the calculated S/B is not the same as assumed S/B, determine the new K_E value from Figure 2.6 based on the calculated S/B value. Use the new K_E value to estimate a new settlement using Equations 2.29 and 2.30.

(g) Repeat this procedure until the assumed and calculated S/B values are the same.

2.2.2 Mayne Method (2000)

Shear stress-shear strain response of a soil is highly nonlinear and the soil behavior is different at different strain ranges. Therefore, hybrid in-situ testing can provide more information about the soil by measuring different properties of the soil at different strain ranges. Mayne (2000) proposes that hybrid testing should consist of the seismic piezocone penetration test (SCPTu) and that this testing is appropriate for settlement analysis of both shallow and deep foundations. SCPTu testing provides four different types of measurements: (1) cone tip resistance (q_c), (2) sleeve friction (f_s), (3) porewater pressure (u), and (4) downhole shear wave velocity (V_s).

The small-strain stiffness, G_{max}, is obtained using V_s measurements from the downhole part of the SCPTu testing. In this model, the reduction in shear modulus with increasing shear strain level is taken into account by reducing the shear modulus as a function of the mobilized strength. The formulation proposed by Fahey and Carter (1993) is used to express the shear modulus reduction by:

$$G/G_{max} = 1 - f(\tau/\tau_{max})^g \tag{2.33}$$

where f and g are fitting parameters. Mayne proposed using $f = 1$ and $g = 0.3$ for uncemented and unaged quartzitic sands and insensitive and unstructured clays. Figure 2.7 shows the comparison of the modulus reduction from triaxial localized measurements and from a modified version of Equation 2.33 where G is converted to E.

The modulus reduction equation is then modified by substituting the mobilized shear strength ratio with mobilized bearing capacity and G with E. The equation becomes:

$$E/E_{max} = 1 - f(Q/Q_u)^g \tag{2.34}$$

where Q is the foundation pressure, Q_u is the ultimate bearing capacity, $f = 1$ and $g = 0.3$. The bearing capacity is calculated using Vesic's (1975) method. The friction angle of the soil, ϕ', is obtained with:

$$\phi' = 17.6^0 + 11.0^0 \log(q_{c1}) \tag{2.35}$$

where q_{c1} is the normalized cone tip resistance and is calculated from:

$$q_{c1} = \frac{(q_c/P_a)}{(\sigma'_{v0}/P_a)^{0.5}} \tag{2.36}$$

where P_a is a reference stress equal to one atmosphere and σ'_{v0} is the vertical effective stress. Mayne also proposed correlations to evaluate the undrained shear strength and the

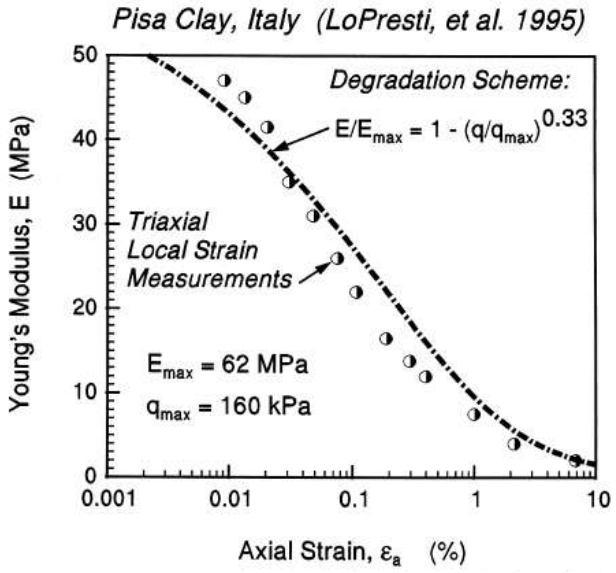

Figure 2.7: Modulus reduction for Pisa clay (from LoPresti et al. 1995)

overconsolidation ratio (OCR) of clays, with details found in Mayne (2000). Using the elastic theory method, the settlements are calculated with:

$$S = \frac{QI_{hrv}}{BE_{max}[1-(Q/Q_u)^{0.3}]} \tag{2.37}$$

where I_{hrv} is the displacement influence factor from elastic theory and B is the foundation width.

Mayne analyzed two shallow foundations using this method: (1) a 3-meter square foundation on sand at the Texas A&M national geotechnical experimentation site near College Station, TX and (2) two square foundations with 2.2- and 2.4-meter widths on clay at the Bothkennar test site in Scotland. Figure 2.8 presents the comparison of the predicted and the measured settlements at the Texas A&M site.

The method proposed by Mayne (2000) is based on the approximation of the shear modulus reduction curves; as such, the method incorporates an important factor, the

strain dependency of the shear modulus. However, it should be noted that G/G_{max} curves are significantly affected by mean effective confining pressure, gradation of the soil, plasticity index and OCR. Moreover, the ultimate bearing capacity is not a measured quantity which results in a significant unknown remaining in the solution.

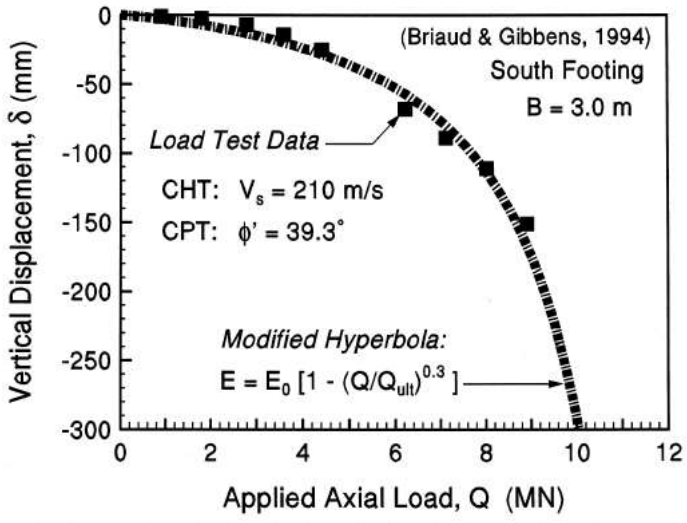

Figure 2.8: Measured and predicted settlements of 3-meter square foundation on sand at College Station, Texas (from Mayne, 2000)

The modulus reduction curves obtained using a calculated ultimate bearing capacity will inherently keep all uncertainties in the bearing capacity calculation.

2.2.3 Lehane and Fahey Method (2002)

Lehane and Fahey developed a simplified method to predict the settlements of shallow foundations on granular soil under typical working loads. Their method includes the effects of strain, stress and void ratio of the soil on soil stiffness. On the other hand, they assume a simplified Boussinesq's stress distribution under the foundation. They compare and calibrate the results obtained with this simplified settlement analysis

procedure with the results obtained with a more sophisticated finite element analysis and with load-settlement tests.

In their stiffness formulation, they describe the modulus of elasticity reduction curves as follows:

$$\frac{E_{sec}}{E_{max}} = \frac{1}{\left[1 + \left(\frac{\varepsilon - \varepsilon_{el}}{\varepsilon_r - \varepsilon_{el}}\right)^n\right]} \tag{2.38}$$

where ε_{el} and ε_r and n are empirical constants to adjust the shape of modulus reduction curve; ε_r is the reference strain at which $E_{sec}/E_{max} = 0.5$ and ε_{el} is the elastic threshold strain. The small strain modulus of elasticity, E_{max}, is evaluated from:

$$\frac{E_{max}}{P_a} = A_E F(e) \left(\frac{\sigma_v'}{P_a}\right)^{n_g} \tag{2.39}$$

where P_a = atmposheric pressure, A_E = a material constant for granular soils, σ_v' = the effective vertical stress, n_g = empirical parameter with a typical value of 0.5. The void ratio function $F(e)$ is evaluated by: $F(e) = \left(e_g - e\right)^2/(1 + e)$ where e_g is typically taken as 2.17. Taking the derivative of E_{sec} expression given in Equation 2.38, the tangent modulus of elasticity, E_t, is determined as follows:

$$E_t = \frac{E_{max}[1 + \xi - n\varepsilon\xi/(\varepsilon - \varepsilon_{el})]}{[1 + \xi]^2\left[1 - n_g(q - q_i)/\sigma_v'\right]} \tag{2.40}$$

where $\xi = (\varepsilon - \varepsilon_{el})^n/(\varepsilon_r - \varepsilon_{el})^n$. They suggest evaluating ε_r based on $\varepsilon_r = C_r(\sigma_h'/P_a)^{1-n_g}$ where is a curve fitting parameter depending on the void ratio, mobilized stress ratio and K_0.

Using the Boussinesq's stress distribution beneath the foundation, the tangent modulus is evaluated based on Equation 2.40 in an incremental form. Then the strain at any given location is then calculated using:

$$\Delta\varepsilon_v = \frac{\Delta\sigma'_v}{E_t} - \frac{2\nu\Delta\sigma'_h}{E_t} \tag{2.41}$$

The settlement at this point is then calculated by summing all the strains from a rigid boundary to this point.

The method proposed by Lehane and Fahey is important since it includes the stress and strain dependency of the modulus of elasticity of the soil. Hence, the nonlinearity of the stress-strain response of the soil under typical working loads is included via a modulus reduction factor. On the other hand, the parameters used in the model can only be obtained by matching the stress-strain response from a high-quality triaxial test with local strain measurements.

2.2.4 Elhakim Method (2005)

Elhakim proposed a closed-form solution to predict the footing settlements based on a modified hyperbolic model. The modified hyperbolic model is the same model used in Mayne (2000) as explained previously:

$$G/G_{max} = 1 - f^*(q/q_{ult})^{g^*} \tag{2.42}$$

where $f^*$and $g^*$are empirical curve fitting parameters, q is the applied pressure on the footing and q_{ult} is the calculated ultimate bearing pressure. Elhakim attempted to provide a relationship of the empirical curve fitting parameters with the shear-stress response of soils. First, he developed a user-defined soil model integrating the modulus reduction

curves with perfect plasticity and implemented this model into a finite difference program, FLAC. For modulus reduction, he used the one-parameter logarithmic function proposed by Puzrin and Burland (1998). He replaced Young's modulus in the original formulation with shear modulus. In this logarithmic function, the modulus reduction is expressed as:

$$\frac{G_{\sec}}{G_{max}} = 1 - \alpha \frac{x - x_{th}}{x} [ln(1 + x - x_{th})]^R \tag{2.43}$$

where $G_{\sec}$ and G_{max} are the secant shear modulus and small-strain shear modulus, respectively, $x = \gamma_{oct}/\gamma_r =$ normalized octahedral shear strain, $\gamma_r = (\tau_{max} - \tau_0)/G_{max}$, $\tau_{max} =$ shear strength of the soil, $\tau_0 =$ initial shear stress, $x_{th} = \gamma_{th}/\gamma_r$ =normalized threshold shear strain, and γ_{th} = elastic threshold shear strain. The expressions to find R and α are given as:

$$\mathrm{R} = \frac{(1 - x_{th})}{(x_L - x_{th})} \frac{(1 + x_L - x_{th}) ln(1 + x - x_{th})}{x_L - 1} \tag{2.44}$$

$$\alpha = \frac{x_L - 1}{(x_L - x_{th})[ln(1 + x - x_{th})]^R} \tag{2.45}$$

where $x_L = \gamma_f/\gamma_r$ =normalized and limiting strain, γ_f = shear strain at failure.

Elhakim carried out a parametric study where he simulated hypothetical load-settlement tests on granular soils under drained conditions and examined the effects of the small-strain shear modulus, foundation width and x_L which is the controlling parameter of the nonlinearity in Equation 2.43. Then he fitted the modified hyperbolic model given in Equation 2.42 to the simulated hypothetical load-settlement curves

obtained with the user-defined soil model. Thus, he obtained a relationship between x_L and g^* for different values of the soil friction angle, ϕ'. For example, the relationship proposed for $\phi' = 35^0$ is: $g^* \approx 9.09/x_L - 0.03$. He proposed a constant value for f^* equal to 0.99.

As a result, Elhakim proposed a simplified load-settlement prediction procedure with the following steps: (1) Determine the ultimate bearing pressure of the footing, q_{ult} (2) Evaluate the normalized limiting strain, $x_L = \gamma_f/\gamma_r$ from laboratory and/or in-situ testing, and (3) Predict the settlement using:

$$S = \frac{q \cdot B \cdot I}{2 \cdot G_{max} \cdot (1+\nu)} \cdot \left[1 - f^* \left(\frac{q}{q_{ult}}\right)^{g^*}\right] \tag{2.46}$$

where q is the applied pressure on the footing, B is the foundation width, I is the influence factor and ν is Poisson's ratio of the soil.

2.3 SUMMARY

Methods used in predicting the settlements of shallow foundations on granular soil are generally based on in-situ penetration tests. They usually correlate the in-situ test results with the load-settlement curves of shallow foundations based on the theory of elasticity and correction factors to account for the shape, embedment depth and rigidity of the footing. Some recent studies incorporate the strain dependency of soil stiffness into account. Most of these methods use the ratio of the applied pressure on the footing to the shear strength of the soil to account for the nonlinearity.

None of the methods discussed herein incorporate field seismic measurements of V_s to evaluate the G_{max} profile and then combine the profile with nonlinear $G/G_{max} - \log\gamma$ relationships to calculate linear and nonlinear strains. In addition, the following

effects are not explicitly considered in the methods: (1) gradation effects on the nonlinear stress-strain behavior of granular soil, and (2) the combined effects on soil stiffness of changing levels of stress state and shear strain.

Chapter 3: Dynamic Soil Properties

3.1 INTRODUCTION

In this chapter, a literature review of the dynamic properties of granular soils is presented. The term "dynamic" is used because the initial mid-range portions of the shear stress-shear-strain relationship are evaluated with dynamic measurements as discussed herein. For this research, the dynamic shear stress-shear strain relationship of granular soil is separated into four strain ranges or parts as: (1) linear, (2) nonlinear elastic, (3) moderately nonlinear and (4) highly nonlinear parts. This relationship, often expressed in terms of normalized shear modulus vs γ, is shown in Figure 3.1. In this figure, the relationship is expressed as a normalized shear modulus (G/G_{max}) versus log shear strain (γ) plot where G_{max} is the value of shear modulus and G ($=\tau/\gamma$) is the shear modulus at any shear strain. The first part, the linear range is usually referred to as the "elastic" or small-strain range. In this range, shear modulus ($G=\tau/\gamma$) is independent of the value of shear strain (γ) and G is often denoted as G_{max}. An elastic threshold value of shear strain (γ_t^e) is defined to represent the shear strain value beyond which the stress-strain response becomes strain dependent. The value of γ_t^e for granular soil varies with mean effective confining pressure σ_0', and gradation, usually expressed by the uniformity coefficient, C_u and median grain size D_{50} (Menq, 2003). For working stresses associated with shallow foundations, γ_t^e likely ranges from 0.0001 to 0.003%.

Above γ_t^e, the value of shear modulus, G, decreases with increasing shear strain so that the stress-strain relationship is nonlinear. In part, dynamic laboratory testing methods, such as the torsional resonant column, have made it possible to investigate the linear and nonlinear behavior of granular soils over a wide range in shear strain

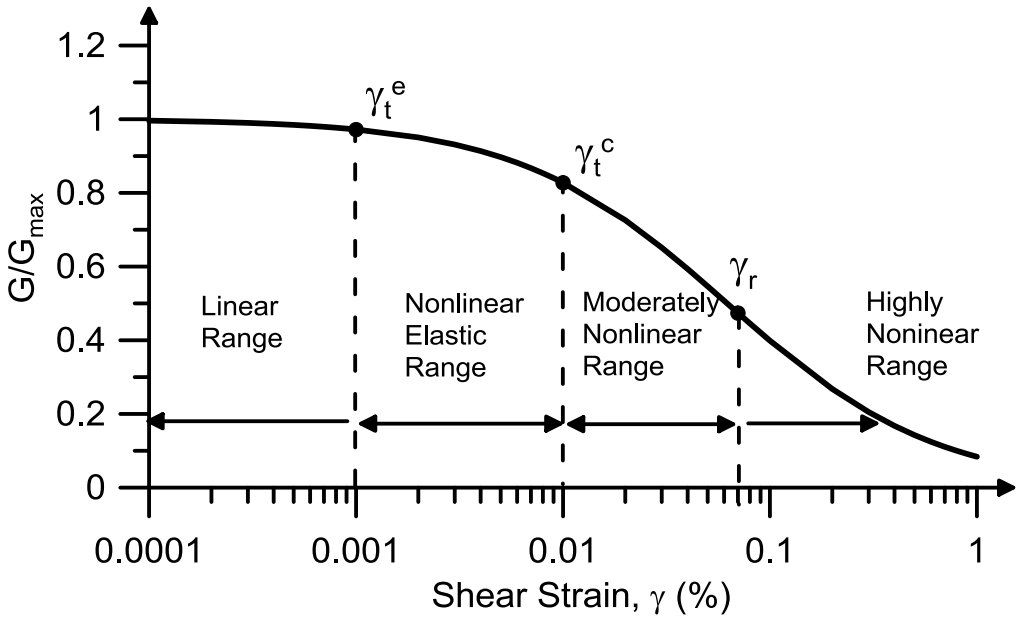

Figure 3.1: Idealized $G/G_{max} - \log\gamma$ curve with the linear, nonlinear elastic, moderately nonlinear and highly nonlinear and nonlinear ranges

(e.g., 0.0001 to 0.2 %). This range in shear strain encompasses the linear and moderately nonlinear ranges and extends somewhat into the highly nonlinear range.

The small-strain shear modulus of granular soil and parameters affecting its value in the small-strain range are discussed in Section 3.2. Some proposed correlations to evaluate the small-strain shear modulus are also presented in this section. Shear modulus of granular soil at larger strain range (nonlinear range) and parameters affecting the nonlinearity in this range are discussed in Section 3.3.

3.2 SMALL-STRAIN BEHAVIOR OF GRANULAR SOILS

Shear modulus of granular soil in the small-strain range is essentially independent of the shear strain up to an elastic threshold shear strain level, γ_t^e, as shown in Figure 3.1. Shear modulus in this range is denoted as G_{max} or G_0, although G_{max} is used herein. G_{max} can be evaluated in both the laboratory and field by dynamic testing, a key aspect of

using dynamic soil properties in this research. The value of G_{max} is evaluated by measuring the shear wave velocity in these in-situ or laboratory tests and then using:

$$G_{max} = \rho V_s^2 \tag{3.1}$$

where V_s is the shear wave velocity and ρ is the mass density of the soil. Field seismic methods such as downhole, crosshole and Spectral-Analysis-of-Surface-Waves (SASW) and seismic cone penetration testing (SCPT) can be used to evaluate V_S (Stokoe and Santamarina, 2000). The SASW or other surface-wave methods permit small-strain profiles to be evaluated very near the ground surface and in all types of granular soils, even soils with gravel and cobbles. G_{max} can also be evaluated by dynamic laboratory testing such as the torsional resonant column test and by cyclic torsional shear testing or cyclic or static triaxial tests with local measurements. The small-strain dynamic properties of granular soils measured in laboratory can be different from those measured in the field due to sample disturbance. Sample disturbance effects are discussed in Section 3.2.1.3.

3.2.1 Parameters Affecting the Small-Strain Shear Modulus of Granular Soil

The value of G_{max} of granular soils is affected by several soil parameters such as the gradation, effective confining pressure, void ratio, cementation, overconsolidation and sample disturbance. Hardin and Richart (1963) studied the effects of confining pressure and void ratio on the small-strain characteristics of sandy soils using free-free and fixed-free resonant column devices. They showed that the small-strain shear wave velocities of sandy soils are a function of confining pressure and void ratio. Hardin (1973) tested granular soils and aggregates in a fixed-free resonant column device. He found that the dynamic properties of granular soils were affected by the mean effective

pressure, void ratio, particle shape and grain size. Seed et al. (1986) proposed shear modulus reduction curves for sands and gravels based on dynamic properties of granular soils using measured with resonant column and cyclic triaxial testing. Chang and Ko (1982) used a fixed-free resonant column device to investigate the effects of gradation characteristics on dynamic properties of sandy soils. They reported that the small-strain shear modulus of medium loose sand specimens is mainly a function of uniformity coefficient (C_u). Intact gravelly soil specimens recovered by ground freezing method were tested in Japan and their dynamic properties were investigated (Kokusho and Tanaka, 1994, Kokusho et al., 1995).

A major study was conducted by Menq (2003) at the University of Texas. Menq developed a large-scale, multi-mode, free-free resonant column device (MMD) and investigated the dynamic properties of 59 reconstituted sandy and gravelly soil specimens. He studied the effects of mean effective stress, void ratio, coefficient of uniformity, median grain size, water content and measurement frequency. He found that the small-strain shear modulus can be expressed as a function of mean effective stress, coefficient of uniformity, median grain size and void ratio. Hardin and Kalinski (2005) used a special large-scale torsional resonant column to tests gravelly soil. They investigated the effect of gradation characteristics and tried to find a representative particle size that could be an indicator of G_{max}. They found that G_{max} for relatively clean and graded gravels increases with increasing particle size, e.g., the median grain size (D_{50}). They also proposed D_5 as an approximate effective particle size in determining G_{max}. Wichtmann and Triantafyllidis (2009) conducted resonant column tests on quartz sand with 25 different grain-size distributions. They found that G_{max} is not dependent on D_{50} at a constant void ratio for the particle size range they considered (0.1 mm $\leq D_{50} \leq$6

mm). However, the test results showed that G_{max} decreased significantly with increasing coefficient of uniformity (C_u). One likely contributor to this decrease is that relative density, (D_r), decreases as C_u increases if e is kept constant.

3.2.1.1 Effect of Mean Effective Confining Pressure and Void Ratio on G_{max} of Granular Soil

Mean effective confining pressure, is one of the most important parameters affecting shear wave velocity, V_s, and small-strain shear modulus, G_{max}, of granular soils. Hardin and Richart (1963) conducted free-free and fixed-free resonant column tests on sandy soils and they found that the shear wave velocity was a power function of the mean effective confining pressure. Their results for V_s of sandy soil can be formulated with the following expression:

$$G_{max} = A_G F(e)(\sigma_0')^{n_G} \tag{3.2}$$

where A_G and n_G are constants, $F(e)$ is the void ratio function and e is the void ratio. Hardin and Richart recommended $n_G = 0.25$.

There are various void ratio functions, $F(e)$, proposed in the literature. Two of the most commonly used functions are:

$$F(e) = \frac{(2.97 - e)^2}{1 + e} \quad \text{by Hardin and Black (1968)} \tag{3.3}$$

$$F(e) = \frac{1}{0.3 + 0.7e^2} \quad \text{by Hardin (1978)} \tag{3.4}$$

Table 3.1 shows A_G and n_G values reported in the literature (Kokusho, 1987; Ishihara, 1996; as presented in Menq, 2003). As can be seen in the table, n_G values are around 0.5

Table 3.1 Values of A_G and n_G for sandy and gravelly soils (taken from Menq, 2003)

	References	F(e)	A_G	n_G	Soil description
Sandy Soils	Hardin and Richart (1963)	$\frac{(2.17-e)^2}{1+e}$	7000	0.5	Round grain Ottawa sand
		$\frac{(2.97-e)^2}{1+e}$	3300	0.5	Angular grained crushed quartz
	Iwasaki et al. (1978)	$\frac{(2.17-e)^2}{1+e}$	9000	0.38	Eleven kinds of clean sand
	Kokusho (1980)	$\frac{(2.17-e)^2}{1+e}$	8400	0.5	Toyoura sand
	Yu and Richart (1984)	$\frac{(2.17-e)^2}{1+e}$	7000	0.5	Three kinds of clean sand
Gravelly Soils	Prange (1981)	$\frac{(2.97-e)^2}{1+e}$	7230	0.38	Ballast (D_{50} = 40 mm, C_u = 3.0)
	Kokusho and Esashi (1981)	$\frac{(2.17-e)^2}{1+e}$	13000	0.55	Crushed rock (D_{50} = 30 mm, C_u = 10)
		$\frac{(2.17-e)^2}{1+e}$	8400	0.60	Round Gravel (D_{50} = 10 mm, C_u = 20)
	Tanaka et al. (1987)	$\frac{(2.17-e)^2}{1+e}$	3080	0.60	Gravel (D_{50} = 10 mm, C_u = 20)
	Goto et al. (1987)	$\frac{(2.17-e)^2}{1+e}$	1200	0.85	Round Gravel (D_{50} = 2 mm, C_u = 10)

Note: 1. $G_{max} = A_G F(e) (\sigma_o')^{n_G}$, and 2 . G_{max} and σ_o' are in kPa.

for sandy soils, whereas they are higher for gravelly soils. There is a variation in the A_G values for both sandy soils and gravelly soils.

Seed et al. (1986) suggested a formulation where G_{max} is expressed as a function of mean effective confining pressure:

$$G_{max} = 1000(K_2)_{max}(\sigma_0')^{n_G} \tag{3.5}$$

Table 3.2 $(K_2)_{max}$ values for sandy and gravelly soils (from Seed et al., 1986)

	Soil Type	Location	Depth (ft)	$(K_2)_{max}$
Sandy Soils	Loose Moist Sand	Minnesota	10	34
	Dense Dry Sand	Washington	10	44
	Dense Saturated Sand	Southern California	50	58
	Dense Saturated Sand	Georgia	200	60
	Dense Saturated Silty Sand	Georgia	60	65
	Dense Saturated Sand	Southern California	300	72
	Extremely Dense Silty Sand	Southern California	125	86
Gravelly Soils	Sand, Gravel and Cobbles with Little Clay	Caracas	200	90
	Dense Sand and Gravel	Washington	150	122
	Sand, Gravel and Cobbles with Little Clay	Caracas	255	123
	Dense Sand and Sandy Gravel	Southern California	175	188

where G_{max} and σ_0' are in units of psf and $(K_2)_{max}$ is a material constant that depends on the soil type and relative density. Table 3.2 shows the values of $(K_2)_{max}$ for different sand and gravelly soils. It can be seen in the table that $(K_2)_{max}$ values for gravelly soils are generally two to three times higher than the $(K_2)_{max}$ values for sand soils.

Menq (2003) investigated the effects of σ_0' and void ratio along with the effects of gradation characteristics on G_{max} of granular soils. Figure 3.2 shows the effect of σ_0' on G_{max} of soils with C_u of ~1.2 and varying D_{50} values. It can be seen in the figure that the effect of σ_0' on G_{max} is the same for all values of D_{50}. Therefore, Menq proposed an expression for G_{max} as a function of G_{max} at a mean effective confining pressure of one atmosphere (C_{G1}) and a normalized mean effective pressure raised to a power as:

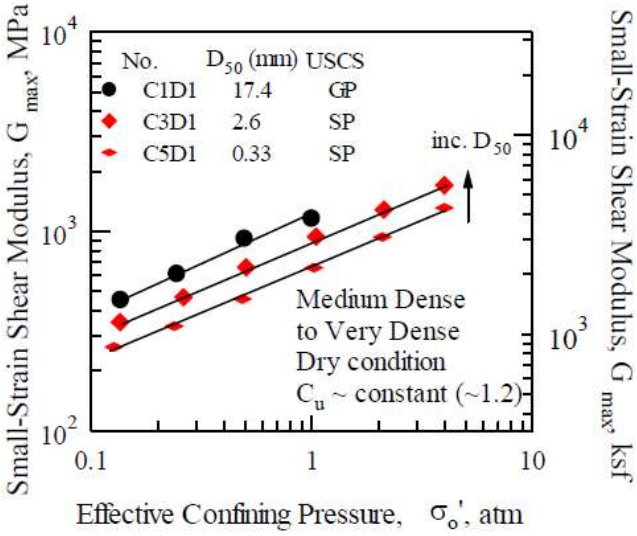

Figure 3.2: Variation in small-strain shear modulus with effective confining pressure of sandy and gravelly soils with a constant C_u of about 1.2 (from Menq, 2003)

$$G_{max} = C_{G1}(\sigma_0'/P_a)^{n_G} \tag{3.6}$$

where P_a is a reference mean effective confining pressure of one atm and n_G is a material dependent constant.

3.2.1.2 Effect of Soil Gradation Characteristics on G_{max} of Nonplastic Granular Soil

Gradation characteristics affect the small-strain shear modulus of nonplastic granular soil significantly. Soil gradation is usually expressed in terms of a coefficient of uniformity (C_u), and some grain size such as median grain size (D_{50}) or a representative particle diameter such as D_5. Hardin (1973) tested granular soils and aggregates in a free-free resonant column device. He found that D_5 is the significant particle diameter in defining G_{max} of granular soil. Iwasaki and Tatsuoka (1977) noted the significance of the gradation curve of granular soils on G_{max}. They found that C_u was a more important

parameter than D_{50}. Seed et al. (1986) tested gravels in cyclic triaxial device and he found that G_{max} for gravels are significantly higher than for sands. Chang and Ko (1986) tested sand specimens in a fixed-free resonant column device to investigate the effects of soil gradation on G_{max} of sand and gravelly soils. They reported that G_{max} is affected significantly by C_u and the effect of D_{50} was less pronounced. Kalinski and Hardin (2005) tested 17 specimen of sand and gravelly soil in a large-scale, free-free resonant column device. They found that G_{max} increases with increasing particle size for relatively clean uniform and graded gravels. They suggested to use D_5 as an approximate effective diameter in evaluating G_{max} based on their study.

Menq (2003) found in his study that the small-strain shear modulus of granular soil at a mean effective confining pressure of one atmosphere, C_{G1}, was not only a function of void ratio but also a function of gradation characteristics. The effects of gradation characteristics were investigated systematically by categorizing the specimens based on C_u and D_{50}. Figure 3.3 shows examples of $C_{G1} - e - D_{50}$ and $C_{G1} - e - C_u$ relationships. Menq also studied the effects of C_u and void ratio on n_G and he found that the effect of C_u on n_G was more dominant compared to the effect of void ratio (Figure 3.4). Based on these results, Menq proposed the following expression to evaluate G_{max} of granular soil as a function of σ_0', C_u, D_{50} and void ratio:

$$G_{max} = C_{G3} \cdot C_U^{b1} \cdot e^{x} \cdot \left(\frac{\sigma_0'}{P_a}\right)^{n_G} \tag{3.7}$$

where $C_{G3} = 67.1$ MPa, $C_U =$ coefficient of uniformity, $D_{50} =$ median grain size, $b1 =$ -0.20, $e =$ void ratio, $x =$-1-$(D_{50}/20)^{0.75}$ and $n_G = 0.48 \cdot C_U^{0.09}$. Figure 3.5 shows the change

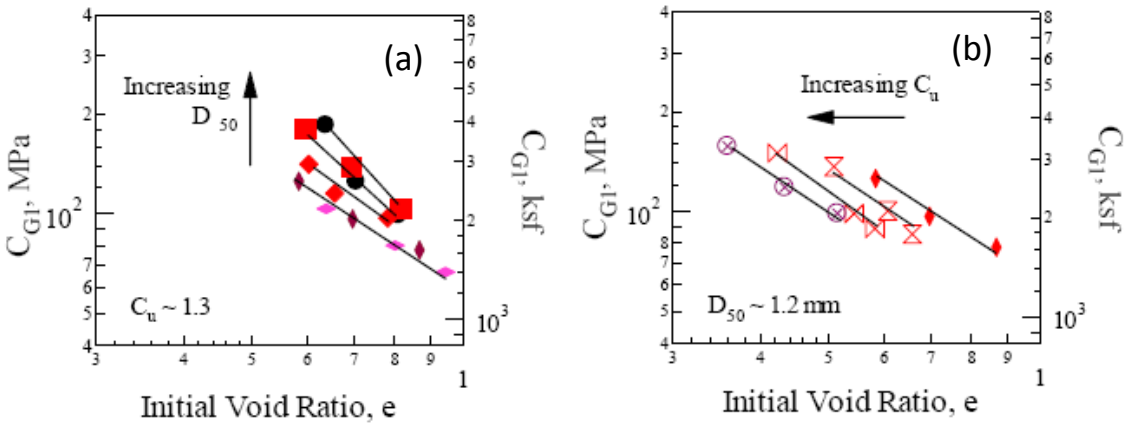

Figure 3.3: (a) Log C_{G1}- log (e) relationships for a constant C_u and (b) log C_{G1}- log (e) relationships for a constant D_{50} (from Menq, 2003)

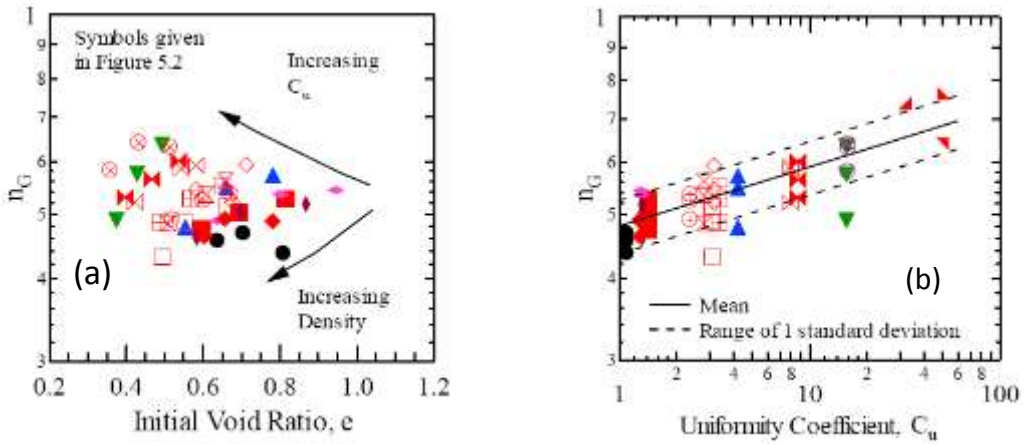

Figure 3.4: (a) Log n_G - (e) relationships and (b) log n_G - Log C_u relationships sand and gravelly soils (from Menq, 2003)

in G_{max} values for three different types of soil (SP, SW and GW) with σ_0' based on the formulation given in Equation 3.7.

The formulation proposed by Menq (2003) can be used in cases where there are no in-situ seismic measurements available. As noted earlier, G_{max} can be evaluated using

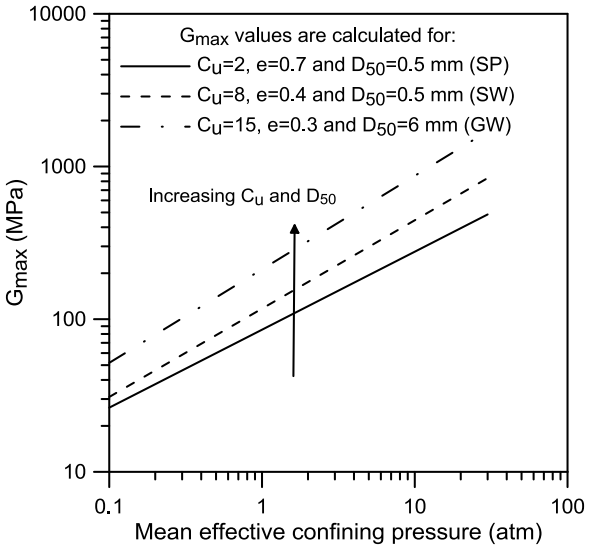

Figure 3.5: Effects of coefficient of uniformity, median grain size and mean effective confining pressure on G_{max} based on Menq's (2003) formulations

various field seismic methods such as downhole, crosshole and Spectral-Analysis-of-Surface-Waves (SASW) testing (Stokoe and Santamarina, 2000). Field measurements of dynamic soil properties in the small-strain range implicitly incorporate the effects of σ_0', gradation characteristics, void ratio, and cementation.

3.2.1.3 Effects of Sample Disturbance

Dynamic tests on intact specimens of granular soil are not commonly reported in the literature due to difficulties in obtaining undisturbed samples of granular soil. Therefore, comparisons of field tests and laboratory tests of granular soil at small-strain range are limited. The ground freezing method was perfected in Japan to extract high-quality undisturbed samples that was needed in the nuclear power plant industry (Ishihara, 1996).

Kokusho and Tanaka (1994) used ground freezing to obtain high-quality samples from four gravelly sites. Figure 3.6 shows values measured in the laboratory and values

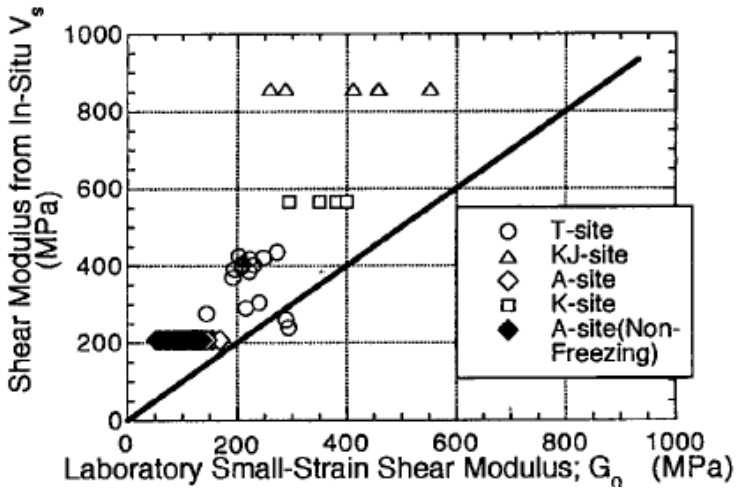

Figure 3.6: Comparison of small-strain shear modulus between in-situ and laboratory (from Kokusho and Tanaka, 1994)

measured in the field using suspension and downhole testing methods. It can be seen in the figure that the G_{max} values measured in the laboratory are smaller than the G_{max} values measured in the field. It should also be noted that G_{max} values of samples recovered from A-site with ground freezing are higher than the G_{max} values of samples from the same site recovered without ground freezing.

Darendeli (2001) compared shear wave velocities (V_s) of 40 samples measured in the laboratory with V_s values measured in-situ. This comparison, presented in Figure 3.7, shows that the V_s and G_{max} values from in-situ measurements are higher than those from laboratory tests. He also indicates that this difference increases as soil stiffness increases.

3.3 NONLINEAR BEHAVIOR OF GRANULAR SOILS

Shear modulus of granular soil becomes dependent on shear strain beyond the elastic threshold shear strain value, γ_t^e, with G decreasing as shear strain increases. Therefore, the shear stress- shear strain relationship becomes nonlinear. This nonlinearity is usually expressed in terms of shear modulus and shear strain as G-$log\ \gamma$ or G/G_{max}-

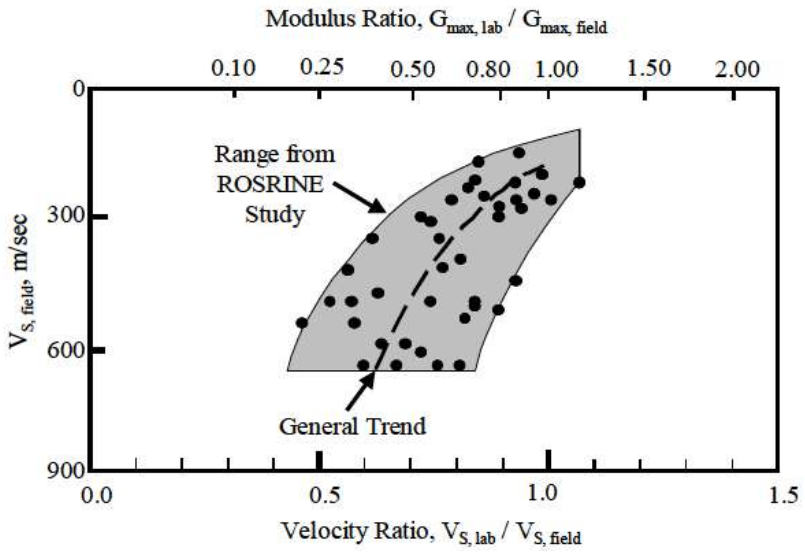

Figure 3.7: Variation of sampling disturbance expressed in terms of $V_{s,lab}/V_{s,field}$ and $G_{max,lab}/G_{max,field}$ with the in-situ shear wave velocity (from Darendeli, 2001)

$log\,\gamma$ which are called as shear modulus reduction curve and normalized shear modulus reduction curve, respectively.

The G/G_{max}-$log\,\gamma$ curves are usually expressed in semi-logarithmic plots where the shear strain starts at a very small value (0.00001-0.0001%) and extends approximately to several percent. In geotechnical earthquake engineering, the G/G_{max}-$log\,\gamma$ curves are usually separated into three ranges (Figure 3.8). The first range is where G is strain independent, is called "linear" and it extends up to an elastic threshold strain value, γ_t^e, as noted earlier. The second range is called "nonlinear elastic" and it extends from γ_t^e to a cyclic threshold shear strain value, γ_t^c. The range beyond γ_t^c generally is denoted simply as "nonlinear". However, if the G/G_{max}-$log\,\gamma$ curves are converted to shear stress-shear strain (τ-γ) curves to be used in problems where the shear strains extend to strains well beyond γ_t^c (say 20 to 30 times γ_t^c), another distinction of the strain

ranges should be made. This distinction is needed in problems where the soil mass goes under relatively large deformations such as footing settlements considered in this study. In this case, the G/G_{max}-$log\ \gamma$ curves (or τ-γ curves) can be separated into four ranges as: (1) "linear", (2) "nonlinear elastic", (3) "moderately nonlinear" and (4) "highly nonlinear" parts. The linear part extends to strains up to γ_t^e. The range between γ_t^e and γ_t^c is denoted as "nonlinear elastic". and beyond γ_r, G/G_{max}-$log\ \gamma$ (or τ-γ curves) curves become highly nonlinear. This type of distinction of G/G_{max}-$log\ \gamma$ (or τ-γ curves) is presented in Figure 3.9.

The G/G_{max}-$log\ \gamma$ relationships can be evaluated in the laboratory using tests such as Resonant Column, Torsional Shear or Triaxial tests with local measurements. If there is no laboratory test available, G/G_{max}-$log\ \gamma$ relationships are usually found from empirical correlations. There are also recent studies on determining the G/G_{max}-$log\ \gamma$ relationships in-situ (Kurtulus and Stokoe, 2008; Park, 2010).

3.3.1 Comparison of Field and Laboratory G/G_{max}-$log\ \gamma$ Relationships

Dynamic laboratory testing methods, such as the torsional resonant column, have made it possible to investigate the nonlinear behavior of granular soils over a wide shear strain range (i.e., 0.00005 to 0.2 %). On the other hand, there are few studies to determine the nonlinear dynamic soil properties directly in the field. Henke and Henke (1993) developed a method called the "torsional-cylindrical-impulse-shear-test (TCIST). In the TCIST, an instrumented probe is pushed in the soil and is exited at different levels of torsional impulses. Comparison of the modulus reduction curves measured in the field by Henke and Henke (1993) with those obtained in the laboratory and from empirical curves shows a considerable difference.

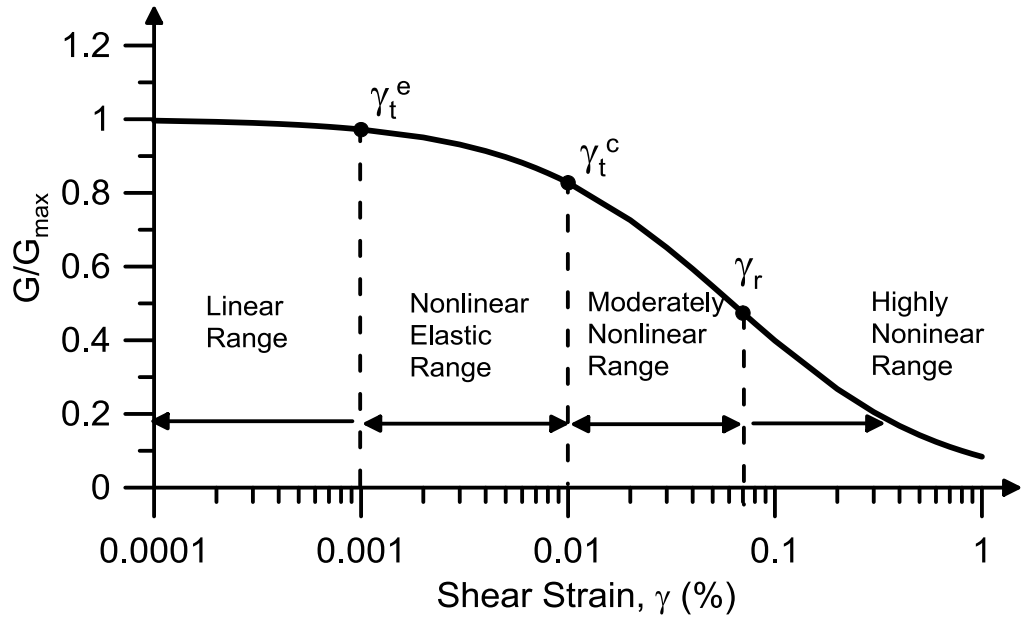

Figure 3.8: Idealized $G/G_{max} - log\,\gamma$ curve with the linear, nonlinear elastic, moderately nonlinear and highly nonlinear ranges

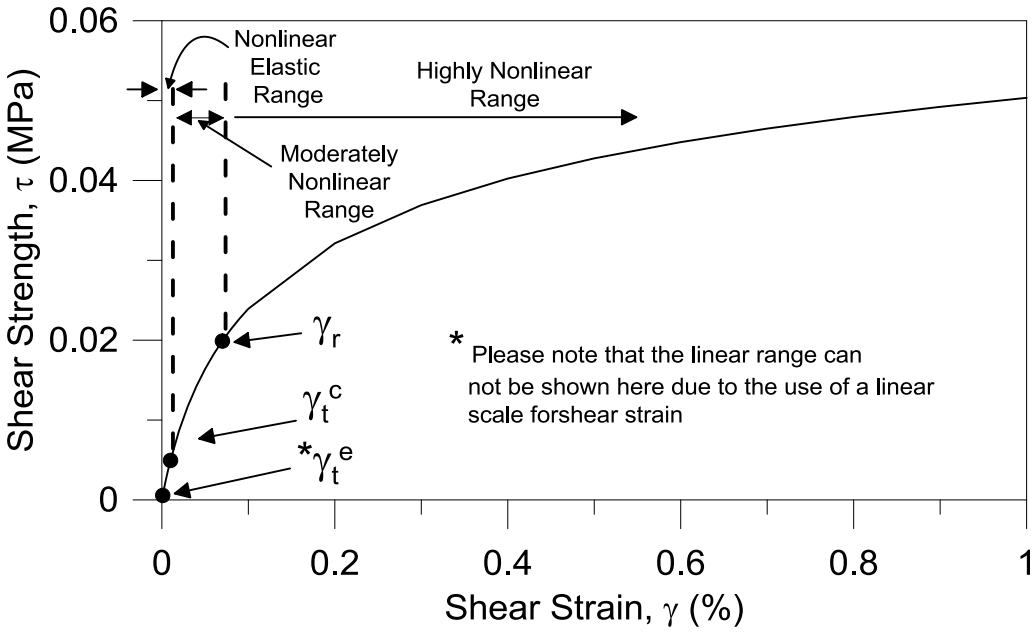

Figure 3.9: Typical $\tau - \gamma$ curve acquired using $G/G_{max} - log\,\gamma$ relationship and the linear, nonlinear and highly nonlinear ranges on $\tau - \gamma$ curve

Another attempt to measure nonlinear dynamic properties in-situ was made by Salgado et. al (1997). They used a method called the "large-strain-seismic-crosshole-test" (LSCT) to measure nonlinear dynamic properties.

Kurtulus and Stokoe (2008) developed a method where they used a drilled shaft as a cylindrical, axisymmetric source for shear loading of the soil. They used a vibroseis truck as dynamic energy source and they conducted small-strain and intermediate-strain seismic testing to measure G_{max}, G-$log\ \gamma$ and G/G_{max}-$log\ \gamma$ relationships in-situ. The soil was a nonplastic silt (ML) with silty sand (SM) layers. The shear wave velocities (V_s) measured in the field were higher than those measured in the laboratory. The authors attributed this difference mainly to sample disturbance. They also pointed out that differences in effective stresses or capillary stresses between laboratory and field conditions could cause this deviation between laboratory and field values of V_s . However, they observed that G/G_{max}-$log\ \gamma$ relationships from laboratory and field measurements were similar. The field and laboratory relationships also followed trends suggested by empirical relationships, such as Darendeli (2001) and Menq (2003). Figure 3.10 shows the comparison of G/G_{max}-$log\ \gamma$ relationship obtained in the field with the same relationship obtained in the laboratory. Figure 3.11 shows the comparison of G/G_{max}-$log\ \gamma$ curves obtained at the field with empirical curves suggested Darendeli (2001).

Park (2010) completed a similar study at the University of Texas to measure the in-situ linear and nonlinear shear moduli values of silty sands and cemented alluvium. The method consists of applying static vertical and dynamic horizontal loads on cast-in-place reinforced concrete footings and measuring the dynamic response of the soil with embedded sensors beneath the footings. An initial test was conducted at Fitzpatrick Ranch, located in Austin, TX. The soil at this site is poorly graded silty sand (SM-SP).

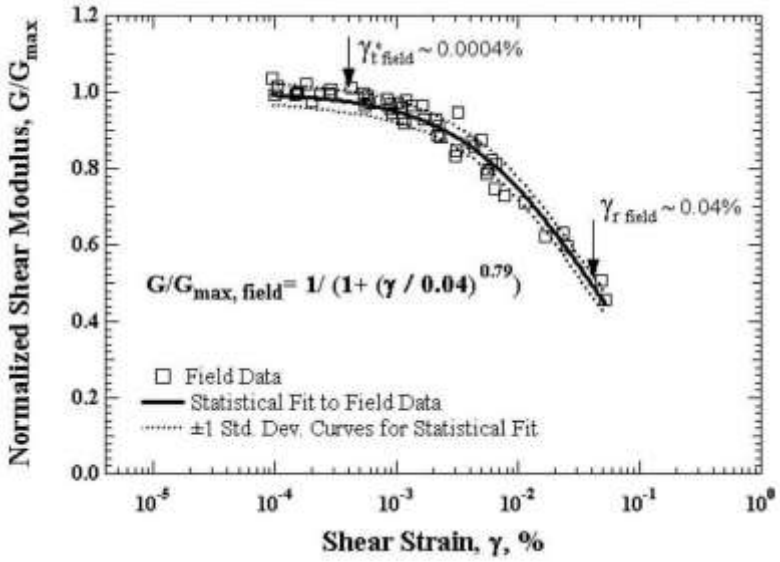

Figure 3.10: Comparison of Shear Modulus Reduction Curves in the Field and in the Laboratory (from Kurtulus and Stokoe, 2008)

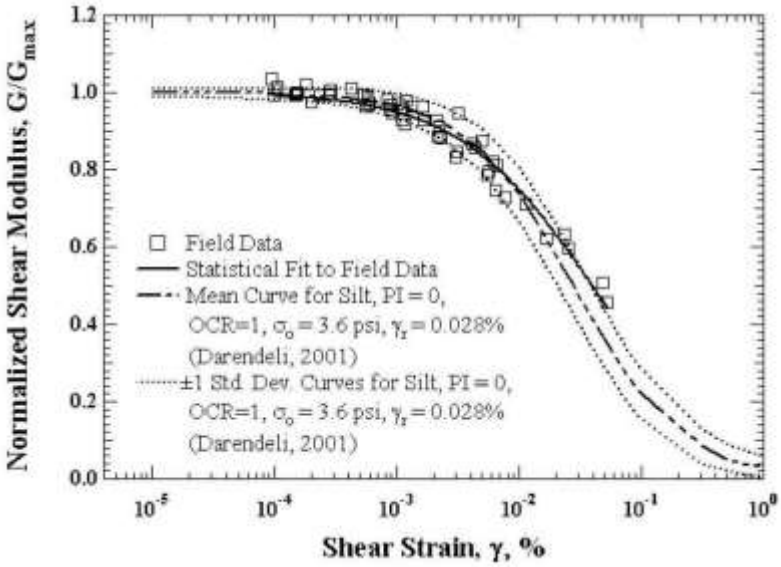

Figure 3.11: Comparison of Field Data with Empirical Curves for Silts from Darendeli (2001) (from Kurtulus and Stokoe, 2008)

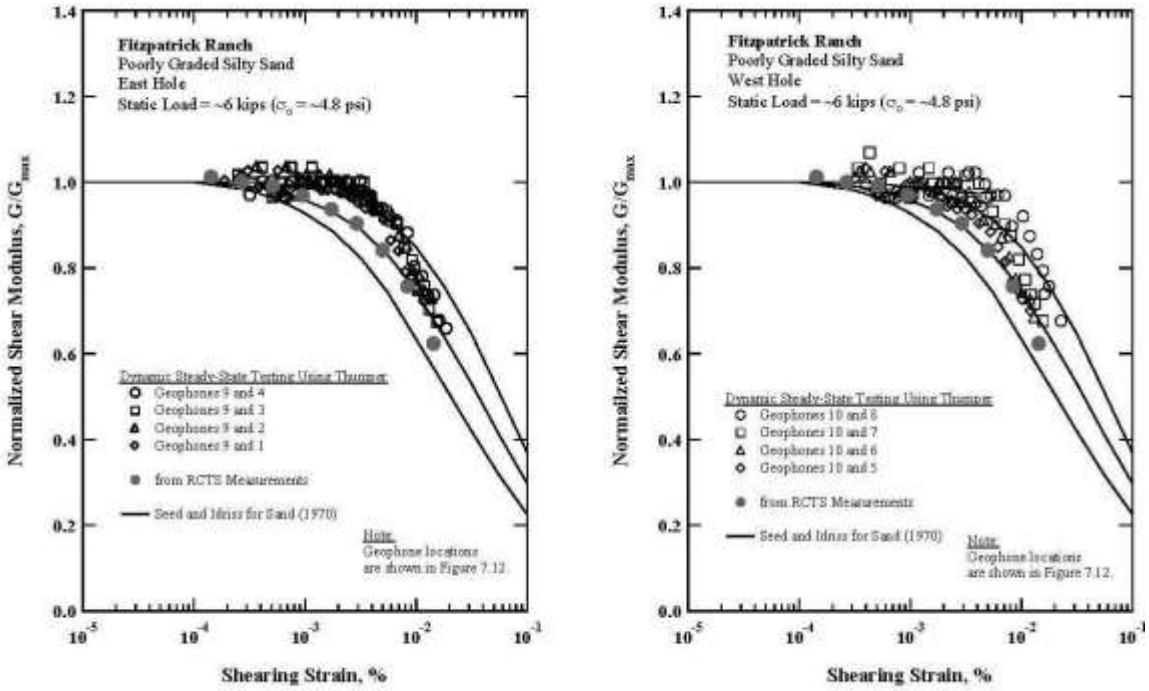

Figure 3.12: The G/G_{max}-$log\ \gamma$ relationships developed from the linear and nonlinear dynamic tests at Fitzpatrick Ranch (from Park, 2010)

Figure 3.12 shows the comparison of normalized modulus reduction curves measured in the field with those measured in the laboratory. As seen in the figure, there is some difference between the curves. Park attributed the difference primarily to the fact that soil sampling was performed after shaking the soil and disturbing the soil skeleton. The second part of Park's study involved evaluating the linear and nonlinear shear moduli at three sites at Yucca Mountain, Nevada. The soil at these sites is a cemented alluvium. Details of the site and testing procedure can be found in Park (2010). Figure 3.13 shows the comparison of normalized shear modulus curves from field tests with those from

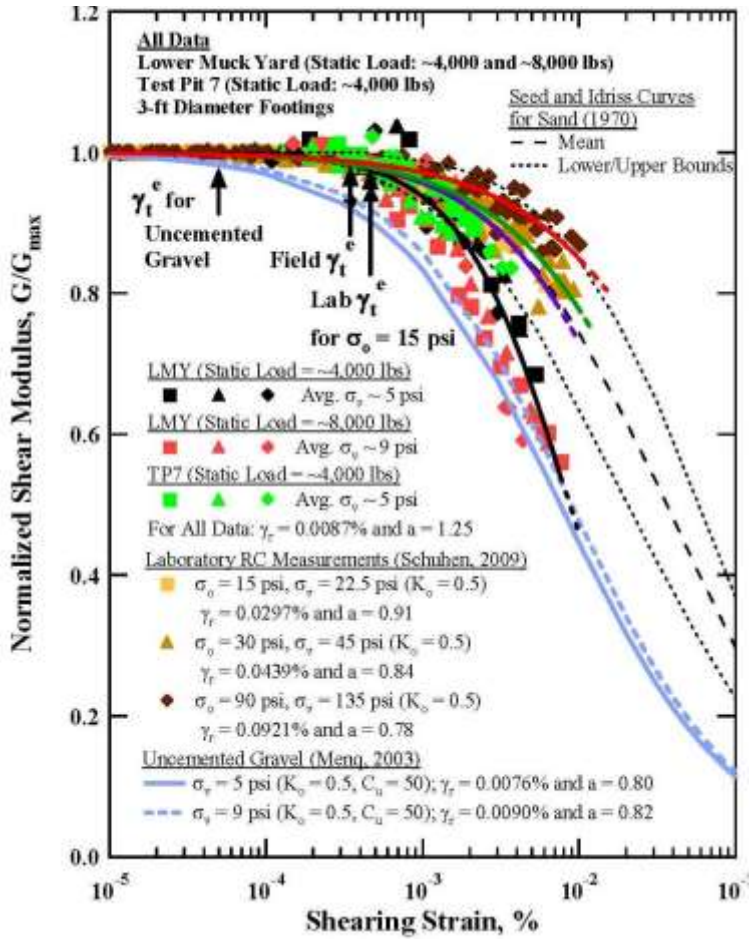

Figure 3.13: Comparison of the G/G_{max}-$log\ \gamma$ relationships of the cemented alluvium from field dynamic tests at LMY and TP7 and laboratory RC measurements

laboratory tests. Empirical curves proposed by Menq (2003) are also included for comparison purposes.

If there are no in-situ nonlinear dynamic measurements, of G-$log\ \gamma$, then G_{max} and G/G_{max}-$log\ \gamma$ relationships measured in the laboratory are correlated with G_{max} measured *in–situ*. In this correlation it is assumed that the G/G_{max}-$log\ \gamma$ relationship from

laboratory measurements have the same shape as the in-situ G/G_{max}-$log\,\gamma$ relationship. This correlation is expressed as:

$$G_{\gamma,field} = \left(G_{max,field}/G_{max,lab}\right) \cdot G_{\gamma,field} \tag{3.8}$$

While using the correlation presented in Equation 3.8, effective stresses, capillary stresses, anisotropy and cementation in the field should be considered as these parameters affect the shear moduli and the shape of the G-$log\,\gamma$ relationship.

3.3.2 Parameters Affecting the Nonlinear Shear Modulus of Granular Soil

Due to the difficulties in soil sampling and testing of granular soil, the number of studies investigating the parameters affecting the nonlinear dynamic shear modulus of granular soil is limited. One of the earliest comprehensive studies of nonlinear shear modulus and the important parameters affecting the G-$log\,\gamma$ relationship was conducted by Hardin and Drnevich (1972). They tabulated the parameters affecting the nonlinear shear modulus according to their relative importance (Table 3.3). They noted that the three most important parameters affecting nonlinear shear modulus of granular soils are strain amplitude, confining pressure and void ratio. Kokusho (1980) conducted cyclic triaxial tests on Toyura Sand to investigate the effect of confining pressure on nonlinear shear modulus. Figure 3.14 shows the normalized shear modulus reduction curves reported by Kokusho (1980). It can be seen in the figure that the normalized shear modulus gets more linear with increasing confining pressure for Toyura sand. Tanaka (1987) tested reconstituted gravelly soils under different effective isotropic confining pressures and found that the effective isotropic confining pressure has a significant impact on the modulus reduction curves. Seed and Idriss (1970) proposed a mean

Table 3.3 Parameters affecting the nonlinear soil behavior and their relative importance (from Hardin and Drnevich, 1972)

Parameter	Impact on Modulus		
	Clean Sands	Cohesive Soils	
Strain Amplitude	***	***	
Mean Effective Confining Pressure	***	***	
Void Ratio	***	***	*** Very Important
Number of Loading Cycles	+	*	** Less Important
Degree of Saturation	*	***	* Relatively Unimportant
Overconsolidtaion Ratio	*	**	+ Relatively Unimportant Except for Saturated Sands
Effective Strength Envelope	**	**	
Octahedral Shear Stress	**	**	- Unknown
Frequency of Loading (above 0.1 Hz)	*	*	
Other Time Effects (Thixotropy)	*	**	
Grain Characteristics, Size, Shape, Gradation, Mineralogy	*	*	
Soil Structure	*	*	
Volume Change Due to Shearing Strain below 0.5%	-	*	

normalized shear modulus reduction curves for sands and they also proposed a range. The upper and lower limits can be attributed to the effects of gradation characteristics, uncertainties in the measurements, confining pressure and variability in shear modulus reduction curves (Darendeli, 2001). Seed et al. (1986) re-analyzed these curves and they proposed a set of shear modulus reduction curves for sands and gravels. These curves are shown in Figure 3.15.

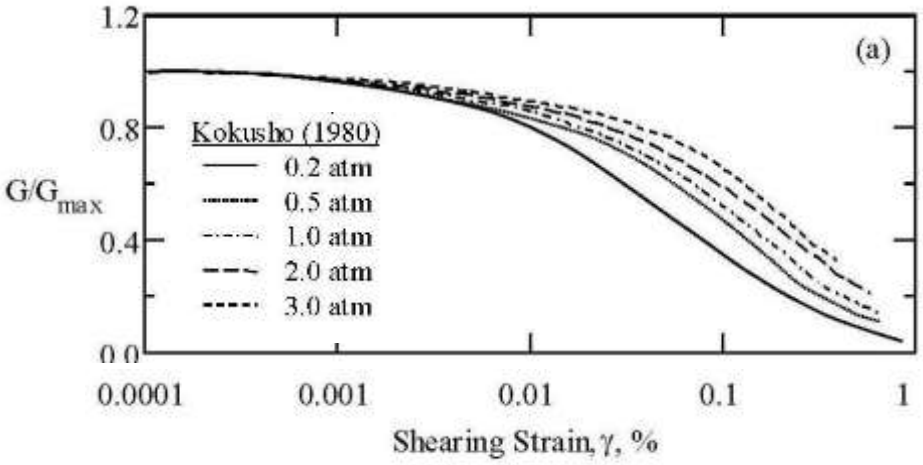

Figure 3.14: Effect of confining pressure on normalized modulus reduction curves (from Kokusho, 1980)

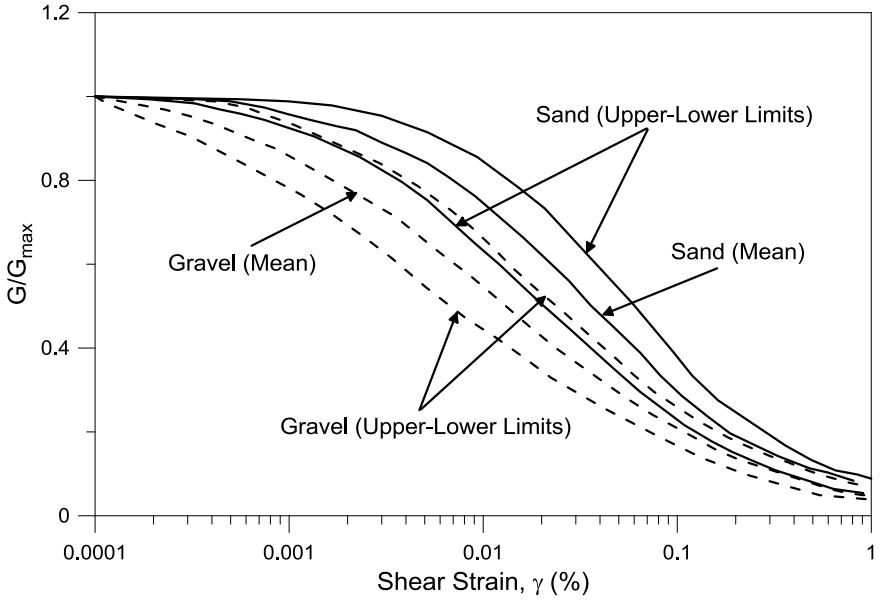

Figure 3.15: Normalized Modulus Reduction Curves Proposed by Seed et al. (1986) (Note: $\sigma_o' \sim$ 1 atm)

3.3.2 Empirical Relationships for Nonlinear Shear Modulus of Granular Soil

Hardin and Drnevich (1972) conducted one of the earliest studies on nonlinear shear modulus of granular soil. They proposed an empirical formulation to estimate the

nonlinear shear modulus of granular soil in terms of normalized shear modulus, shear strain and shear strength of the soil. They suggested using a modified hyperbolic relationship as:

$$\tau = \frac{\gamma}{\frac{1}{G_{max}} + \frac{\gamma}{\tau_{max}}} \tag{3.9}$$

where γ is shear strain, τ is shear stress, G_{max} is the small-strain shear modulus and τ_{max} is the shear strength. If the expression in Equation 3.9 is rearranged, the following expression can be obtained:

$$\frac{G}{G_{max}} = \frac{1}{1 + \frac{\gamma}{\gamma_r}} \tag{3.10}$$

where γ_r is the reference shear strain and is defined as $\gamma_r = \tau_{max}/G_{max}$. This hyperbolic model was modified by Darendeli (2001) based on a large dataset of combined resonant column and torsional shear tests (RCTS) as follows:

$$G/G_{max} = \frac{1}{1 + \left(\frac{\gamma}{\gamma_r}\right)^a} \tag{3.11}$$

where a = curvature coefficient; γ_r = reference shear strain which is equal to γ at $G/G_{max} = 0.5$; and G is the shear modulus at a shear strain value of γ. Darendeli studied the parameters affecting the value of γ_r by running statistical analyses on a large data set of combined resonant column and torsional shear tests performed only at the University of Texas. Darendeli reported mean and standard deviations for the normalized shear

modulus reduction curves. Since Darendeli's (2001) study was mainly focused on cohesive soils, the modified hyperbolic model was further refined for sands and gravels by Menq (2003). Using a large-scale, free-free resonant column device that he developed, Menq tested 59 reconstituted specimens of sands and gravels. He studied the effects of confining pressure, gradation characteristics of the soil, void ratio and sample disturbance on the normalized shear modulus curves of granular soil. Menq proposed an empirical relationship which is discussed in detail below

3.3.3 Empirical Relationships for Nonlinear Shear Modulus of Nonplastic Granular Soil Proposed by Menq (2003)

Menq (2003) tested 59 reconstituted specimens of nonplastic granular soil in a large-scale, free-free resonant column device to investigate the dynamic properties of granular soil in the small- to-moderate-strain ranges. The parameters affecting the small-strain properties of the soil are discussed in Section 3.2 In this section, Menq's (2003) study of the nonlinear behavior of granular soil in moderate-strain range will be discussed.

Menq (2003) used the modified hyperbolic formula presented in Equation 3.3 to define the nonlinear behavior of granular soil in the moderate-strain range (from γ_t^e to γ_r) in terms of $G/G_{max} - \log\gamma$ relationships. The two parameters in Equation 3.11; reference shear strain, γ_r, and curvature coefficient, "a", were studied by determining the effects of mean effective confining pressure, void ratio and gradation characteristics on these parameters. The reference shear strain, γ_r, is the shear strain where the value of G/G_{max} is equal to 0.5. Although, it does not provide physical information about the soil, it is very useful in defining the nonlinearity of the $G/G_{max} - \log\gamma$ relationships. On the other

hand, the curvature coefficient is a scaling factor for the shape of the $G/G_{max} - \log\gamma$ curve, mainly over the range of γ_t^e to γ_r.

Figure 3.16 shows the effects of C_u, D_{50} and void ratio on γ_r. Figure 3.16a shows the effect of void ratio on γ_r for specimens with approximately same C_u (~1.3) and different D_{50} values. On the other hand, Figure 3.16b shows the effect of void ratio on γ_r for specimens with approximately same D_{50} (~1.2 mm) and different $C_u$values. As seen

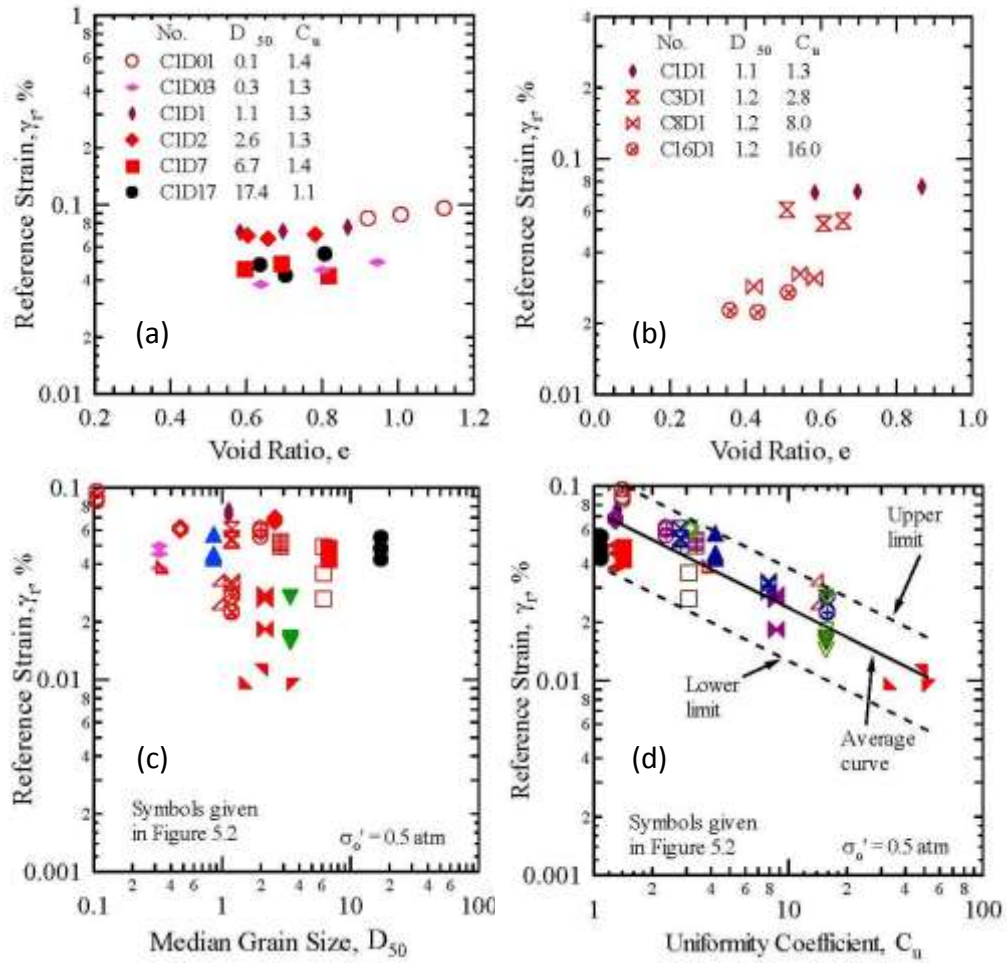

Figure 3.16: Variation of reference strain with (a) void ratio where C_u is constant, (b) void ratio where D_{50} is constant, (c) D_{50} and (d) C_u (from Menq, 2003)

in these figures, void ratio does not have a significant effect on γ_r. Figure 3.16c and 3.16d present the effects of the gradation characteristics of granular soil on γ_r . As seen in the figures, C_u is a significant parameter affecting γ_r of granular soil while D_{50} does not exhibit any consistent and discernable effect on γ_r. The effects of the gradation characteristics and void ratio on the curvature coefficient,"a", was also investigated by

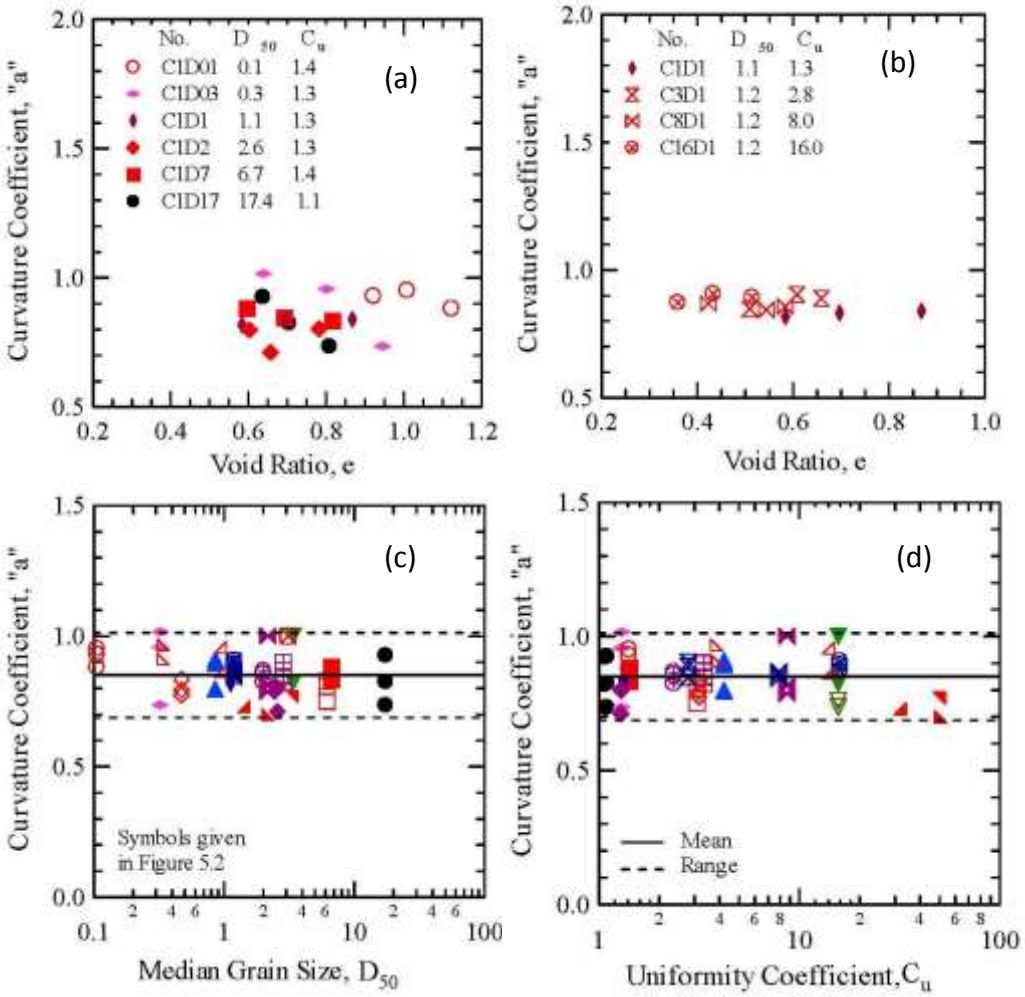

Figure 3.17: Variation of curvature coefficient "a" with (a) void ratio where C_u is constant, (b) void ratio where D_{50} is constant, (c) D_{50} and (d) C_u (from Menq, 2003)

Menq (2003). The variation of "a" with void ratio, C_u and D_{50} is given in Figure 3.17. Figure 3.17a shows the effect of void ratio on "a" of soils with an approximately constant C_u (~1.3) and different D_{50} values whereas Figure 3.17b shows the effect of void ratio on "a" of soils with an approximately constant D_{50} (~1.2 mm) and different C_u values. As seen in these figures, there is no trend between the void ratio and "a" values of granular soils. The effects of C_u and D_{50} on "a" are presented in Figure 3.1c and 3.17d. It is interesting to note that the gradation characteristics do not affect the "a" value of granular soils.

Another important parameter affecting the normalized shear modulus of granular soil is mean effective confining pressure. Menq (2003) investigated the effects of mean effective confining pressure on γ_r and "a", thus he found how the nonlinearity of the shear modulus is changing with mean effective confining pressure. Figure 3.18 shows the effects of mean effective confining pressure on γ_r and "a". It should be noted that Darendeli (2001) proposed a constant value of "a" whereas Menq (2003) suggest that "a" is a function of mean effective confining pressure.

Menq (2003) analyzed the tests results systematically by grouping them according to gradation, void ratio and mean effective confining pressures. Using the least square estimates method, he proposed the following relationships to calculate γ_r and "a" for nonplastic granular soil:

$$\gamma_r = 0.12{C_u}^{-0.6}\left(\frac{\sigma_0'}{P_a}\right)^{0.5{C_u}^{-0.15}} \tag{3.12}$$

$$a = 0.86 + 0.1\,log\left(\frac{\sigma_0'}{P_a}\right) \tag{3.13}$$

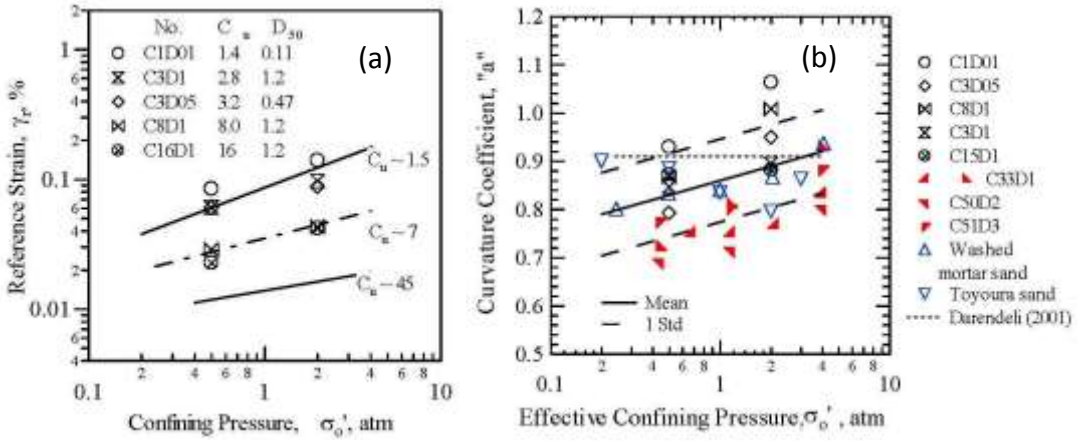

Figure 3.18: Variation of (a) reference strain with effective confining pressure (b) curvature coefficient "a" with effective confining pressure

where γ_r is in %; C_u = uniformity coefficient; σ_0' = mean effective confining pressure in the same units as P_a; and P_a = reference mean effective confining pressure (1 atm). The relationships presented in Equation 3.12 and 3.13 indicate that $G/G_{max} - \log\gamma$ curves are mainly a function of σ_0' and C_u. Variation of $G/G_{max} - \log\gamma$ curves with σ_0' and C_u based on Menq's (2003) formulation for three types of granular soil are presented in Figure 3.19a and 3.19b, respectively. The $G/G_{max} - \log\gamma$ curves in Figure 3.19 show that the linearity of these curves increases with increasing σ_0' and decreases with increasing C_u. Another way to look at these curves is to plot $G - \log\gamma$ and $\tau - \gamma$ relationships obtained using the curves. The $G - \log\gamma$ relationships for the soils given in Figure 3.19 are determined by multiplying the G/G_{max} values with G_{max} found using Equation 3.7. The effect of σ_0' and C_u on $G - \log\gamma$ relationships are given in Figure 3.20a and 3.20b, respectively. It should be noted that the G values for a given soil are lower for smaller confining pressures at all strain ranges. On the other hand, for soils with different C_u

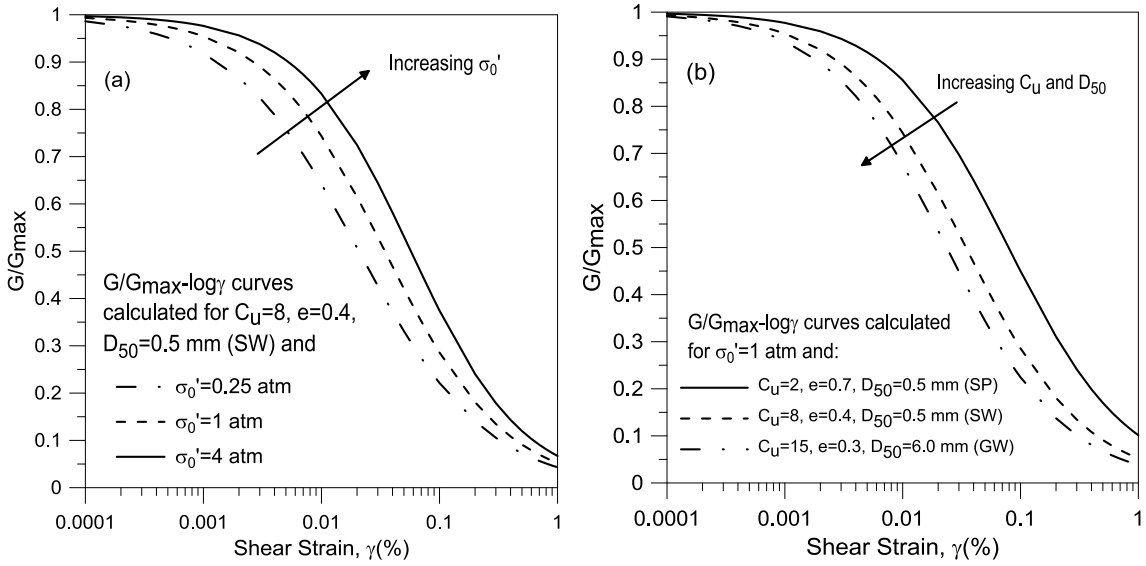

Figure 3.19: Effects of (a) mean effective confining pressure and (b) coefficient of uniformity on $G/G_{max} - \log\gamma$ curves based Menq's (2003) formulation

and D_{50} values and under the same mean effective confining pressure, G values are higher at smaller strains and they become smaller at larger strains with increasing C_u and D_{50} values. The $G - \log\gamma$ relationships in Figure 3.20 can be converted to $\tau - \gamma$ relationships with $\tau = G \cdot \gamma$. These $\tau - \gamma$ relationships are presented in Figure 3.21. The increase in the shear strength of the soil given in Figure 3.20a is a result of the increase of G_{max} and increase in the linearity of $G/G_{max} - \log\gamma$ curves due to mean effective confining pressure increase. If the $\tau - \gamma$ relationships of three types of granular soil (SP,SW and GW) in Figure 3.20b are investigated, it is seen that SW has smallest shear strength. Moreover, GW has a smaller strength than SP, which is the opposite of the general trend in shear stress-shear strain behavior of granular soil. This behavior is the combined result of the increase of G_{max} with increasing C_u and the decrease in the nonlinearity of the

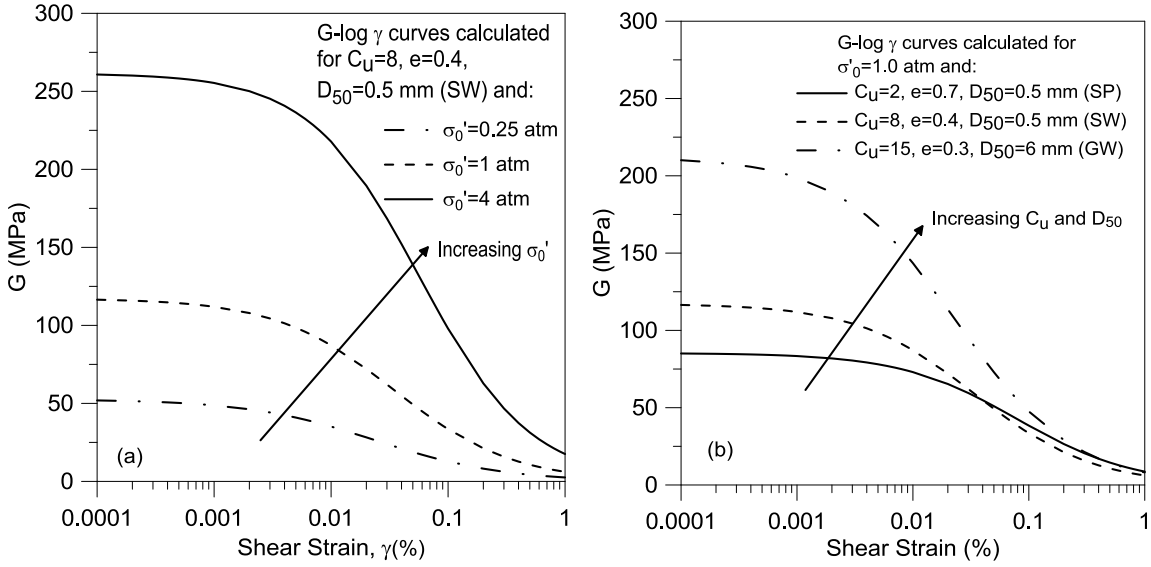

Figure 3.20: Effects of (a) mean effective confining pressure and (b) coefficient of uniformity on $G - \log\gamma$ curves based Menq's (2003) formulation

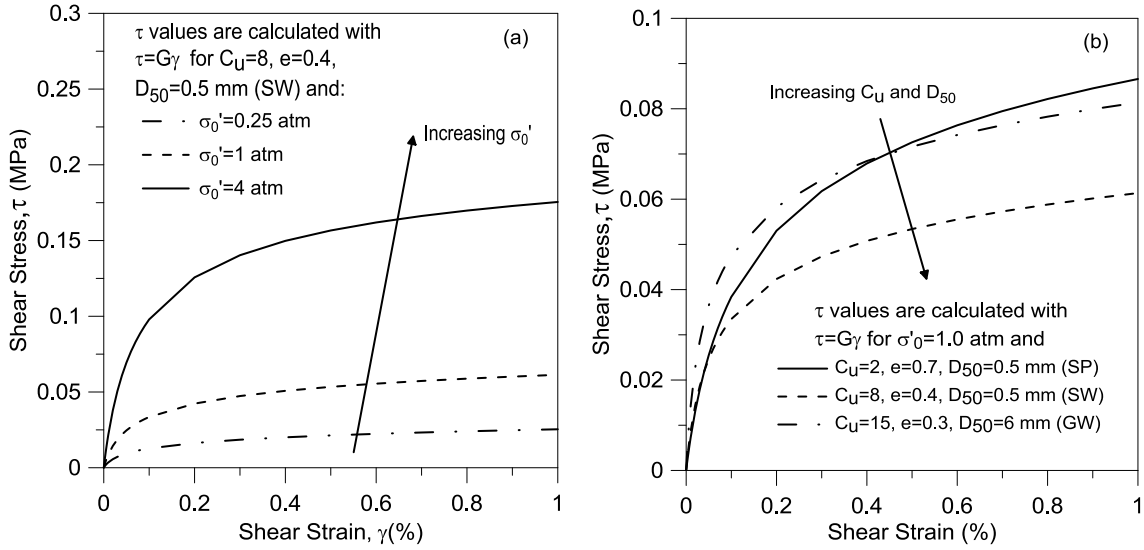

Figure 3.21: Effects of (a) mean effective confining pressure and (b) coefficient of uniformity on $\tau - \gamma$ curves based Menq's (2003) formulation

$G/G_{max} - \log\gamma$ curves with increasing C_u. This indicates that the $G/G_{max} - \log\gamma$ curves might need to be modified for problems that extend to larger strains, such as footing settlements, to adjust for the shear strength value of the soil. Since the $G/G_{max} - \log\gamma$ relationships are controlled by γ_r and "a" values, the acquired $\tau - \gamma$ curves are also a function of these parameters. To manifest this dependency, one of these two parameters is varied while the other one is kept constant and the $G/G_{max} - \log\gamma$ relationships are plotted (Figure 3.22). The acquired $\tau - \gamma$ curves are shown in Figure 3.23. As seen in Figure 3.21a, the nonlinearity of the $G/G_{max} - \log\gamma$ curves increase with increasing γ_r at all strains. However, $G/G_{max} - \log\gamma$ curves become more nonlinear with increasing "a" up to strains equal to γ_r, however they become less nonlinear with increasing "a" at strains beyond γ_r (Figure 3.22b). The $\tau - \gamma$ curves shown in Figure 3.23 present that the shear stress response of granular soil obtained with $G/G_{max} - \log\gamma$ relationships are highly dependent on γ_r and "a". The value of γ_r is obtained with confidence in most of the RCTS tests since most of these tests extend to strains beyond γ_r. On the other hand, the value of "a" comes from the shape of the $G/G_{max} - \log\gamma$ curves that usually do not extend beyond 0.1-0.3 % of shear strain and therefore the value of "a" can be different at larger strains. One should be careful when converting $G/G_{max} - \log\gamma$ curves into $\tau - \gamma$ curves to use in problems involving large strains, such as footing settlements as in this study.

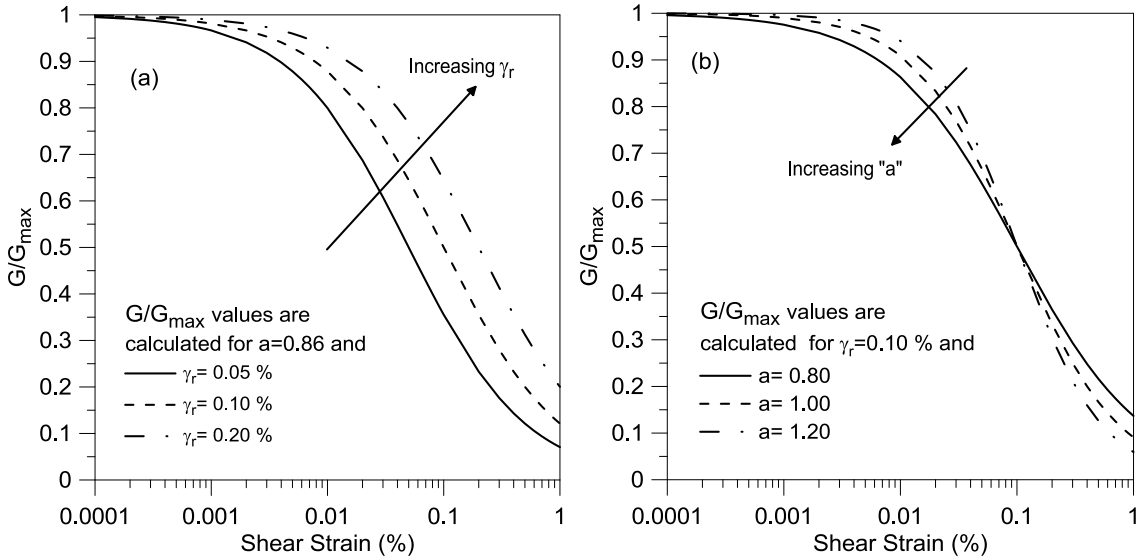

Figure 3.22: Effects of (a) reference shear strain, γ_r and (b) curvature coefficient, "a" on $G/G_{max} - \log\gamma$ curves based on Menq's (2003) formulation

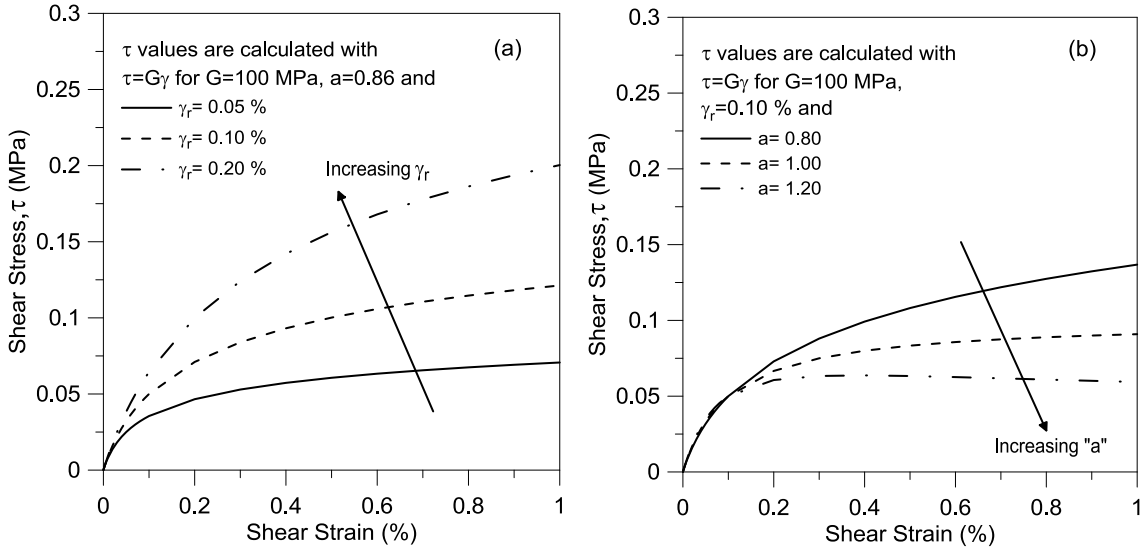

Figure 3.23: Effects of (a) reference shear strain, γ_r and (b) curvature coefficient, "a" on $\tau - \gamma$ curves based on Menq's (2003) formulation

3.4 SUMMARY

Dynamically measured shear modulus of granular soil in small-strain (linear) and large-strain (nonlinear) ranges are discussed in this chapter. The parameters affecting the small-strain shear modulus (G_{max}) of granular soil are presented. Empirical formulations to determine (G_{max}) of granular soil are discussed next. It is shown that G_{max} is a function of mean effective confining pressure, grain characteristics and void ratio. Menq's (2003) proposed empirical relationship to determine G_{max} is presented briefly. The effect of sample disturbance on G_{max} is introduced by comparing the laboratory and in-situ test results. Shear modulus of granular soil at large strains (nonlinear range) is discussed based on the studies in the literature. The parameters controlling the shear modulus at large strains are presented. The modified hyperbolic model first proposed by Darendeli (2001) and later refined by Menq (2003) for granular soil is discussed next. The $G/G_{max} - log\,\gamma$ curves proposed by Menq (2003) are studied in detail since they take the gradation characteristics of granular soils into account. The effect of the reference strain, γ_r, and the curvature coefficient, "a" on $G/G_{max} - log\,\gamma$ curves and on $\tau - \gamma$ response derived from these curves are presented. It is shown that these parameters have a great impact on the $\tau - \gamma$ response of granular soil and "a" values at larger strains might need to be modified if $G/G_{max} - log\,\gamma$ curves are being used in problems where the expected strains are well beyond γ_r.

Chapter 4: Development of the Model of Dynamically Measured Properties (MoDaMP)

4.1 INTRODUCTION

Deformations of a soil mass can be determined if the stresses and stress-strain relationships of the soil layers are known. Shear failure is usually the governing failure mode in soils. Therefore, shear stress-shear strain response of soils provides the main parameters for the design in many geotechnical applications. Shear stress-shear strain response of soils is evaluated from in-situ and/or laboratory tests. Parameters such as shear modulus, angle of friction, cohesion or parameters pertaining the plasticity and viscous effects of the soil are determined based on these tests. A set of mathematical relationships, called constitutive models, are then formulated to model the stress-strain response of the soil to be used in analytical or numerical analyses.

One of the key parameters in many constitutive models is the shear modulus of the soil. Shear modulus can be defined as the slope of the shear stress-shear strain curve. However, the stress-strain responses of soils are highly nonlinear. The shear modulus decreases as the shear strain increases as explained in Chapter 3. Hence, in a deformation based analysis, the value of the shear modulus used in the analysis should be compatible with the expected strain level. It should be noted that field tests and laboratory tests are generally performed at different strain levels depending on the type of test. Figure 4.1, from Mayne (2001), shows typical strain levels associated with different field and laboratory tests. Clearly, the values of shear modulus determined with different tests or with the same test at different operating strain levels will be different. Therefore, it is crucial to use a strain-dependent shear modulus value in design, especially in deformation-based analysis.

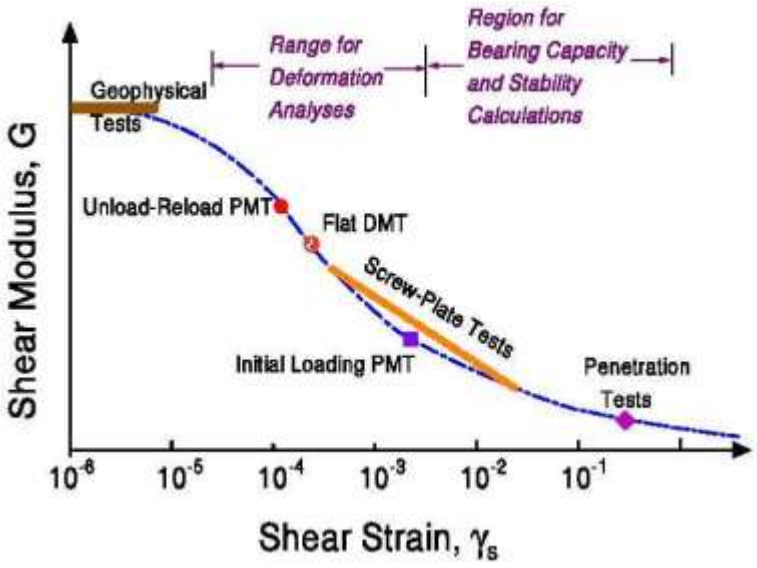

Figure 4.1: Shear modulus reduction with increasing shear strain and typical shear strain levels associated with different field and laboratory tests (from Mayne, 2001)

In this chapter, development of a constitutive model based on normalized shear modulus reduction curves for granular soil is presented. First, the general relationships between stress and strain are introduced. Next, general trends of Poisson's ratio and how values change with strain level based on laboratory and in-situ measurements are discussed. The implied Poisson's ratio derived from the relationships between $G/G_{\max} - \log\gamma$ bulk modulus (K) and constrained modulus (M) are introduced and discussed. The tangential stiffness matrix based on $G/G_{\max} - \log\gamma$ relationships and Poisson's ratio is formulated. Then, the general procedure for creating user defined-soil models (UDSM) in PLAXIS is presented. Finally, implementation of the constitutive model based on dynamically measured soil properties, given the acronym MoDaMP, and verification of

the model with element tests are discussed. A summary of the chapter is presented at the end of the chapter.

4.2 STRESSES AND STRAINS

Stresses and strains in a material are correlated through mathematical formulations such as elasticity, plasticity and viscosity or a combination of them which are called constitutive models. In soil mechanics, the soil is considered as a continuum and stresses and strains are calculated using constitutive models which are based on observed trends in actual tests on soils.

Elastic theory relies on the assumption that there is a one-to-one correspondence between stress and strain, or in other words, the strains are recoverable. The first order approximation to model a material behavior is linear elasticity. If a material behavior is linear elastic, the elastic modulus of this material is constant and all strains will be recovered upon unloading. However, shear stress-shear strain ($\tau - \gamma$) response of soils is highly nonlinear; therefore a linear elastic model is a crude first order approximation and cannot accurately model soil behavior as a stand-alone model. On the other hand, the nonlinear behavior of granular soil can be modeled by using a nonlinear elastic model, where the shear modulus is a function of the shear strain, stress state and gradation characteristics, as proposed in this study. It should be noted that the nonlinear elastic models assume that the strains are recoverable which contradicts the observations made in the field and laboratory tests. To overcome this difficulty in a model, there should be a distinction between the loading and unloading behavior of the soil. This distinction can be achieved by utilizing different shear modulus for loading and unloading as it is done in this study. The formulation used herein to define the loading and unloading/reloading shear moduli of soil is presented in Section 4.4.

Another approach to model the soil behavior under loading and unloading/reloading is to combine elastic behavior with plastic behavior. The material is assumed to behave elastically up to a yield stress state and the stress-strain relationship after yielding is expressed with plasticity theory. Strain magnitudes and directions after yielding are defined thorough a plastic flow and strain hardening/softening rules. Plastic deformations are irrecoverable and the stress-strain relationship is a function of the loading type (loading, unloading or reloading). In addition to plasticity, viscous effects can also be incorporated in a soil model. The viscosity theory defines the rate and time dependencies of the stress-strain relationships in soils. For this study, the viscous effects in soil are neglected as the main focus of this study is to model the immediate behavior of granular materials at small to intermediate strain levels. Moreover, it has been shown by Menq (2003) that the rate of loading on modulus reduction curves of granular soils is negligible.

The state of stress acting on a point can be completely defined by three stress vectors, which can be represented by a 3x3 stress tensor as presented in Equation 4.1. The components of the second order stress tensor, σ_{ij} are presented in Figure 4.2a. As it is shown in Equation 4.1, the notation "x, y, z" is used interchangeably with the "1, 2, 3" notation. Similar to stresses, the strains at a given point can be fully described by a strain tensor, ε_{ij}, as presented in Equation 4.2.

$$\sigma_{ij} = \begin{bmatrix} \sigma_{11} & \sigma_{12} & \sigma_{13} \\ \sigma_{21} & \sigma_{22} & \sigma_{23} \\ \sigma_{31} & \sigma_{32} & \sigma_{33} \end{bmatrix} = \begin{bmatrix} \sigma_{xx} & \tau_{xy} & \tau_{xz} \\ \tau_{yx} & \sigma_{yy} & \tau_{yz} \\ \tau_{zx} & \tau_{zy} & \sigma_{zz} \end{bmatrix} \quad (4.1)$$

$$\varepsilon_{kl} = \begin{bmatrix} \varepsilon_{11} & \varepsilon_{12} & \varepsilon_{13} \\ \varepsilon_{21} & \varepsilon_{22} & \varepsilon_{23} \\ \varepsilon_{31} & \varepsilon_{32} & \varepsilon_{33} \end{bmatrix} = \begin{bmatrix} \varepsilon_{xx} & 1/2\,\gamma_{xy} & 1/2\,\gamma_{xz} \\ 1/2\,\gamma_{yx} & \varepsilon_{yy} & 1/2\,\gamma_{yz} \\ 1/2\,\gamma_{zx} & 1/2\,\gamma_{zy} & \varepsilon_{zz} \end{bmatrix} \tag{4.2}$$

The components of the strain tensor in three-dimensional space are presented in Figure 4.2b. The stresses and strains are related to each other with constitutive laws of different orders of complexity, as discussed previously.

According to the well-known Hooke's law, the elastic stresses and strains are linearly correlated via a fourth-order tensor, C_{ijkl}, of 81 elements, which is also known as the stiffness tensor. This relationship is shown in Equation 4.3. In this equation, i and j are 1, 2 and 3 (x, y, z). Due to symmetry, the number of elements of the stiffness tensor, c_{ijkl} reduces to 21 independent elastic coefficients. For isotropic materials, only two independent elastic coefficients are enough to describe the elastic stiffness tensor. These elastic coefficients can be any two of the following parameters; Young's Modulus, E, Shear Modulus, G, Bulk Modulus, K, Constrained Modulus, M, or Poisson's Ratio, ν. Each of these elastic coefficients can be expressed as a function of any other two. Equation 4.4 shows the stress-strain relationship for a linear, elastic, isotropic material according to Hooke's law in matrix notation.

$$\sigma_{ij} = \sum_{k=1}^{3} \sum_{l=1}^{3} c_{ijkl}\, \varepsilon_{kl} \tag{4.3}$$

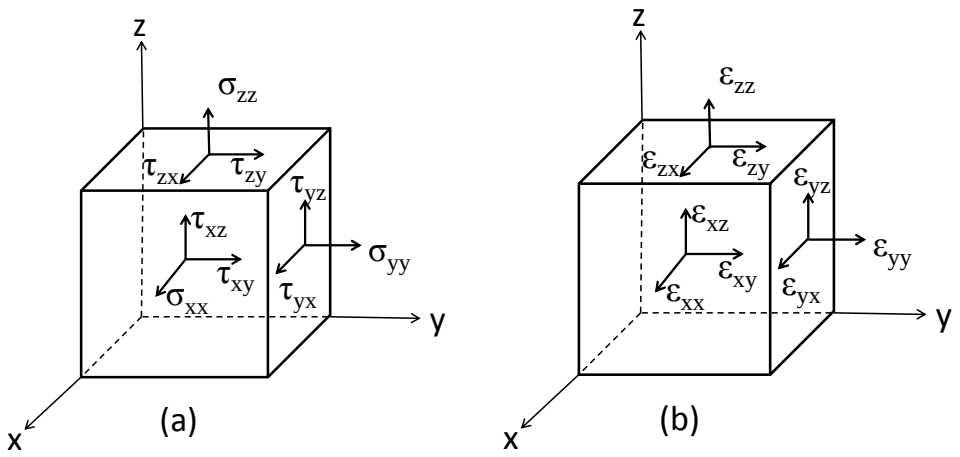

Figure 4.2: Presentation of (a) stresses (b) strains acting at a point in the Cartesian coordinate system

$$\begin{bmatrix}\sigma_{11}\\ \sigma_{22}\\ \sigma_{33}\\ \sigma_{23}\\ \sigma_{31}\\ \sigma_{12}\end{bmatrix} = \frac{E}{(1-2\nu)(1+\nu)}\begin{bmatrix}1-\nu & \nu & \nu & 0 & 0 & 0\\ \nu & 1-\nu & \nu & 0 & 0 & 0\\ \nu & \nu & 1-\nu & 0 & 0 & 0\\ 0 & 0 & 0 & (1-2\nu)/2 & 0 & 0\\ 0 & 0 & 0 & 0 & (1-2\nu)/2 & 0\\ 0 & 0 & 0 & 0 & 0 & (1-2\nu)/2\end{bmatrix}\begin{bmatrix}\varepsilon_{11}\\ \varepsilon_{22}\\ \varepsilon_{33}\\ 2\varepsilon_{23}\\ 2\varepsilon_{31}\\ 2\varepsilon_{12}\end{bmatrix} \quad (4.4)$$

In soil mechanics, the stress-strain relationships are often expressed in terms of shear modulus, shear stress and shear strain because the soil is more likely to fail in shear. Shear modulus can be expressed in terms of Young's modulus or bulk modulus, or constrained modulus and Poisson's ratio as presented below:

$$G = \frac{E}{2(1+\nu)} = \frac{3K(1-2\nu)}{2(1+\nu)} = \frac{M(1-2\nu)}{2(1-\nu)} \quad (4.5)$$

Although Hooke's law is valid for linear elastic materials, it can be extended to nonlinear materials by modifying it to a piecewise linear elastic model (Chen and Mizuno, 1990). The material nonlinearity is taken into account by discretizing the nonlinear-elastic part into smaller regions and assigning different linear, elastic material parameter values to each region. This procedure is explained in detail in Section 4.4.

4.3 POISSON'S RATIO, BULK MODULUS AND CONSTRAINED MODULUS

Poisson's ratio is a parameter that relates the vertical and horizontal strains in an elastic medium and is defined as:

$$\nu = -\frac{\varepsilon_h}{\varepsilon_v} \tag{4.6}$$

where ε_v is the vertical strain and ε_h is the horizontal strain. The value of Poisson's ratio in the small-strain range can be determined from dynamic in-situ or dynamic laboratory tests. The constrained compression wave velocity (V_p) and shear wave velocity (V_s) can be used to determine Poisson's ratio for an isotropic material with:

$$\nu = \frac{{V_p}^2 - 2{V_s}^2}{2\left({V_p}^2 - {V_s}^2\right)} \tag{4.7}$$

In most geotechnical analyses, Poisson's ratio is assumed to be constant. The assumed value is usually between 0.20 and 0.35. In an elastic analysis, the value of the Poisson's ratio defines the ratio between the vertical strains and horizontal strains. Also, it relates different types of moduli (G, E, K or M). A constant Poisson's ratio implies that the decrease in shear modulus with increasing shear strain is similar to the decrease in the other moduli with the increasing shear strain. In other words, $G/G_{\max} - log\gamma$ curves and

other normalized modulus reduction curves such as $M/M_{\max} - log\gamma$ or $E/E_{\max} - log\gamma$ will have the same shape. However, several studies showed that Poisson's ratio increases with increasing strain. Lehane and Cosgrove (2000) compiled a data set of triaxial tests with local-deformation measurements on granular soil over a wide range of void ratios. They determined Poisson's ratios from available localized measurements of vertical and horizontal strains. Change of Poisson's ratio (ν) with increasing vertical strain, ε_v, determined by Lehane and Cosgrove (2000) are shown in Figure 4.3. It should be noted that the theoretical, upper-bound value for Poisson's ratio for an elastic material is 0.5. If a material has a Poisson's ratio of 0.5, then the material is incompressible; theoretically the bulk modulus is infinite.

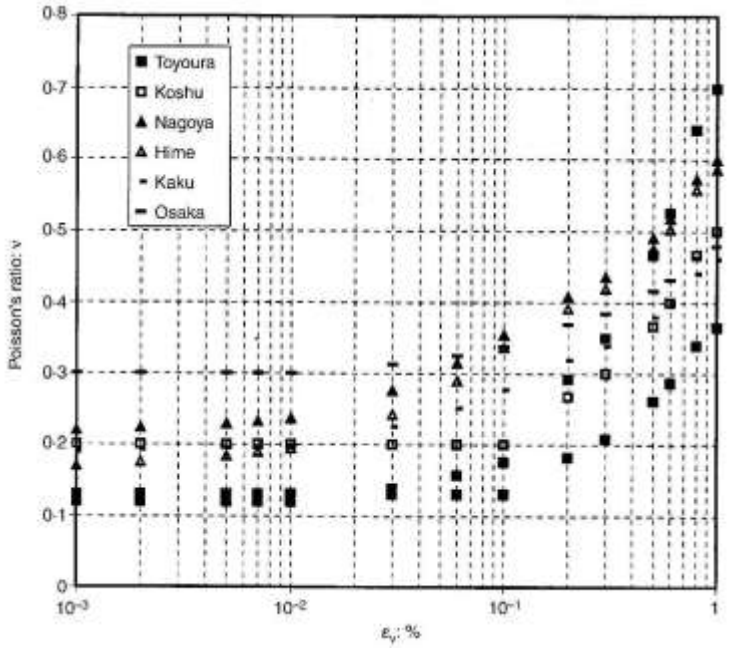

Figure 4.3: Change in Poisson's ratio with increasing vertical strain (from Lehane and Cosgrove, 2000)

The volumetric changes upon loading of a soil mass are a combination of: (1) mean compression and (2) shear. Dense sand is usually dilative and therefore when the dense sand is sheared, the volume changes due to the particle reorientation. In case of dense sand, Poisson's ratio determined from local vertical and horizontal strain measurements is higher than 0.5 as shown in Figure 4.3.

A change in the Poisson's ratio value with increasing strain implies that the ratio of different elastic moduli is not constant but a function of strain. Other elastic moduli that are often used in geotechnical engineering are the bulk modulus, K and the constrained modulus, M. Bulk modulus, K, is the elastic modulus that relates the uniform pressure (confining pressure, σ_0) applied on a material to the change in material volume. If we assume that infinitesimal theory is valid, the volumetric change or volumetric strains are defined as:

$$\varepsilon_v = \varepsilon_x + \varepsilon_y + \varepsilon_z \tag{4.8}$$

where ε_x, ε_y and ε_z are the normal strains in x-,y- and z-directions, respectively. (See Figure 4.4a) If a uniform confining pressure of magnitude P, is applied over the soil body and the resulting volumetric strain is ε_v, then the bulk modulus, K is defined:

$$K = \frac{P}{\varepsilon_v} \tag{4.9}$$

The bulk modulus of an elastic material can be expressed as a function of shear modulus and Poisson's ratio with the following relationship:

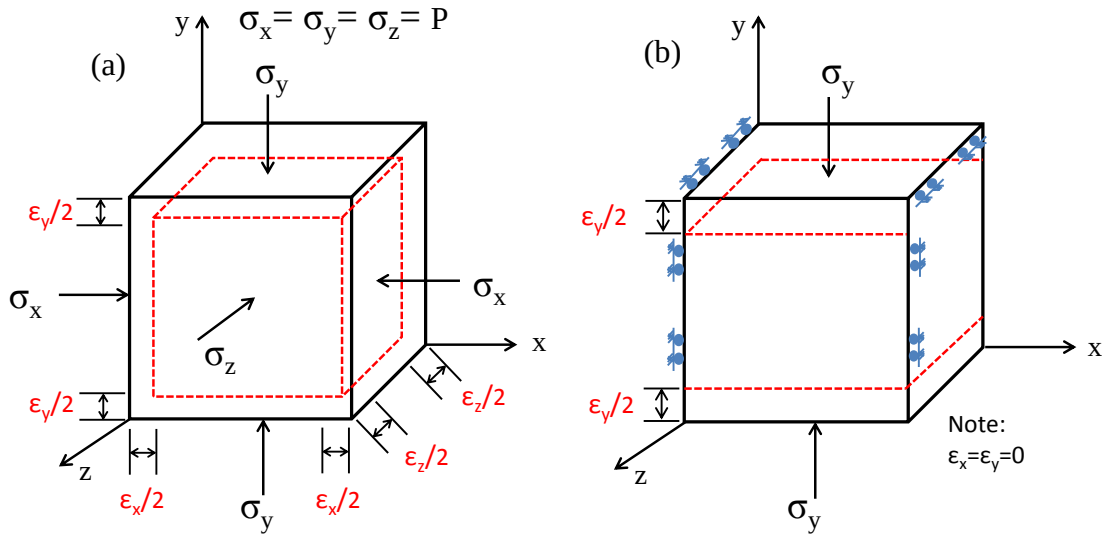

Figure 4.4: Examples of (a) volumetric and (b) constrained compressive strains in a soil mass in 3-dimensional space

$$K = \frac{2G(1+\nu)}{3(1-2\nu)} \tag{4.10}$$

For a constant value of Poisson's ratio, the relationship in Equation 4.10 indicates that the ratio of shear modulus to bulk modulus is constant at all strain and stress levels. This relationship is true at small strains since the values of Poisson's ratio and shear modulus are strain independent at small strains. However, the shear modulus decreases with increasing shear strain as discussed in Chapter 3. If Poisson's ratio remains constant throughout moderate to large strains, the bulk modulus will approach zero at large strains. To avoid the bulk modulus decreasing with increasing strain, changes in Poisson's ratio can be inversely related to changes in G/G_{max} with $\log\gamma$; hence to $G/G_{max} - \log\gamma$ relationship. This procedure was also suggested in Fahey and Carter (1993). If the bulk modulus is assumed to be constant at all strain levels, then $K_{max} = K$, where K_{max} is the

small-strain bulk modulus and K is the bulk modulus at a given shear strain value. Using Equation 4.10, K_{max} and K can be expressed in terms of $G_{max} - \nu_0$, and $G - \nu$ pairs, respectively where ν_0 is the small-strain Poisson's ratio. Since $K_{max} = K$, ν can be determined manipulating this equality which results in:

$$\nu = \frac{(1+\nu_0) - \frac{G}{G_{max}}(1-2\nu_0)}{2(1+\nu_0) + \frac{G}{G_{max}}(1-2\nu_0)} \tag{4.11}$$

Figure 4.5 presents the change in ν for a typical $G/G_{max} - \log\gamma$ relationship of well-graded sand according to Equation 4.11 with an assumed value of $\nu_0 = 0.25$.

In Equation 4.11 where K is assumed to be constant, it is apparent that the change in the value of Poisson's ratio is a function of $G/G_{max} - \log\gamma$ relationship. Hence, any parameter affecting $G/G_{max} - \log\gamma$ relationships also affects the change in Poisson's ratio. The degree of dependency of Poisson's ratio on $G/G_{max} - \log\gamma$ relationships is investigated by plotting the Poisson's ratio change with shear strain for different γ_r and "a" values. These $\nu - \log\gamma$ curves for different "a" and γ_r values are shown in Figure 4.6. As seen in the figure, both "a" and γ_r values affect the change in Poisson's ratio. However, the effect of γ_r is more prominent. The values of Poisson's ratio is increasing more rapidly for smaller values of γ_r since the $G/G_{max} - \log\gamma$ relationships become more linear with increasing γ_r. Other elastic coefficients such as Young's modulus, E, or constrained compression modulus, M, can be expressed in terms of G and K (or any other pair of elastic coefficients). Equations 4.12 and 4.13 show these relationships for E and M, respectively, as:

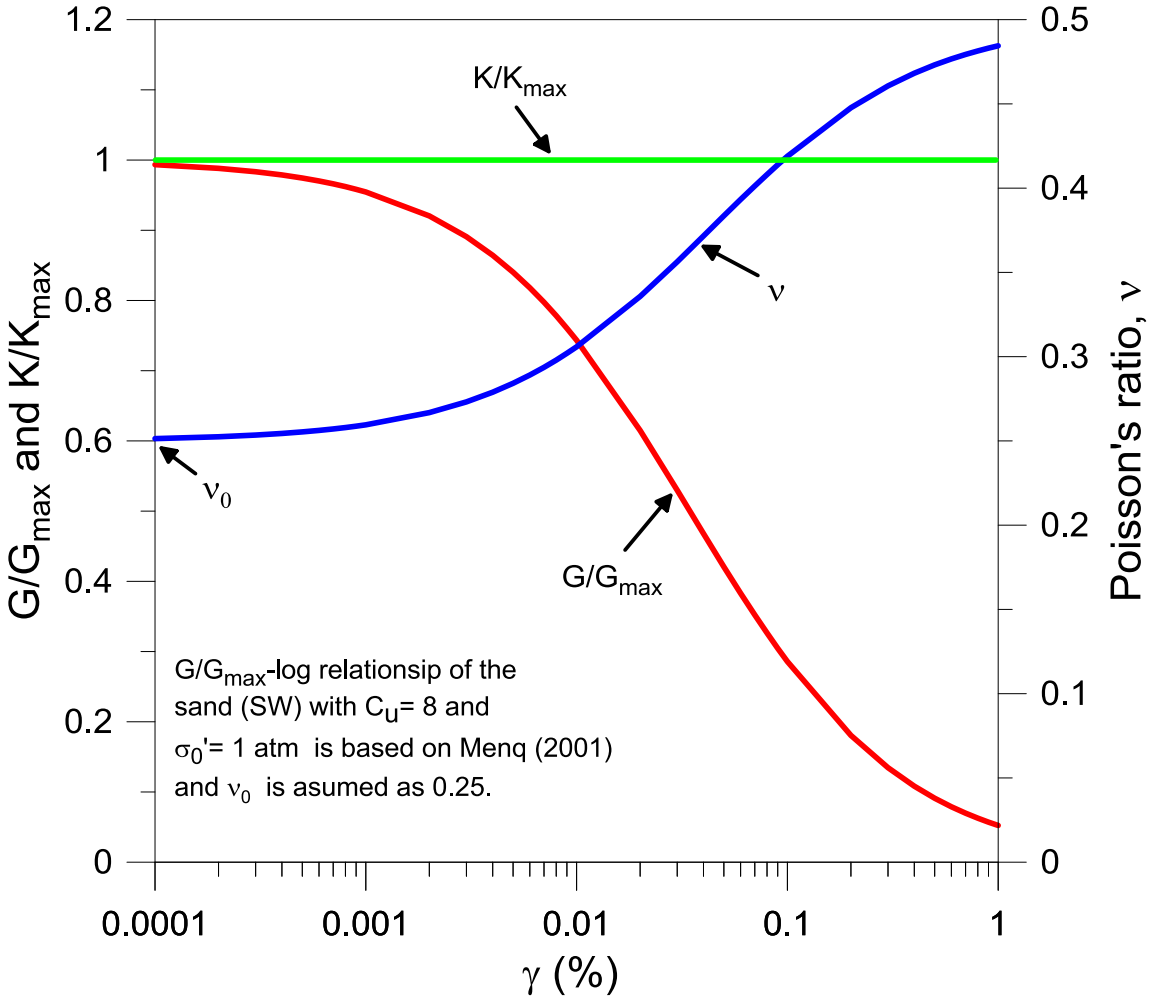

Figure 4.5: Change in Poisson's ratio of a SW soil with increasing shear strain if K is assumed to be constant at all strain levels (using Equation 4.11)

$$E = \frac{9KG}{3K + G} \tag{4.12}$$

$$M = K + \frac{4G}{3} \tag{4.13}$$

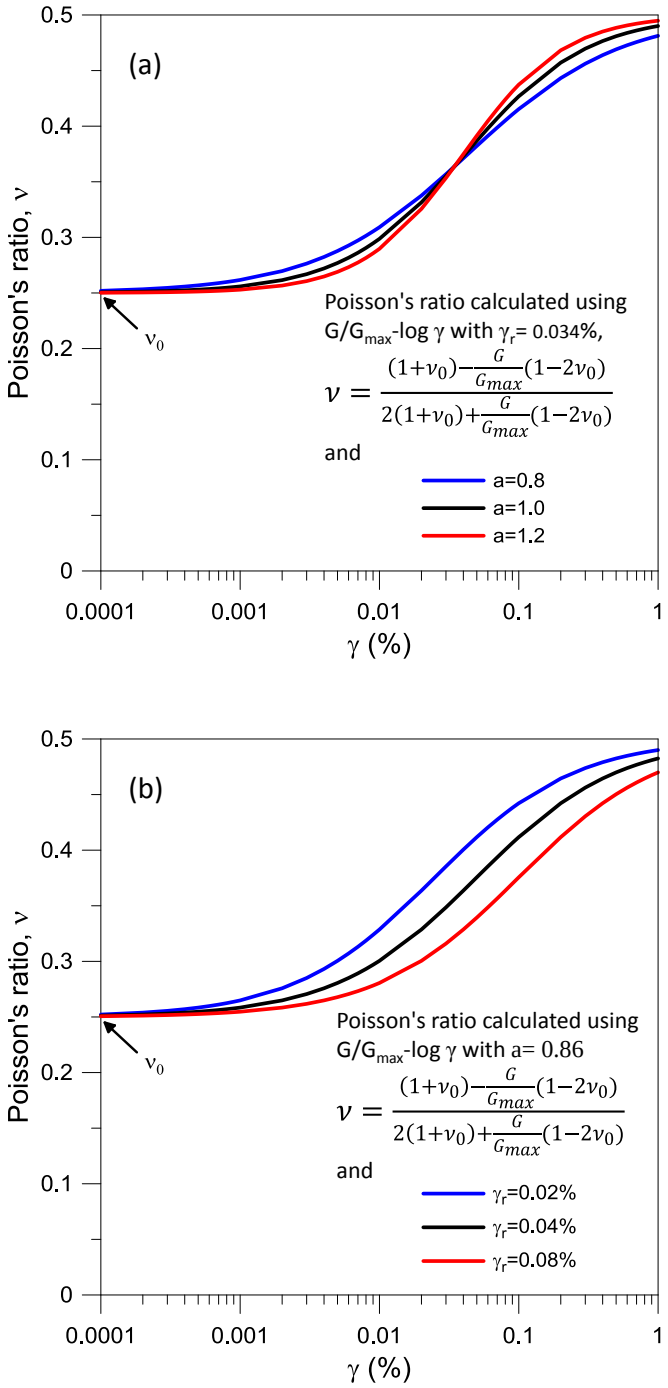

Figure 4.6: Change in Poisson's ratio with increasing shear strain for different values of (a) "a" and (b) γ_r in the $G/G_{max} - \log\gamma$ relationships if K is assumed to be constant at all strain levels

Relative changes in the values of E and M with increasing γ based on: (1) the $G/G_{max} - \log\gamma$ relationships, (2) assuming a constant K, and (3) using Equations 4.12 and 4.13, are plotted in Figure 4.7. As seen in the figure, the trend of decrease in E/E_{max} is similar to the trend of decrease in G/G_{max}. The decrease in M is less compared to decrease in G or E. It should be noted that these changes are based on $G/G_{max} - \log\gamma$ relationships and assuming Hooke's law is valid with a varying Poisson's ratio. In order to fully define the changes in the elastic moduli, different moduli and the associated strains should be measured.

As discussed in Chapter 3, in the last decade $G/G_{max} - \log\gamma$ relationships have been measured successfully by newly developed in-situ methods (Kurtulus and Stokoe, 2008; Park, 2010). Although $E/E_{max} - \log\varepsilon$ relationships are measured in the laboratory successfully using triaxial devices with local measurements, direct in-situ measurements are not possible since all soil particles are confined by adjacent soil particles and they are not free to move horizontally during vertical loading. Therefore, the elastic moduli determined in the field by seismic measurements of compression wave velocities (V_p) are normally under conditions where the horizontal movement of soil particles is constrained; hence, M_{max}. Moreover, comparison of $E/E_{max} - \log\varepsilon$ and $G/G_{max} - \log\gamma$ curves obtained in the laboratory are complicated. The first reason for this complication is that the shear strains and axial vertical strains occurring during deviatoric loading in the triaxial device can be correlated only if the Poisson's ratio is known. The second reason is that the shape of the $E/E_{max} - \log\varepsilon$ and $G/G_{max} - \log\gamma$ curves are similar and if there is only a small scatter in one of these curves, the comparison of these curves will reveal unrealistic Poisson's ratios.

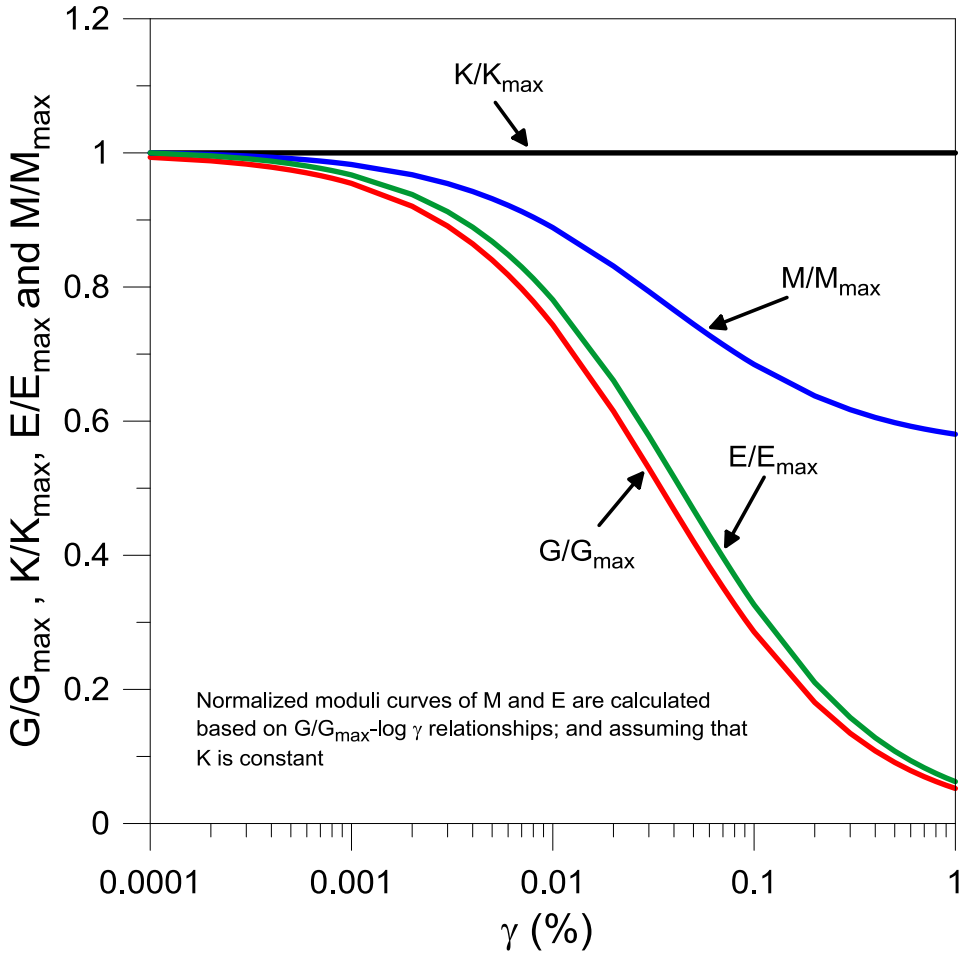

Figure 4.7: Change in E/E_{max} and M/M_{max} with increasing γ obtained using $G/G_{max} - \log\gamma$ relationships and assuming a constant K

The few studies attempting to determine $M/M_{max} - \log\varepsilon$ relationships in the field can be categorized into two groups: (1) methods that use strong ground motions due to earthquakes or large detonations, and (2) methods using seismic devices to generate and measure controlled ground motions (LeBlanc, 2013). Only the results from the second group will be briefly discussed herein. The first in-situ constrained compression modulus measurements at linear and slightly nonlinear ranges were conducted by Axtell et al. (2002). Axtell measured compression wave velocities in the linear range by applying a

static load on a cast-in-place concrete footing using a hydraulic ram and conducting transient downhole and crosshole testing. In the nonlinear range, both static loads and steady-state excitations were applied with a vibroseis truck. The compression wave velocities, V_p, were measured by the geophones that were embedded beneath the footing. This method was then refined and improved by other researchers at the University of Texas at Austin to measure shear and constrained moduli of soil in-situ (Rathje et al., 2001; Stokoe et al., 2001; Kurtulus and Stokoe, 2008; Park, 2010 and LeBlanc, 2013).

LeBlanc (2013) used two vibroseis trucks, namely "T-Rex" and "Thumper" to measure the constrained and shear moduli of a sandy silt (ML) in-situ. A vertical static load was applied directly to the soil surface providing confining pressure to the soil beneath the loading plate where a sensor array was embedded. Steady-state sinusoidal vertical and horizontal excitations were applied in a gradually increasing magnitude to cover both linear and nonlinear strain ranges. It should be noted that the depth of the soil which was assumed to be restrained from lateral movement is different for tests conducted using T-Rex and Thumper since the area of the base plate for these two shakers are different. T-Rex has a base plate area of 44.2 ft^2 whereas Thumper has a base area of 7.50 ft^2. The generalized $M/M_{max} - \log \varepsilon$ relationships obtained by LeBlanc (2013) and Axtell et al. (2002) are shown together in Figure 4.8. It is seen in the figure that, the normalized constrained modulus increases with increasing axial strain for the case where T-Rex was used (blue lines). On the other hand, the $M/M_{max} - \log \varepsilon$ relationships decrease with increasing axial strain above $\varepsilon =$ ~ 0.004% for the case where Thumper was used. This difference is mainly attributed to two facts by LeBlanc (20013) depending upon (1) the location of the sensors relative to the load plate of the mobile shakers and (2) the changes in the soil structure due to the staged loading. LeBlanc emphasizes that the "active

Rankine zone" beneath T-Rex includes the whole sensor array whereas the zone beneath Thumper only includes the shallow sensors due to different sizes of the loading plates of two shakers. Also, he mentions that the loading at early stages could have altered some soil properties such as cementation, relative density, structure which would result in a different soil behavior in the following stages of the testing.

The observed $M/M_{max} - \log \varepsilon$ relationships reported by Axtell et al. (2002) and by LeBlanc (2013) for Stage 2 are similar. On the other hand, LeBlanc shows that M/M_{max} is increasing with increasing ε for the case where T-Rex was used.

LeBlanc (2013) also measured the $G/G_{max} - \log \gamma$ relationships in-situ, using V_s. These $G/G_{max} - \log \gamma$ relationships and $M/M_{max} - \log \varepsilon$ relationship can be used to evaluate the Poisson's ratio change with shear or axial strain using Equation 4.14:

$$\nu = \frac{M - 2G}{2(M - G)} \tag{4.14}$$

To compare M and G values obtained by LeBlanc in-situ, the strain state at a given stress state should be known. In other words, a relationship between the axial strain and shear strain should be established. Since it is assumed that, soil particles in the vicinity of the centerline beneath the loading plate are horizontally restrained from movement, this case can be assumed reasonably approximate a uniaxial strain case. The shear strain, γ becomes equal to the axial strain, ε. Therefore, comparison of M and G can be made directly. If G_{max} is assumed as 1 unit pressure, then the value of $M_{max} = 3.94$ unit pressure, calculated using the small-strain Poisson's ratio (ν_0), which is given as approximately 0.33 by LeBlanc (2013) for test Site 2. Combining these M_{max} and G_{max} values with $G/G_{max} - \log \gamma$ and $M/M_{max} - \log \varepsilon$ relationship and utilizing Equation 4.14,

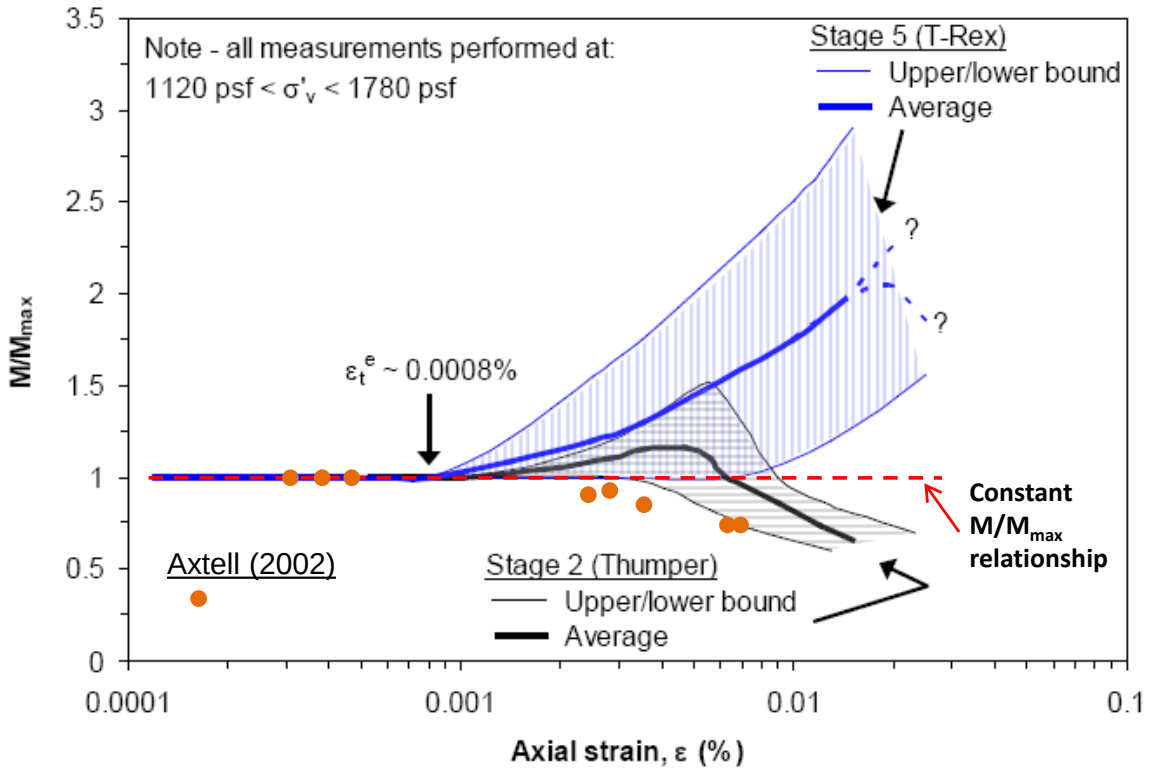

Figure 4.8: Generalized $M/M_{max} - \log \varepsilon$ relationships by Axtell, (2002) and LeBlanc, (2013) with proposed constant $M/M_{max} - \log \varepsilon$ relationship

the Poisson's ratios at larger strains were calculated and presented in Figure 4.9. As seen in the figure, for both Stage 2 and Stage 5, the Poisson's ratio is increasing with increasing strain where the increase for Stage 5 is slightly higher compared to Stage 2. Poisson's ratios are only calculated up to the largest strain at which a G measurement was performed.

The measurements presented by LeBlanc (2013) shows that initially M/M_{max} is increasing for both stages. However, it is decreasing with increasing axial strain for Stage

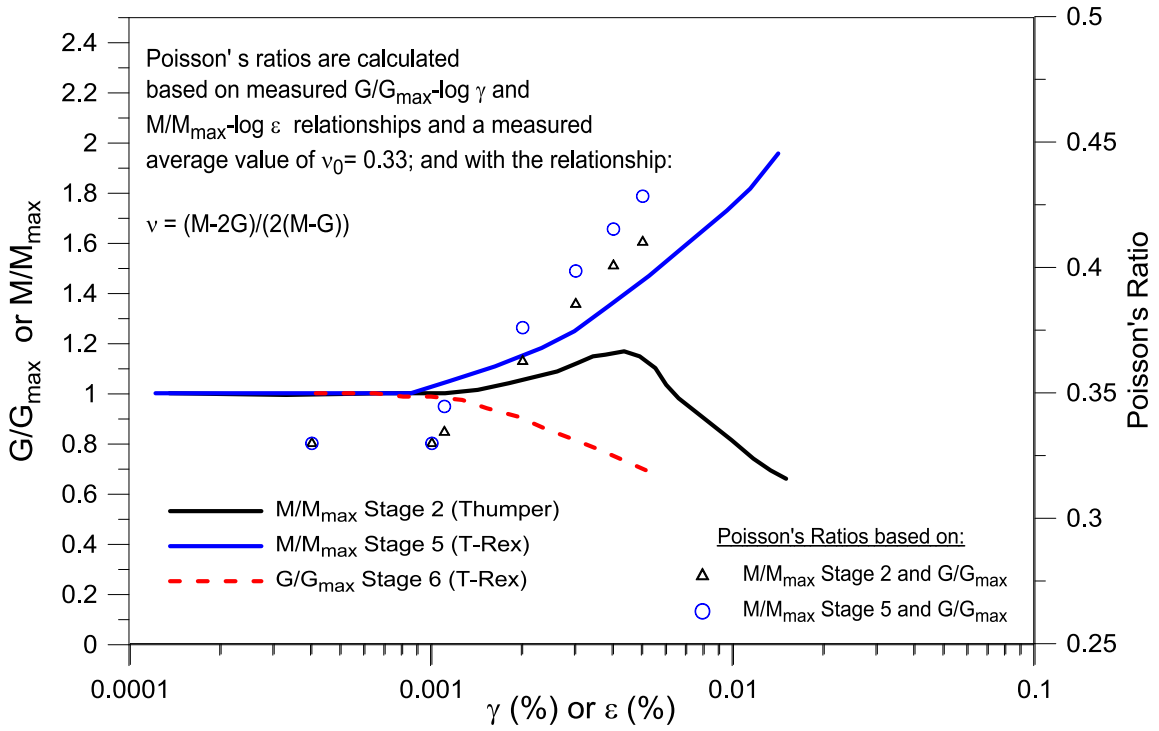

Figure 4.9: Generalized $M/M_{max} - \log \varepsilon$ and $G/G_{max} - \log \gamma$ relationships for Site 2 (LeBlanc, 2013) and the calculated Poisson's ratios

2 beyond $\varepsilon \sim 0.005$ %. As an average trend for Stages 2 and 5, one can assume that the constrained modulus remains constant at all strain levels; hence, $M_{max} = M$, where M_{max} is the small-strain constrained modulus and M is the constrained modulus at a given shear strain value. By manipulating Equation 4.14, M_{max} and M can be expressed in terms of $G_{max} - \nu_0$, and $G - \nu$ pairs, respectively where ν_0 is the small-strain Poisson's ratio. Because of the constant M_{max} assumption, ($M_{max} = M$), therefore ν can be determined with:

$$\nu = \frac{(1-\nu_0) + \frac{G}{G_{max}}(2\nu_0 - 1)}{2(1+\nu_0) + \frac{G}{G_{max}}(2\nu_0 - 1)} \tag{4.15}$$

The change in Poisson ratio with increasing γ for a well-graded sand (SW) based on $G/G_{max} - \log\gamma$ relationships obtained using Menq (2003) formulation and based on Equation 4.15 is presented in Figure 4.10. The small-strain Poisson's ratio,ν_0, is assumed as 0.25. The Poisson's ratio and $G/G_{max} - \log\gamma$ relationships reported by Le Blanc (2013) is not used in Figure 4.10 because G/G_{max} relationships are measured only up to strains of 0.005% in his study.

As seen in Figure 4.10, ν increases with increasing γ if M/M_{max} is assumed to be equal to 1.0 at all strains. The upper boundary of ν is 0.5 since Eqution 4.15 is based on the theory of elasticity which indicates that ν cannot be greater than 0.5.

Similar to the case where we assumed a constant K, in the case of a constant M, Equation 4.15, indicates that Poisson's ratio change is a function of the $G/G_{max} - \log\gamma$ relationship. Hence, any parameter affecting $G/G_{max} - \log\gamma$ relationships also affects the change in Poisson's ratio. The degree of dependency of Poisson's ratio on $G/G_{max} - \log\gamma$ relationships is investigated by plotting the Poisson's ratio change with shear strain for different γ_r and "a" values. These relationships are shown in Figure 4.11. As seen in the figure, both "a" and γ_r values affect the change in the Poisson's ratio.

Young's modulus, E, and bulk modulus, K, can also be expressed in terms of G and M to investigate how these elastic coefficients change based on $G/G_{max} - \log\gamma$ relationships with constant M. Equation 4.16 and Equation 4.17 shows the relationships between $G - M - E$ and $G - M - K$, respectively. With these equations and the $G/G_{max} - \log\gamma$ relationships and assuming a constant M, the change in E and K with increasing γ is presented in Figure 4.12. As seen in Figure 4.12, the trend of E/E_{max} decreasing more with increasing $\log\gamma$ is similar to the $G/G_{max} - \log\gamma$ trend. However,

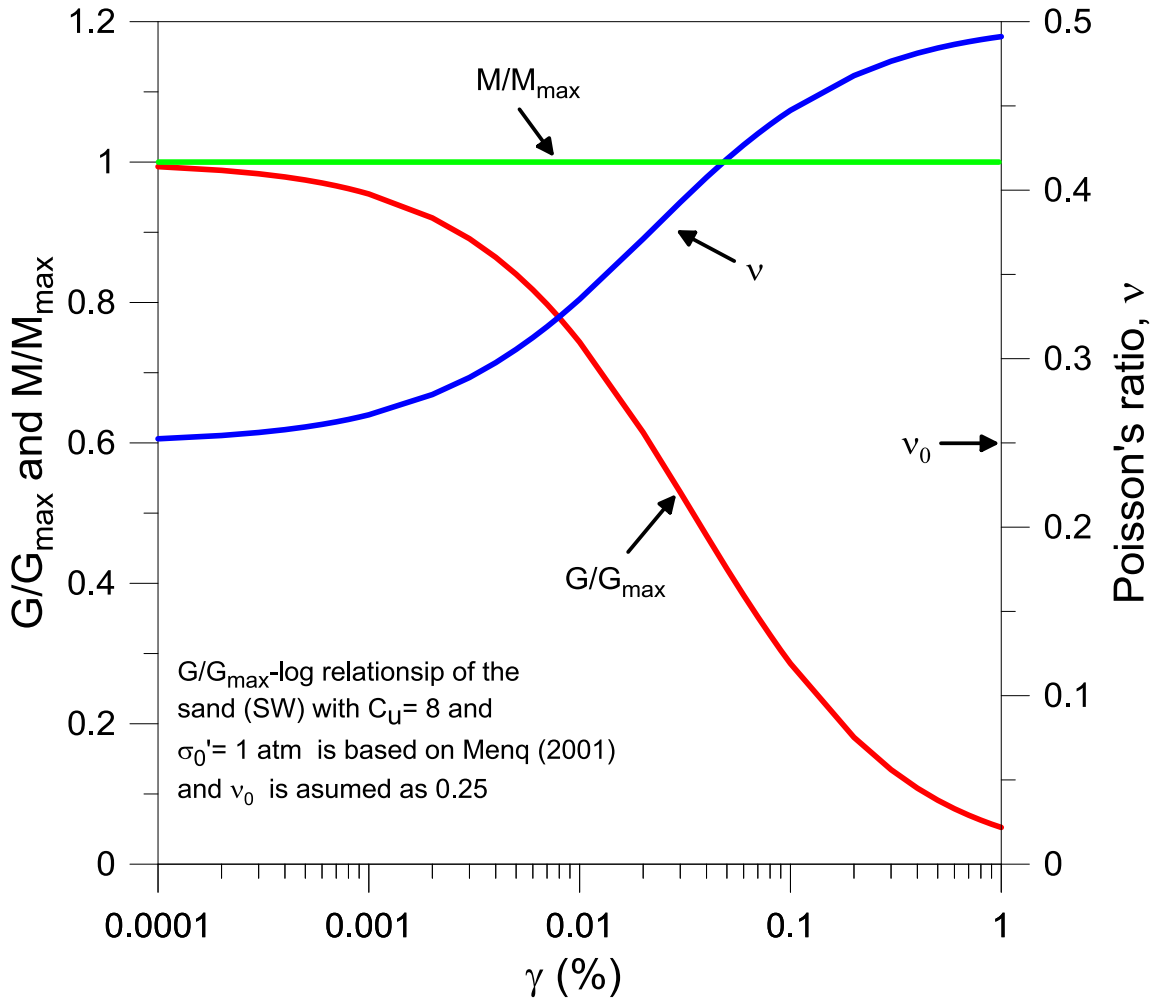

Figure 4.10: Change in Poisson's ratio of a SW soil with increasing shear strain if M is assumed to be constant at all strain levels (Equation 4.15)

$$E = \frac{G(3M - 4G)}{M - G} \tag{4.16}$$

$$K = M - \frac{4G}{3} \tag{4.17}$$

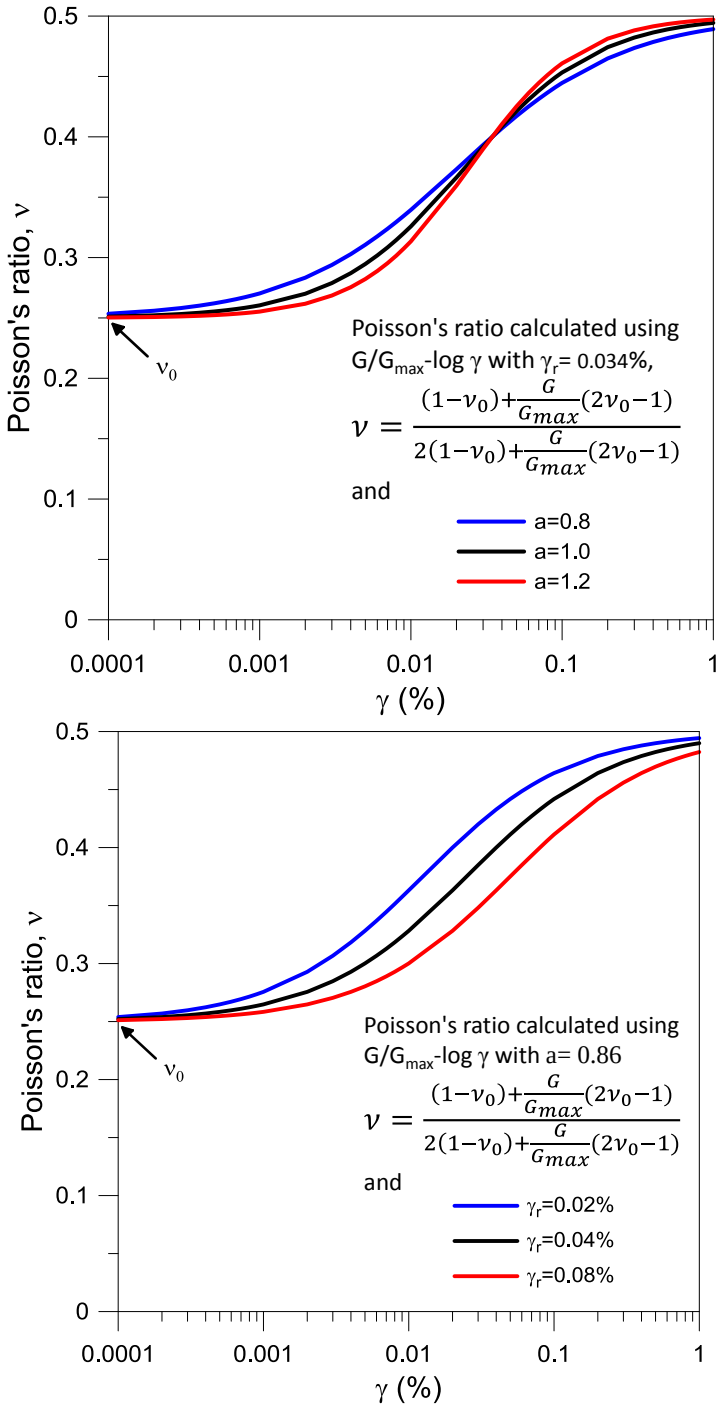

Figure 4.11: Change in Poisson's ratio with increasing shear strain for different values of (a) "a" and (b) γ_r in the $G/G_{max} - \log\gamma$ relationships if M is assumed to be constant at all strain levels

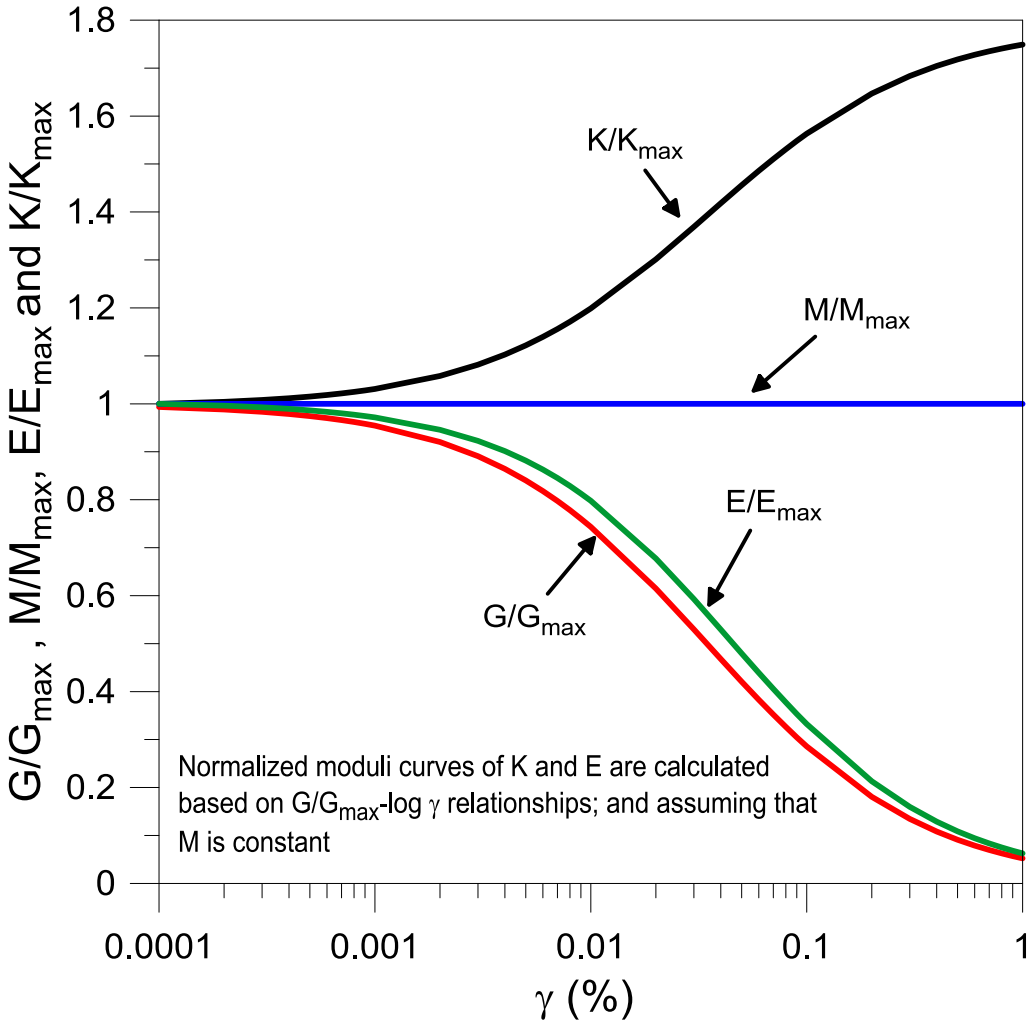

Figure 4.12: Change in E/E_{max} and K/K_{max} with increasing γ obtained using $G/G_{max} - \log\gamma$ relationships and assuming a constant M

K/K_{max} increases with increasing shear strain. It should be noted that K is associated with the volumetric change in the soil. If is K increasing, the volume change due to a mean confining pressure is decreasing. However, the volume change in soils is not only due to mean confining pressure; dense sand dilates due to shear strains and the volume increases which cannot be modeled with K. Dilative behavior of soils are usually modelled with a nonassociated flow rule and using a dilation angle. The effects of

dilation on foundation settlements are not included in the developed model, MoDaMP. However, MoDaMP-P, which is still under development, incorporates plasticity and dilation angles and it can be a promising model for settlement predictions in the future.

4.4 Derivation of the Stiffness Matrix

Nonlinearity in soil behavior is evident from laboratory tests such as Resonant Column (RC), Torsional Shear (TS) and Triaxial tests. Nonlinear behavior and parameters affecting this behavior are discussed in Chapter 3.

The general case of Hooke's law is valid for linear elastic materials. Strains occurring at a given point can be calculated using the stresses acting at this point and the stiffness matrix for this material (Equation 4.4) for a linear elastic material. This equation can be extended to nonlinear elastic materials by discretizing the nonlinear elastic part of the stress-strain curve into smaller regions and assigning different linear elastic material coefficients to each region (Chen and Mizuno, 1990). The number of independent elastic material coefficients is two for isotropic materials. The most commonly used coefficients are G, E, K and ν. Any coefficient can be expressed in terms of any other two coefficients.

As discussed in detail in Chapter 3, shear modulus of granular soil decreases with increasing shear strain and the rate of decrease is a function of several parameters such as mean effective confining pressure and gradation characteristics. The nonlinear soil behavior can be expressed in terms of normalized modulus reduction curves by the formulation developed by Darendeli (2001) and Menq (2003) as:

$$\frac{G_s}{G_{max}} = \frac{1}{\left(1 + \left(\frac{\gamma}{\gamma_r}\right)^a\right)} \tag{4.18}$$

where G_s is the secant shear modulus at a shear strain of γ, G_{max} is the small-strain shear modulus of the soil, γ is the shear strain, γ_r is the reference shear strain, and a is the curvature coefficient. The relationship between G_s and γ is utilized to create the nonlinear elastic stiffness matrix for granular soil. Secant shear modulus is preferred usually in closed-form analytical solutions. However, in numerical applications, the stress-strain relationships are expressed usually in incremental form and tangent shear modulus is more suitable in numerical applications (Benz, 2007). The definition of secant and tangent shear moduli and the incremental formulation of shear stress-shear strain relationship is shown in Figure 4.13. The secant shear modulus reduction curve in Equation 4.18 is converted to a tangent shear modulus reduction curve by taking the derivative of the shear stress with respect to the shear strain as shown in Equation 4.19:

$$\tau = G_s \gamma \tag{4.19a}$$

$$G_t = \frac{d(G_s\gamma)}{d\gamma} = \frac{G_{max}\left[1 + \left(\frac{\gamma}{\gamma_r}\right)^a - a\left(\frac{\gamma}{\gamma_r}\right)^a\right]}{\left[\left(\frac{\gamma}{\gamma_r}\right)^a + 1\right]^2} \tag{4.19b}$$

To calculate the equivalent G_t over a small shear strain increment, Equation 4.19b can be integrated over the interval of shear strain at the beginning of the current calculation step and the shear strain at the end of the current calculation step (Benz, 2007) The integration of Equation 4.19b over the shear strain increment between γ^{i+1} and γ^i results in the following expression:

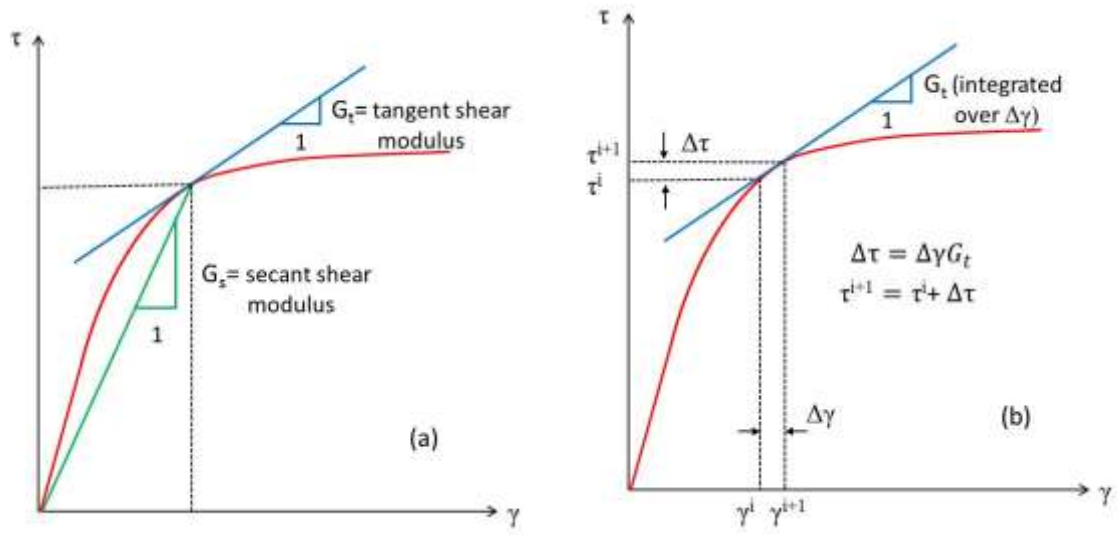

Figure 4.13: Definition of (a) G_s and G_t and (b) incremental formulation of shear stress-shear strain curve based on G_t

$$G_t^{i+1} = \frac{G_{max}}{\gamma^{i+1} - \gamma^i} \left[\frac{\gamma^{i+1}}{\left(\frac{\gamma^{i+1}}{\gamma_{ref}}\right)^a + 1} - \frac{\gamma^i}{\left(\frac{\gamma^i}{\gamma_{ref}}\right)^a + 1} \right] \tag{4.20}$$

where the subscripts i and $i+1$ stands for the values at the beginning and at the end of the current calculation step, respectively.

Assuming that the soil is isotropic, it can be assumed that the shear modulus reduction takes place in every direction. Therefore, a scalar valued parameter can be utilized to represent the shear strain in 3D space. In this study, octahedral shear strain is

used to represent the shear strain in 3D. Octahedral shear strain is a scalar measure of the shear strain acting on the octahedral plane, which is a plane making equal angles with the principal strain directions. The definition of octahedral shear strain is as follows:

$$\gamma_{oct} = \frac{2}{3}\sqrt{(\varepsilon_{11} - \varepsilon_{22})^2 + (\varepsilon_{22} - \varepsilon_{33})^2 + (\varepsilon_{11} - \varepsilon_{33})^2 + 6({\varepsilon_{12}}^2 + {\varepsilon_{23}}^2 + {\varepsilon_{13}}^2)} \quad (4.21)$$

Using octahedral shear strain enables definition of the shear stresses in the soil as a positive scalar quantity and hence the load-reversals (unloading/reloading) conditions could be identified in the subroutine by checking the current value and the previous value of the octahedral shear strain. Shear strains, γ, in Equation 4.18 are replaced with octahedral shear strains, γ_{oct}, and the tangent shear modulus, G_t is calculated. The incremental tangent stiffness matrix for the soil is created using this tangent shear modulus and Poisson's ratios as discussed in Section 4.2. Differences between the solutions based on different assumptions of Poisson's ratio are discussed in Chapters 6,7 and 8 where field case studies of settlement predictions are introduced.

4.5 USER DEFINED SOIL MODELS

4.5.1 Existing Soil Models in PLAXIS

The main goal of this study is to provide a soil model that is based on dynamically measured soil properties. This model is implemented in a finite element program, PLAXIS, which is one of the most widely used geotechnical numerical software. PLAXIS provides many built-in soil models including the HS+small soil model which is

an extension of the hardening soil model that considers the small-strain stiffness of soil. However, the HS+small model does not include the effects of gradation and the effect of mean confining pressure on the $G/G_{max} - \log\gamma$ relationships explicitly. Moreover, the HS+small model is based on the strength parameters and there is cut-off value beyond which the soil behavior is governed by plasticity. This cut-off value cannot be altered and therefore the $G/G_{max} - \log\gamma$ relationships cannot be utilized at strain ranges beyond some intermediate strain value.

4.5.2 General Procedures in Implementing User Defined Soil Models in PLAXIS

In addition to the existing soil models, PLAXIS allows users to develop their own constitutive soil models (stress-strain-time relationships). These models are programmed in FORTRAN or other computer languages and then converted to a "dynamic link library" (DLL). The DLL is then placed in the PLAXIS program directory. The DLL needs to have a specific header consisting of 31 variables so that the calculation kernel can recognize the constitutive model. Some of the key variables among these 31 variables are (Brinkgreve et al., 2011):

Props = an array that contains the user-defined soil parameters

Sig0 = an array with previous (at the beginning of the current step) effective stress components of the current stress point

StVar0 = an array with the previous values of state variables of the current stress point (state variables are variables that are used to store information about any relevant parameter such as hardening parameters in plastic calculations).

dEps = an array containing strain increments in the current stress point at the current step

D = effective stiffness matrix of the current stress point

Sig = an array of resulting constitutive stresses of the current stress point, and

StVar = an array with resulting values of state variables of the current stress point

The program works in an incremental form and the user provides the current stresses and state variables while PLAXIS provides the previous values of stress and state variables along with the strain and time increments.

The subroutine consists of several subdivisions which are called "IDTask". There are six IDTasks in total and each of them should be defined correctly in the subroutine so that the calculation kernel can extract or provide data from or to the subroutine. The IDTasks are neither executed in the order they appear nor in the order they are numbered. These tasks and their content are presented in the following sections.

4.5.2.1 IDTask 1 (Initilization of State Variables)

As discussed above, state variables are user-defined variables that can store information about the current and previous calculation steps. In this study, the state variables are used to store information about load reversals, the number of the loading cycle and output parameters.

In IDTask 1, the state variables are declared and the initial values of these variables are assigned. During the stepwise calculation procedure in PLAXIS, the resulting state variables, *StVar*, are determined based on previous values of the state variables, *StVar0* and updated stress and strain state. They are stored and automatically transferred to the next calculation step as *StVar0* to be used in the next step. If the procedure on how the state variables are updated is clearly defined, PLAXIS transfers these values automatically, except the initial step. The state variables should be initialized with the proper values in IDTask 1 for the initial step. If no information is provided about the state variables in IDTask 1, the initial values will be set to zero by PLAXIS.

4.5.2.2 IDTask 4 (Return the Number of State Variables)

The state variables are stored in arrays and before the calculation procedure starts, the size of the array must be input in the program. Therefore, in IDTask 4, the user assigns the size of the array by providing the number of state variables in the subroutine. It is important to avoid unnecessary state variables, as fewer numbers of state variables will result in a shorter calculation time.

4.5.2.3 IDTask 3 (Creation of the Effective Stiffness Matrix)

The effective stiffness matrix created in IDTask 3 can be linear elastic as it is in the built-in soil models in PLAXIS or it can be an elasto-plastic stiffness matrix (tangent stiffness matrix). These two approaches differ in the way the constitutive stresses are calculated. In the first approach, the elastic stiffness matrix is used to calculate the elastic stresses and the stress corrections are made in IDTask 2 based on the constitutive rules defined by the user. In this approach, a modified Newton-Raphson method is utilized. In the second approach, the created effective stiffness matrix is a full elasto-plastic stiffness matrix or a tangent stiffness matrix. If this method is adopted in the subroutine, there is no need for stress corrections in IDTask 2; the stresses are calculated by multiplying the tangent stiffness matrix with the incremental strains. If this method is preferred in the subroutine, then Newton-Raphson method is used to carry out the iterations.

In this study, the second approach (tangent stiffness matrix) is preferred due to the incremental nature of the nonlinear soil behavior. Since the tangent stiffness matrix is created in this task based on the new stress and strain state, this task is the main task in the subroutine.

4.5.2.4 IDTask 2 (Stress Calculation based on the Constitutive Model)

The importance of this task depends on the approach that the user chooses to use in the formulation. If the user chooses to define an elastic stiffness matrix in IDTask 3 and apply nonlinearity of the stress-strain curve or check for yielding and then apply flow/hardening rules in this task, this task becomes the main task of the subroutine. In that case, the stresses calculated from the elastic stiffness matrix are corrected in this task based on the constitutive model defined by the user. The need of a stress correction is triggered by a "plasticity" switch. In other words, even if there is no plastic stress correction in the subroutine and only non-linear elastic behavior is modeled, the switch should be activated so that the program carries out the necessary stress corrections. On the other hand, if the nonlinear-elastic behavior is considered via a tangent stiffness matrix in IDTask 3, there is no need to activate the "plasticity" switch to carry out stress corrections in this task.

4.5.2.5 IDTask 5 (Return Matrix Attributes)

The effective stiffness matrix defined in IDTask 3 can have different properties. It can be stress-dependent, it can be a tangent or secant stiffness matrix or it can be asymmetrical. If the stiffness matrix is a secant stiffness matrix and stress-independent, then the stiffness matrix is created only at the beginning of the first calculation step and it is used throughout the entire calculation procedure. On the other hand, if it is stress-dependent, then it will be created and decomposed at the beginning of each step. The stiffness matrix is created and decomposed at the beginning of each iteration if a tangent stiffness matrix is used. Moreover, if the stiffness matrix is symmetrical, only half of it will be created. The switches control the attributes of the stiffness matrix ensuring that the stiffness matrix is properly updated and stored during the calculation process. The

stiffness matrix created in this study is a stress-dependent, non-symmetric tangent stiffness matrix.

4.5.2.6 IDTask 6 (Creation of the Elastic Stiffness Matrix)

In this task of the subroutine, the elastic stiffness matrix is created. If the matrix created in IDTask 3 contains only elastic components, the same matrix can be adopted here. If a tangent stiffness matrix is created in IDTask 3, then the stiffness matrix created in this task should only include the elastic components. The elastic stiffness matrix is required by the program to calculate the current relative global stiffness of the finite element model. The relative global stiffness is then used in determining the global error during the calculations.

4.5.3 Implementation of the User Defined Soil Model, MoDaMP, into PLAXIS

A soil model based on dynamically measured soil properties (MoDaMP) discussed in Chapter 3 is created and implemented in PLAXIS via a subroutine following the general procedures described in the previous section. In this section, a step-by-step description of implementation of MoDaMP in PLAXIS is presented. This step-by-step procedure addresses both numerical and physical aspects of the model.

The subroutine starts with the declaration of the parameters in IDTask 1 used in the model. The proposed soil model, MoDaMP consists of 5 input parameters. However, these parameters can be changed and modified if the user prefers to use a different type of information. For example, if the user prefers to define the reference shear strain, γ_r, explicitly rather than having it calculated based on C_u and σ_0', then these input parameters can be modified accordingly. The 5 input parameters are as follows:

(1) $G_{\max\_1atm}$ = Shear modulus of the granular soil under a mean effective confining pressure (σ_0') of 1 atm (C_{G1} in Equation 3.6). This value is preferably determined from the $\log V_s - \log \sigma_0'$ relationships of the soil based on the in-situ small-strain measurements. If no in-situ measurements are available, it can be determined from laboratory measurements and adjusted to field conditions or it can be estimated by the formulation proposed by Menq (2001) based on the soil gradation characteristics and also adjusted to field conditions.

(2) $n\_g =$ This parameter is the slope of the $\log V_s - \log \sigma_0'$ relationship (n_G). It is determined from in-situ measurements. However if these measurements are not available, laboratory measurements can also be utilized with judgment. This value also can be estimated using $n_G = 0.48 \cdot C_U^{0.09}$ as explained in Chapter 3 and adjusted to field conditions.

(3) c_u = Coefficient of uniformity (C_U) determined from soil gradation curves.

(4) x_nu_0 = Small-strain Poisson's ratio (ν_0) which can be determined using in-situ V_s and V_p measurements.

(5) $c\_pres\_0 =$ Additional mean effective confining pressure to account for capillary stresses or to fit the shear wave velocity profile better at shallower depths.

There are 120 state variables used in this subroutine. $StateVar0(115)$, which is the mean effective confining pressure, σ_0', is the only state variable that has a non-zero initial value and it is declared in IDTask 1 as:

$$StVar0(115) = (-1.0 * (c\_press\_0) + Sig0(1) + Sig0(2) + Sig0(3))/3.0) \quad (4.22)$$

where $Sig0(1)$ is the stress values in x, y and z direction at the beginning of the current step. The next task is IDTask 2 which involves multiplying the strain increment, $dEps$,

with the effective stiffness matrix, D, which gives the stress increment, $dSig$. Also, based on the new stress state, σ_0', state variables are updated in this task.

Next task is IDTask 3 which is the main task in the MoDaMP subroutine since the tangent stiffness matrix is created in this task based on strain and stress states and the loading condition. First, G_{max} is calculated based on the new stress state using Equation 3.6.

The strain increments, $StVar0(i)$ where $i = 1, 6$, that are stored in IDTask 2 are used to determine the cumulative strain increments in IDTask 3 via state variables $StVar0(i)$, where $i =$ 7, 84. These 78 state variables refer to 6 cycles of loading/unloading/reloading. A maximum of 13 loading cycles based on the extended Masing rules are allowed in the subroutine. The unloading/reloading can also be modeled using different (n_G) values for the soil in loading and unloading/reloading. However, the extended Masing criteria is preferred in this formulation since the hysteresis loops obtained with extended Masing criteria can be modified to obtain damping curves. This approach allows MoDaMP to be used in ground response analysis in the future. Masing behavior consists of two main criteria and two extended criteria defining the hysteresis loop of a soil under loading/unloading/reloading cycles. These criteria are defined as follows:

(1) For initial loading, the stress-strain curve follows the backbone curve

(2) If a stress reversal occurs at a point $(\gamma_{rev}, \tau_{rev})$, the stress-strain curve follows a path defined as:

$$\left(\frac{\tau - \tau_{rev}}{2}\right) = f_b\left(\frac{\gamma - \gamma_{rev}}{2}\right)$$

where f_b is the backbone curve.

(3) If the unloading/reloading curve exceeds the previous shear strain, then the stress-strain curve follows the backbone curve

(4) If the unloading or reloading curve crosses the unloading/reloading curve from a previous cycle, the stress-strain curve cannot surpass the curve of that cycle; it follows the curve from that previous cycle.

Chitas (2008) proposed a user defined soil model for PLAXIS to predict the ground response under seismic loading conditions and he implemented the Masing behavior in this model to predict the damping ratios. The extended Masing rules are implemented in MoDaMP by using a modified version of the code proposed by Chitas (2008). The main principles of the code are explained briefly below. To implement the extended Masing rules, detection of the octahedral shear strain reversals is crucial. This detection is achieved by storing the maximum octahedral shear strain in state variables $StVar0(i)$ where $i = ild + 100$. The variable "ild" identifies the loading case. If $= 1$, it refers to initial loading; if $ild = 2n$, the soil is being unloaded and if $ild = 2n + 1$ then the soil is being reloaded where $n = 1{,}13$. The maximum octahedral shear strain stored in the proper $StVar0(i)$ is compared with the octahedral shear strain in the next calculation step. If the octahedral shear strain exceeds the maximum octahedral shear strain, there is no load reversal at that step and the octahedral shear strain at this step becomes the new maximum octahedral shear strain. If the octahedral shear strain is less than the maximum octahedral shear strain, then there is a load reversal and ild is increased by one and the comparison procedure is repeated by moving to the next state variable with an initial value of zero. If the loading case is unloading/reloading, then second rule of the extended Masing criteria should be applied. This rule can be achieved by doubling the reference

shear strain in Equation 3.11 (Benz, 2007 and Chitas 2008). Increasing the value of γ_r in Equation 4.22 by a factor of two gives:

$$G_t^{i+1} = \frac{G_{max}}{\gamma^{i+1} - \gamma^i}\left[\frac{\gamma^{i+1}}{\left(\frac{\gamma^{i+1}}{2\gamma_r}\right)^a + 1} - \frac{\gamma^i}{\left(\frac{\gamma^i}{2\gamma_r}\right)^a + 1}\right] \tag{4.22}$$

To fulfill the fourth rule of the extended Masing criteria which implies that an inner hysteresis cycle at n^{th} cycle cannot surpass the $n-1^{th}$ cycle, the strain values of the n^{th} cycle needs to be erased when moving from the n^{th} cycle to the $n-1^{th}$ loop. Another variable, "itd", is defined which controls the erasing of the state variables containing the strain values for each loading cycle. If the unloading/reloading has to follow the $n-1^{th}$cycle after the n^{th} cycle, then the strain values of n^{th} cycle are erased so that the stress-strain path follows the $n-1^{th}$ cycle (Chitas, 2008).

Once the loading case is determined, the next step is determine G and Poisson's ratio, ν. The mean effective confining pressure, σ_0', at the beginning of each calculation step is used to determine the γ_{ref} and "a" values, which are inserted in Equation 4.12 to determine G from $G/G_{\max} - log\ \gamma_{oct}$ relationships and $G_{\max}$. The value of Poisson's ratio is determined based on one of the two different approaches presented in Section 4.3 (assuming a constant K or M value). The tangent stiffness matrix is then created based on the G and ν values at the beginning of each iteration step. An important feature of MoDaMP is that G and ν values are updated based on the strain and stress levels. This updating process of the $G_{\max}$, $G/G_{\max} - \log\ \gamma_{oct}$ relationships and ν of an arbitrary point in the soil mass is illustrated in Figure 14. As seen in the figure, before any loading takes

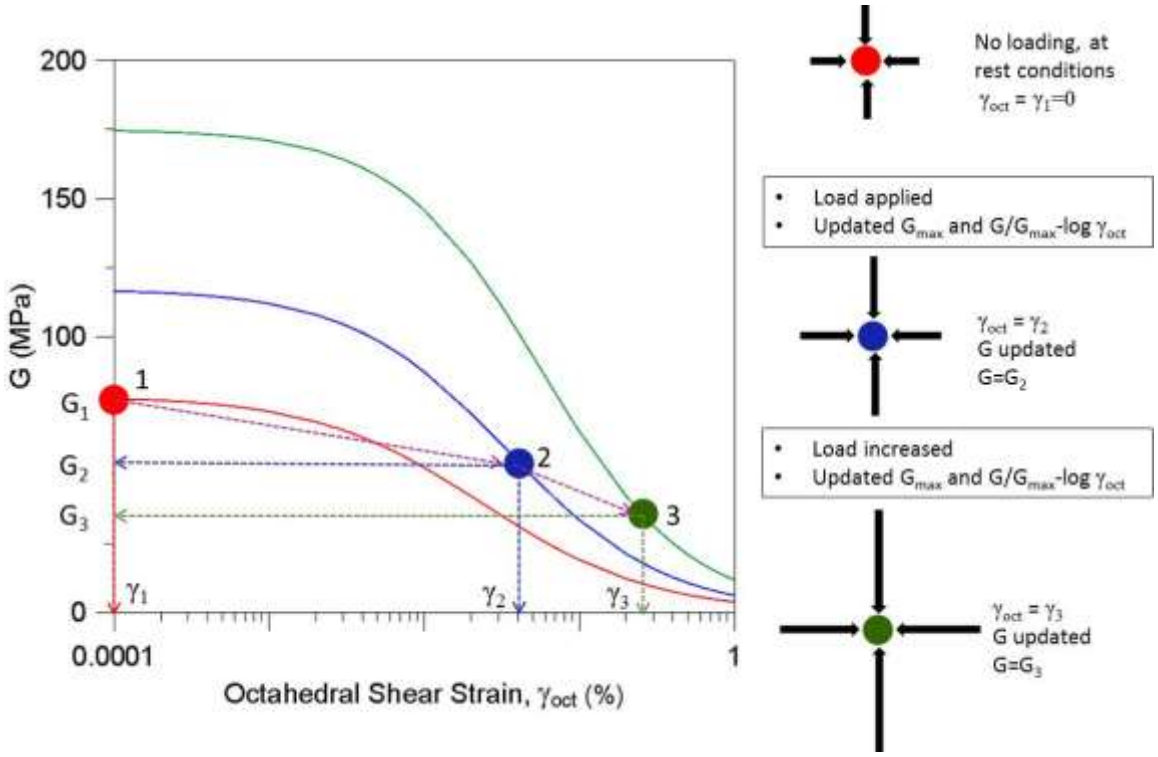

Figure 4.14: Illustration of the updating procedure of G_{max}, $G/G_{\max} - log\ \gamma_{oct}$ relationships and G with increasing load levels

place, the soil is at rest conditions and there are horizontal and vertical stresses acting on that chosen point in the soil mass. At this stage, $G = G_{\max}$ since no displacement has yet taken place and $\gamma_{oct} = 0.0$. It should be noted that the value of $G_{\max}$ is stress dependent and it is determined based on the stress state prior to loading. When a load is applied on the soil mass, both horizontal and vertical stresses will increase resulting in a higher mean effective confining pressure. A new $G_{\max}$ is computed using the updated mean effective confining pressure. This new $G_{\max}$ value is inserted in the updated $G/G_{\max} -$ log γ_{oct} relationship and a new G is computed. When the load is increased further, the process will be repeated. Since G is stress and strain dependent, assembling of the stiffness matrix requires an iterative procedure. However, this procedure would add more

computation time since the finite element program utilizes already an iterative scheme to compute the stresses from a defined stiffness matrix. In order to reduce the computation time, G value and $G/G_{\max} - \log \gamma_{oct}$ relationships at a calculation step are determined based on the stresses at the end of the previous calculation step which rendered the iteration unnecessary. The difference between using the stresses at the beginning of a calculation step and using iteration to determine the stresses for that calculation step is negligible since the load increments are very small.

The next step in the subroutine is creating the stiffness matrix. As discussed earlier, the created stiffness matrix is a tangent stiffness matrix and it is based on the shear modulus (G) and the Poisson's ratio (ν) which are determined based on the stress and strain states in the soil mass. The created effective tangent stiffness matrix, D, is then used in calculating the incremental stresses, $dSig$, in IDTask 2 by multiplying the incremental strains, $dEps$, with the tangent stiffness as shown in Equation 4.23.

$$dSig = (dEps)D \tag{4.23}$$

The attributes of the tangent stiffness matrix is defined in IDTask 5 by using the stiffness matrix switches. All switches except the time dependency switch is assigned as 1since the matrix is a nonsymmetric, stress-dependent tangent stiffness matrix.

4.5.4 Verification of the User Defined Soil Model, MoDaMP

The soil model MoDaMP is developed to predict the settlement of shallow foundations on granular soil. It can be used both in drained and undrained analyses. It can be potentially used in ground response analysis with an added damping-ratio function since it utilizes a modulus reduction scheme and obeys the extended Masing behavior.

Before using the model in settlement prediction analyses, the model was verified. The following capabilities of MoDaMP were tested to verify that the model was correctly developed, from theoretical and numerical points of view, for the following conditions:

(1) monotonic loading,

(2) pressure dependency of the model, and

(3) loading and unloading/ reloading.

First, the model was tested under pure shear loading. An incremental prescribed shear displacement with an ultimate value 0.01 ft was applied at the very top layer of a soil body with a 1ft x 1ft geometry. The bottom of the soil body was restrained from movement in both the horizontal and vertical directions whereas the sides of the soil body are only restrained from movement in the vertical direction. The resulting shear strains are constant throughout the soil with a value of 1.0%. In two-dimensional pure shear loading, the octahedral shear strains are about 82% of the shear strains applied (Chitas, 2008). The soil was assumed to have $G_{\max} = 1{,}000{,}000$ psf, $n_G = 0.50$ and $a = 0.92$.

Next, three simulations using PLAXIS and MoDaMP with different mean effective confining pressures, σ_0' , are carried out. The results from the numerical simulations were compared with the results found analytically. These comparisons are presented in Figure 4.15. As seen in the figure, the numerical and analytical results match very well for each pressure. It can be concluded that MoDaMP is working correctly in monotonic loading. Moreover, the stress dependency of the model is also verified since γ_r is calculated correctly.

Another feature of MoDaMP is its ability to model loading and unloading/reloading correctly by obeying extended Masing rules. To verify that MoDaMP can correctly simulate different loading stages, the same geometry and soil

used in pure shear monotonic loading were used to create hysteresis loops. These hysteresis loops are created analytically, both by using secant shear moduli and tangent shear moduli to verify that the tangent stiffness formulations works correctly and it gives the same results as the secant stiffness matrix formulation. As seen in Figure 4.16, the secant and tangent shear moduli formulations give identical results. The numerical solution is found by utilizing PLAXIS with MoDaMP. It is seen in the figure that, MoDaMP is working correctly because: (1) shear stress-shear strain curve follows the backbone curve during initial loading and it is identical to the analytical solution, (2) upon unloading the stress-strain curve follows the same shape as the backbone curve, but it is doubled, (3) the stress-strain curve follows the backbone curve if the strain level during reloading exceeds the maximum previous strain, and (4) the inner loop follows the previous hysteresis loop after being closed.

MoDaMP is developed mainly to predict settlements of shallow foundations on granular soil using field seismic combined with laboratory dynamic tests results as well as large-strain triaxial test results. One of its important features is the ability to take nonlinearity of the soil into account by following the $G/G_{\max} - \log \gamma_{oct}$ relationships. MoDaMP can be converted to a stress-independent, elastic linear model by assigning a very large value to γ_r and $n_G = 0.0$. With this modification, MoDaMP can be verified by comparing the settlements of a shallow foundation found on an elastic half-space with the settlements prediction obtained using MoDaMP. The theoretical solution for a rigid circular footing on an elastic half-space (Richart et al., 1970) is:

$$S = Q\frac{1-\nu}{2GB} \tag{4.24}$$

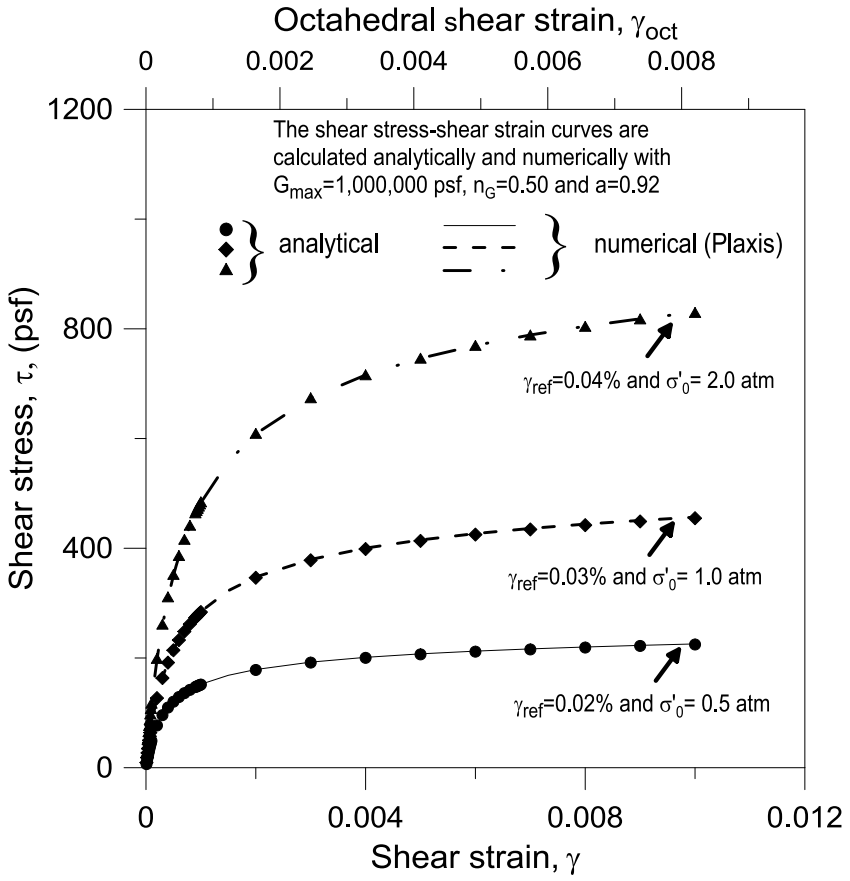

Figure 4.15: Verification of MoDaMP in pure shear loading by comparing $\tau - \gamma$ curves obtained numerically and analytically for different values of σ'_0

where S is the settlement, Q is the applied load and B is the footing diameter (Figure 4.17). This settlement is compared with the settlement of the same footing calculated with PLAXIS and MoDaMP. The soil is modeled by assuming γ_r =1000%, a =1.0 and n_G =0.0 so that the initial G value (G_{max}) stays constant during loading and thus MoDaMP becomes a linear elastic model. The depth of the elastic layer, H, was varied between 5B and 100B. G and ν were assumed to be 65MPa and 0.3, respectively, the same values as in the theoretical elastic solution. As seen in Figure 4.17, the settlement

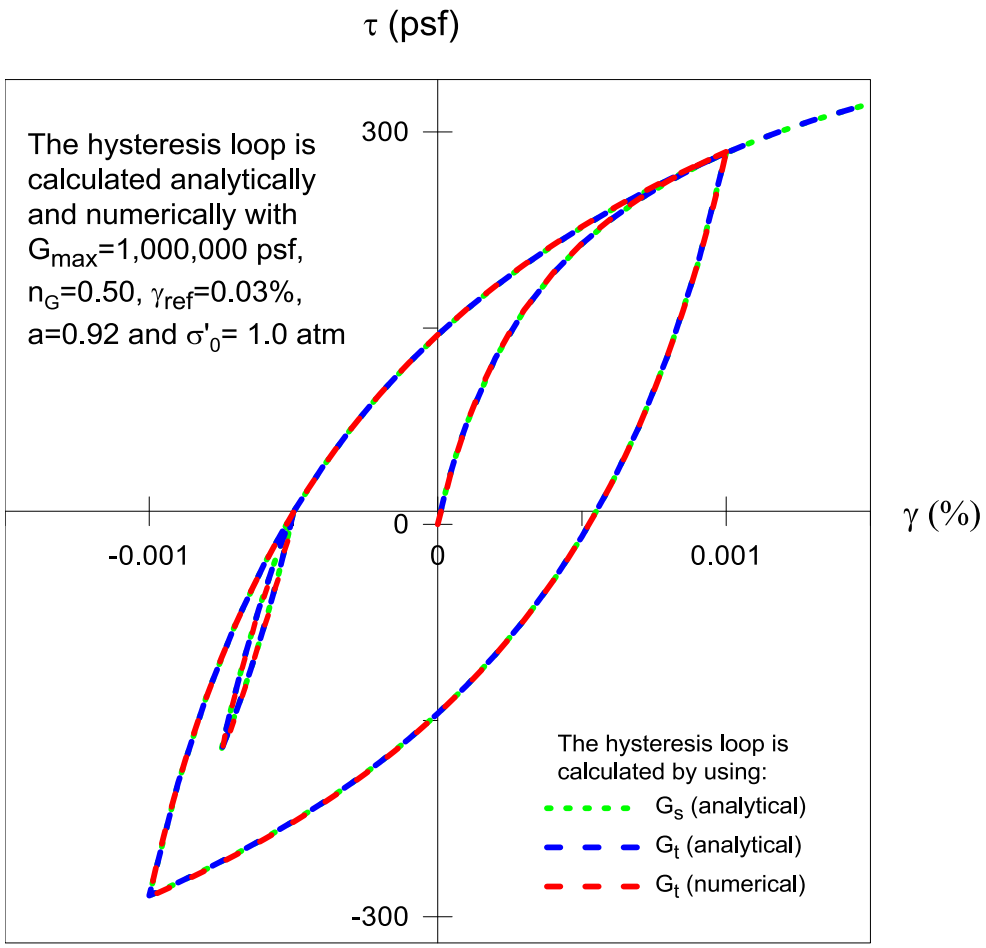

Figure 4.16: Verification of MoDaMP in pure shear loading by comparing $\tau - \gamma$ curves during loading and unloading/reloading obtained numerically and analytically

calculated with elastic theory where $H/d = \infty$ is about 1.17 mm and the settlement calculated with MoDaMP for $H/d = 100$ is about 1.16 mm. Therefore, the difference between these two methods is about 1%. This result show that: (1) MoDaMP can be used for linear elastic calculations such as footing settlements at low load levels where the soil is assumed to behave as linearly elastic and (2) the developed model, MoDaMP, has been verified in the linear elastic range.

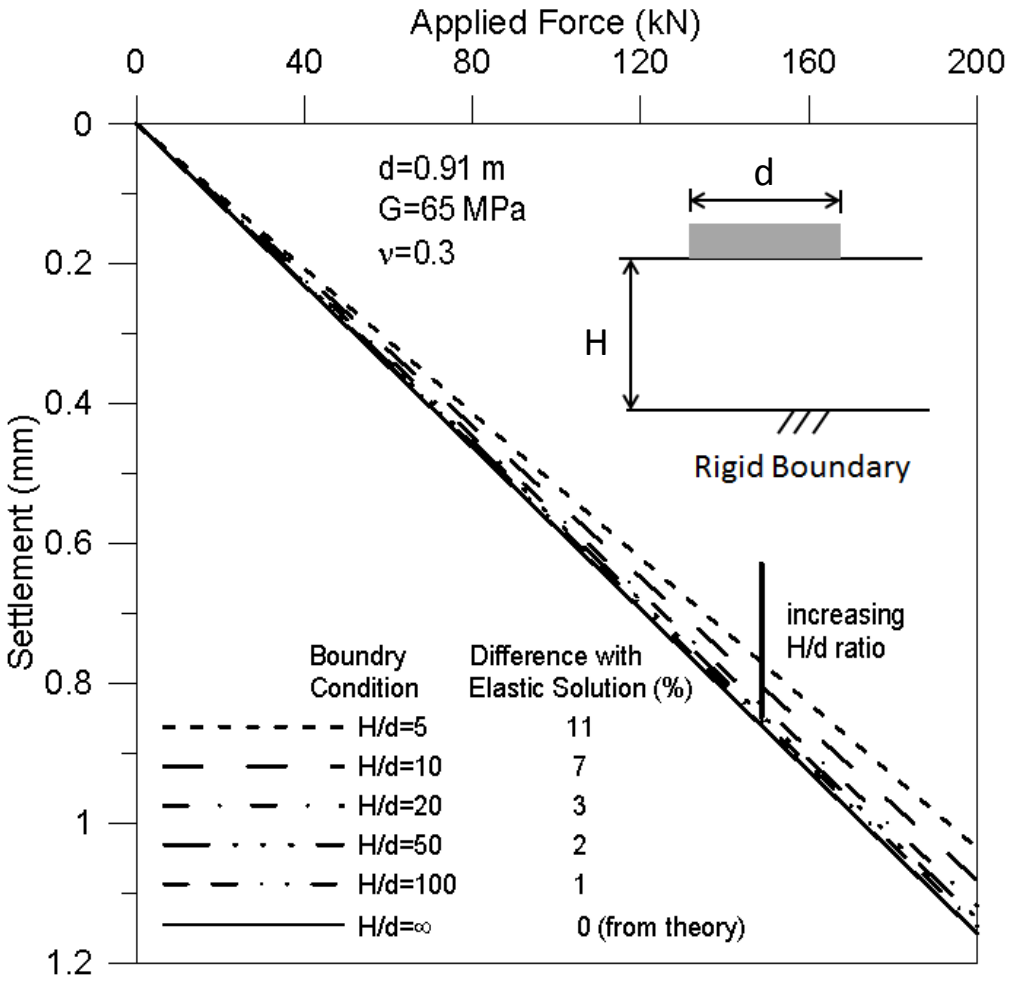

Figure 4.17: Verification of MoDaMP by comparing the settlements of a rigid footing on an elastic half space with theoretical approach with the predicted settlements obtained using MoDaMP as a linear elastic model

4.6 SUMMARY

In this chapter, development, implementation and verification of the soil model MoDaMP are discussed. First, the nonlinear and strain-dependent nature of the $\tau - \gamma$ curves in soils are discussed. Then, the general definitions of stresses and strains acting on a point in a continuum medium are given. The relationships between stresses and strains for an elastic material are presented.

The elastic material coefficients and the equations relating these coefficients to each other are discussed. The behavior in Poisson's ratio upon loading and unloading, which is usually assumed to have constant value, is investigated. Studies showing the change in Poisson's ratio with increasing strains are presented. Moreover, in-situ measurements of M by Axtell et al. (2002) and LeBlanc (2013) are introduced and based on these measurements, the behavior of Poisson's ratio with increasing strain levels is investigated. This investigation revealed that if M or K is assumed constant, Poisson's ratio is increasing with increasing shear strain based on the $G/G_{\max} - \log\gamma$ relationships for soils.

In Section 4.4, the derivation of the stiffness matrix is discussed. The $G/G_{\max} - log\,\gamma$ relationships proposed by Menq (2003) are used to define G at a given strain. The derivation of the tangent stiffness matrix with strain-dependent G and ν is explained.

In Section 4.5, the general procedures in implementing a user defined soil model into PLAXIS are presented. The general structure of the subroutine is explained. Next, a user defined soil model that utilizes field seismic test results combined with laboratory dynamic tests results as well as large-strain triaxial test results, is developed. Numerical issues in creating the model such as updating of the stress and strain states, and distinguishing between loading and unloading/reloading, and modifying the tangent stiffness matrix accordingly are explained.

In the final section, the developed soil model, MoDaMP, is verified with element tests and an elastic settlement analysis. It is shown that MoDaMP is working correctly and it is capable of following the rules defined by the writer pertaining to stress and strain updates, $G/G_{\max} - \log\gamma$ relationships and Masing behavior. It is also shown that MoDaMP can correctly predict footing settlements in the linear elastic range.

Chapter 5: Development of the Model of Dynamically Measured Properties Combined with Perfect Plasticity (MoDaMP-P)

5.1 INTRODUCTION

A soil model of dynamically measured properties (MoDaMP) was developed in this research. MoDaMP is and presented in Chapter 4. MoDaMP is a nonlinear elastic model and mainly based on G_{max} and $G/G_{max} - \log\gamma$ relationships that are obtained from in-situ and laboratory testing. Although MoDaMP is based on elastic theory, defining different soil moduli during loading and unloading/reloading enhanced the model with the ability of predicting irrecoverable (plastic) strains as well. The varying Poisson's ratio based on $M/M_{\max} - \log\varepsilon$ measurements and K improved the model in predicting volumetric changes occurring in the soil under loading.

As explained in Chapter 4, since MoDaMP is based on Hooke's Law, the model is not intended to be used in predicting the dilative behavior of dense soils. Dilative behavior implies that the soil increases in volume when it is sheared. In MoDaMP, Poisson's ratios are $0.0 \leq \nu \leq 0.5$ and therefore only contractive behavior is taken into account. Highly dilative behavior would result in smaller magnitudes of settlements for shallow foundations and ignoring this highly dilative behavior is a conservative approach in the settlement prediction analysis.

On the other hand, comparing MoDaMP with a model which has the capability of modelling the dilative behavior of dense sands can give more insight about the effects of volumetric changes in the soil to the settlements. Therefore, MoDaMP was modified by adding a yield criterion (Drucker-Prager) and a nonassociated flow rule that uses a dilatancy angle. The new model is named as MoDaMP-P since the new model is working exactly the same as MoDaMP until the soil yields. After yielding, the $\tau - \gamma$ response of

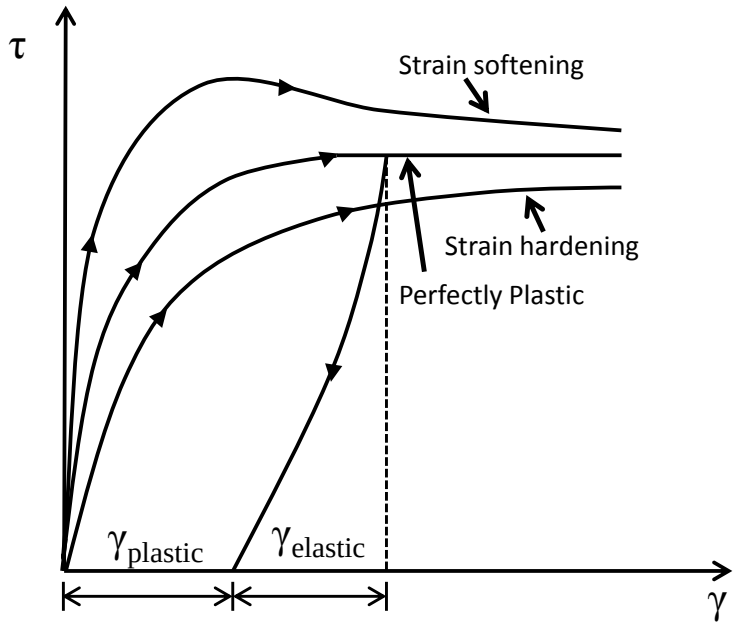

Figure 5.1: Illustration of $\tau - \gamma$ responses of strain softening, strain hardening and perfectly plastic soils

the soil is modelled as perfectly plastic as illustrated in Figure 5.1. The definition of yield functions in general and a more detailed discussion of Drucker-Prager yield function are presented in Section 5.2. Next, the flow rule and plastic potential concepts are introduced in Section 5.3. The flow rule and plastic potential function utilized in MoDaMP-P are discussed. The formulation and implementation of MoDaMP-P into PLAXIS is discussed in Sections 5.4 and 5.5, respectively. Finally, the developed model is verified with element tests and boundary value problems.

5.2 YIELD FUNCTION

A yield function describes a curve in 2D stress space and a surface in 3D stress space. The yield curves or surfaces separate the elastic and elastic-plastic regions from each other in stress space. When the state of stress reaches the yield surface, the material

is assumed to reach the plastic state. The stress paths within the yield surface produce recoverable (elastic) strains whereas the stress paths that intersect the yield surface produce both recoverable and permanent (plastic) strains (Chen and Mizuno, 1990). The yield function $f\left(\sigma_{ij}, \varepsilon_{ij}^{p}\right)$ in general can be described as:

$$f\left(\sigma_{ij}, \varepsilon_{ij}^{p}\right) = 0 \tag{5.1}$$

where σ_{ij} is the stress tensor and ε_{ij}^{p} is the plastic strain tensor. For perfectly plastic materials, the yield function is fixed and it is only a function of the stress tensor. Plastic deformations can only occur if the stress path moves on the yield surface. For strain hardening or strain softening materials, the yield surfaces are not fixed and they are expressed with hardening parameters. Hardening parameters define how the yield surface is evolving. The hardening parameters are functions of stress, strain and other soil parameters. The strain hardening or strain softening behavior of soils are modeled by adding hardening-softening rules in the plasticity formulation. However in this study; the main focus of developing MoDaMP-P is to investigate the effect of volumetric changes on settlements rather than the $\tau - \gamma$ response at larger strains and failure. Therefore, hardening-softening rules in plasticity formulation are out of the scope of this study and they will not be discussed herein.

The following expressions define the complete stress conditions for elastic and plastic deformation as:

$$Elastic: f < 0 \; or \; df = \frac{\partial f}{\partial \sigma_{ij}} d\sigma_{ij} < 0 \tag{5.2}$$

$$Plastic: f = 0 \; and \; df = \frac{\partial f}{\partial \sigma_{ij}} d\sigma_{ij} = 0 \tag{5.3}$$

If the stress state falls inside the yield surface, $f < 0$ and the deformations are all elastic. If $f = 0$, the stress state is on the yield surface and the deformations are a combination of elastic and plastic deformations. For perfectly plastic materials, the consistency condition, $df = 0$, forces the stress state to stay on the yield surface. In other words, it is not possible to have $f > 0$ (Figure 5.2). As seen in the figure, there is another surface similar to the yield surface which is called a plastic potential function. This function is discussed in Section 5.3.

There are numerous yield functions proposed in the literature with different level of complexities. Usually, the number of parameters of the constitutive model increases with increasing complexity of the model. The most commonly used yield criterion in geotechnical engineering is probably the Mohr-Coulomb yield criterion. It is simple and its validity is verified for many types of soils. However, it neglects the effect of the intermediate principal stress and the corners of the yield surface cause singularities in the numerical applications (Chen and Mizuno, 1990). Drucker-Prager yield function is a smoother form of Mohr-Coulomb yield criterion as shown in Figure 5.3. The Drucker-Prager yield surface is a right-circular cone with the symmetry about the hydrostatic axis. The yield surface is an extension of the Von Mises criterion but it is pressure dependent and it matches the behavior of granular geotechnical material better than the Von Mises

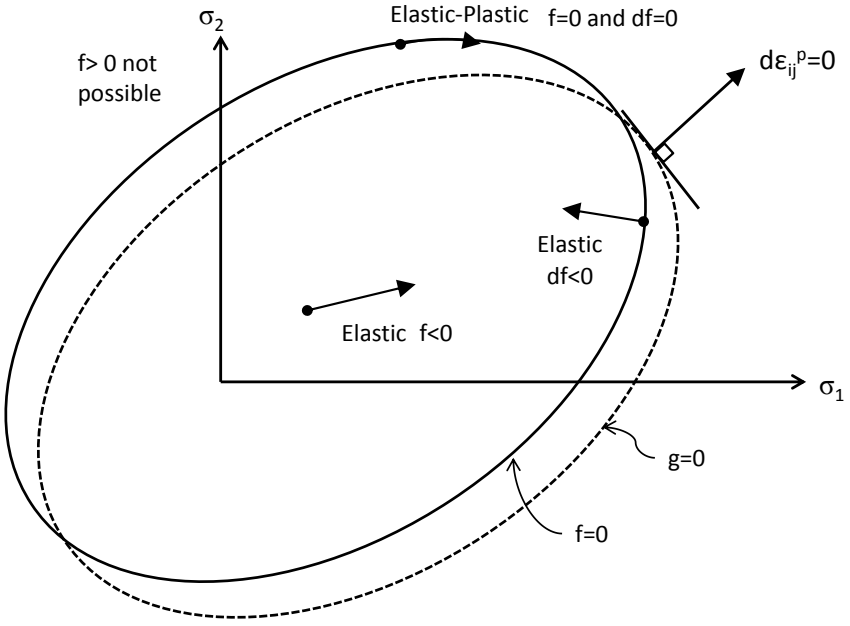

Figure 5.2: Definition of Yield and Flow Conditions for an Elasto-Plastic Material

criterion (Chen and Mizuno, 1990). The mathematical expression for Drucker-Prager yield function is given as:

$$f = \sqrt{J_2} + \alpha I_1 - k = 0 \tag{5.4}$$

where α and k are material constants. J_2 is the second invariant of the deviatoric stress tensor and I_1 is the first invariant of stress tensor. These invariants are defined as:

$$J_2 = \frac{1}{6}[(\sigma_{11} - \sigma_{22})^2 + (\sigma_{22} - \sigma_{33})^2 + (\sigma_{33} - \sigma_{11})^2] + {\sigma_{12}}^2 + {\sigma_{23}}^2 + {\sigma_{31}}^2 \tag{5.5}$$

$$I_1 = \sigma_{11} + \sigma_{22} + \sigma_{33} \tag{5.6}$$

The Drucker-Prager yield surface can be matched with the Mohr-Coulomb yield surface by selecting proper values for α and k, the model parameters. This selection can be achieved by matching the major vertices or the minor vertices of Mohr-Coulomb

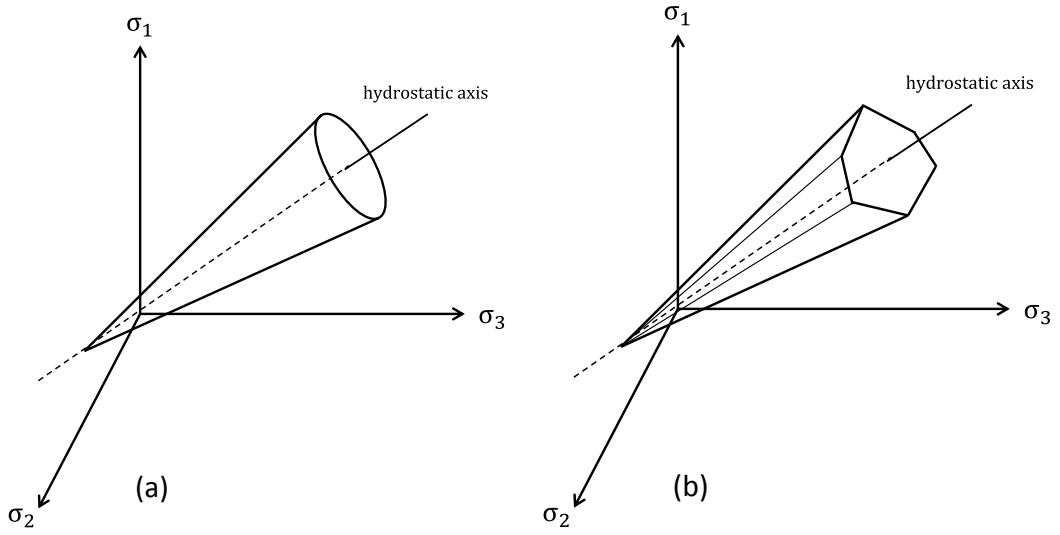

Figure 5.3: Drucker-Prager (a) and Mohr-Coulomb (b) yield surfaces in the π -plane

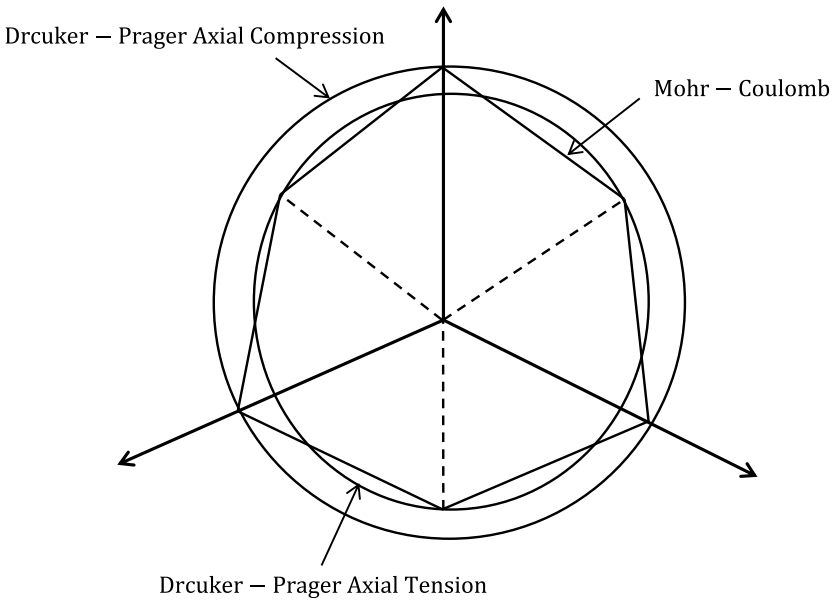

Figure 5.4: Drucker-Prager and Mohr-Coulomb yield surfaces matched at the major and minor vertices

surface representing axial compression and axial tension, respectively (Figure 5.4). Based on the matching process, α and k can be expressed in terms of ϕ and c. The matching process for the axial-compression case results in Equations 5.7 and 5.8 giving the relationships between α, k and ϕ, c (Chen and Mizuno, 1990).

$$\alpha = \frac{2\ sin\phi}{\sqrt{3}(3 - 3sin\phi)} \tag{5.7}$$

$$k = \frac{6c\ cos\phi}{\sqrt{3}(3 - 3sin\phi)} \tag{5.8}$$

The reason for selecting axial compression for matching these two yield criteria is that soil is stronger in compression and, in vast majority of cases, the soil is under compression rather than tension. This type of matching can be used if the problem is an axisymmetric problem like settlement of circular footings as in this study.

Drucker-Prager and Mohr-Coulomb models can also be matched to give identical limit loads for the plane strain case. The model parameters α and k of the Drucker-Prager model expressed in terms of the model parameters ϕ and c of the Mohr-Coulomb model for the plane strain case are:

$$\alpha = \frac{tan\phi}{\sqrt{(9 + 12tan^2\phi}} \tag{5.9}$$

$$k = \frac{3c}{\sqrt{(9 + 12tan^2\phi}} \tag{5.10}$$

The model MoDaMP-P gives the user the option to choose between axial compression matching and plane strain matching. Depending on the nature of the

problem, the user can decide which matching process suits better the problem in hand. A switch, *pln_strn* is added into the subroutine as a model parameter. The user should assign a value of "1" for the plane strain case or "0" for the axisymmetric case to the *pln_strn* parameter to have the Drucker-Prager and Mohr-Coulomb parameters matched accordingly.

5.3 FLOW RULE AND PLASTIC POTENTIAL

The strains in a soil body are purely elastic if the stress state is inside the yield surface; in other words, if $f < 0$. Upon further loading, the stress state will reach yield surface and beyond this point, the strains will be a combination of elastic and plastic components:

$$\varepsilon_{ij} = \varepsilon_{ij}^{p} + \varepsilon_{ij}^{e} \tag{5.11}$$

The elastic strains are calculated using Hooke's law as explained in Chapter 4 for both linear and nonlinear $\tau - \gamma$ response curves. The plastic strains are determined based on a flow rule which states that the plastic strain increments can be expressed as a function of the current stress state, σ_{ij}, a plastic multiplier $d\lambda$ and a plastic potential function, g as:

$$d\varepsilon_{ij}^{p} = d\lambda \frac{\partial g}{\partial \sigma_{ij}} \tag{5.12}$$

The plastic potential function can be the same with the yield function, $f = g$ for which Equation 5.12 becomes an associated flow rule. If g is different than f, then the flow rule is called a nonassociated flow rule. Equation 5.12 indicates that the direction of the strain increment $d\varepsilon_{ij}^{p}$ is normal to the surface of the potential function at the current stress state, σ_{ij}, as shown in Figure 5.2 The associated flow rule assumption is valid for metals but for granular materials such as soil and concrete, associated flow rule overpredicts the

volumetric changes in the soil. Therefore, soils are modeled usually using a nonassociated flow rule.

A plastic potential function with the same form as the yield function given in Equation 5.4 is used in MoDaMP-P. The proposed potential function includes the same stress invariants, J_2 and I_1. However the friction angle parameter, α , in the yield function is replaced with a dilatancy angle parameter, $\bar{\alpha}$, expressed by:

$$g = \sqrt{J_2} + \bar{\alpha} I_1 = 0 \tag{5.13}$$

The same procedure followed to obtain the relationship between α and ϕ can be applied to relate $\bar{\alpha}$ and ψ, where ψ is the dilatancy angle of the soil.

5.4 FORMULATION OF THE ELASTO-PLASTIC STIFFNESS MATRIX

An elasto-plastic stiffness matrix can be formulated using Equations 5.4, 5.11, 5.12 and 5.13. The derivation of this stiffness matrix is beyond the scope of this study but the details can be found in Chen and Mizuno (1990). The derived stiffness matrix is a function of f, g and the elastic stiffness matrix D_E. The form of the matrix is:

$$d\sigma = \left[D_E - \frac{D_E \left(\frac{\partial g}{\partial \sigma}\right) \left(\frac{\partial f}{\partial \sigma}\right)^T D_E}{\left(\frac{\partial f}{\partial \sigma}\right)^T D_E \left(\frac{\partial g}{\partial \sigma}\right)} \right] d\varepsilon \tag{5.14}$$

The whole term in the bracket reduces to D_E if the stress state is in the elastic range. The evaluation of the elasto-plastic stiffness matrix requires the derivatives of g and f with respect to σ. Using the chain rule, the derivative of the yield function with respect to stress tensor is:

$$\left(\frac{\partial f}{\partial \sigma}\right) = \left(\frac{\partial f}{\partial J_2}\right)\left(\frac{\partial J_2}{\partial \sigma}\right) + \left(\frac{\partial f}{\partial I_1}\right)\left(\frac{\partial I_1}{\partial \sigma}\right) \tag{5.15}$$

$$\left(\frac{\partial f}{\partial J_2}\right) = 0.5J^{-0.5} \;\; and \;\; \left(\frac{\partial f}{\partial I_1}\right) = \alpha \tag{5.16}$$

$$\frac{\partial J_2}{\partial \sigma} = \begin{bmatrix} \frac{1}{3}(2\sigma_{11} - \sigma_{22} - \sigma_{33}) \\ \frac{1}{3}(2\sigma_{22} - \sigma_{11} - \sigma_{33}) \\ \frac{1}{3}(2\sigma_{33} - \sigma_{22} - \sigma_{11}) \\ 2\sigma_{12} \\ 2\sigma_{23} \\ 2\sigma_{31} \end{bmatrix} \tag{5.17}$$

$$\frac{\partial I_1}{\partial \sigma} = \begin{bmatrix} 1 \\ 1 \\ 1 \\ 0 \\ 0 \\ 0 \end{bmatrix} \tag{5.18}$$

$$\frac{\partial f}{\partial \sigma} = 0.5J^{-0.5} \begin{bmatrix} \frac{1}{3}(2\sigma_{11} - \sigma_{22} - \sigma_{33}) \\ \frac{1}{3}(2\sigma_{22} - \sigma_{11} - \sigma_{33}) \\ \frac{1}{3}(2\sigma_{33} - \sigma_{22} - \sigma_{11}) \\ 2\sigma_{12} \\ 2\sigma_{23} \\ 2\sigma_{31} \end{bmatrix} + \alpha \begin{bmatrix} 1 \\ 1 \\ 1 \\ 0 \\ 0 \\ 0 \end{bmatrix} \tag{5.19}$$

The same procedure used for $\partial f/\partial\sigma$ is applied to evaluate $\partial g/\partial\sigma$. Using the chain rule, the derivative of the potential function with respect to the stress tensor is:

$$\left(\frac{\partial g}{\partial \sigma}\right) = \left(\frac{\partial g}{\partial J_2}\right)\left(\frac{\partial J_2}{\partial \sigma}\right) + \left(\frac{\partial g}{\partial I_1}\right)\left(\frac{\partial I_1}{\partial \sigma}\right) \tag{5.20}$$

$$\left(\frac{\partial g}{\partial J_2}\right) = 0.5J^{-0.5} \;\; and \;\; \left(\frac{\partial g}{\partial I_1}\right) = \bar{\alpha} \tag{5.21}$$

By combining Equations 5.20 and 5.21, the derivative of the potential function can be expressed as:

$$\frac{\partial g}{\partial \sigma} = 0.5J^{-0.5}\begin{bmatrix} \frac{1}{3}(2\sigma_{11} - \sigma_{22} - \sigma_{33}) \\ \frac{1}{3}(2\sigma_{22} - \sigma_{11} - \sigma_{33}) \\ \frac{1}{3}(2\sigma_{33} - \sigma_{22} - \sigma_{11}) \\ 2\sigma_{12} \\ 2\sigma_{23} \\ 2\sigma_{31} \end{bmatrix} + \bar{\alpha}\begin{bmatrix} 1 \\ 1 \\ 1 \\ 0 \\ 0 \\ 0 \end{bmatrix} \tag{5.22}$$

The matrices given in Equations 5.19 and 5.22 and their transpose matrices are then inserted into Equation 5.14 to create the elasto-plastic stiffness matrix. The resulting stiffness matrix is then multiplied with the incremental strains to evaluate the stress increments.

5.5 IMPLEMENTATION OF MODAMP-P INTO PLAXIS

The procedure explained in Section 5.4 presents the mathematical background of the derivation of the stiffness matrix. Implementation of this mathematical formulation into PLAXIS as a constitutive model requires a certain procedure as explained in Chapter 4.

The main steps of the subroutine are similar to the subroutine of MoDaMP explained in detail in Section 4.5.3 and the explanation is not repeated. Only additional steps, variables and switches created for MoDaMP-P are discussed.

The subroutine starts with IDTask 1 where the soil parameters are defined and the state variables are initialized. In addition to the 5 soil parameters in Section 4.5.3, four new parameters are defined. These parameters are as follows:

(1) $phi =$ The friction angle of soil, ϕ'. It is converted to α using Equation 5.7 or 5.9 depending on whether the problem is an axisymmetric or a plane strain case, respectively.

(2) $c\_coh =$ The cohesion of the soil, c is in psf. It is converted to k by using Equation 5.8 or 5.10 depending on whether the problem is an axisymmetric or a plane strain case, respectively.

(3) $dilt =$ The dilation angle of the soil, ψ. It is converted to $\bar{\alpha}$ in the same way ϕ' is converted to α.

(4)) $pln\_strn =$ This is the switch that controls the matching procedure of Drucker-Prager and Mohr-Coulomb model parameters. For plane strain condition, $pln\_strn = 1$ and for axisymmetric case $pln\_strn = 0$.

IDTask 2 is the same as in MoDaMP where incremental stresses, $dSig$, are calculated based on the stiffness matrix, D, and incremental strains, $dEps$. The main difference between MoDaMP and MoDaMP-P is in IDTask 3. First, G_{max} and G_t are calculated based on the formulation explained in Section 4.5.3 following the $G/G_{\max} - log\ \gamma_{oct}$ relationships. An additional state variable, $StVar(118)$, is defined in MoDaMP-P to store the value of G_t. In the elastic range, at each step, G_t will be updated and the new value will be assigned to $StVar(118)$. However, if the soil yields, then $StVar(118)$ will

not be updated and the value of $StVar0(118)$ will be assigned to $StVar(118)$. Thus, the G_t value of the soil at the time of yielding will be used throughout the plastic calculation range. If G_t is not kept constant after the soil yields, then the calculated strains will be excessive as the strains will be duplicated from the plastic flow rule and from the nonlinear elastic formulation.

If the stress state reaches a point where the soil yields, the next step in MoDaMP-P is defining and evaluating the derivatives presented in Equations 5.15 through 5.22. Using these derivatives, the elasto-plastic stiffness matrix defined in Equation 5.14 is created and the stresses are calculated in IDTask 2 according to this new elasto-plastic stiffness matrix.

The IDTasks 4, 5 and 6 are the same as in MoDaMP which is explained in Section 4.5.3.

5.6 VERIFICATION OF THE NONLINEAR ELASTO-PLASTIC MODEL

After MoDaMP-P was implemented into PLAXIS following the procedures explained in Sections 4.5.3 and 5.5, the model was verified with numerous tests.

Verification of the model included comparison of triaxial test simulations of one-element models using MoDaMP-P and Mohr-Coulomb model in the: (1) nonlinear elastic range, and (2) perfectly plastic range.

5.6.1 Element Tests

PLAXIS has a module to simulate different geotechnical tests. This module uses the selected constitutive model (built-in or user defined) to run element tests according to loading and boundary conditions for different geotechnical tests, including triaxial tests and simple shear tests. This module is utilized to verify MoDaMP-P by running triaxial

tests. These triaxial tests are simulated under different assumptions and the results are compared with results obtained using the Mohr-Coulomb model.

5.6.1.1 Nonlinear-Elastic Range of MoDaMP-P

MoDaMP-P consists of linear and nonlinear elastic and perfectly plastic parts as explained previously. The plastic part governs after the yielding state of stress is reached. The model can be verified in these ranges separately. To verify the linear and nonlinear elastic parts, the soil can be forced not to yield by increasing the ϕ' or c' values of the soil. If the soil is forced not to yield, then MoDaMP-P should behave as a purely nonlinear elastic model. Simple shear tests are simulated in PLAXIS using MoDaMP-P and the results from the tests were compared with the analytical solution based on the $G/G_{max} - \log\gamma$ curves. It should be noted that the ϕ' value is assumed to be 100^{o} which is physically unrealistic but it is used to prevent the soil from yielding, and resulting in pure nonlinear elastic response. Three simulations with different mean effective confining pressures were carried out. The comparison of the simulation results and the analytical solutions based on $G/G_{max} - \log\gamma$ curves is presented in Figure 5.5. As seen in the figure, there is an excellent match between the numerical and analytical solution which verifies that the linearity and nonlinearity based on the $G/G_{max} - \log\gamma$ curves is successfully implemented in the model. Moreover, the comparisons at different σ_0' values show that the stress-dependency of the $G/G_{max} - \log\gamma$ curves is also taken into account correctly.

5.6.1.2 Perfectly-Plastic Range of MoDaMP-P

After the soil yields according to Equation 5.4, the strains occurring in the soil are controlled by the flow rule given in Equation 5.12. In MoDaMP-P, yielding is only a function of the stress state and therefore the linearity and nonlinearity in the elastic part

does not affect the values of the stress invariants at yielding. MoDaMP-P is tested in the plastic range to verify the yield and flow rules by assuming linear elastic behavior until yielding. This condition is achieved by assigning large constant value to γ_r in the $G/G_{max} - \log\gamma$ relationships to keep the G/G_{max} value always 1.0 (or very close 1.0). The soil behaves linearly elastic pre-yielding and perfectly plastic post-yielding with this modification. The soil testing simulation module in PLAXIS is used to model triaxial tests using MoDaMP-P and the Mohr-Coulomb model. In the simulation with

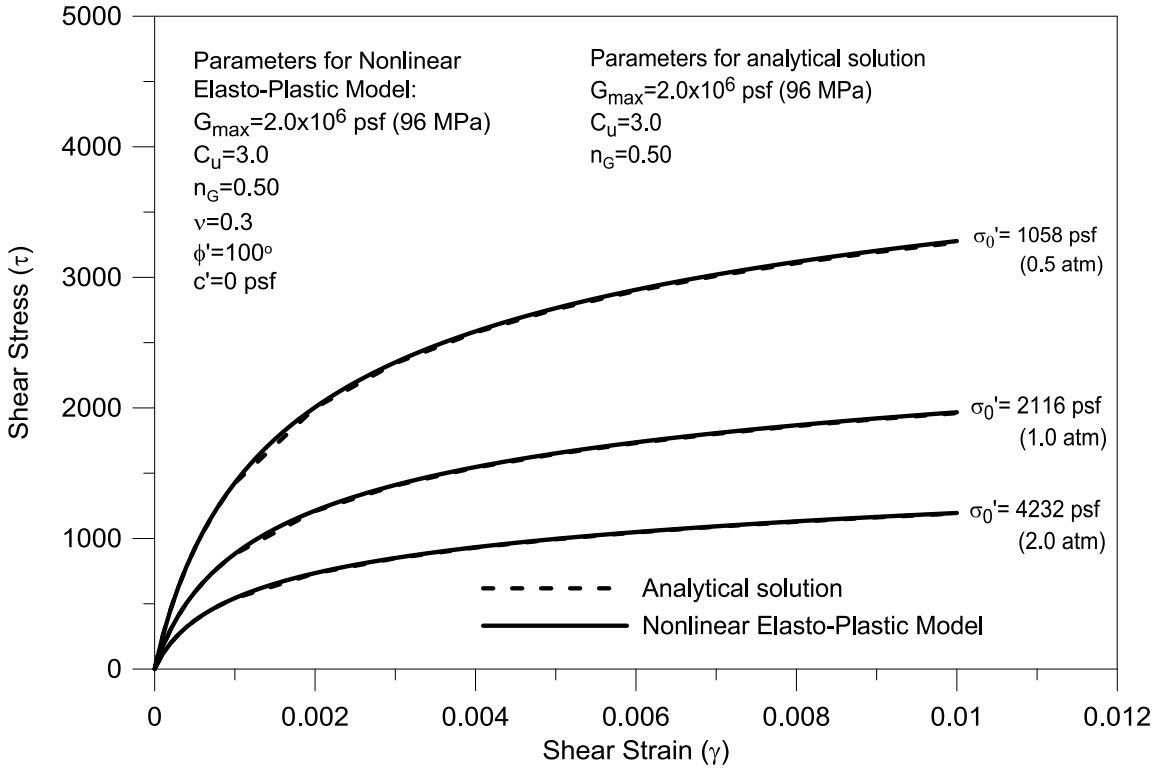

Figure 5.5: Comparison of shear stress-shear strain curves obtained numerically with MoDaMP-P and obtained analytically based on the $G/G_{max} - \log\gamma$ curves determined from Menq (2003) model

MoDaMP-P, the value of γ_r is assumed to be 1000 % so that a comparison between these two models is possible. The soil parameters for MoDaMP-P are determined by matching α and k with ϕ and c, respectively, considering an axisymmetric case.

Figure 5.6 shows the deviatoric stress-axial strain response of soils with different stiffness and strength values. As it is seen in the figure, the nonlinear elasto-plastic model constrained to an insignificant modulus reduction by assuming γ_r=1000 % gives almost identical results with the Mohr-Coulomb model. The agreement in yield stresses and strains from the models verify that the plastic formulation of the nonlinear elasto-plastic model is implemented correctly in the subroutine.

5.7 SUMMARY

The soil model based on the dynamically measured soil properties, MoDaMP was modified by incorporating a yield function and plastic flow rules to the existing nonlinear elastic model. The motivation for developing this new elasto-plastic model, called MoDaMP-P, is to investigate the effects of the volumetric changes in the soil or in other words the effect of the dilation angle. A very well-known yield function, Drucker-Prager, is used in this model along with a non-associated flow rule that uses the soil dilatancy angle.

In Sections 5.2 and 5.3, general definitions of yield functions and plastic flow rules are introduced. The specific yield function and plastic flow rule for MoDaMP-P are also discussed. In Section 5.4, the formulation of the elasto-plastic stiffness matrix of MoDaMP-P is explained. The implementation procedure of MoDaMP-P into PLAXIS is discussed in Section 5.5. Finally, MoDaMP-P is verified by using element tests and comparing the results of the tests with the analytical results and Mohr-Coulomb soil model in the nonlinear-elastic and perfectly plastic ranges, respectively.

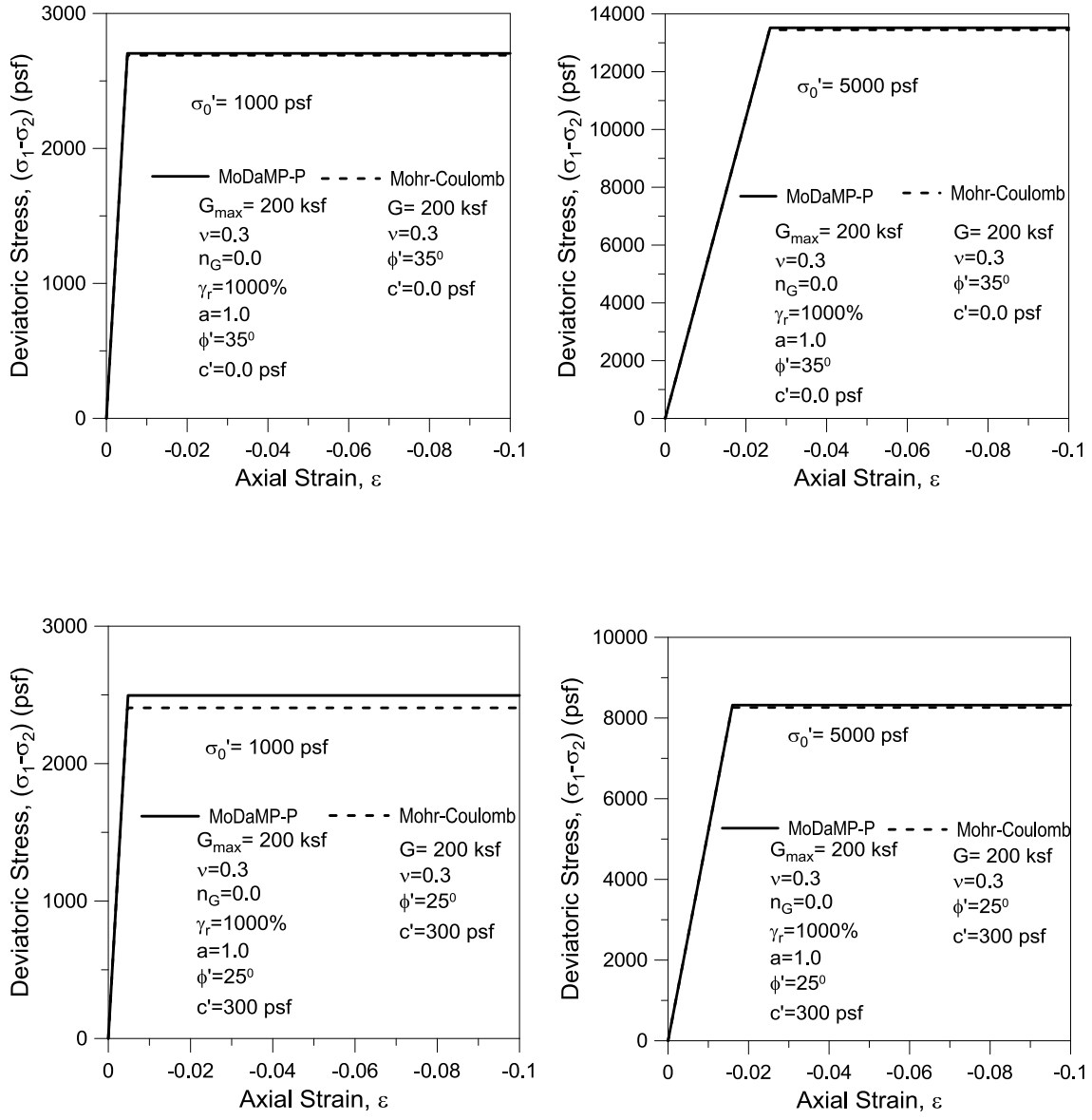

Figure 5.6: Comparison of shear stress-shear strain curves obtained numerically with MoDaMP-P and Mohr-Coulomb to verify MoDaMP-P in the plastic range

Chapter 6: Load-Settlement Tests at the NGES Test Site

6.1 INTRODUCTION

Two small-scale footings with diameters of 3.0 and 1.5 ft (0.91 m and 0.46 m) were constructed at the National Geotechnical Experimentation Site (NGES) at Texas A&M University (see Figure 6.1). The footings were constructed as a part of a long-term project to create a dataset of load-settlement curves of footings on granular soil that had been evaluated with in-situ seismic measurements and either nonlinear dynamic $G_{max} - \log\gamma$ relationships measured in the laboratory or in-situ, or both. The small-scale footings were in the vicinity of the test site reported by Briaud and Gibbens (1994) where different- sized footings were tested for an ASCE Geo-Institute settlement prediction symposium in 1994. Several field tests, including SPT, CPT, pressuremeter, dilatometer and seismic crosshole tests, were conducted at the site (Briaud and Gibbens, 1994). Additional SASW tests near the small-scale footings were conducted by Park et al. (2009). Moreover, RCTS tests were conducted on two undisturbed samples at the University of Texas at Austin.

The general soil properties at the test site are discussed in Section 6.2 and the results of SPT, CPT and triaxial test results are presented in Section 6.3. Then, the in-situ SASW test results and RCTS test results from laboratory measurements are presented in Section 6.4. The representative $\log V_s - \log\sigma_o'$ relationships based on SASW tests and the $G_{max} - \log\gamma$ relationships based on RCTS results are discussed in Section 6.5. Next, the field load-settlement tests are presented in Section 6.6. Finally, the settlement predictions with MoDaMP are discussed in Section 6.7 and are compared with the field load tests.

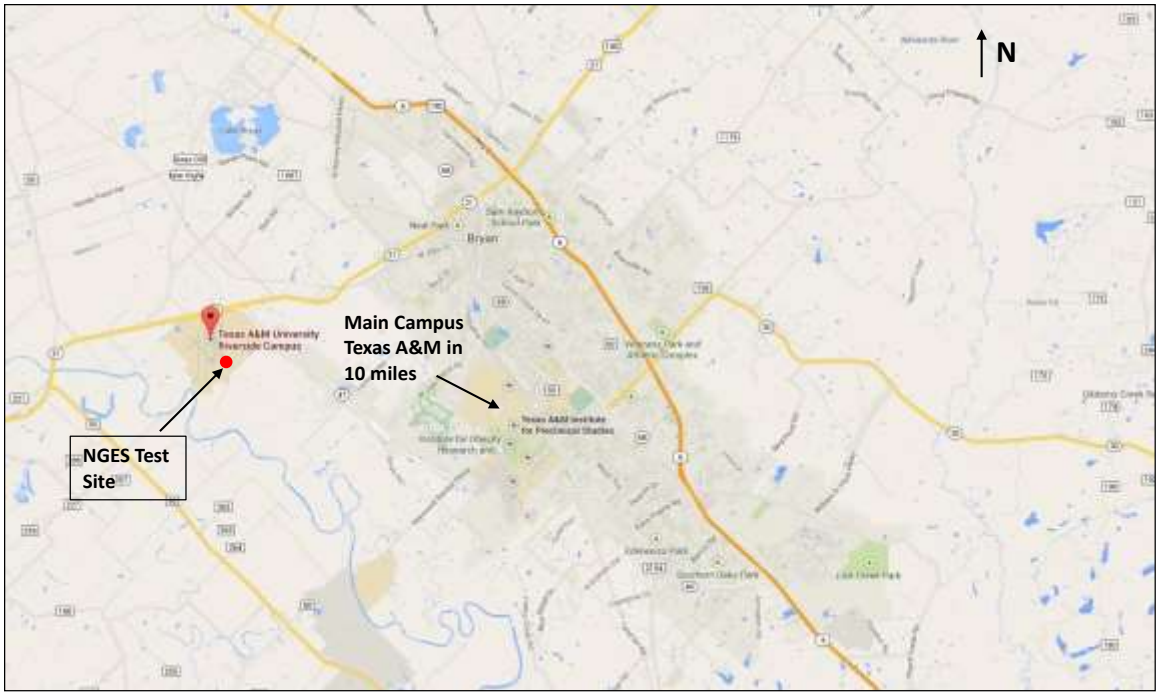

Figure 6.1: Location of the NGES Test Site at College Station, Texas

6.2 Soil Properties at the NGES Test Site

The soil at the NGES site is generally cohesionless. The soil profile reported by Briaud and Gibbens (1994) is shown in Figure 6.2. Four main layers were indicated over the 108-ft (33-m) depth of investigation at the field site. As seen in the Figure 6.2, the soil at the NGES site is predominantly sand to a depth of 36 ft (11 m). The gradation curves for the upper 30 ft (9.0 m) are given in Figure 6.3. The upper 11.5 ft (3.5 m) is medium dense, silty fine sand, classified as SP-SM in the USCS. The silty sand is underlain by an 11.5-ft (3.5-m) thick layer of medium dense sand with clay and gravel. From a depth of 23 ft to 36 ft, the soil is silty sand to sandy clay. The soil below this layer is hard clay which has a negligible effect on the field load-settlement tests because of its depth below the footings. The water table is at a depth of 16.1 ft (4.9 m) .

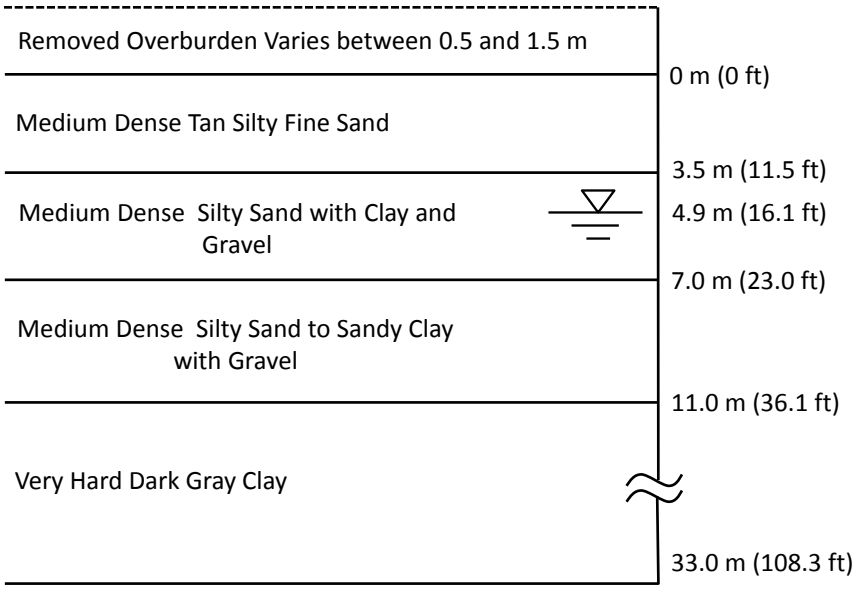

Figure 6.2: Soil types and layer depths at the NGES test site at Texas A & M University (after Briaud & Gibbens, 1994)

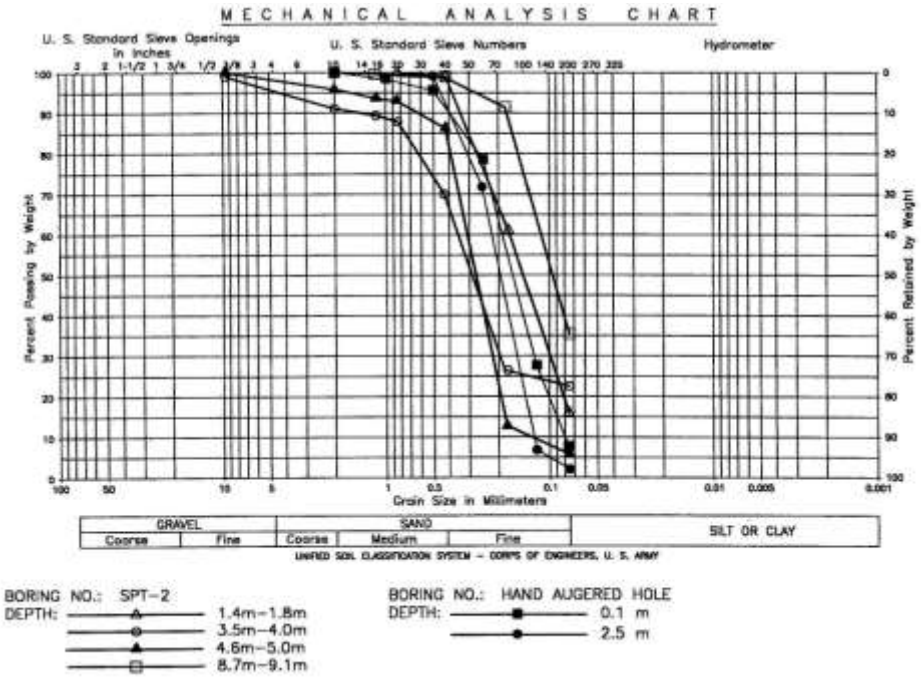

Figure 6.3: Grain size analysis (from Briaud & Gibbens, 1994)

Briaud and Gibbens (1994) report that the water content results from samples obtained using a drilling rig ranges from 11.1% to 33.5% whereas the results from samples obtained using a hand auger is about 5%. They attribute this variation to the seasonal moisture fluctuation occurring in the test site. Park et al. (2009) report a water content of 12-14 % and a total unit weight of about 126 lb/ft^3 near the surface at the load-settlement test site which is in the vicinity of the test site reported by Briaud and Gibbens (1994).

6.3 SPT,CPT AND TRIAXIAL TEST RESULTS

Standard Penetration Tests were performed on the NGES test site as a part of the extensive in-situ testing program for the settlement prediction symposium reported by Briaud and Gibbens (1994). The SPT energy measurements indicated that the average energy efficiency during the tests was about 53%. The results of the two SPT tests that were in the vicinity of the footing tests are shown in Figure 6.4. As seen in the figure, the average blow count between 3.5 ft and 36.1 ft (1.1 m and 11.0) is about 12 and it increases after 30 ft (9 m) where the hard clay layer starts.

A total of five CPT soundings were performed in the vicinity of the NGES test site. Only three of the CPT tests are reported since the other two soundings had to be stopped because of high levels of pore pressures. The tip resistance and the side friction measured in these tests are shown in Figure 6.5. Only two of the three tests are shown in Figure 6.5 because they were close to the footing tests.

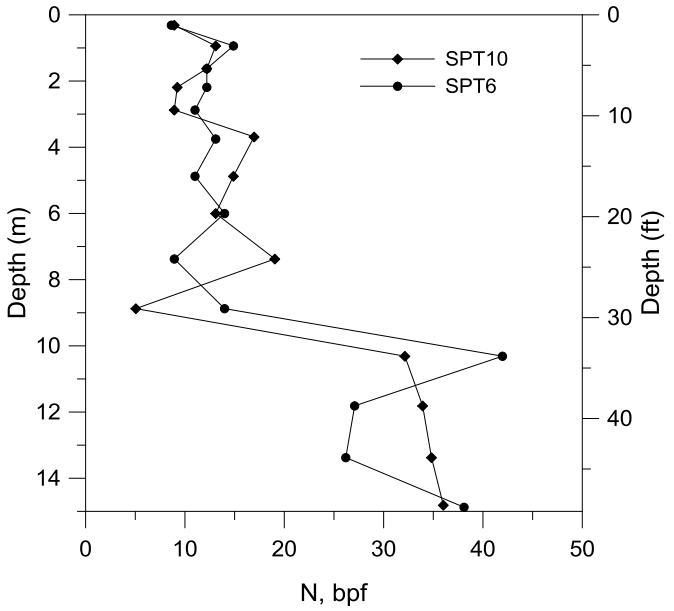

Figure 6.4: SPT profiles at the NGES sand site (from Briaud and Gibbens, 1994)

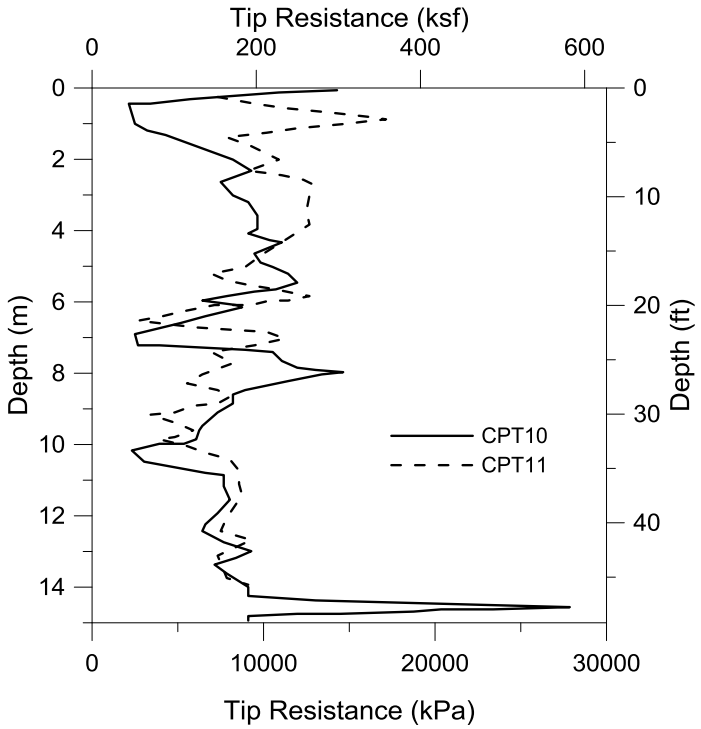

Figure 6.5: CPT profiles at the NGES sand site (from Briaud and Gibbens, 1994)

6.4 SEISMIC IN-SITU AND DYNAMIC LABORATORY MEASUREMENTS

6.4.1 SASW Tests

As a part of the investigation of in-situ measurements of linear and nonlinear soil properties at the NGES test site, Park et al. (2009) performed Spectral-Analysis-of-Surface-Wave (SASW) tests along three lines around the two footings. Small-scale downhole tests were also conducted beneath the 3.0-ft (0.9 m) footing. The shear wave velocity, (V_s), measurements from SASW and downhole tests were combined to find a best-estimate V_s profile. This best-estimate V_s profile from SASW tests is shown in Figure 6.6 along with the crosshole data reported by Briaud and Gibbens (1994). As seen in the figure, the SASW and crosshole seismic measurements are generally in good agreement. However, the crosshole test data starts at a depth of about 6 ft, and most of the soil in which the strains and settlements beneath the footings are occurring is within this 6-ft (1.8-m) layer. Figure 6.6b is the expanded version of Figure 6.6a and shows the V_s profile more closely for depths that contribute most to the settlements of the footings. The average shear wave velocity at depths between 0-6 ft (0-1.8 m) is about 650 ft/s (198 m/s). These shear wave velocities are used in determining the $\log V_s - \log \sigma_o'$ relationships as explained in Section 6.5.

6.4.2 RCTS Tests

Two, hand-carved, intact specimens were obtained at the NGES test site and they were transported to the Soil Dynamics Laboratory at the University of Texas at Austin. These two specimens, denoted as UTA-62-A(1C) and UTA-62-B(2C) were tested in the combined Resonant Column Torsional Shear (RCTS) device by Mr. Bohyoung Lee. Both specimens were classified as silty sand (SM). UTA-62-A(1C) and UTA-62-B(2C)

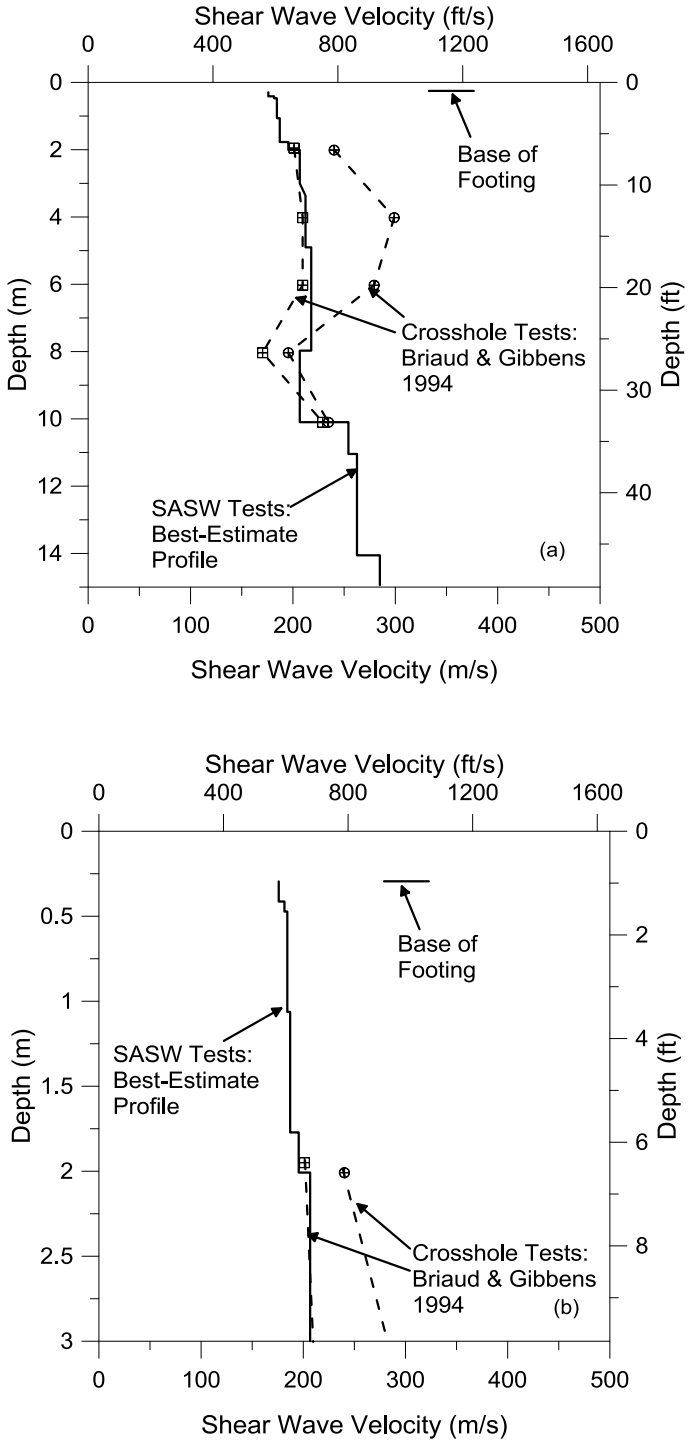

Figure 6.6: Shear wave velocity profiles at the NGES sand site (a) to a depth of 49 ft (15 m) and (b) expanded to show the top 10 ft (3 m) (from Park et al., 2009)

had average water contents of 8.0% and 9.9%, and total unit weights of 126.3 lb/ft^3 and 126.6 lb/ft^3, respectively.

Figure 6.7 shows V_s measurements in the small-strain range under different mean effective confining pressures, σ_0', assuming negligible capillary stresses. As seen in the figure, V_s is increasing with increasing σ_0'. The shear wave velocities of UTA-62-A(1C) are slightly lower than the shear wave velocities of UTA-62-B(2C) . Also the slope of $\log V_s - \log \sigma_o'$ relationship of UTA-62-A(1C) is slightly higher than the slope of UTA-62-B(2C). As previously discussed in Chapter 3, the slope of the $\log V_s - \log \sigma_o'$ relationships, n_s, define the stress dependency of the V_s. A normally consolidated, uncemented sand typically exhibits a value of n_s in the range of 0.23-0.26 (generally assumed to be 0.25). The small-strain measurements of V_s of UTA-62-A(1C) and UTA-62-B(2C) shows that n_s is smaller than 0.25, possibly indicating a cementation. The best fit to the $\log V_s - \log \sigma_o'$ relationships of both specimens in the form of

$$V_s = V_{s\_1atm}\left(\frac{\sigma_0'}{Pa}\right)^{n_s} \tag{6.1}$$

are shown in Figure 6.7. In this formulation, V_{s_1atm} (also denoted as A_s) is the shear wave velocity at a σ_0' of 1 atm, and Pa is the atmospheric pressure in the same units as σ_0'. These $\log V_s - \log \sigma_o'$ relationships obtained from RCTS testing are compared with the same $\log V_s - \log \sigma_o'$ relationships interpreted from the in-situ measurements in Section 6.5. If no in-situ measurements were available, the laboratory measurements would be used in establishing the $\log V_s - \log \sigma_o'$ relationships which are then used to determine the $\log G_{max} - \log \sigma_o'$ relationships. MoDaMP incorporates the $G_{\max\_1atm}$ value obtained

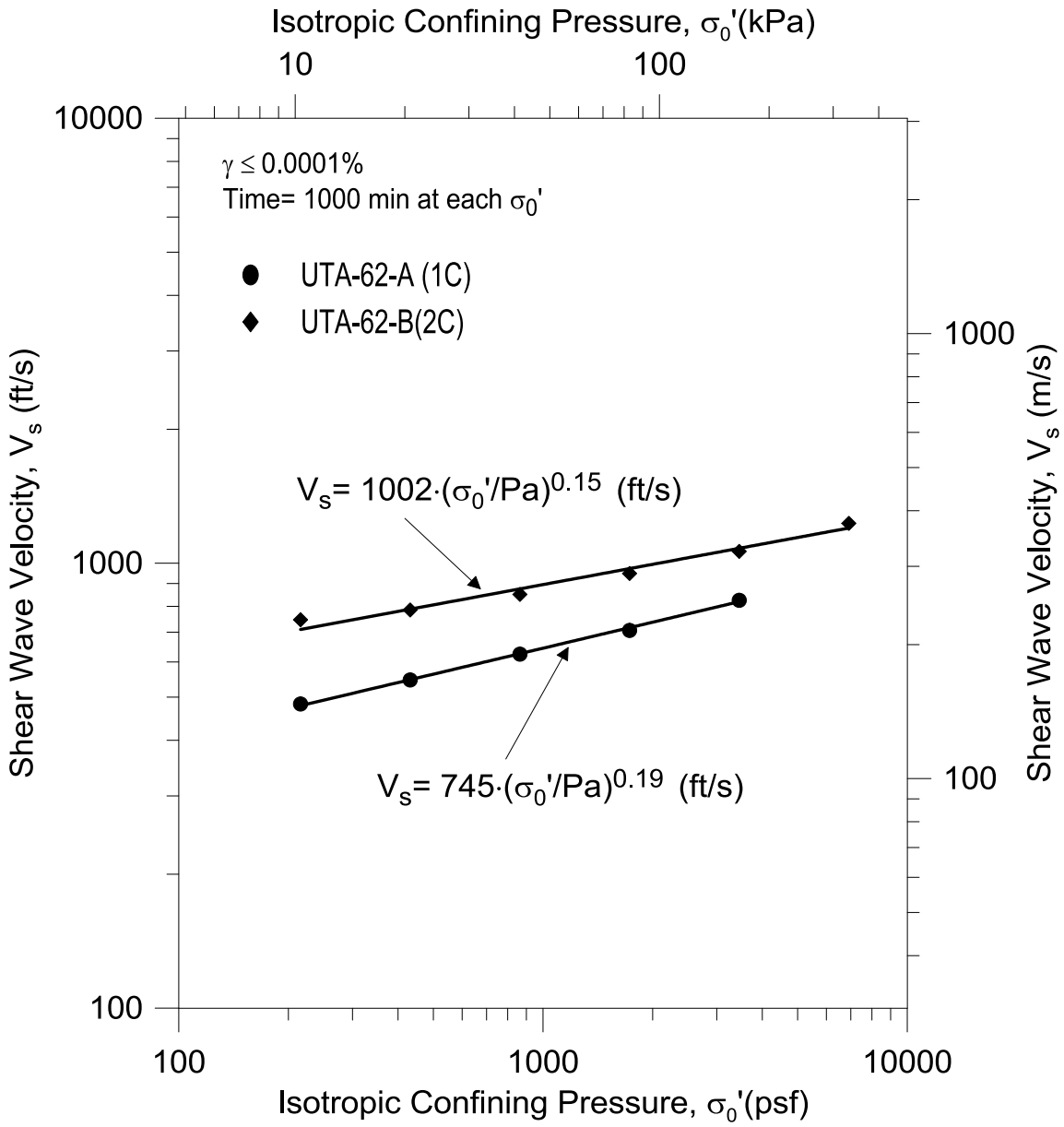

Figure 6.7: Log V_s-log σ'_o relationships for the NGES test site obtained from RCTS tests

using $\log G_{max} - \log \sigma_o'$ relationships as one of the main input parameters. Evaluation of $G_{\max\_1atm}$ is discussed in Section 6.5.

Specimens UTA-62-A(1C) and UTA-62-B(2C) were also tested at large strains to determine the $G - \log \gamma$ behavior of the silty sand at the NGES site. The tests were performed under different σ_o' to investigate the stress dependency of the $G - \log \gamma$ relationships. The results from the combined RCTS tests are presented in Figure 6.8 for σ_o' of 6 psi. Figures 6.9 and 6.10 show the $G - \log \gamma$ relationships for σ_o' =24 psi and σ_o' =48 psi, respectively. Comparing the $G - \log \gamma$ relationships from specimens UTA-62-A(1C) and UTA-62-B(2C) shows that specimen UTA-62-B(2C) gives higher G values at all strains. The measurements from Resonant Column (RC) tests are performed at frequencies in the range of 186.7 Hz to 205.1 Hz and 71.6 Hz to 123.2 Hz for specimens UTA-62-A(1C) and UTA-62-B(2C), respectively. The Torsional Shear (TS) tests are performed at f = 0.5 Hz and comparisons of the results from RC and TS tests indicate that the values of G exhibit little frequency dependency, so this dependency can be neglected. Shear moduli of specimen UTA-62-B(2C) from RC tests are slightly higher compared to the TS results at σ_o' =6 psi, but the results of specimen UTA-62-B(2C) at other pressures and the results of specimen UTA-62-A(1C) at all pressures are similar. Moreover, the measurements from the 1st and 10th cycles of the TS tests shows that shear modulus is not affected significantly by the number of cycles as reported by Darendeli (2001).

The nonlinearity in the $G - \log \gamma$ relationships is usually expressed as normalized shear modulus curves, i.e, $G/G_{max} - \log \gamma$ curves. Figures 6.11, 6.12 and 6.13 present the normalized shear modulus curves obtained in RCTS tests of specimens UTA-62-A(1C) and UTA-62-B(2C). The $G/G_{max} - \log \gamma$ curves are linear up to γ_e^t after which they

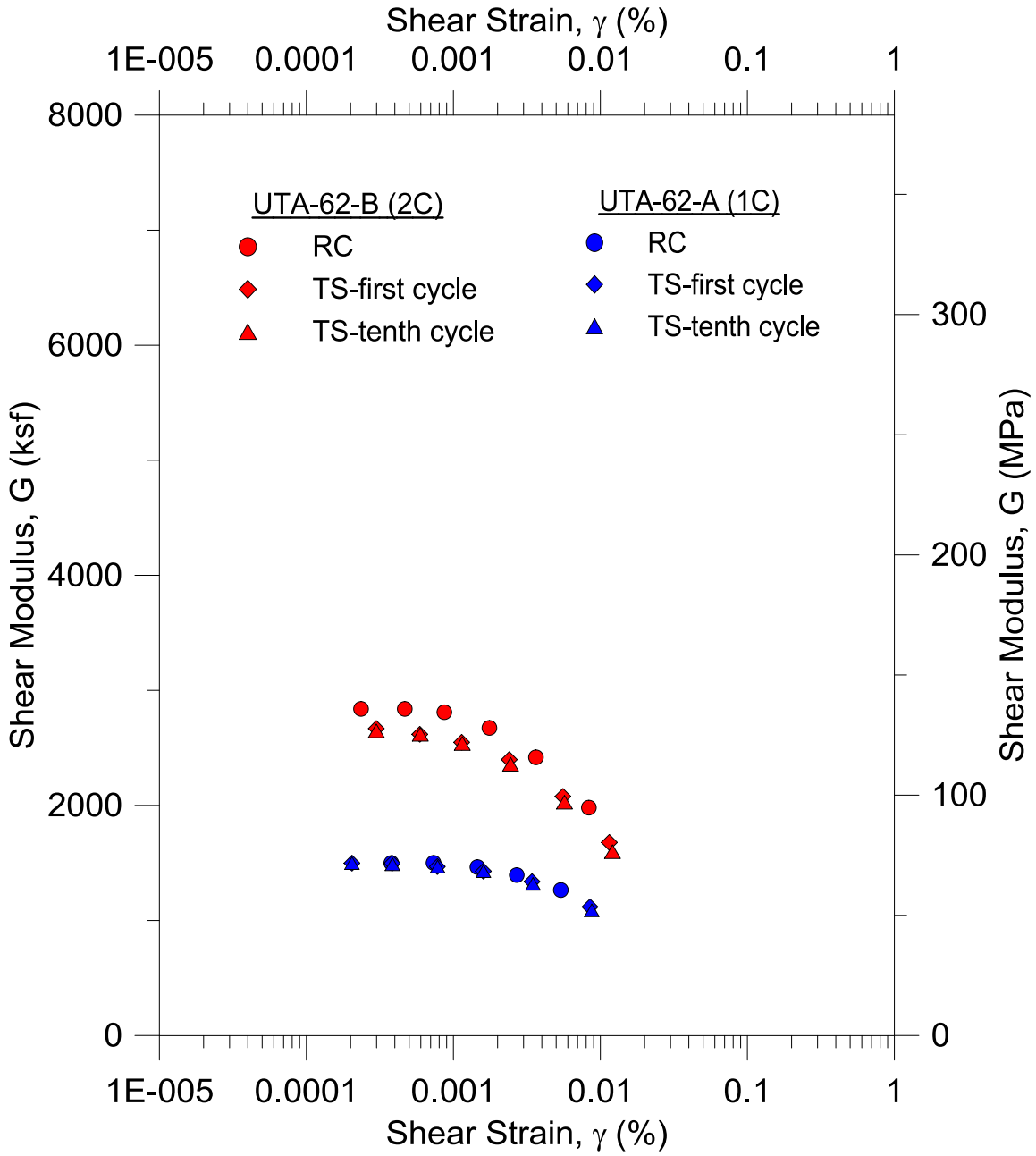

Figure 6.8: $G - \log\gamma$ relationships determined from RCTS tests at $\sigma_o' = 6$ psi of two intact specimen from the NGES test site

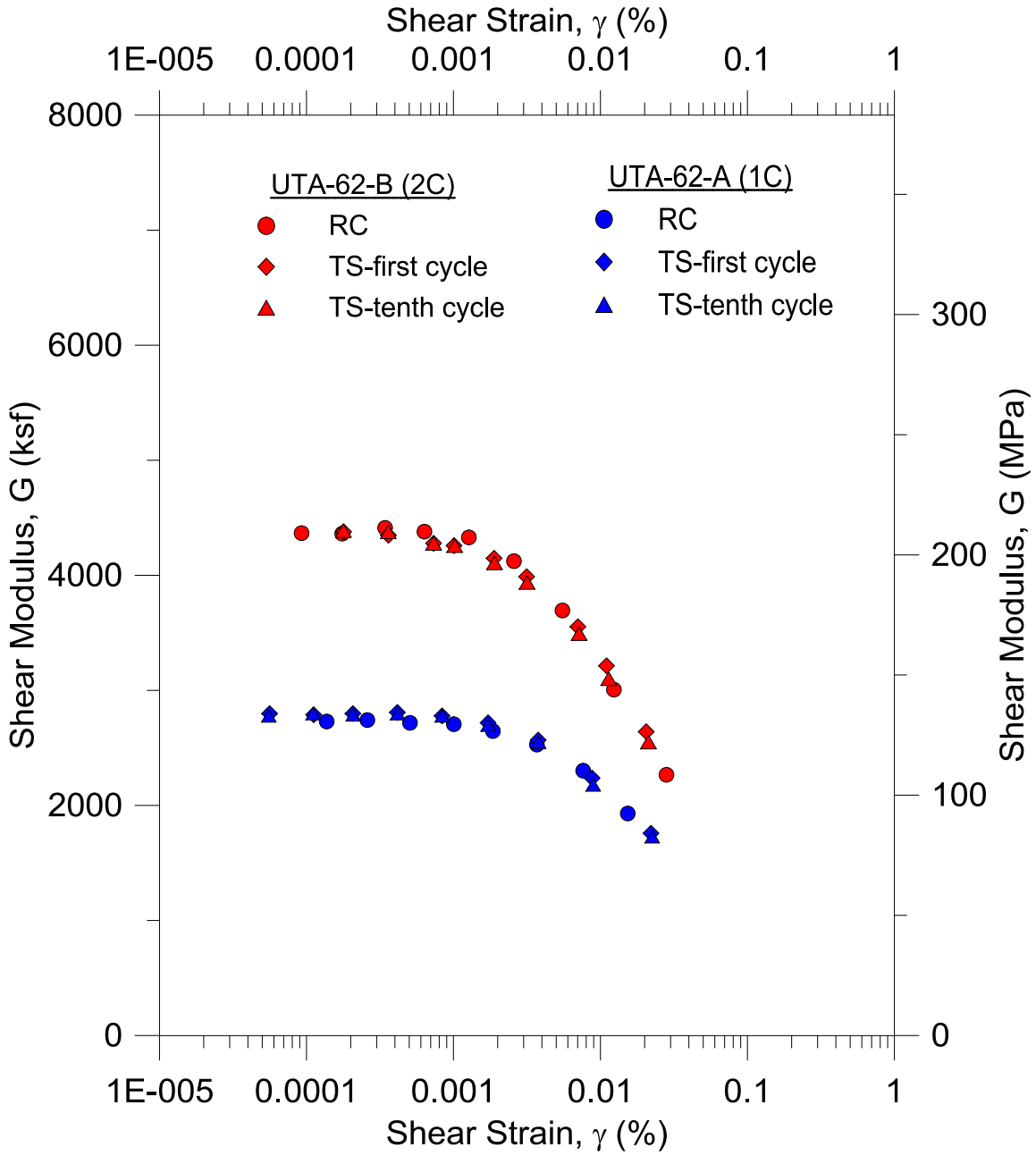

Figure 6.9: $G - \log\gamma$ relationships determined from RCTS tests at $\sigma_o' = 24$ psi of two intact specimen from the NGES test site

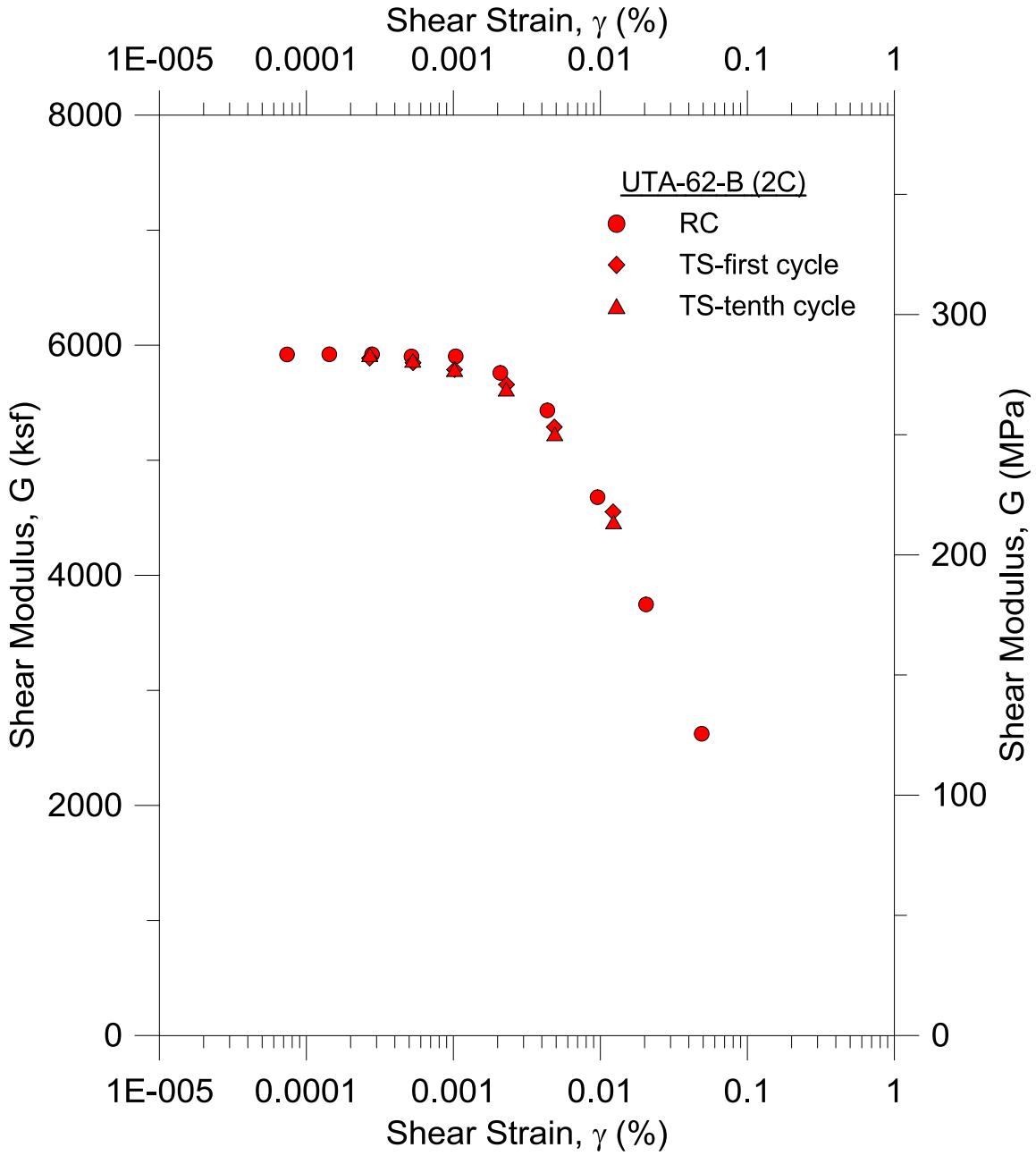

Figure 6.10: $G - \log\gamma$ relationships determined from RCTS tests at $\sigma_o' = 48$ psi of one intact specimen from the NGES test site

become nonlinear. The values of γ_e^t are 0.0007%, 0.0010% and 0.0012% for σ_o' =6 psi, σ_o' =24 psi and σ_o' =48 psi, respectively. The $G/G_{max} - \log\gamma$ curves from UTA-62-A(1C) and UTA-62-B(2C) agree quite well even though measured G values are somewhat higher for specimen UTA-62-B(2C) as seen in Figures 6.7 through 6.10.

It should be noted that $G/G_{max} - \log\gamma$ curves from RCTS tests for the silty sand from NGES site are more nonlinear than the typical $G/G_{max} - \log\gamma$ curves observed in a normally consolidated, uncemented sand. This somewhat higher nonlinearity is an indicator of cementation in the soil. The cementation of the soil might be disturbed during sampling and in that case the dynamic measurements in the laboratory will not manifest the cementation of the soil. In-situ testing of the soil, on the other hand, reveals more information about cementation as it is discussed in Section 6.5.

Figure 6.14 shows all $G/G_{max} - \log\gamma$ measurements from RCTS tests at different σ_o' values. The modified hyperbolic model proposed by Darendeli (2001):

$$G/G_{max} = \frac{1}{1 + \left(\frac{\gamma}{\gamma_r}\right)^a} \tag{6.2}$$

was fit to the data and the corresponding γ_r and a values were determined from these best-estimate fits. The γ_r values determined from these best-estimate curves are plotted against the corresponding σ_o' values (Figure 6.15). The $\gamma_r - \log\sigma_o'$ relationship shows a linear trend on this plot which can be represented by:

$$\gamma_r = 0.0200 \log\left(\frac{\sigma_o'}{Pa}\right) + 0.0277\ (\%) \tag{6.3}$$

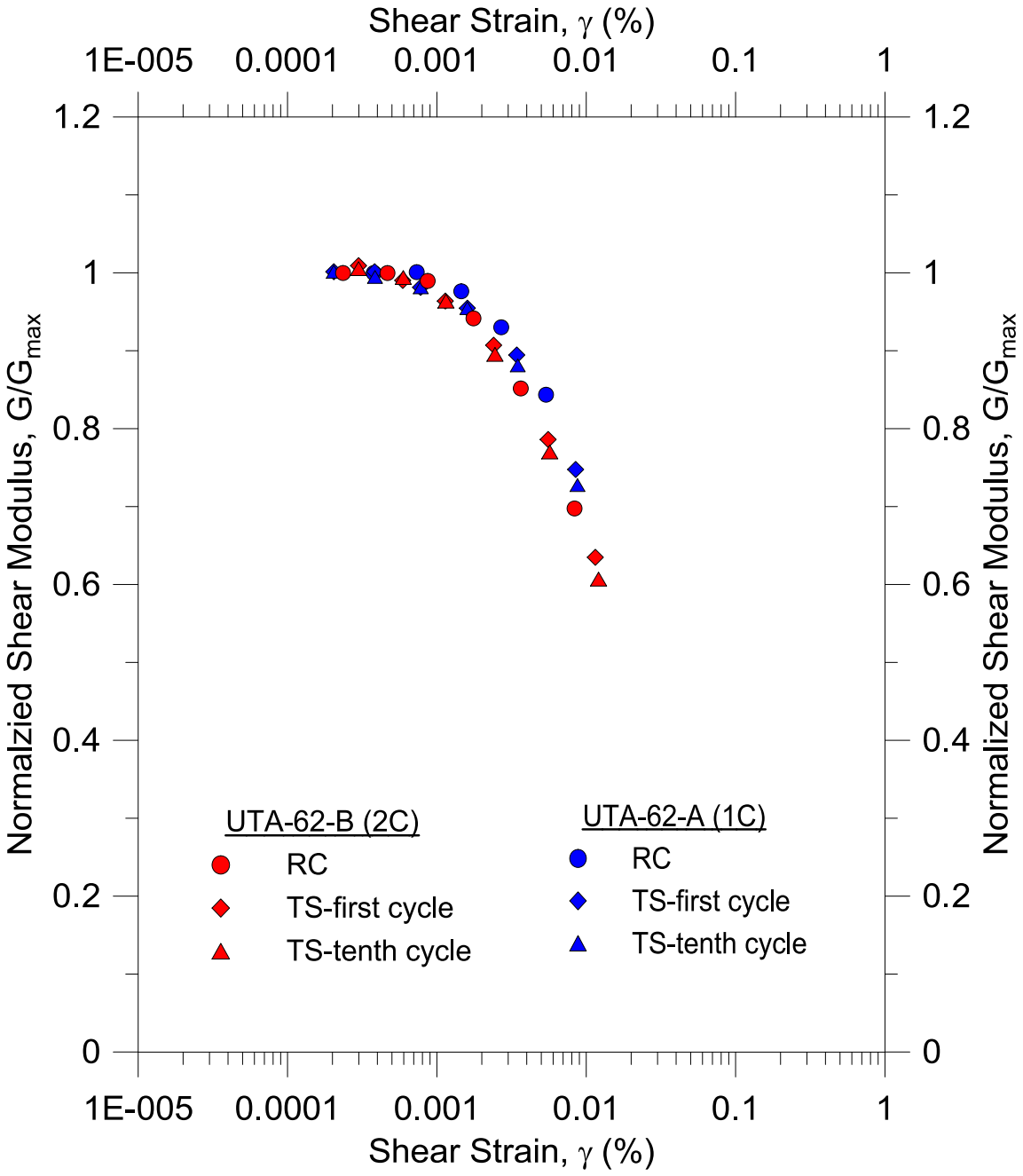

Figure 6.11: $G/G_{max} - \log\gamma$ relationships for the NGES test site obtained from RCTS tests at $\sigma_o' = 6$ psi

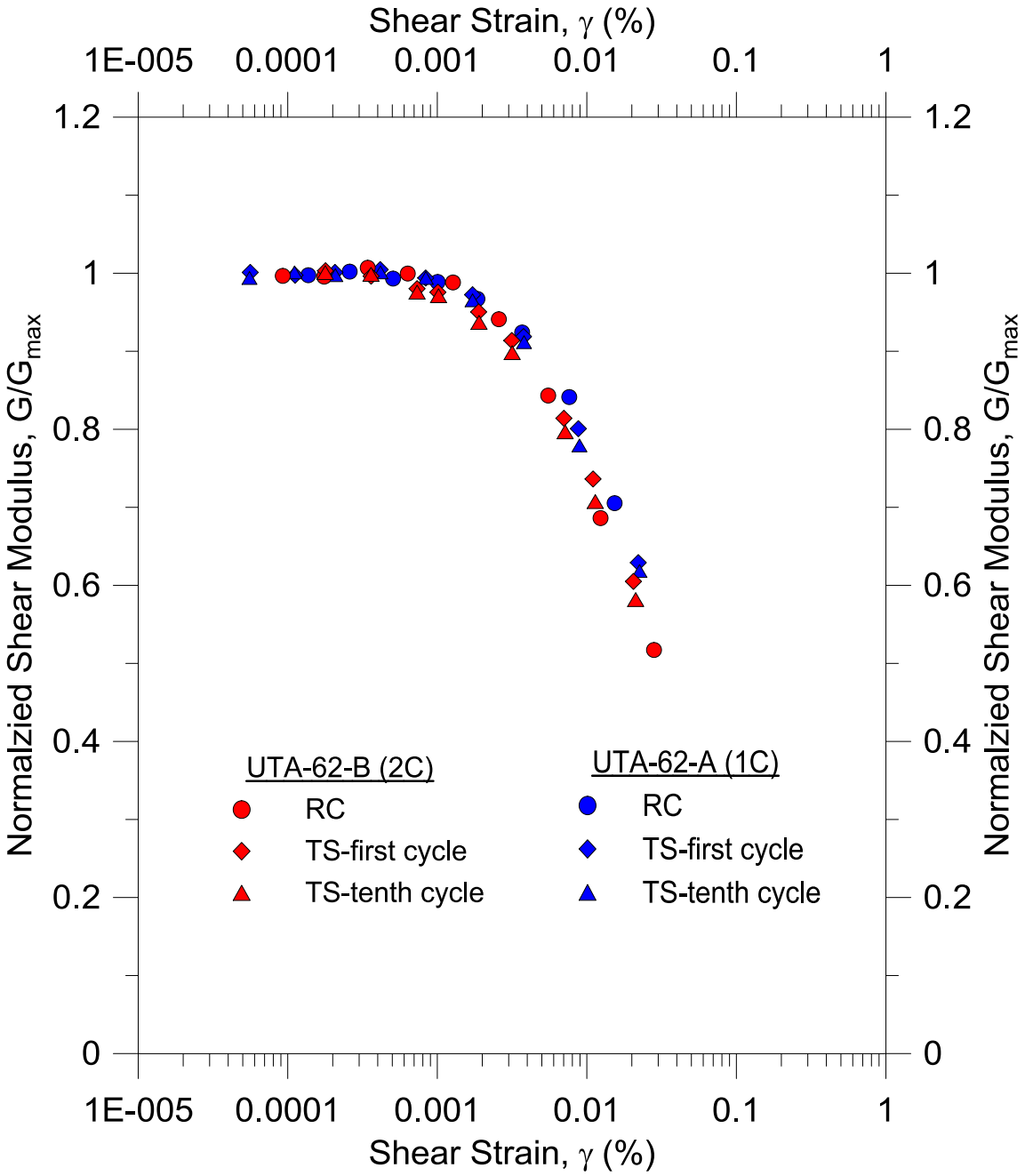

Figure 6.12: $G/G_{max} - \log\gamma$ relationships for the NGES test site obtained from RCTS tests at $\sigma_o' = 24$ psi

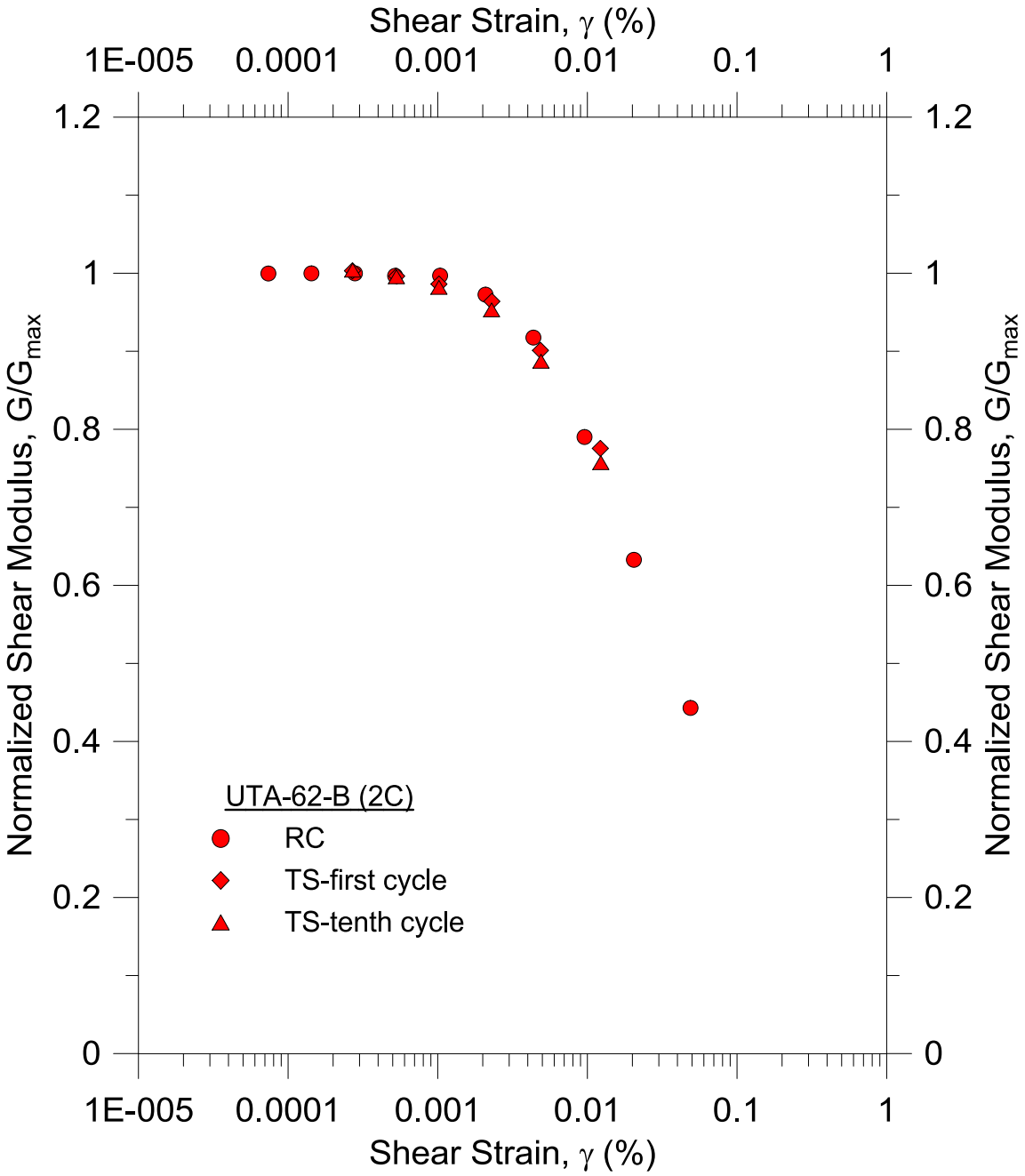

Figure 6.13: $G/G_{max} - \log\gamma$ relationships for the NGES test site obtained from RCTS tests at $\sigma_o' = 48$ psi

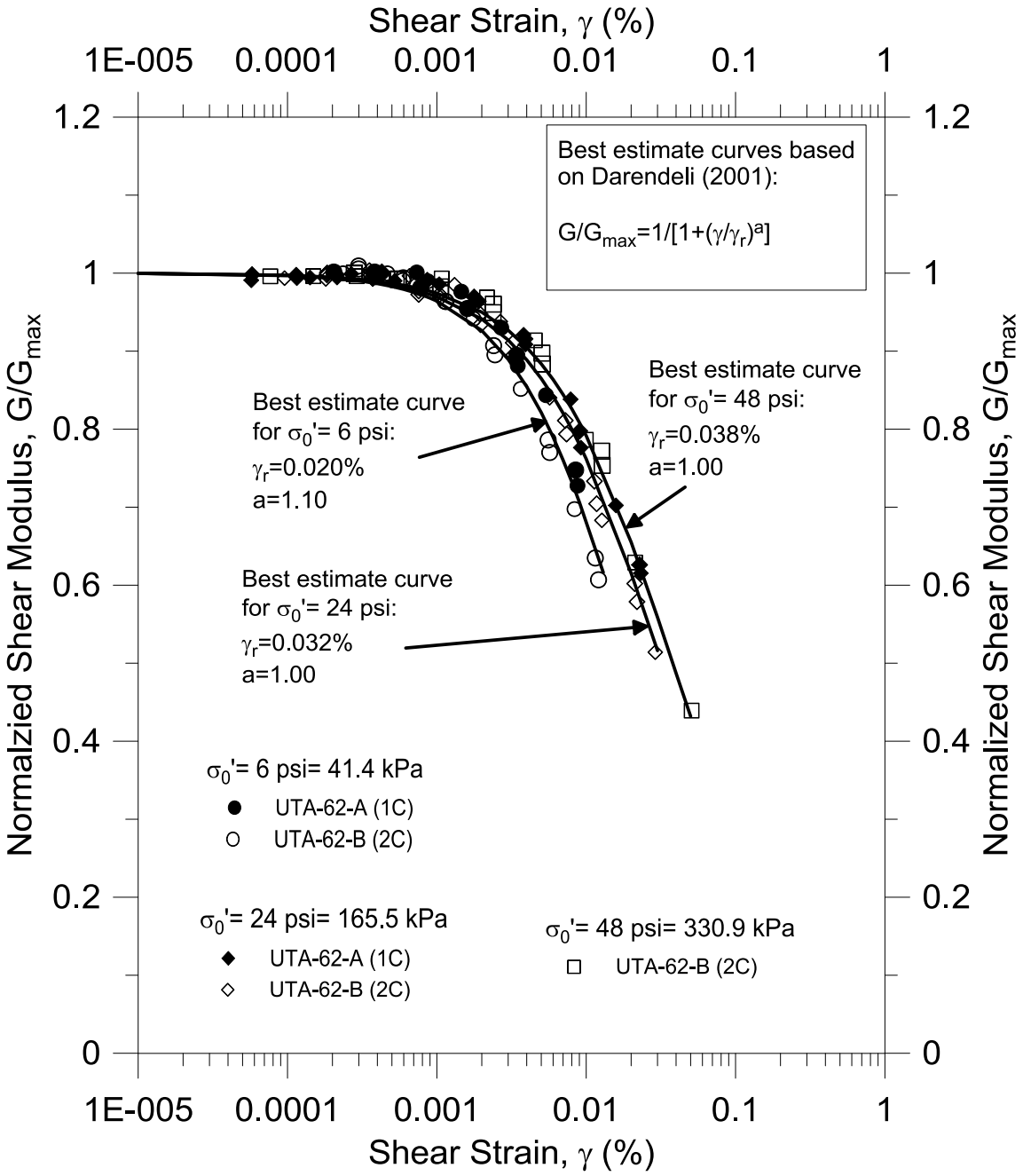

Figure 6.14: $G/G_{max} - log\,\gamma$ relationships for the NGES test site obtained from RCTS tests at all σ_o' values and the best-estimate curves fit to the RCTS data based on the Darendeli (2001) model

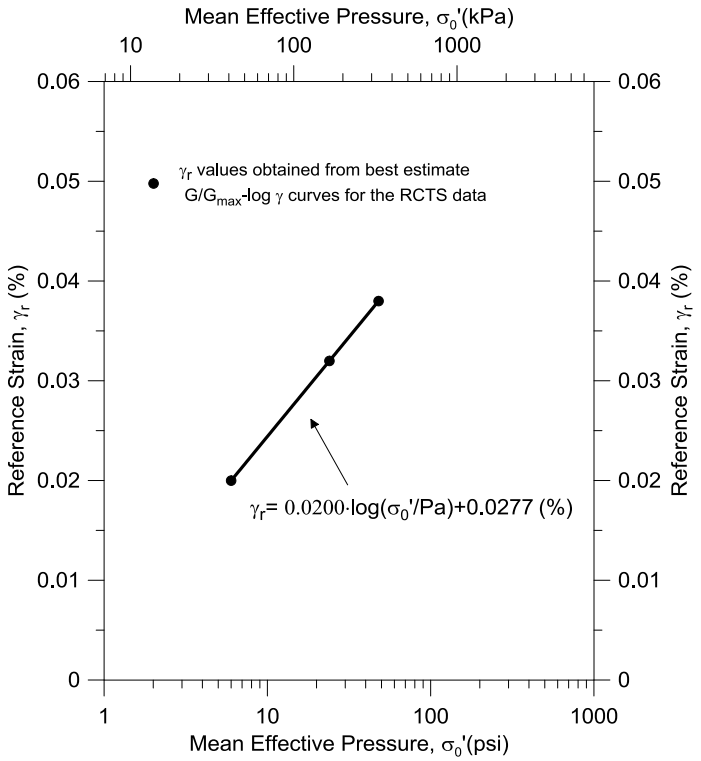

Figure 6.15: $\gamma_r - \log \sigma_o'$ relationship based on the best-estimate curves to the RCTS test data using the Darendeli (2001) model

The γ_r values are smaller than the typical values for sands because of the higher nonlinearity of this material. The "a" values are also higher than the typical values of "a" for sands. An average value of 1.00 is adopted in this study for "a" in the $G/G_{max} - \log\gamma$ curves for $G/G_{max} \geq 0.4$ as explained in Section 6.7.2.

The best-estimate $G/G_{max} - \log\gamma$ curves are shown in Figure 6.16 along with the $G/G_{max} - \log\gamma$ curves suggested by Menq (2003) for sands for comparison purposes. In Menq's formulation, the average coefficient of uniformity, C_u, is taken as 3.0 based on the gradation curves reported by Briaud and Gibbens (1994). As seen in Figure 6.16,

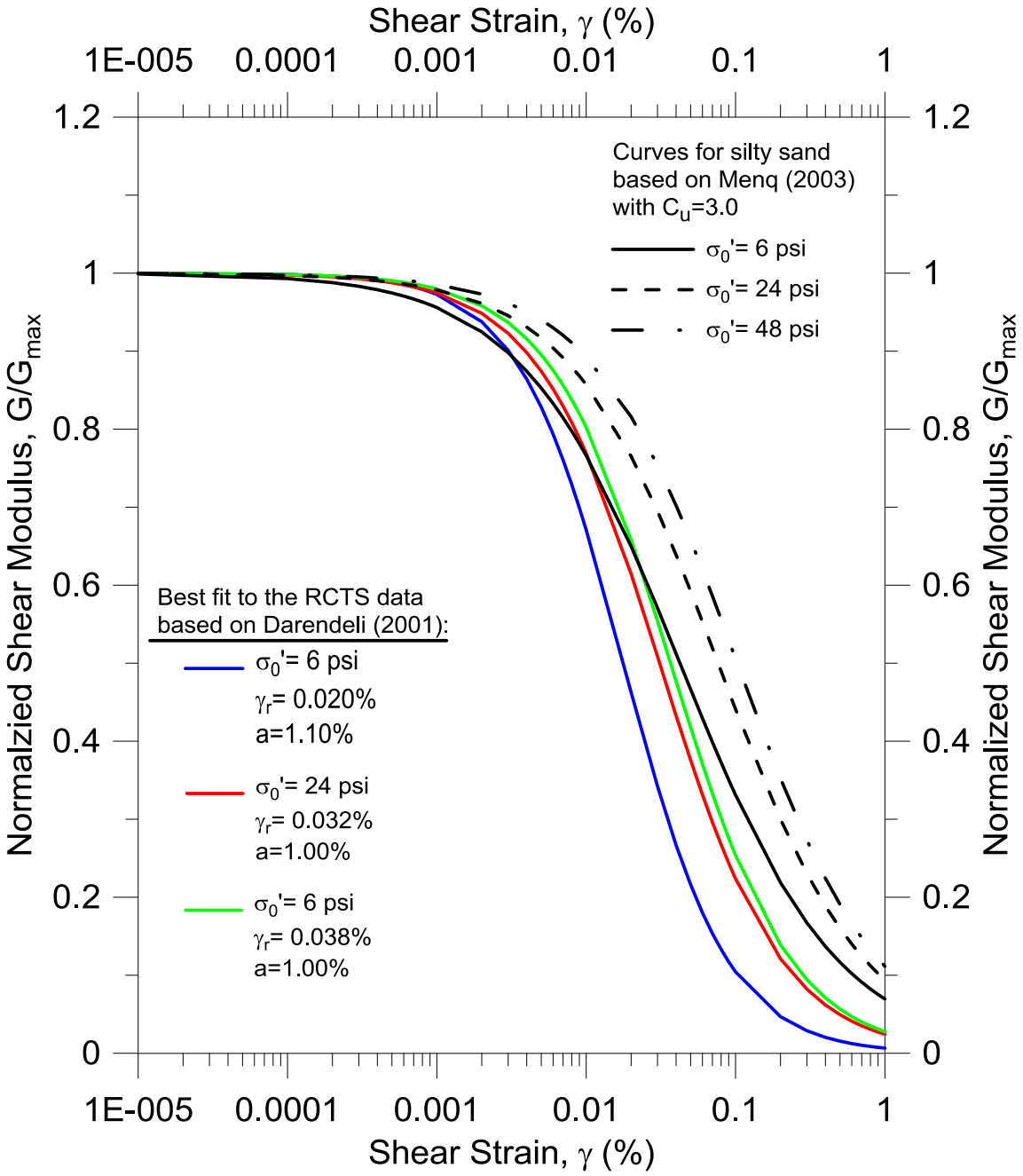

Figure 6.16: Comparison of best-estimate $G/G_{max} - \log\gamma$ relationships for the NGES test site with the $G/G_{max} - \log\gamma$ relationships proposed by Menq (2003)

the best-estimate curves to the RCTS data are more nonlinear compared to the curves proposed by Menq (2003). This behavior is most probably a result of cementation of the silty sand since Menq's formulation is for uncemented sands and gravels. The pressure dependency of the $G/G_{max} - \log\gamma$ curves based on the RCTS data is less pronounced compared to the curves obtained using Menq (2003). Most of the G/G_{max} values obtained from RCTS measurements are larger than 0.6. Hence, the extrapolated curves shown in Figure 6.15 based on γ_r and a from the fitted curves do not completely
reflect the $G/G_{max} - \log\gamma$ behavior at larger strains. This issue is addressed in Section 6.7.2 where the modification of the $G/G_{max} - \log\gamma$ curves based on larger-strain triaxial test data is discussed.

6.5 REPRESENTATIVE SHEAR WAVE VELOCITY PROFILE AT THE FOOTING LOCATIONS

The best-estimate V_s profile from the SASW tests is shown in Figure 6.6 in Section 6.4.1. A representative in-situ $\log V_s - \log\sigma_o'$ profile can be developed based on the best-estimate V_s profile by determining the corresponding in-situ σ_o'. Several points are chosen on the V_s profile and vertical stresses, σ_v' are calculated using the average total unit weight at the site which is 126 lbs/ft^3. The in-situ mean effective stresses, σ_0' are estimated with:

$$\sigma_0' = \frac{\sigma_v' + 2\sigma_v' K_0}{3} \tag{6.4}$$

where K_0 is assumed as 0.75. An initial pressure of 300 psf was added to σ_o', hence, a negative pore water pressure of 300 psf was assumed to match the V_s profile better at shallower depths. The resulting $\log V_s - \log\sigma_o'$ is given in Figure 6.17. As previously

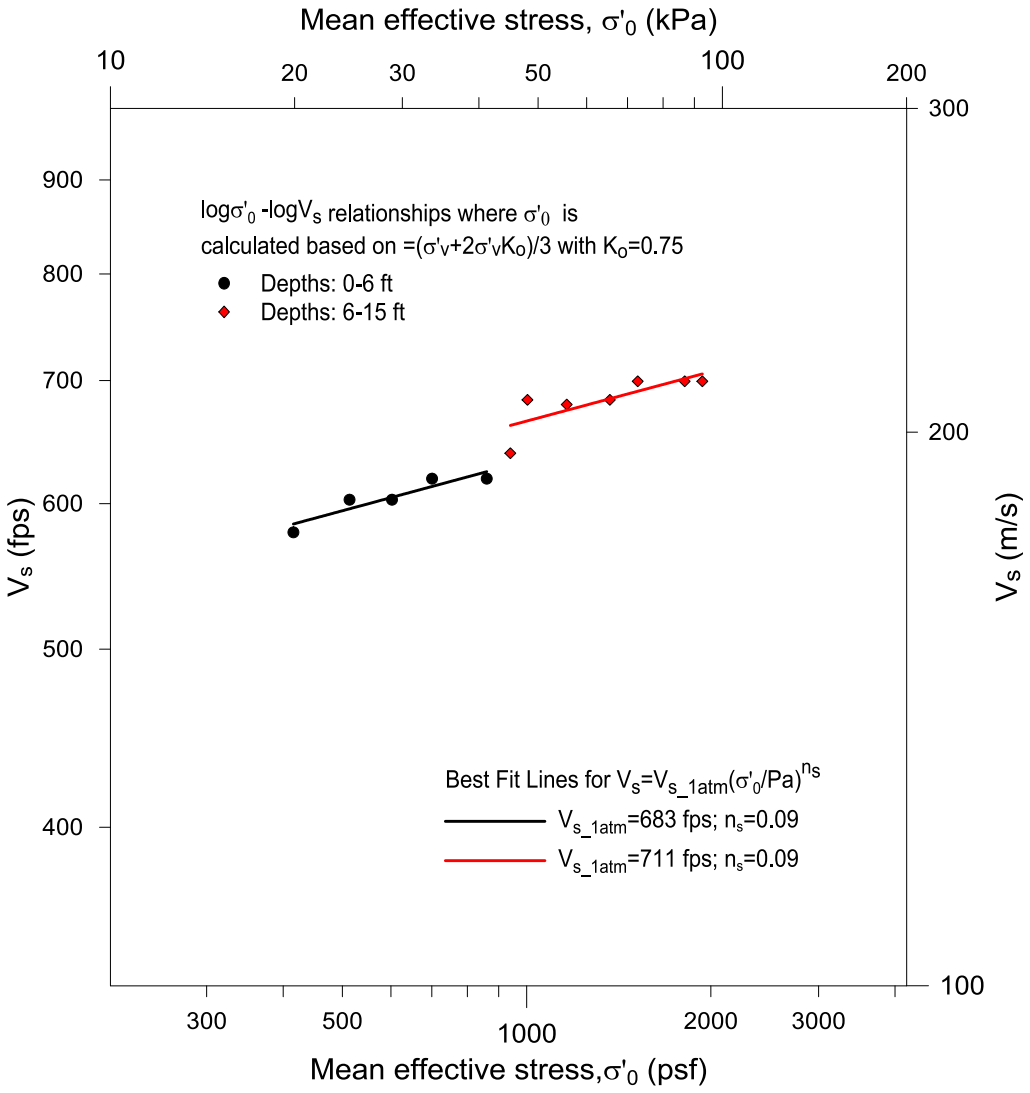

Figure 6.17: Log V_s-log σ_0' relationships for the NGES test site obtained from the average SASW testing results

shown in Equation 6.1, V_s can be expressed as a function of σ_0' and V_{s_1atm} (A_s) which is the shear wave velocity at one atmosphere. The resulting $\log V_s - \log \sigma_o'$ relationships indicate a two-layer system as shown in Figure 6.16. The best-fit lines to the $\log V_s - \log \sigma_o'$ relationships using Equation 6.1 give the following results: (1) for the layer between 0-6.0 ft (0-1.83 m); V_{s_1atm} = 683 fps (208 m/s) and n_s = 0.09 and (2) for the

layer between 6.0 ft-15.0 ft (1.83 m-4.57 m); V_{s_1atm} = 711 fps (216 m/s) and n_s = 0.09. The V_s profile from the relationships given in Figure 6.17 for the two-layer system compare well with the in-situ V_s profile from SASW tests as shown in Figure 6.18. In-situ small-strain shear modulus, G_{max}, can be found by:

$$G_{max} = V_s^2 \cdot \rho \tag{6.5}$$

where ρ is the total mass density of the soil. By combining Equations 6.2 and 6.5, an expression for G_{max} can be found as:

$$G_{max} = \rho \cdot \left(V_{s\_1atm} \cdot \left(\frac{\sigma_0'}{P_a} \right)^{n_S} \right)^2 = G_{max\_1atm} \cdot \left(\frac{\sigma_0'}{P_a} \right)^{2n_S} \tag{6.6}$$

where G_{max_1atm} is the small-strain shear modulus at a mean effective confining pressure of one atm. The resulting G_{max_1atm} and n_G (=2n_s) parameters of the two layers are: Layer 1- G_{max_1atm} = 1827 ksf (87.5 MPa) and n_G= 0.18; and Layer 2-G_{max_1atm} = 1980 ksf (94.8 MPa) and n_G = 0.18. These results are key input parameters for MoDaMP.

6.6 LOAD-SETTLEMENT TESTS

Two, circular, reinforced concrete footings with diameters of 3.0 ft and 1.5 ft (0.91and 0.46 m) were constructed at the NGES test site. Each footing had a thickness of 1.0 ft (0.30 m). Prior to footing construction, a thickness of about 1 ft (0.3 m) of soil was removed from the surface and 0.5 ft (0.15 m) of backfill was placed after footing construction (see Figure 6.19). Before footing construction took place, vertical arrays of 3D geophones were installed beneath each footing, with three arrays beneath the 3.0-ft (0.91-m) diameter footing as shown in Figure 6.19, and one array beneath the center of

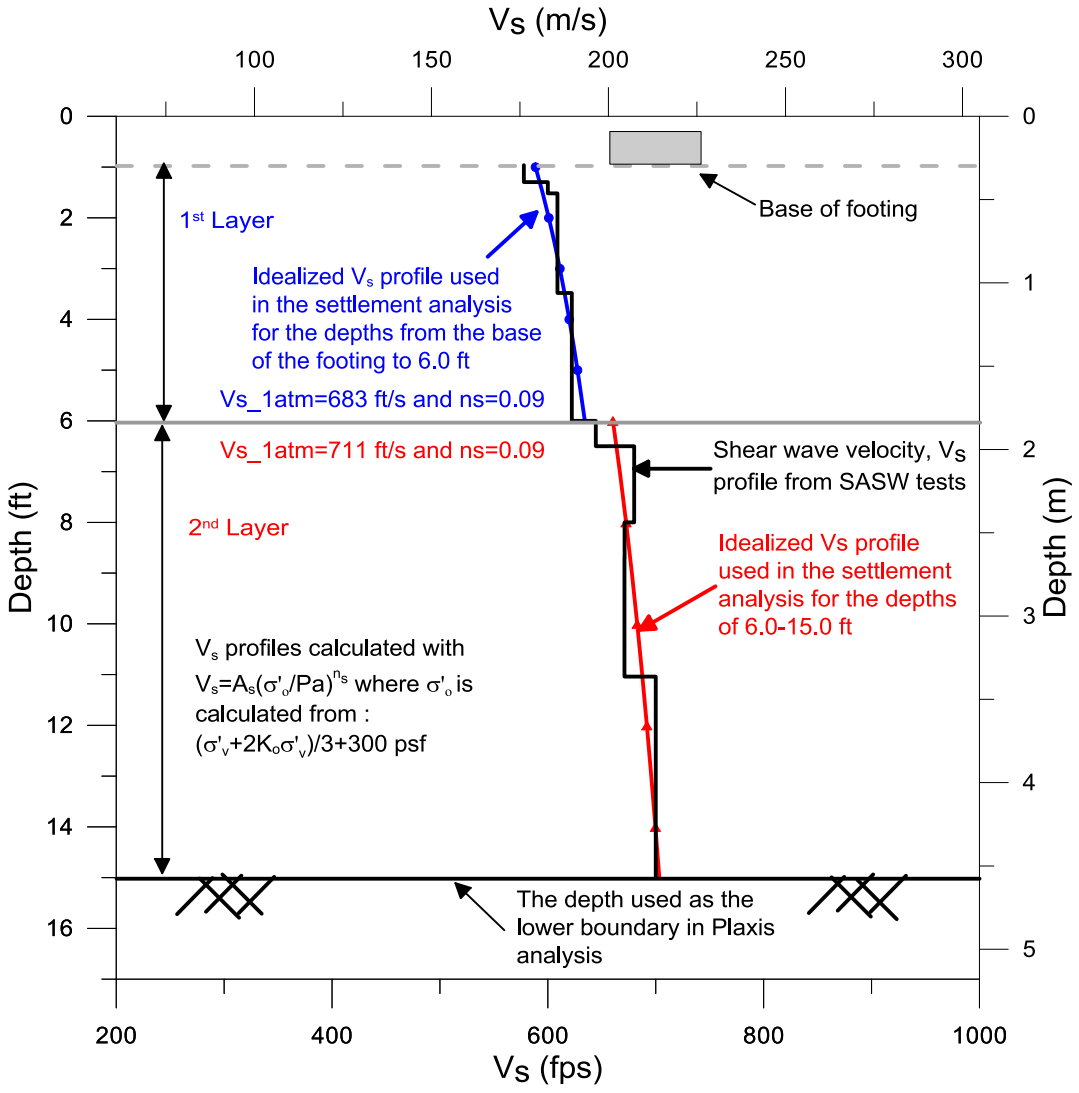

Figure 6.18: Idealized, two-layer shear wave velocity profile from the log V_s-log σ_0' relationships compared with the average shear wave velocity profile from SASW tests

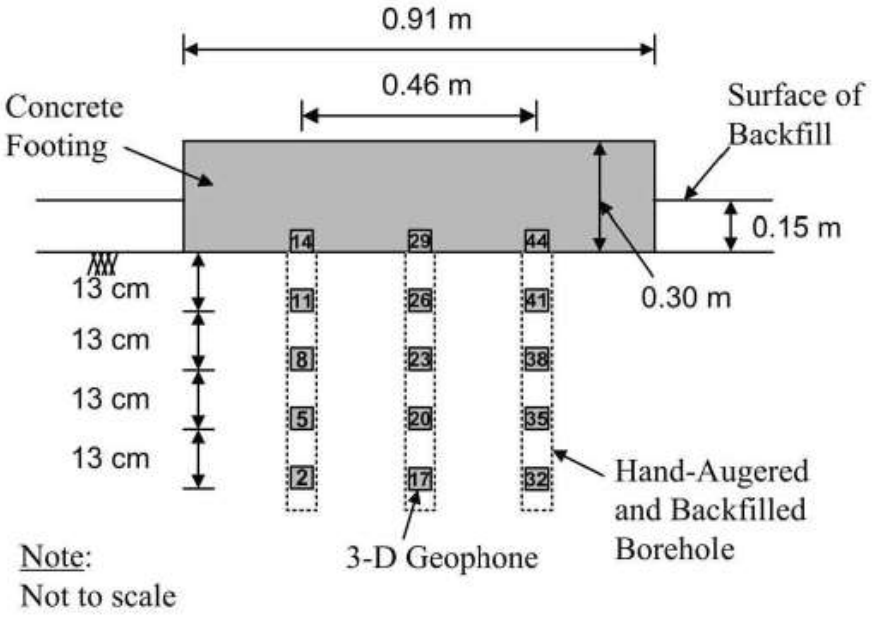

Figure 6.19: Cross-sectional view of 3.0-ft (0.91-m) diameter footing at the NGES test site (from Park et al., 2009)

Figure 6.20: Load-settlement tests at the NGES sand site: (a) T-Rex loading the 3.0-ft (0.91-m) diameter footing, and (b) set-up of the instrumentation to load and measure the settlement of the 1.5-ft (0.46-m) diameter footing (from Park et al. 2009)

the 1.5-ft (0.46-m) diameter footing. These geophone arrays were used to perform small-scale downhole testing beneath each footing. Two reference frames were placed near each footing to support displacement potentiometers which were arranged in an equilateral triangle on each footing. The load was applied by jacking against a large vibroseis truck, named "T-Rex". T-Rex was positioned over each footing and the load was applied incrementally while measuring footing movement (See Figure 6.20).

Each footing was loaded and unloaded in two or three stages, with increasing the peak loads in each subsequent stage. The load-settlement results of the 3.0-ft (0.91-m) and 1.5-ft (0.46-m) diameter footings are shown in Figures 6.21a and 6.22b, respectively. A backbone curve was fit to the staged loading/unloading cycles to approximate one continuous load-settlement curve. These backbone curves are shown by the dashed lines in Figures 6.21a and 6.22b.

6.7 LOAD-SETTLEMENT PREDICTIONS

In this section, load-settlement curves of the two small-scale footings at the NGES test site predicted using MoDaMP are presented and compared with the measured settlements. Two widely-used settlement-prediction methods, Schmertmann et al. (1978) using CPT data and Burland and Burbidge (1985), using SPT data, were also used to predict settlements of the two footings for comparison purposes.

6.7.1 Load-Settlement Predictions with MoDaMP

The user-defined soil model, MoDaMP, was implemented in PLAXIS as explained in Chapter 4. A finite element analysis was carried out to predict the settlements of the small-scale footings. The input parameters are assumed to be the same for both footings. Table 6.1 presents the input parameters values that were obtained in

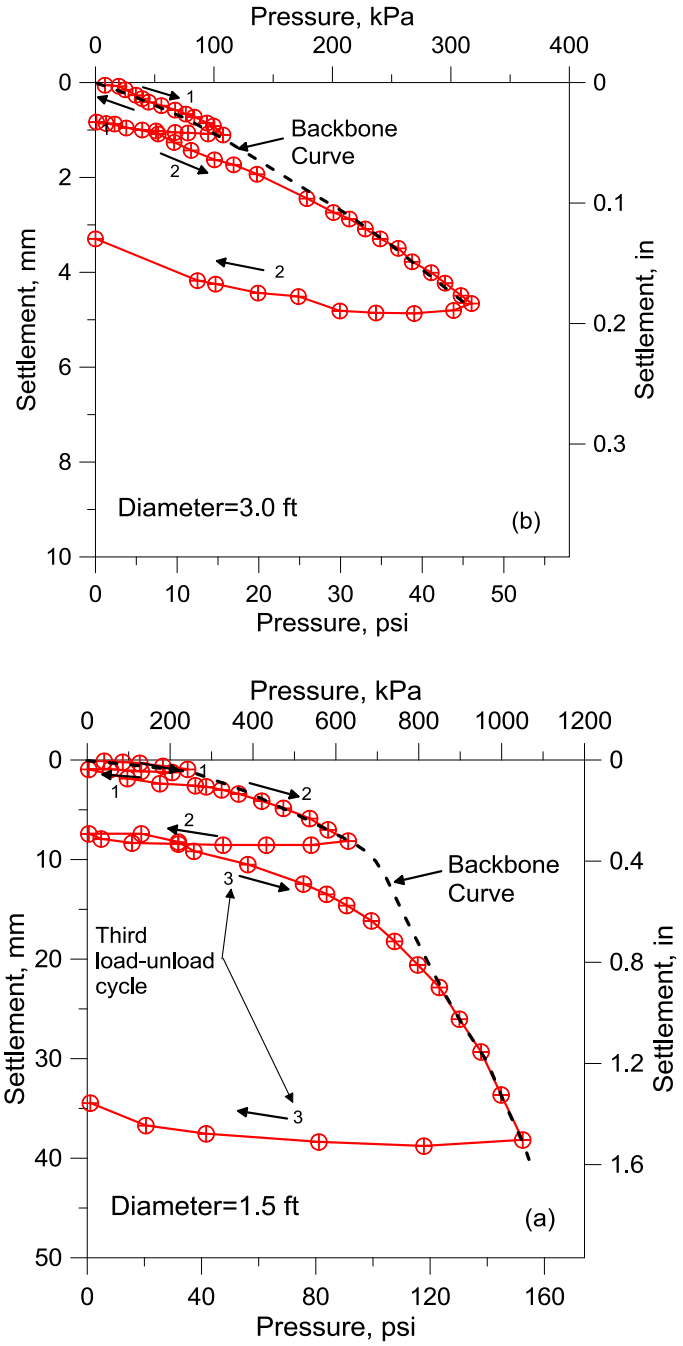

Figure 6.21: Load-unload-reload settlement results for the 3.0-ft (0.91-m) diameter footing (a) and for the 1.5-ft (0.46-m) diameter footing (b) with backbone curves fitted to approximate simple continuous loading (from Park et. al, 2009)

Table 6.1 Input parameters used in the settlement analysis with MoDaMP for NGES test site

	Layer 1	Layer 2
G_{max_1atm}	1827 ksf	1980 ksf
ν_0	0.3	0.3
a	1.00	1.00
γ_r (%)	Equation 6.3	Equation 6.3

Section 6.5 and used in the finite element analysis. Each analysis is given a different identifier (analysis ID) to differentiate the site, footing diameter and Poisson's ratio assumption used. The first two letters indicate the site; NG stands for NGES test site, the following number indicates the diameter of the footing in ft and the following letters (CP, CM or CK) indicates the assumption about the Poisson's ratio. CP indicates a constant Poisson's ratio equal to the small-strain Poisson's ratio determined from shear wave and compression wave velocities whereas CM and CK indicates that the Poisson's ratio is varying based on a constant M or constant K assumption, respectively. If these letters are followed by a "mdf1" or "mdf2", it means that the $G/G_{max} - \log\gamma$ relationships were modified as explained in the following section. For example, NG-3.0-CM-mdf1 is the analysis for the footing at the NGES test site with a 3.0-ft (0.91-m) diameter where the Poisson's ratio is based on a constant M and modified $G/G_{max} - \log\gamma$ relationships are used in the analysis.

6.7.1.1 PLAXIS Model for the Footings

The subroutine MoDaMP was implemented into PLAXIS and finite element analyses of settlements of the footings were carried out using this subroutine. The soil-

footing system was modeled as axisymmetric and symmetrical, therefore only half of the footing was modeled. To eliminate the boundary effects, the thickness of the soil beneath the footing was assumed as 15 ft (4.57 m) (equal to 5 times the footing diameter of the larger footing) as proposed by Brinkgreve et al. (2011). The reinforced concrete footings are modeled as flexible plate members.

All boundaries except the top boundary are restrained from horizontal movement and the bottom boundary is restrained from both horizontal and vertical movements. PLAXIS automatically generates the mesh for the model but the size and type of mesh can be altered by the user. The mesh used in the analyses consisted of 946, 15-node triangular elements. The mesh is refined beneath the footings since most of the deformations are expected to occur in this region. The backfill soil is modeled as a surcharge of 60 psf (2.87 kPa) because the deformations due to loading are occurring beneath the footings. The water table is set at the lower boundary of the model since it is about at 16.1 ft (4.9 m).

The standard settings of PLAXIS are utilized to perform the iterative calculations, which resulted in computational times ranging from 10 minutes to 5 hours depending on the assumptions and modifications in the model. The computation times increased for cases where the shear strain-shear stress response of the soil is flatter at larger strains.

The main feature of MoDaMP is the ability to evaluate the G_{max} values based on the current stress state and the associated $G - \log\gamma_{oct}$ relationships according to both stress and strain states. This procedure requires a continuously updating G_{max}, stress and strain state and $G - \log\gamma_{oct}$ set. G_{max} values are calculated with Equation 6.5 based on the initial stress state. Values of G are calculated using the G_{max} values and Equations 3.11, 3.12, and 3.13. As an example, the variation of G/G_{max} in the soil mass with increased

pressure levels is shown in Figure 6.22 for analysis NG-3.0-CP-mdf2. The G values at these pressure levels are presented in Figure 6.23. Next, values of G and ν are used to establish the nonlinear elastic stiffness matrix. New stresses are calculated based on the nonlinear elastic stiffness matrix and, new G_{max} values are calculated with these stresses.

To illustrate this procedure, three reference points at different depths beneath the 3.0-ft diameter footing are used. These reference points are shown in Figure 6.24a. The octahedral shear strain and shear modulus at each reference point are determined under the five, increasing load levels applied to the footing shown in Figure 6.24b. Five $G - \log\gamma_{oct}$ relationships determined for the five load levels identified in Figure 6.24b are plotted as solid lines in Figures 6.24c, 6.24d and 6.24e for Reference Points X, Y, and Z, respectively. The sets of G, γ_{oct} coordinates that correspond to each of the five load levels on the load-settlement curve are identified on the appropriate $G - \log\gamma_{oct}$ relationship by the solid circles and associated load-level number. The increase in G_{max} and general upward shifting of the $G - \log\gamma_{oct}$ curves (solid lines) with increasing load level is seen in Figures 6.24c, 6.24d, and 6.24e. As loading increases, the net effect is G decreasing as γ_{oct} increases at each reference point. This effect diminishes with increasing depth because the incremental stress change decreases with depth.

6.7.1.2 Predicted Settlements

Settlement analyses with the PLAXIS model using the MoDaMP subroutine are presented in this section. As explained previously, every analysis is given an identification name to distinguish between different footing sizes and different assumptions. The first analysis in this section, NG-3.0-CP, is the analysis for the 3.0-ft diameter footing on NGES site with the assumption of a constant Poisson's ratio. The load-settlement curve predicted with this analysis is shown in Figures 6.25. It should be

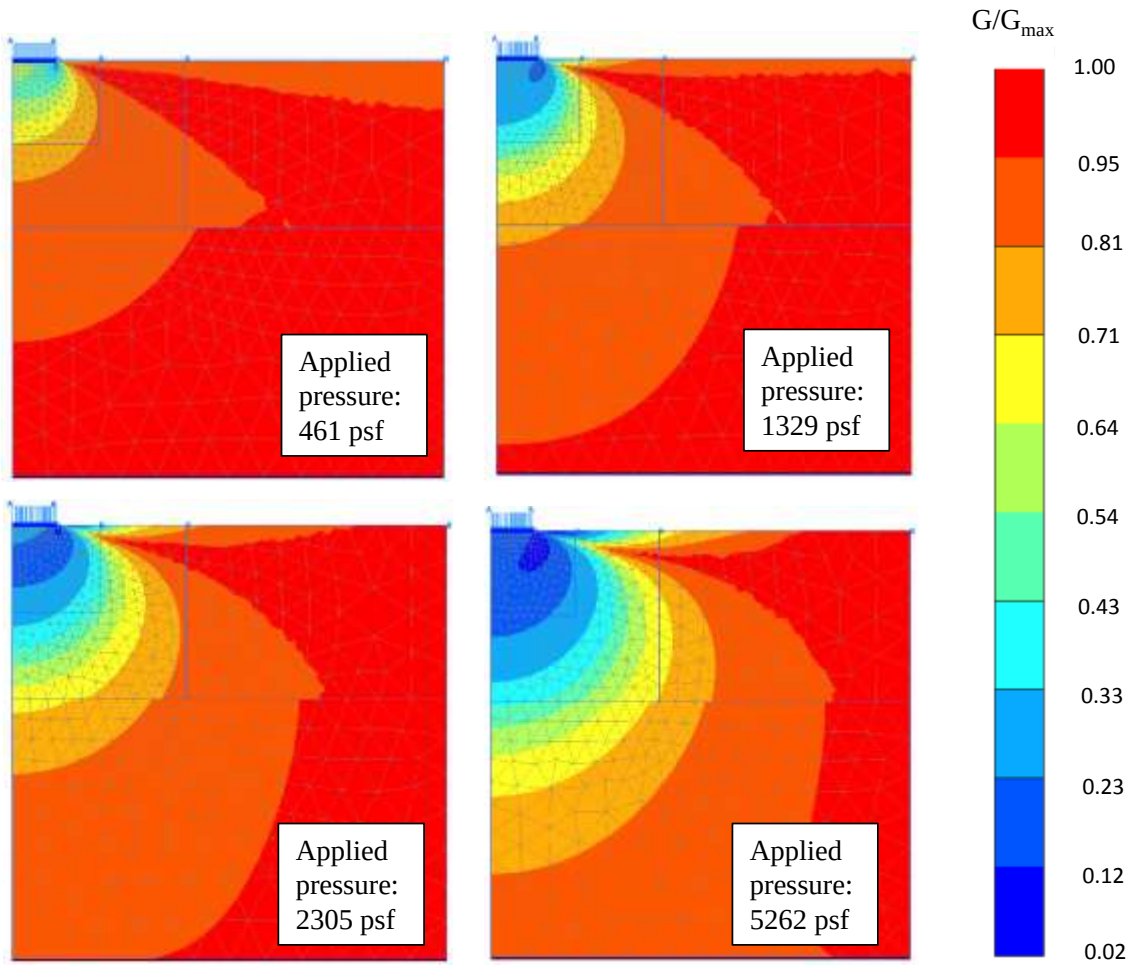

Figure 6.22: Variation of G/G_{max} in the soil mass with increased applied pressure levels for analysis NG-3.0-CP-mdf2.

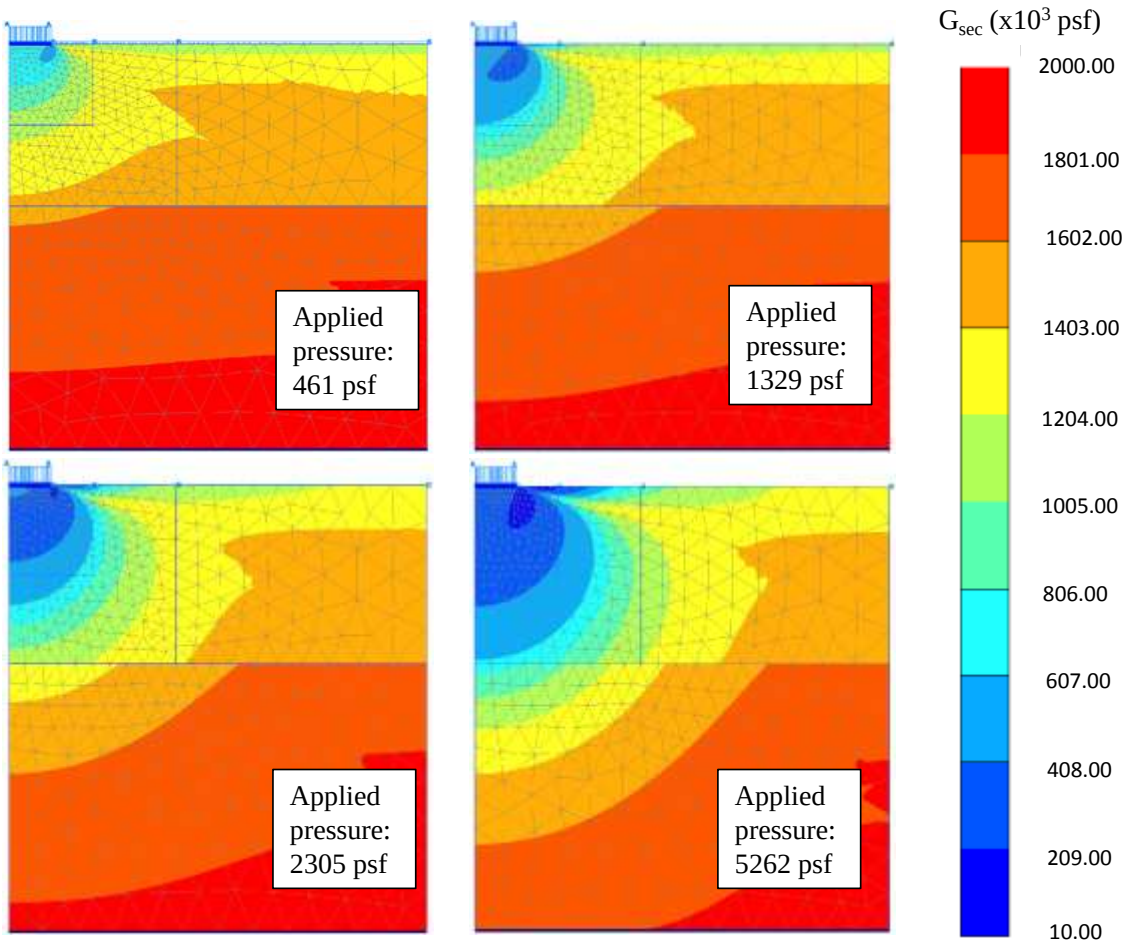

Figure 6.23: Variation of G (psf) in the soil mass with increased applied pressure levels for analysis NG-3.0-CP-mdf2.

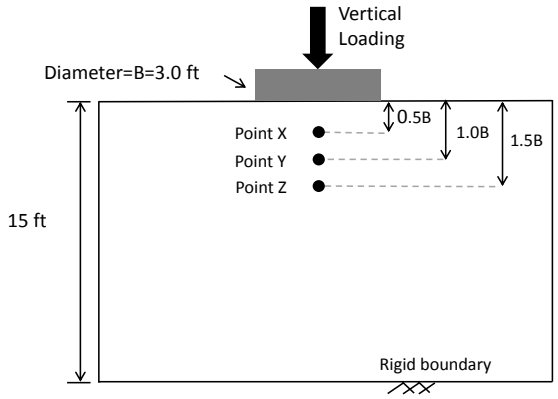

(a) Geometry of soil-foundation model and reference points

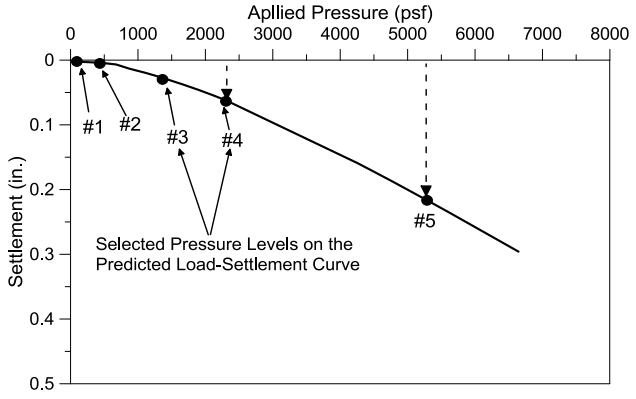

(b) Load-settlement curve and five load levels

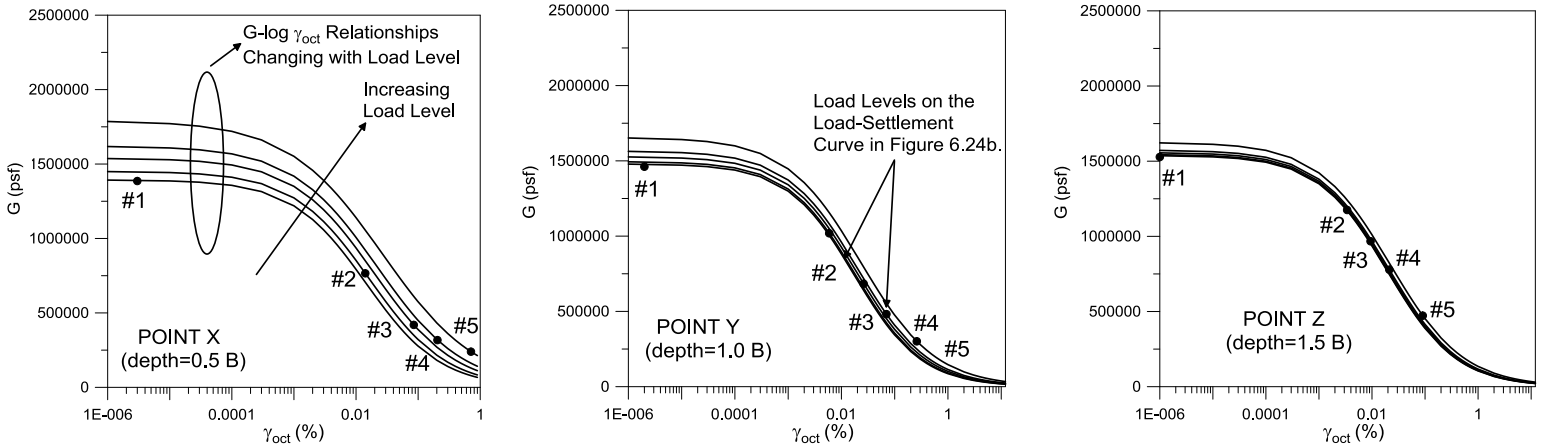

Figure 6.24: Illustration showing how the modulus-strain relationships and secant shear moduli change in the numerical model during loading at three reference points beneath the 3.0-ft (0.91-m) diameter footing for NG-3.0-CP-mdf2

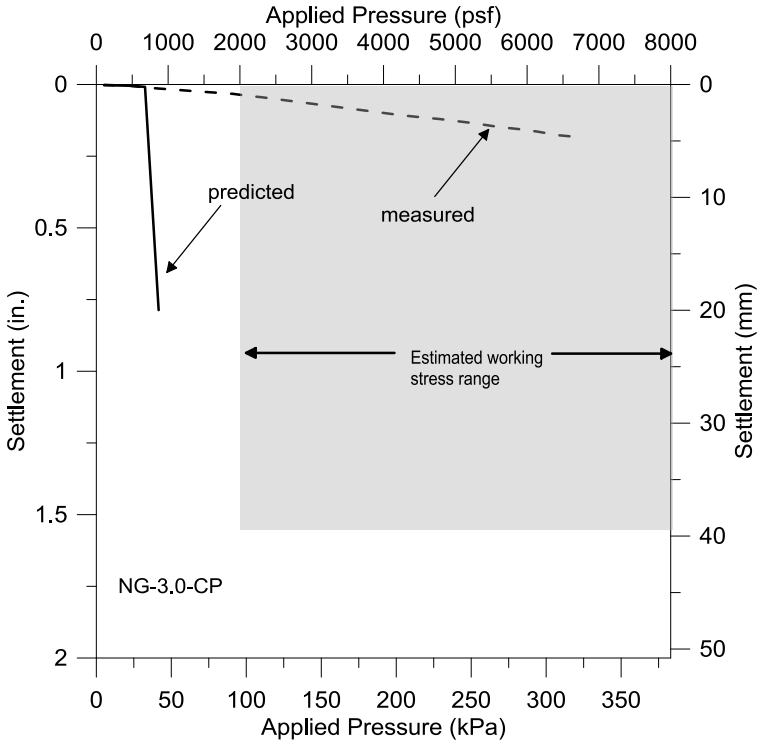

Figure 6.25: Predicted footing settlements for the 3.0-ft (0.91-m) diameter footing at the NGES site using MoDaMP assuming constant Poisson's ratio during loading

noted that in this analysis, Poisson's ratio is assumed constant and the $G - \log\gamma_{oct}$ relationship are based solely on the RCTS test results presented in Section 6.4.2.

As seen in Figure 6.25, the predicted settlements match the measured settlements only up to ~ 600 psf (28.7 kPa) which is about 10% of the maximum applied pressure. Beyond 600 psf, the predicted settlements become extremely large and footing settles continuously almost with no additional load. This indicates a very soft behavior of the model. Therefore the settlement of the 1.5-ft (0.46-m) diameter footing is not presented here since the $G - \log\gamma_{oct}$ relationship needs to be modified before performing further analyses. The reason for this modification is that the $G/G_{max} - \log\gamma$ relationships described in Chapter 3 have been primarily developed by torsional resonant column testing over small-to-moderate values of strains, typically shear strains less than 0.2 %.

The relationships need to be modified to use them in MoDaMP at larger strains which occur in problems such as shallow foundation settlements.

6.7.2 Modification of $G/G_{max} - \log\gamma$ Relationships in MoDaMP

The $\tau - \gamma$ results from CD triaxial tests conducted on reconstituted samples from the NGES site (Briaud and Gibbens, 1994) are presented in Figure 6.26. The $\tau - \gamma$ curves are found from the $\sigma - \varepsilon$ results from the triaxial tests by using the relationships proposed by Kokusho (1980):

$$\gamma = (1 + \nu)\varepsilon \tag{6.7}$$

$$\tau = \sigma/2 \tag{6.8}$$

The $\tau - \gamma$ relationships obtained by converting the $G/G_{max} - \log\gamma$ relationships to $\tau - \gamma$ relationships are also shown in the same figure for comparison purposes. As seen in Figure 6.26, the $\tau - \gamma$ responses from the $G/G_{max} - \log\gamma$ relationships are stiffer at strains less than 0.1 % compared to the triaxial results. However, as the shear strains increase, the $\tau - \gamma$ responses from the $G/G_{max} - \log\gamma$ relationships are softer at strains above 0.1 to 0.2 %. Therefore, the $G/G_{max} - \log\gamma$ relationships need to be modified in the larger strain range. This modification is achieved by adjusting the "a" parameter (only) in the larger strain range of the $G/G_{max} - \log\gamma$ relationships to match the triaxial results. The effect of the modified "a" parameter on the $G/G_{max} - \log\gamma$ relationships is shown in Figure 6.27 as an example. This adjustment of the "a" parameter consists of two parts as:

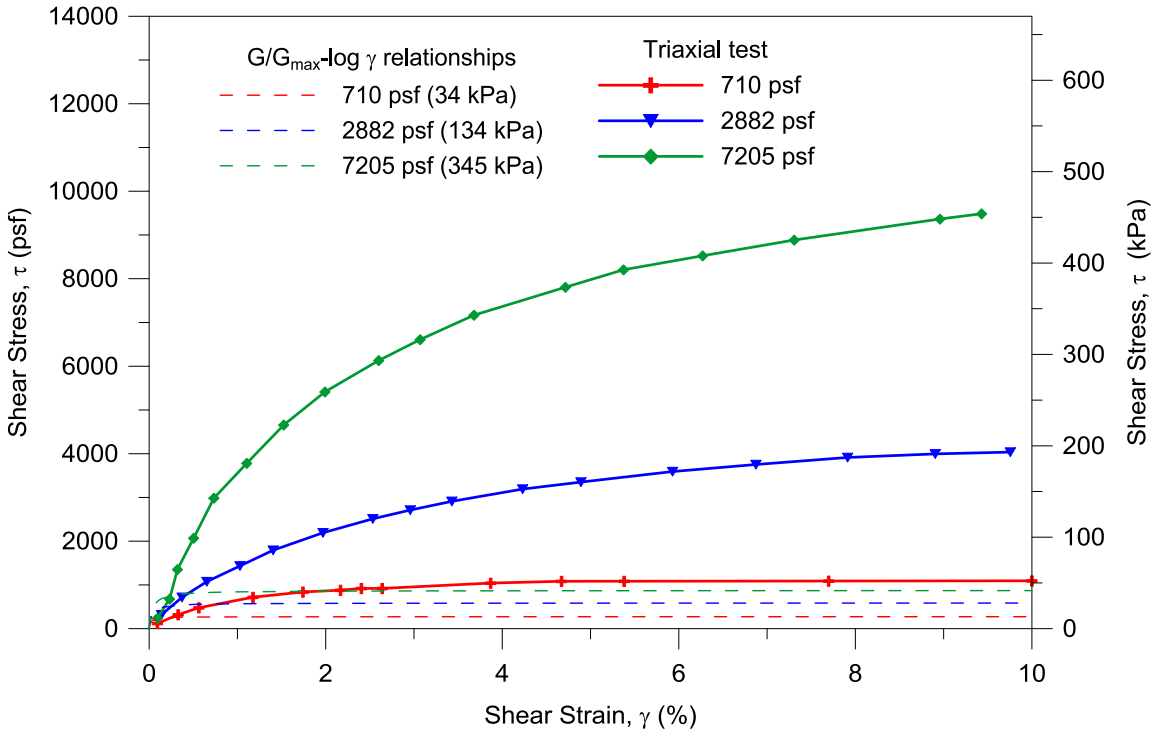

Figure 6.26: Comparison of shear stress-shear strain curves from triaxial tests and from $G/G_{max} - \log\gamma$ relationships

(1) for $G/G_{max} \geq 0.4$; $a = 1.0$ (6.9)

(2) for $G/G_{max} < 0.4$; $a = 0.6806 - 0.2164 \log\left(\frac{\sigma_0'}{P_a}\right)$ (6.10)

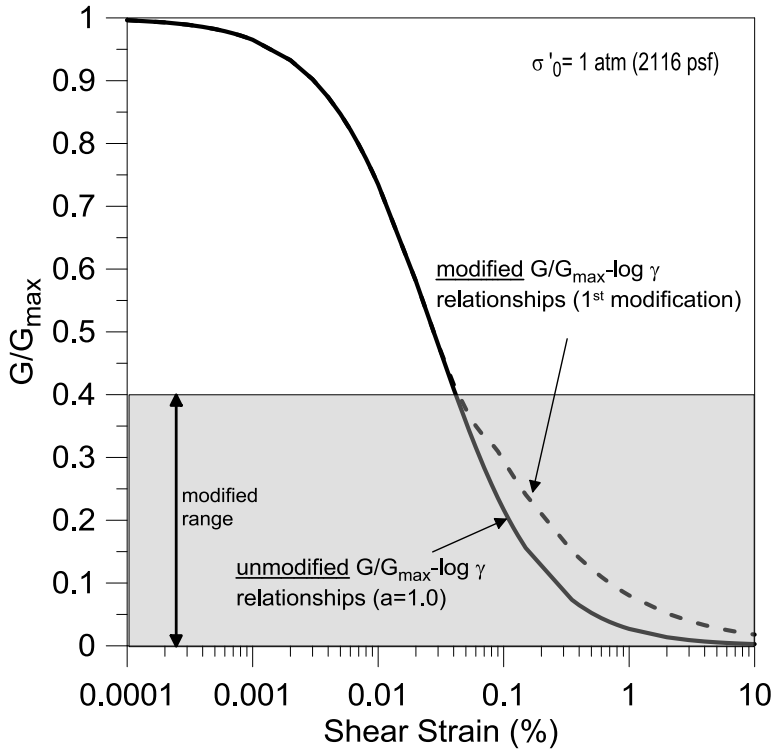

Figure 6.27: Comparison of unmodified and modified (1st modification) $G/G_{max} - \log\gamma$ relationships

As the value of "a" changes from 1.0 to a smaller value at G/G_{max} smaller than 0.4, there is a sudden change in the $G/G_{max} - \log\gamma$ relationship. To avoid the discontinuity in the $G/G_{max} - \log\gamma$ relationships at $G/G_{max} = 0.4$, the "a" parameter is changed gradually from the original value to the modified value between $G/G_{max} = 0.4$ and $G/G_{max} = 0.3$. The $\tau - \gamma$ responses obtained using the $G/G_{max} - \log\gamma$ relationships with the modified "a" parameter are presented in Figure 6.28 .The modified $G/G_{max} - \log\gamma$ relationships are implemented in MoDaMP and the model with the modified relationships, now designated as MoDaMP-1, is used to predict the settlements of the footings to investigate the effect of the adjustment on footing settlements.

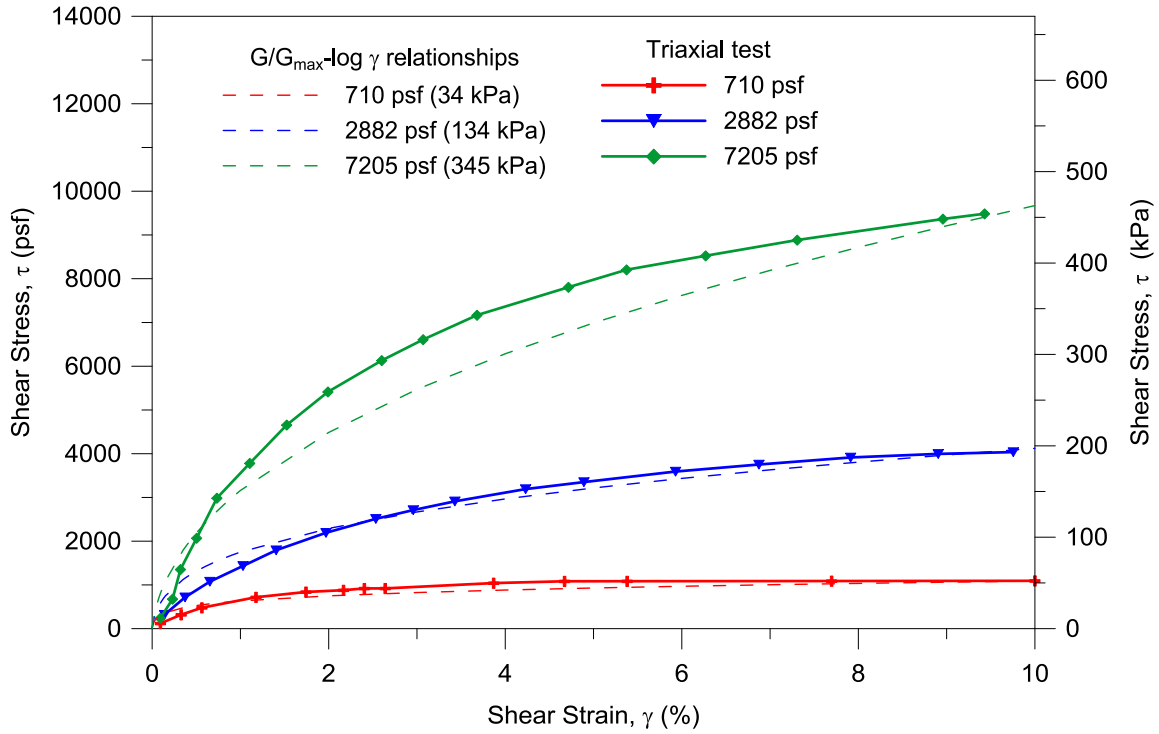

Figure 6.28 Comparison of shear stress-shear strain responses from triaxial tests and from the modified (1st modification) $G/G_{max} - \log\gamma$ relationships

6.7.2.1 Settlement Predictions with modified $G/G_{max} - \log\gamma$ Relationships implemented in MoDaMP

The settlements predicted using the modified $G/G_{max} - \log\gamma$ relationships are shown in Figure 6.29. As seen in the figure, the predicted settlements for the 3-ft (0.91-m) diameter footing match the measured settlements up to pressures of about 2000 psf (95.8 kPa). Beyond this point, the predicted settlements become higher compared to the measured settlements. For the 1.5-ft (0.46-m) footing, the predicted settlements are higher than the measured settlements for almost all pressures, with the exception of pressures below about 2000 psf.

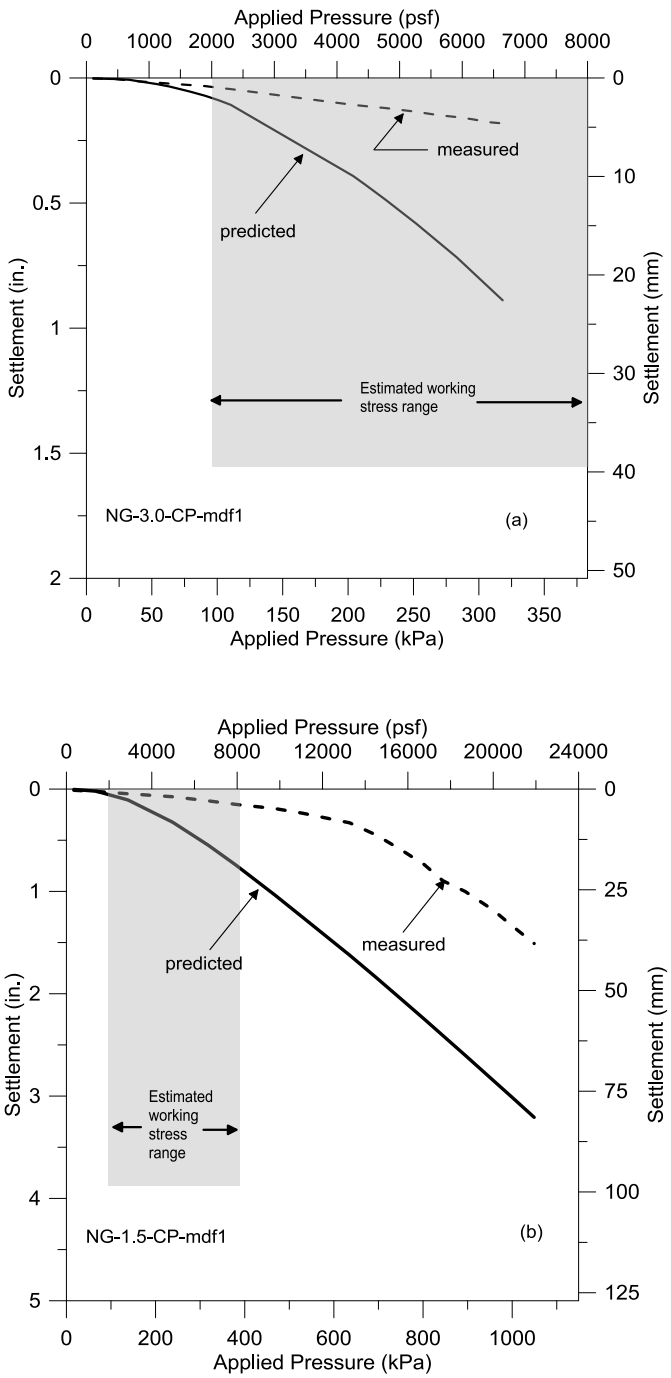

Figure 6.29: Predicted footing settlements using MoDaMP-1 with a constant Poisson's ratio and modified (1st modification) $G/G_{max} - \log\gamma$ relationships for (a) 3.0-ft (0.91-m) diameter and (b) 1.5-ft (0.46-m) diameter footings at the NGES Site

The comparison of the predicted settlements of 3.0-ft (0.91-m) and 1.5-ft (0.46-m) diameter footings with the measured settlements indicates that the modified $\tau - \gamma$ responses are still softer than the actual soil behavior. This behavior is attributed to two different phenomena: (1) horizontal stresses that increase in-situ during loading but which were not during loading in the triaxial test, and (2) the specimens used in the triaxial tests are reconstituted and are disturbed. The silty sand at the NGES test site is slightly cemented based on the field $\log V_s - \log \sigma'_o$ relationships in Section 6.5. The low value of n_G (n_G=0.18) is an indication for cementation since an uncemented, normally consolidated sand typically has n_G=0.50 (also see Figure 6.17 in terms of field V_s).

Based on these facts, $G/G_{max} - \log \gamma$ relationships need to be modified for the second time to obtain a stiffer $\tau - \gamma$ response. This second modification is achieved following the same procedure as explained in the first modification but it is made stiffer to represent the increase in horizontal stresses during footing loading. This second modification resulted in the following set of equations:

(1) for $G/G_{max} \geq 0.4$; $a = 1.0$ (6.11)

(2) for $G/G_{max} < 0.4$; $a = 0.5566 - 0.2579 \log\left(\frac{\sigma'_0}{P_a}\right)$ (6.12)

The effect of the modified "a" parameter on the $G/G_{max} - \log \gamma$ relationships is shown in Figure 6.30 as an example. The $\tau - \gamma$ responses obtained using the $G/G_{max} - \log \gamma$ relationships with the 2nd modification of the "a" parameter are presented in Figure 6.31. The settlements of the 3.0-ft (0.91-m) and 1.5-ft (0.46-m) diameter footings are predicted with the MoDaMP with the second modification on the $G/G_{max} - \log \gamma$ relationships

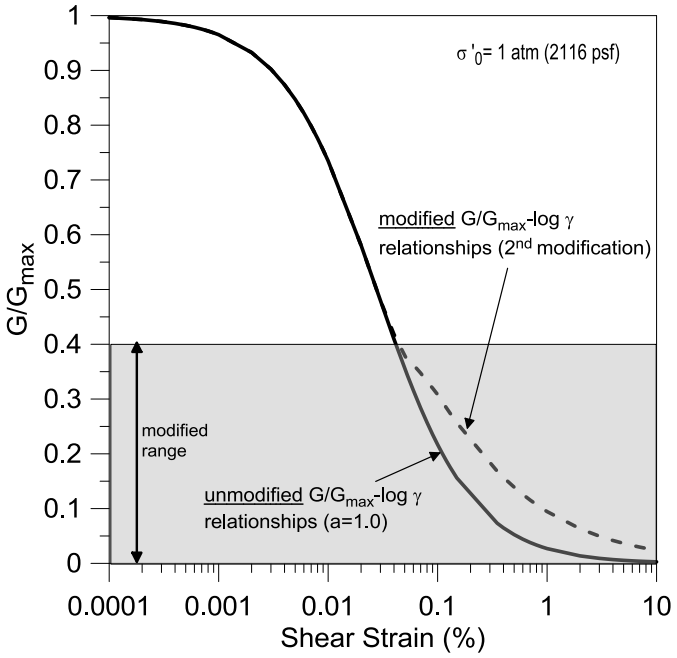

Figure 6.30: Comparison of unmodified and modified (2nd modification) $G/G_{max} - \log\gamma$ relationships

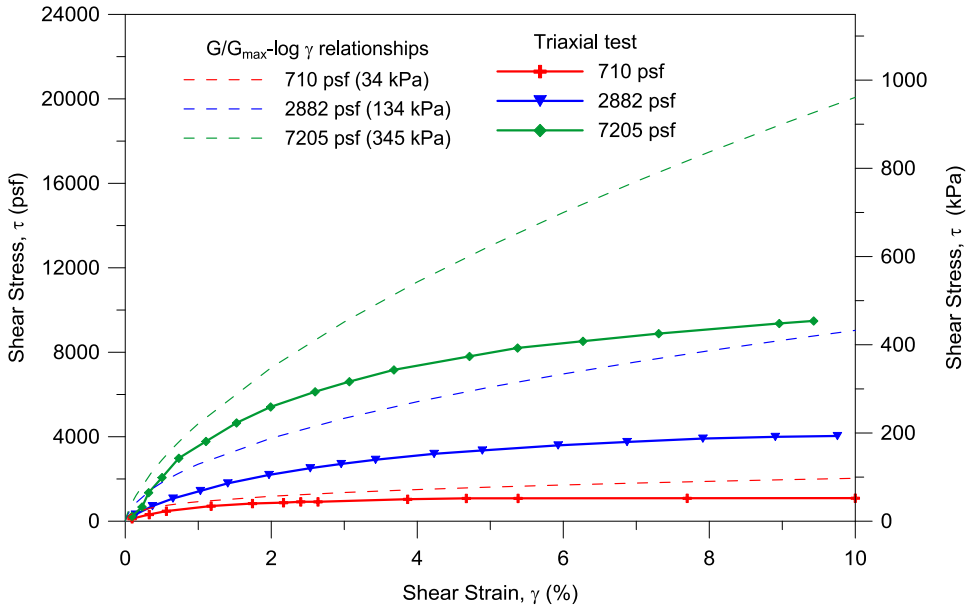

Figure 6.31: Comparison of shear stress-shear strain responses from triaxial tests and from the 2nd modification of the $G/G_{max} - \log\gamma$ relationships to account for increases in the horizontal stresses during footing loading

implemented in it (MoDaMP-2). The results of the settlement analyses for the 3.0-ft (0.91-m) diameter and 1.5-ft (0.46-m) diameter footings are presented in Figure 6.32a and 6.32b, respectively. As seen in the figure, the predicted settlements with the second modification of the $G/G_{max} - \log\gamma$ relationships are reasonably matching the measured settlements.

6.7.3 Load-Settlement Predictions with CPT and SPT Based Methods

The commonly-used, empirically-based, load-settlement prediction methods of Schmertmann et al. (1978) with CPT measurements, and Burland and Burbidge (1985) with SPT measurements are viewed in Chapter 2. These methods are used to predict the settlements of the two, small-scale footings tested at NGES test site.

For the Schmertmann et al. (1978) method, the elastic modulus is calculated with $E = 2.5q_c$. The average tip resistance of the soil is assumed to be 50 tsf (4.8 MPa) based on the CPT results (Briaud and Gibbens, 1994). The upper 6 ft (1.83 m) of the soil beneath the footings is divided into 5 layers. Equations 2.6, 2.7 and 2.9 are then used to predict the settlements. The predicted settlements are compared with the measured settlements in Figure 6.33a for the 3.0-ft (0.91-m) diameter footing and in Figure 6.33b for the 1.5-ft (0.46-m) diameter footing. As seen in the figures, the settlements are overpredicted for both footings and the nonlinearity of the load-settlement curves is not captured.

The Burland and Burbidge (1985) method utilizes SPT results in settlement predictions as explained in Chapter 2. Average SPT blow counts (N_{60}) at the NGES site over the depth of influence, which about 3 ft for a 3-ft diameter footing is 10. Using Equation 2.10, the settlements are predicted and compared with the measure settlements in Figure 6.33a for the 3.0-ft (0.91-m) diameter footing and in Figure 6.33b for the 1.5-ft

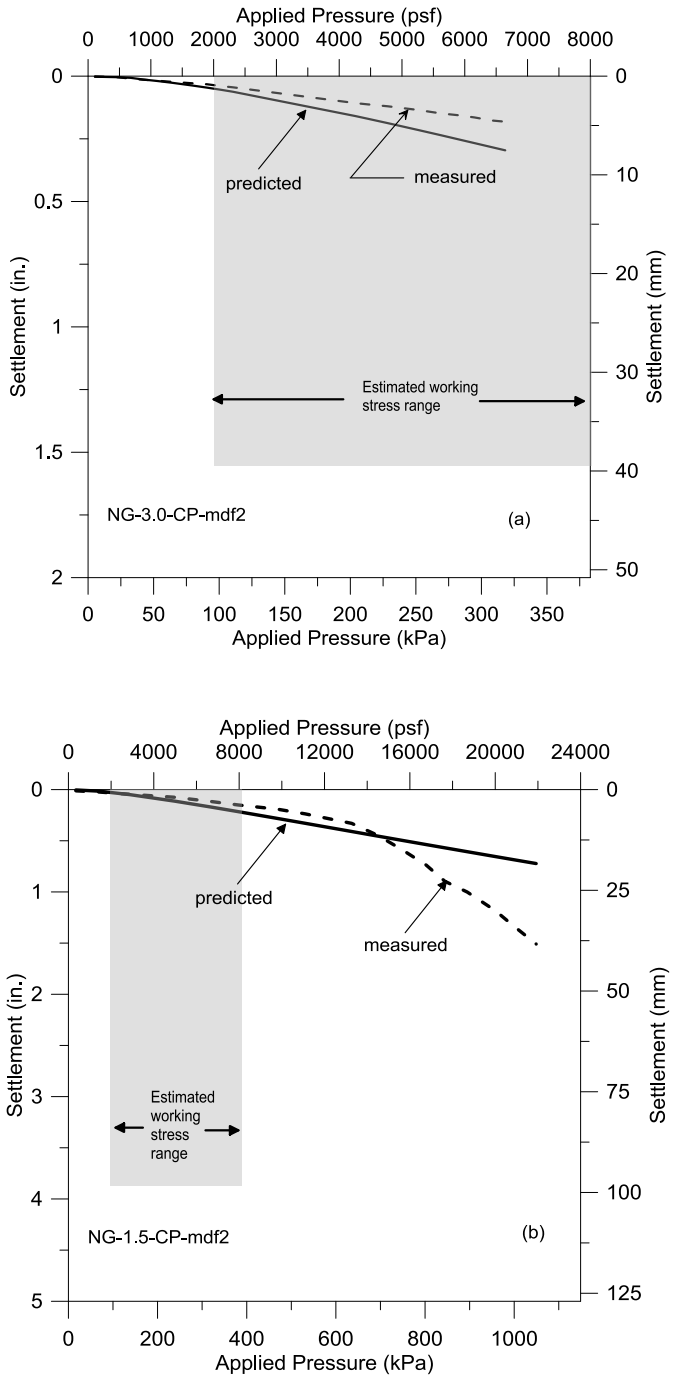

Figure 6.32: Predicted footing settlements using MoDaMP-2 with a constant Poisson's ratio and the second modification of the $G/G_{max} - \log\gamma$ relationships for (a) 3.0-ft (0.91-m) diameter and (b) 1.5-ft (0.46-m) diameter footings at the NGES Site

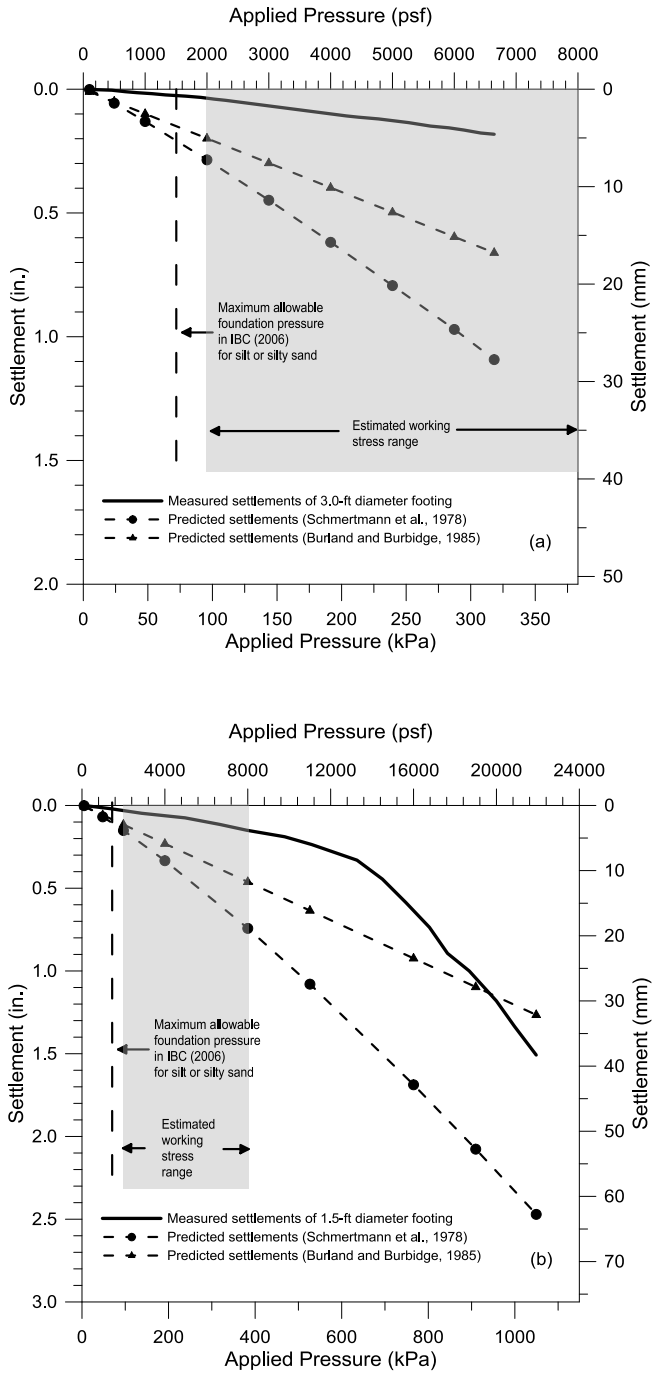

Figure 6.33: Comparison of settlements predicted using the CPT-based and SPT-based methods of Schmertmann et al. (1978) and Burland and Burbidge (1985), respectively with the measured settlements for the (a) 3.0-ft (0.91-m) and (b) 1.5-ft (0.46-m) diameter footings at the NGES test site

(0.46-m) diameter footing. As seen in the figures, the settlements with Burland and Burbidge (1985) method are higher than the measured settlements except for the settlements of 1.5-ft (0.46-m) diameter footing at applied pressures of above 20,000 psf. The predictions with Burland and Burbidge (1985) method are closer to the measured settlements compared to the predictions with Schmertmann et. al (1978) method. However none of these two methods captures the nonlinearity of the load-settlement curves.

It should be noted that in both methods there is a correction for the creep, however, the load-settlement tests were not continued long enough to investigate the creep. Therefore, creep is neglected in these predictions.

6.7.4 Load-Settlement Predictions with varying Poisson's Ratio

In the previous settlement predictions, the value of Poisson's ratio is assumed constant for all strain ranges. On the other hand, a change in the value of Poisson's ratio occurs with increasing shear strain levels as discussed in Chapter 4. In this section, the effect of the varying value of Poisson's ratio on the settlement predictions of the footings is investigated. The initial values of Poisson's ratios and their variation are determined following the procedures explained in Section 4.4. Figure 6.34a presents the results of the settlement analyses of the 3.0-ft (0.91-m) diameter footing by assuming a constant constrained compression modulus, M. The results of the settlement analyses with the constant bulk modulus, K, assumption are shown in Figure 6.34b. Figure 6.35a and 6.35b show the results of the settlement analyses of the 1.5-ft (0.46-m) diameter footing by assuming a constant constrained compression modulus, M, and constant bulk modulus, K, respectively.

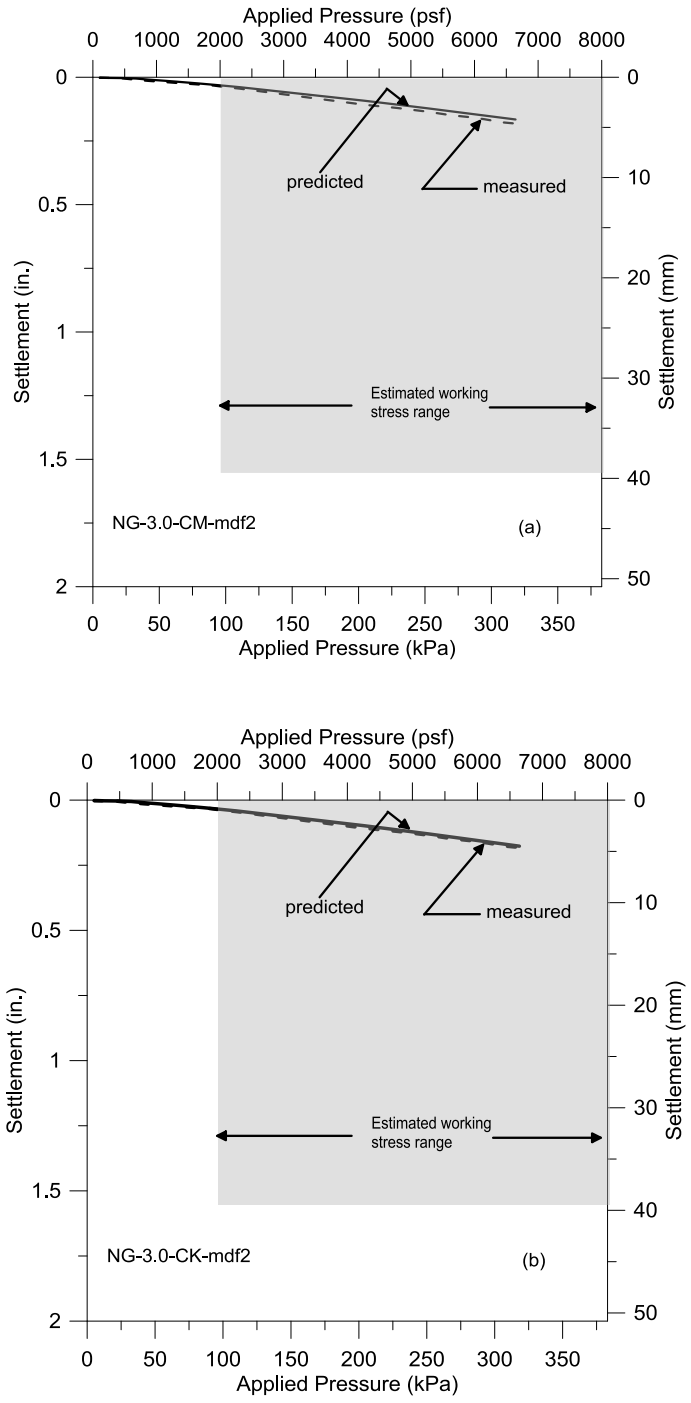

Figure 6.34 Predicted footing settlements using MoDaMP with a varying Poisson's ratio (a) M = constant and (b) K = constant and modified $G/G_{max} - \log\gamma$ relationships for 3.0-ft (0.91-m) diameter footing at the NGES test site

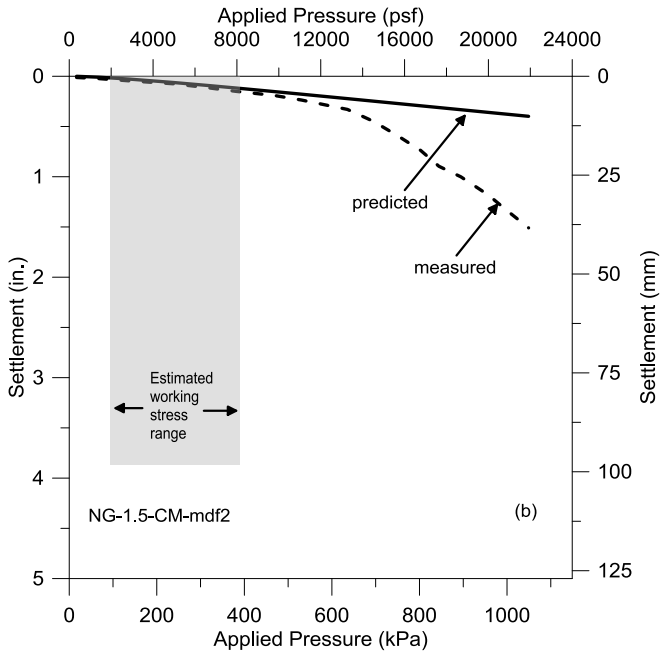

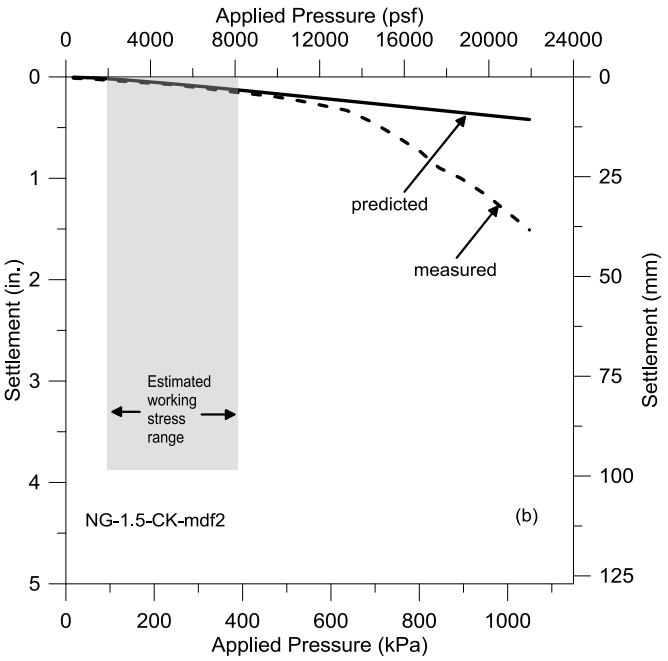

Figure 6.35 Predicted footing settlements using MoDaMP with a varying Poisson's ratio (a) M = constant and (b) K = constant and modified $G/G_{max} - \log\gamma$ relationships for 1.5-ft (0.46-m) diameter footing at the NGES test site

As seen in Figures 6.34 and 6.35, the predicted settlements with the varying Poisson's ratio assumption are smaller than the predicted settlements with a constant Poisson's ratio assumption. This result can be attributed to the smaller volumetric strains occurring with the varying Poisson's ratio assumption. Based on the predicted settlements, it can be concluded that varying Poisson's ratio assumption can be a more realistic assumption in terms of the change in the material properties under changing stress state.

6.7 SUMMARY

The load-settlement tests of two, small-scale footings at the NGES test site at Texas A & M University in College Station, Texas are discussed. The load-settlement tests were performed in a study by Park et al. (2009) in the vicinity of the test site reported by Briaud and Gibbens (1994) where several field and laboratory tests were conducted to characterize the soil for a symposium. In addition to the tests reported by Briaud and Gibbens, SASW and downhole tests were also conducted at the site by Park et al.,(2009). Two, undisturbed soil samples were tested dynamically using RCTS equipment at the University of Texas at Austin by Mr. Bohyoung Lee. SASW measurements are then used in the settlement prediction procedure to create representative shear wave velocity profiles of the granular soil layers beneath the footings. These profiles were obtained by developing $\log V_s - \log \sigma_0'$ relationships based on the average V_s profiled from SASW tests and the calculated mean effective confining pressures. Using the $\log V_s - \log \sigma_0'$ relationship, V_s at one atmosphere ($V_{s\,1atm}$) and the slope of the $\log V_s - \log \sigma_0'$ relationship were determined. Then $V_{s\,1atm}$ is converted to $G_{\max 1atm}$ and used in the settlement analyses with MoDaMP. The $G/G_{max} - \log \gamma$ relationships are determined from the RCTS measurements with two undisturbed samples. The $\tau - \gamma$ relationships were determined from the $G/G_{max} - \log \gamma$ relationships

over the range of G/G_{max} from 1.0 to 0.4. Beyond this point, the $\tau - \gamma$ relationships were determined from modified $G/G_{max} - \log\gamma$ relationships which were modified to match the larger-strain triaxial test data. Due to horizontal stress increase beneath the footings during loading in the field and due to cementation in the granular soil, the $G/G_{max} - \log\gamma$ relationships were modified for a second time. Settlement predictions after implementing these modifications into MoDaMP are in reasonable agreement with the measured settlements for both, 3.0- and1.5- ft (0.91- and 0.46-m) diameter footings. The effect of the Poisson's ratio on the settlement predictions was also investigated. This investigation was done by varying the value of Poisson's ratio with increasing shear strain by assuming that: (1) the constrained compression modulus was constant during loading and (2) the bulk modulus was constant during loading. The predicted settlements with both of these assumptions are smaller compared to the constant Poisson's ratio assumption. The reason for this difference is the smaller volumetric strains due to the increased Poisson's ratio with the constant constrained compression modulus and bulk modulus assumption.

Chapter 7: Load-Settlement Tests at the Hornsby Bend Test Site

7.1 INTRODUCTION

Two, small-scale footings with diameters of 3.0 ft and 1.5 ft (0.91 m. and 0.46 m) were constructed at the Hornsby Bend Site at Austin, Texas by Van Pelt (2010). The test area is located close to the Austin Bergstorm International (ABI) Airport. The location of the test site is shown in Figure 7.1. A detailed site investigation and soil characterization was conducted at this site between 2009 and 2010. In-situ field tests performed at this site included Cone Penetration Test (CPT), Spectral-Analysis-of-Surface-Waves (SASW) and crosshole seismic tests. Undisturbed and disturbed samples were obtained to perform laboratory tests to determine several soil properties. Figure 7.2 shows the plan view and locations of the footings and the locations of the various field and sampling tests at the site.

Laboratory tests including grains size distribution, Atterberg limit tests and CD triaxial tests are discussed in Section 7.2. In-situ testing including CPT, crosshole and SASW, is discussed in Section 7.3. In Section 7.4, representative V_s profiles are determined and $\log V_s - \log \sigma'_o$ relationships are developed. In Section 7.5, the load-settlement tests are introduced. The settlement predictions using MoDaMP are presented in Section 7.6. The settlement predictions with MoDaMP are compared with other settlement prediction methods. The effect of varying Poisson's ratio on the settlement predictions is also studied.

7.2 LABORATORY TESTS AND GENERAL SOIL PROPERTIES

Disturbed samples obtained at various depths at the project site were used to perform grains size distribution analysis. Based on these grain size distribution tests (Figure 7.3), it was concluded that the soil at the site is primarily a "sandy silt" or a "silt with sand" (classified as ML according to the USCS). The coefficient of uniformity, C_u,

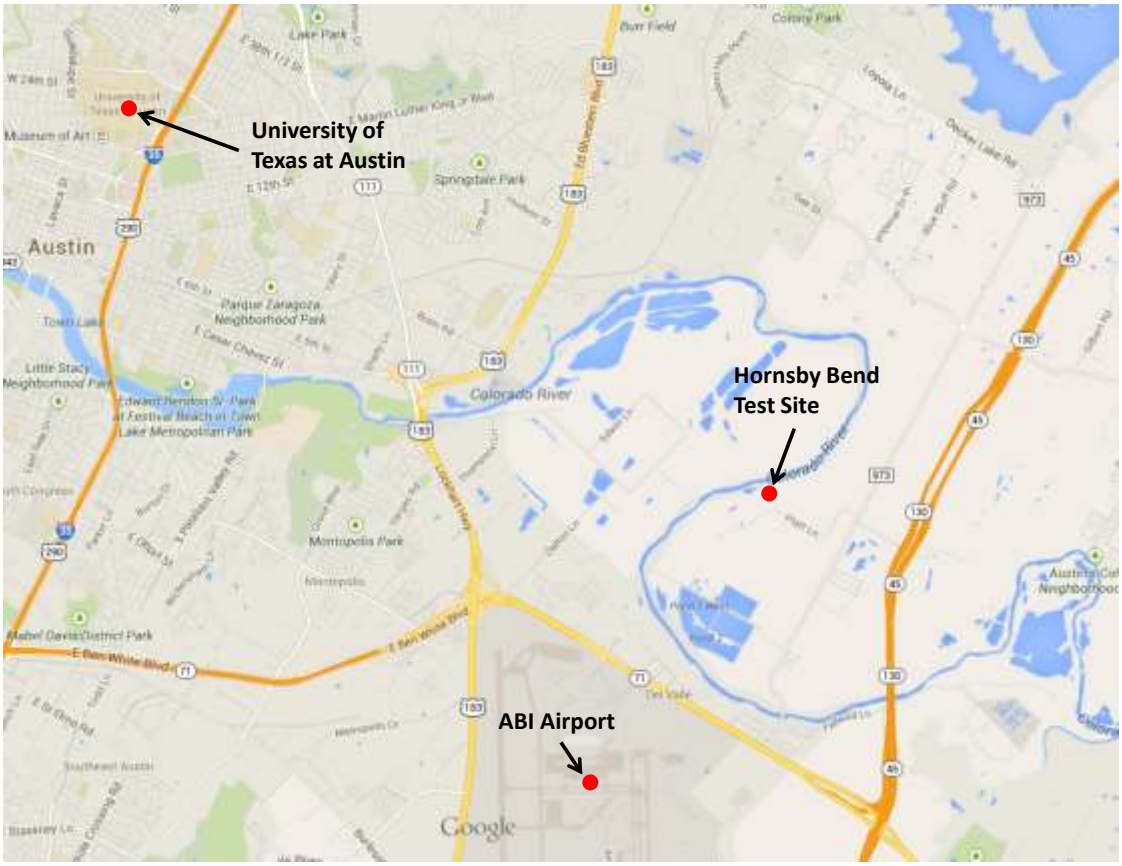

Figure 7.1: Location of the Hornsby Bend Test Site at Austin, Texas

is about 3.5. Also, Atterberg limit tests were performed on disturbed samples and they verified the result of the grain size distribution tests, revealing that the soil is non-plastic. The specific gravity of the soil was found to be 2.69 (Van Pelt, 2010).

Consolidated-drained (CD) triaxial tests were performed with disturbed samples to investigate the strength properties of the soil at Hornsby Bend Site (Van Pelt, 2010). Undisturbed soil samples could not be used in triaxial testing due to the sandy and silty nature of the soil which made trimming of the soil difficult because samples would not remain intact. The specimens were prepared using the under-compaction method with a

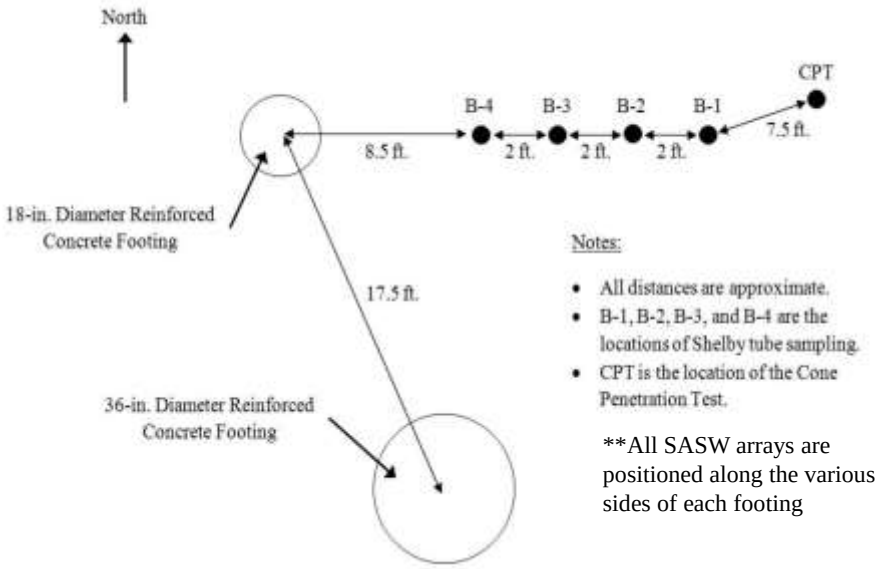

Figure 7.2: Plan view of the layout of the project site (from Van Pelt, 2010)

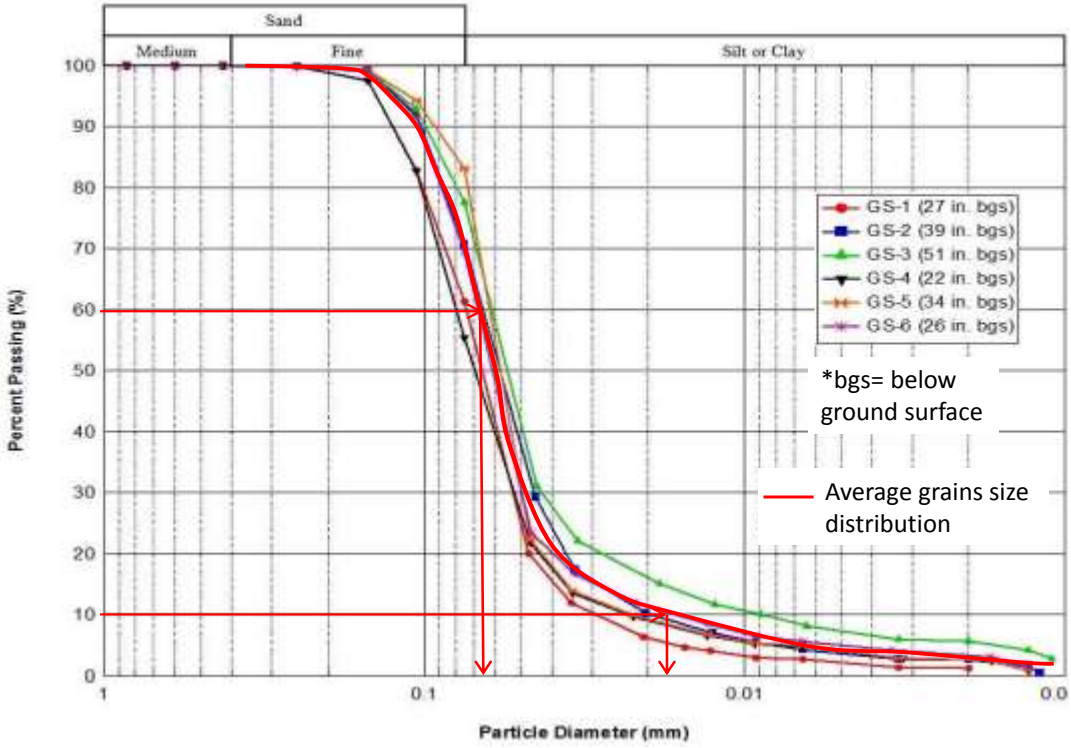

Figure 7.3: Grain size distribution of the soil at the Hornsby Bend Site (from Van Pelt, 2010)

target unit weight, γ_t, of 106 pcf and a water content, w, of 10%. The tests were conducted at three different confining pressures; 3, 9 and 27 psi. Figure 7.4 shows deviatoric stress vs. the axial strain curves from the CD triaxial test results. The strain rate was chosen as 0.005 inches per minute so that any excess pore pressures developed during loading also dissipated which resulted in freely draining conditions in the sandy silt soil at the Hornsby Bend site. Figure 7.5 presents the Modified Mohr-Coulomb failure envelope obtained from the CD triaxial tests results and the failure envelope results in a friction angle, ϕ, of 39^0 and a cohesion, c, of 0.88 psi. The cohesion is thought to be a result of a slight overconsolidation and/or possible cementation. This "cohesion" discussed further in Section 7.4.

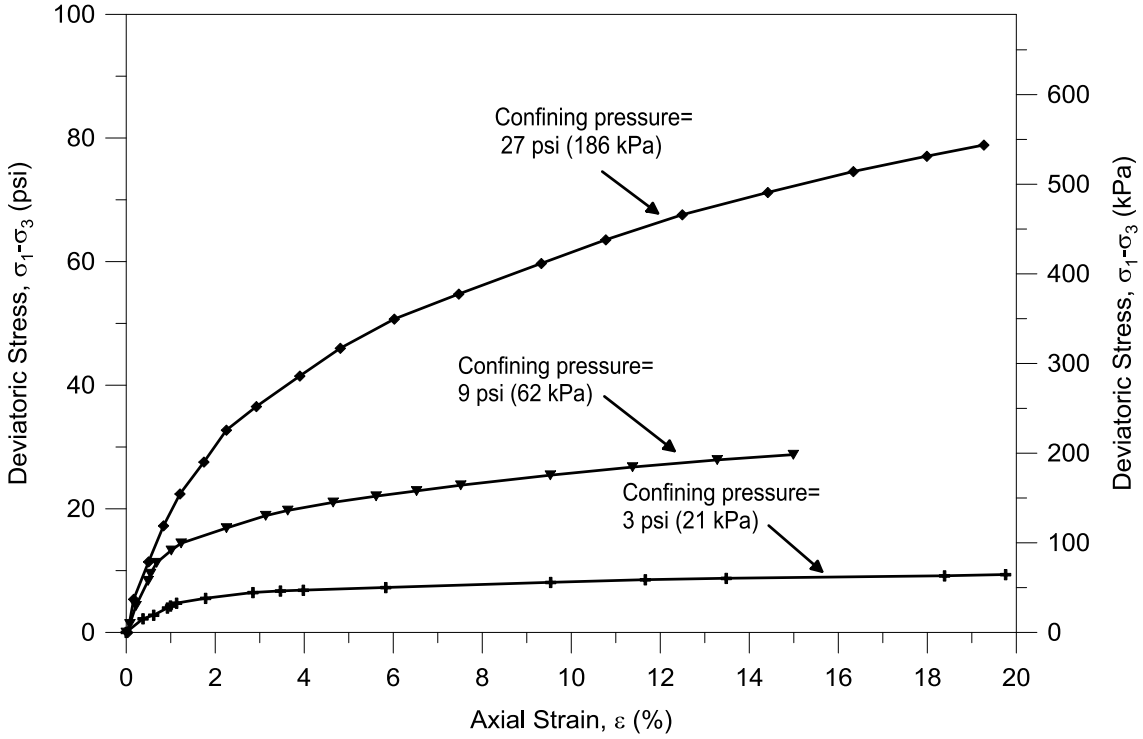

Figure 7.4: Deviatoric stress-axial strain curves from CD Triaxial tests (from Van Pelt, 2010)

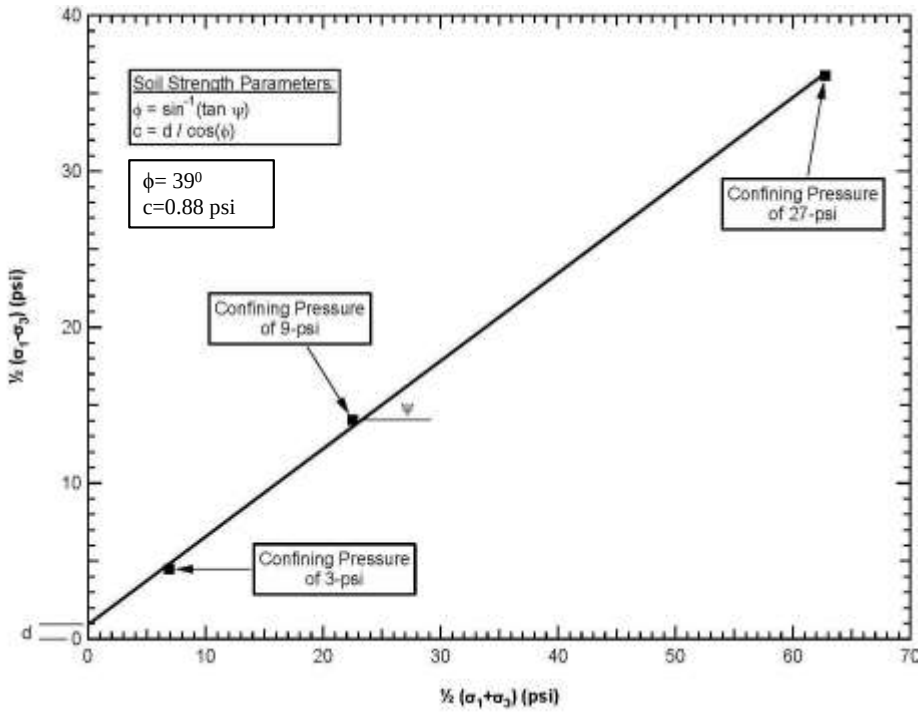

Figure 7.5: Total-stress envelope from CD Triaxial tests (from Van Pelt, 2010)

Undisturbed samples were obtained at the site using thin-walled Shelby tubes. Density tests and combined one-dimensional compression and permeability tests were conducted on these samples. The average total unit weight, γ_t, of the soil was 106 pcf and the average dry unit weight, γ_d, of the soil was 91 pcf. The initial void ratio and the degree of saturation of the specimen are found as 0.85 and 52 %, respectively.

7.3 IN-SITU TESTS

Cone Penetration (CPT), Spectral-Analysis-of-Surface-Waves (SASW) and crosshole seismic tests were conducted over several months at the Hornsby Bend Site. The results of all these tests are discussed herein, albeit SASW is the main in-situ test used in the settlement analysis of the footings at the Hornsby Bend site.

7.3.1 CPT Tests

CPT testing was performed at the site using a hydraulic ram mounted to the vibroseis truck "T-Rex". The cone tip resistance (q_c), sleeve friction (f_s), and the pore water pressures (u), were measured up to a depth of 44 ft (13.4 m). The results from this testing indicated a layered soil profile with the top of the layers at 0, 0.75, 7, 33, 39 and 42 ft (0, 0.23, 2.13, 10.06, 11.89 and 12.80 m). The test was terminated due to refusal at a depth of approximately 44 ft (13.4 m) which was assumed to be shale. A visual inspection of the soil layers were also made with a exploration pit extending up to 8 ft (2.44 m) below the ground surface. The soil up to a depth of 0.75 ft (0.23 m) is classified as sandy clay (CL), between 0.75 (0.23 m) and 7 ft (2.13 m) as sandy silt and between 7 ft (2.13 m) and 8 ft (2.44 m) as a clay with sand (CL). The results of the CPT testing are shown in Figure 7.6. Average representative tip resistance (q_c) and sleeve friction (f_s) profiles are added to the test results. These average profiles are used in settlement predictions using Schmertmann's (1978) and Burland and Burbidge methods (1985) for comparison purposes. Figure 7.7 presents an expanded version of the CPT test results up to a depth of 15 ft (~4.9 m) which is the lower boundary in the numerical analysis using MoDaMP. Based on the pore water pressure measurements, it was found that the water table is at a depth of about 34 ft (10.4 m).

7.3.2 SASW Tests

As the main part of the in-situ testing at the Hornsby Bend Site, SASW testing was performed in 2009 and 2010. Several arrays positioned along various sides of the two small-scale footings were used to test the soil. The details of the testing procedures and the dispersion curves can be found in Van Pelt (2010). Figure 7.8 and 7.9 show the shear wave velocities, V_s, measured near the 3.0-ft. and 1.5-ft. diameter footings. The average shear wave velocities are also shown

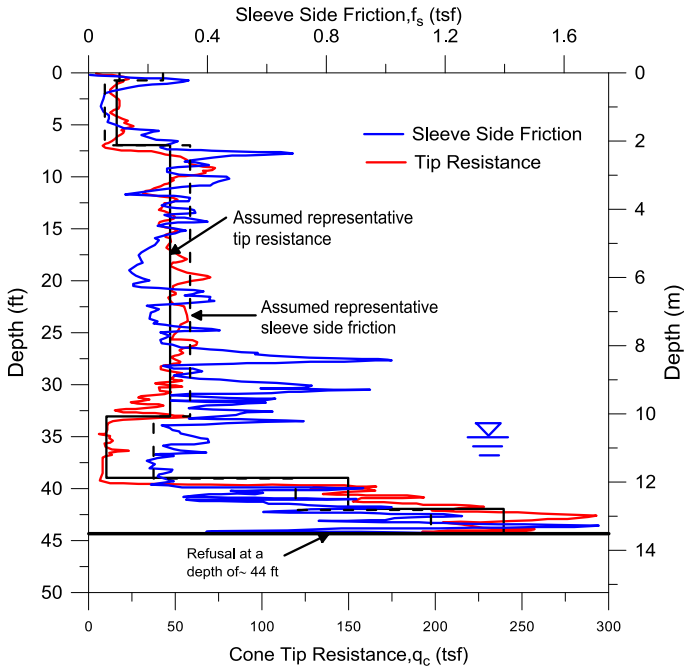

Figure 7.6: Tip resistance and side friction profiles from CPT testing at the Hornsby Bend Site (after Van Pelt, 2010)

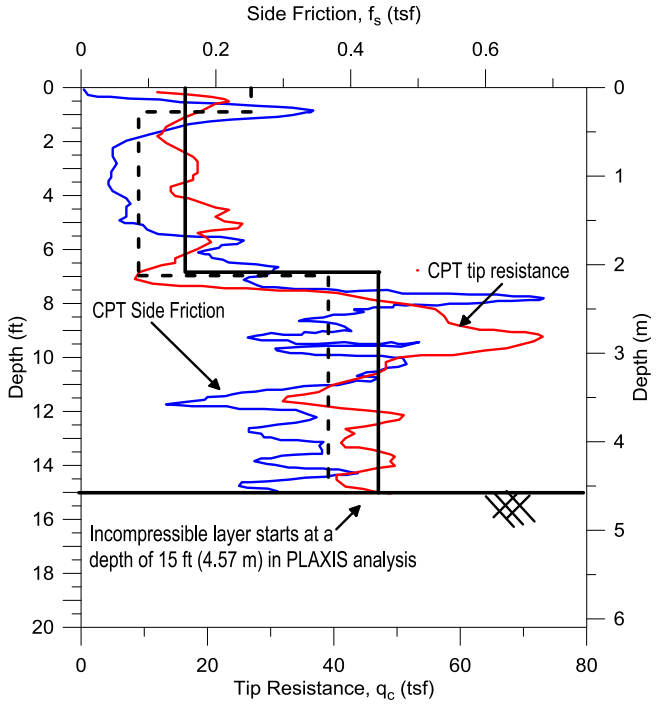

Figure 7.7: Tip resistance and side friction profiles from CPT testing at the Hornsby Bend Site up to 15 ft below the ground surface (after Van Pelt, 2010)

in these figures. The shear wave velocity profiles show that the variation of the shear wave velocity measurements is slightly higher close to the surface, especially for the 1.5-ft. diameter footing. As the depth increases, shear wave velocities become more uniform except for measurements from the array located along the east side of the footings which is slightly lower than the other three arrays.

7.3.3 Crosshole Tests

Crosshole seismic testing was conducted beneath the footings to determine both the compression wave velocity, V_p, and also to measure the shear wave velocity profile directly beneath the footings (Van Pelt, 2010). Two borings were drilled on opposite sides of the footing, with the center of each boring being about 1ft (0.3 m) away from the outer edge of the footing. A Shelby tube attached to steel extension rods was used as the source. The top of the rods was hit with a hammer. A 3D geophone placed in the bottom of the other boring served as the receiver.

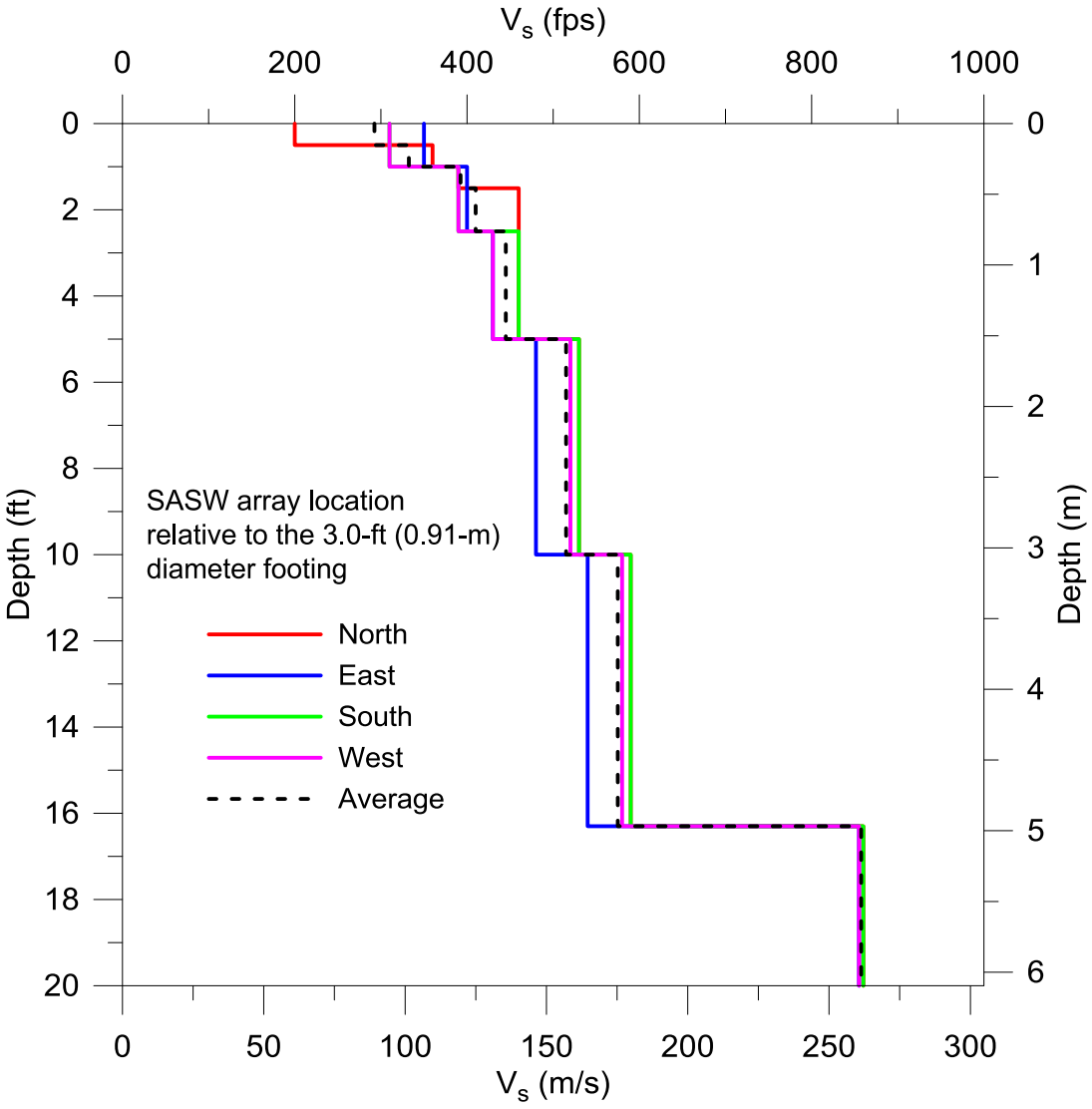

Figure 7.8: Shear wave velocity profiles near the 3.0-ft (0.91-m). diameter footing at the Hornsby Bend site (after Van Pelt, 2010)

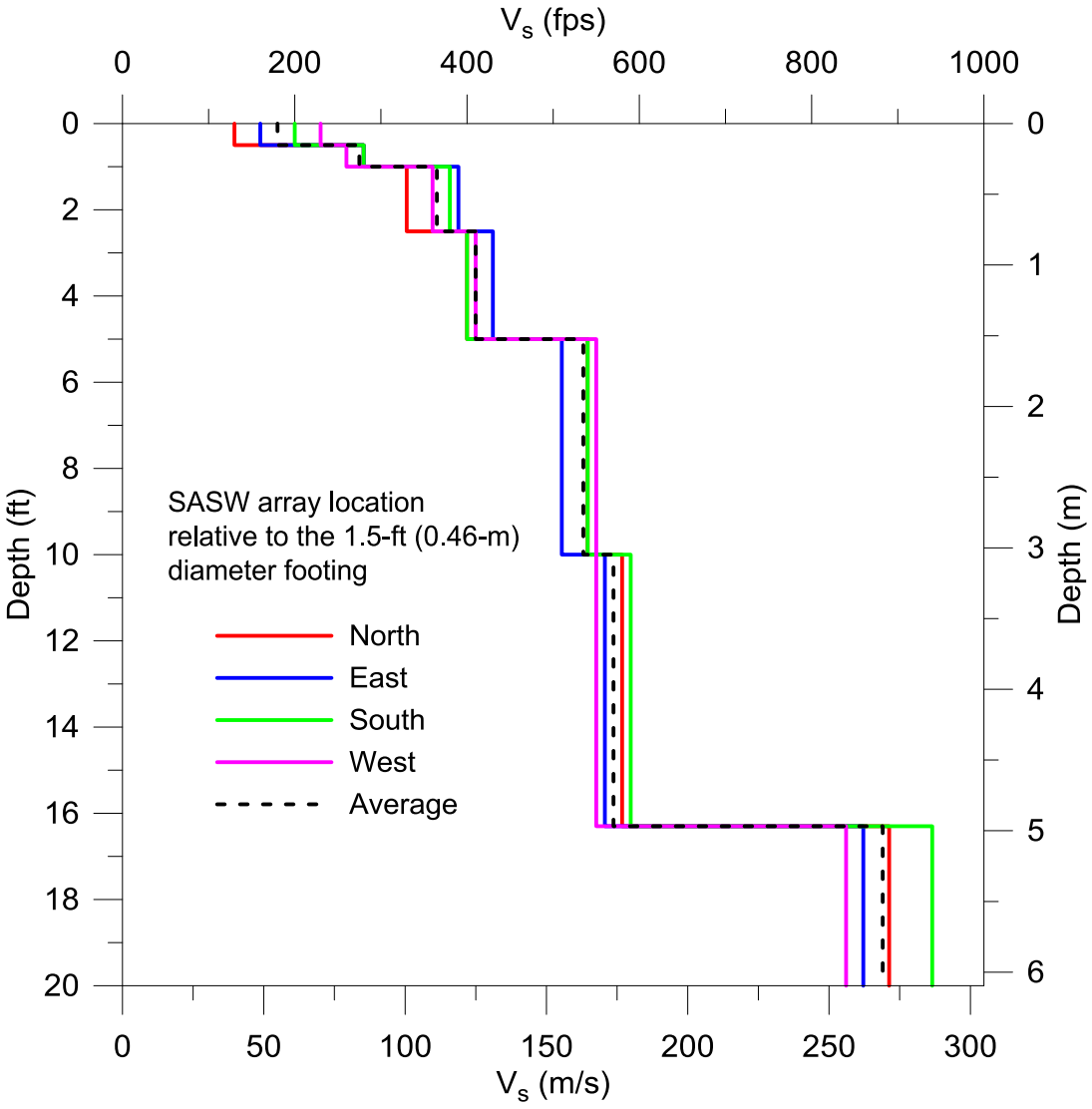

Figure 7.9: Shear wave velocity profiles near the 1.5-ft (0.46-m) diameter footing at the Hornsby Bend site (after Van Pelt, 2010)

The compression and shear wave velocities were measured directly beneath each footing which made the calculation of the Poisson's ratio at small strains possible. Figure 7.10 shows the V_p and V_s measurements from crosshole testing. As it is seen in the figure, V_s values from crosshole testing are very similar to the average V_s values obtained with SASW testing. Due to the good agreement between the V_s values evaluated with these two testing, the average SASW profile is used in the numerical analysis with MoDaMP in the settlement predictions. By using Equation 4.7, the small-strain Poisson's ratios were calculated and an average value of 0.30 was found for the sandy silt. The small-strain Poisson's ratios were slightly higher at shallower depths whereas they have a slightly smaller value at depths beyond ~1.5 ft (0.46 m).

7.4 REPRESENTATIVE SHEAR WAVE VELOCITY PROFILE AT THE FOOTING LOCATIONS

The average V_s profiles beneath the 3.0-ft (0.91-m) and 1.5-ft (0.46-m) diameter footings from SASW testing are shown in Figures 7.8 and 7.9, respectively. A representative in-situ $\log V_s - \log \sigma_o'$ profile was developed based on the average V_s profile by determining the corresponding in-situ σ_o' in a similar way to that explained in Section 6.5. Several points were chosen on the V_s profile and vertical stresses, σ_v', were calculated using an average total unit weight of 106 lbs/ft^3. Using Equation 6.3, and assuming a K_0 value of 0.75, the in-situ $\log V_s - \log \sigma_o'$ profiles were evaluated and are presented in Figures 7.11 and 7.12. An initial pressure of 100 psf (4.79 kPa) (hence, a negative pore water pressure of 100 psf was assumed) was added to σ_o' to match the V_s profile better at shallower depths. The resulting $\log V_s - \log \sigma_o'$ profiles beneath the 3.0-ft (0.91-m) diameter and 1.5-ft (0.46-m) diameter footings can be expressed with Equations 7.1 and 7.2, respectively.

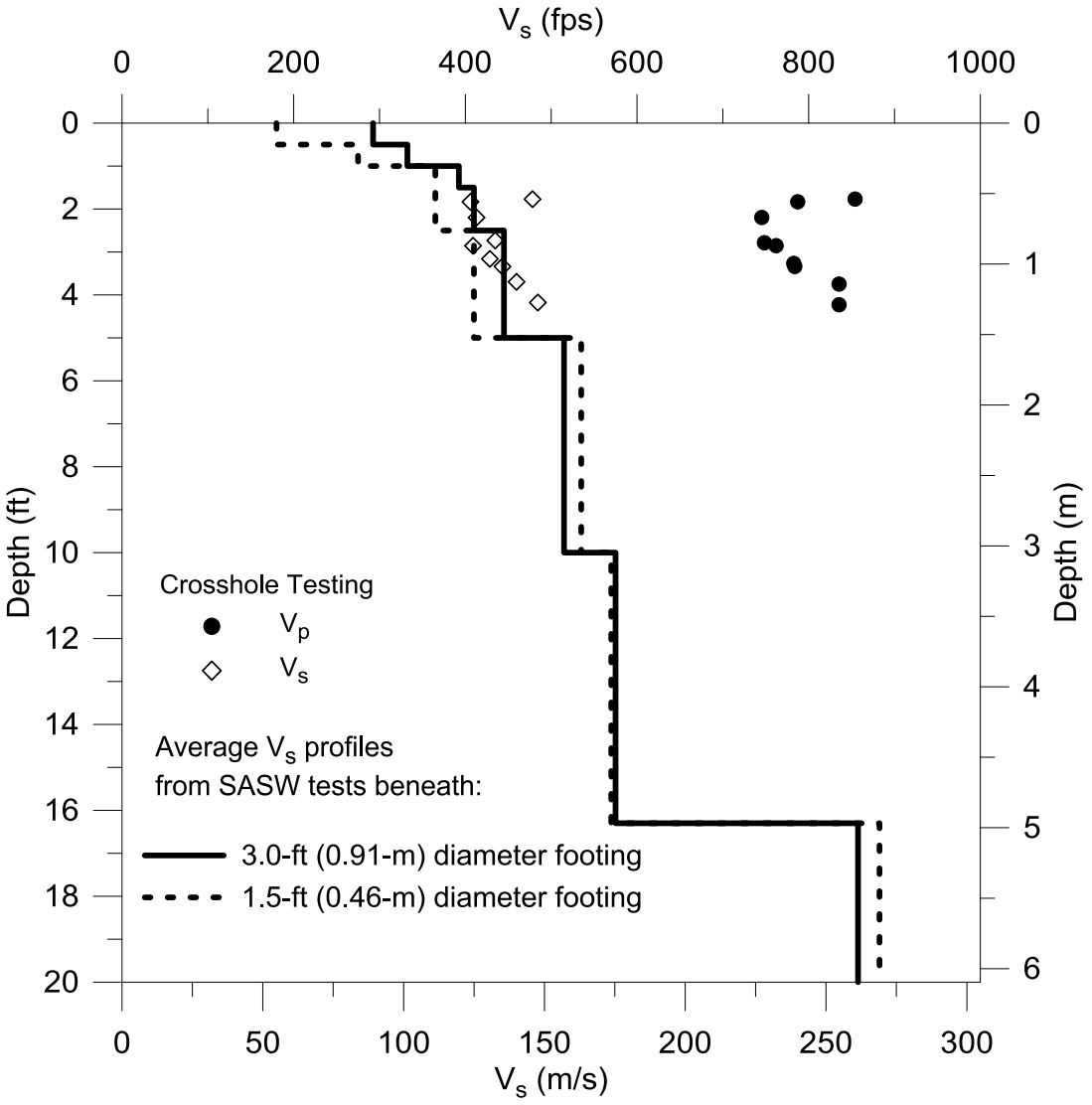

Figure 7.10: Comparison of compression and shear wave velocities measured with crosshole seismic testing beneath the small-scale footings along with the average shear wave velocity profile obtained with SASW testing (after Van Pelt, 2010)

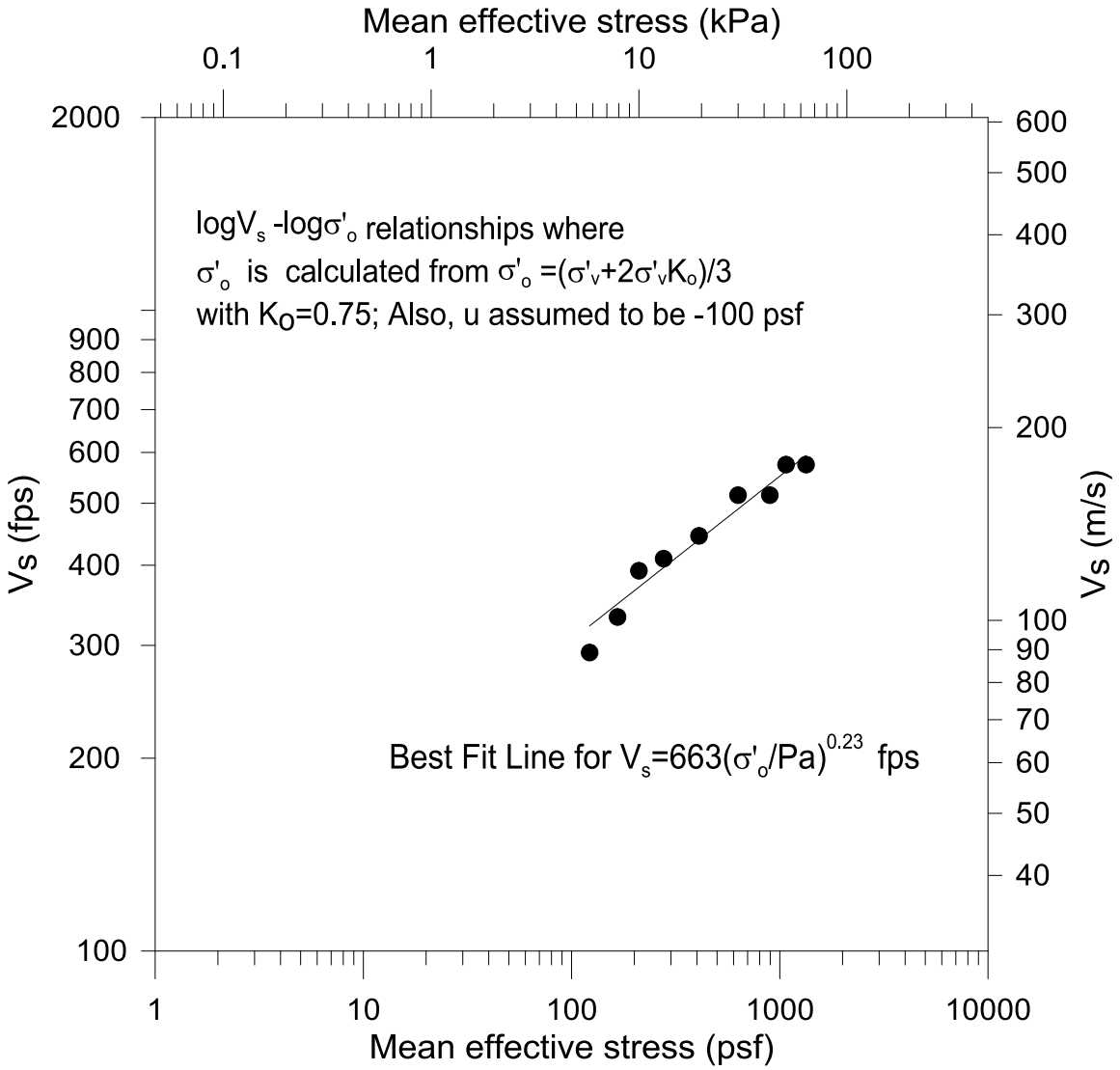

Figure 7.11: Log V_s-log σ‘$_o$ relationships for the Hornsby test site obtained from the average SASW testing results near the 3.0-ft (0.91-m) diameter footing

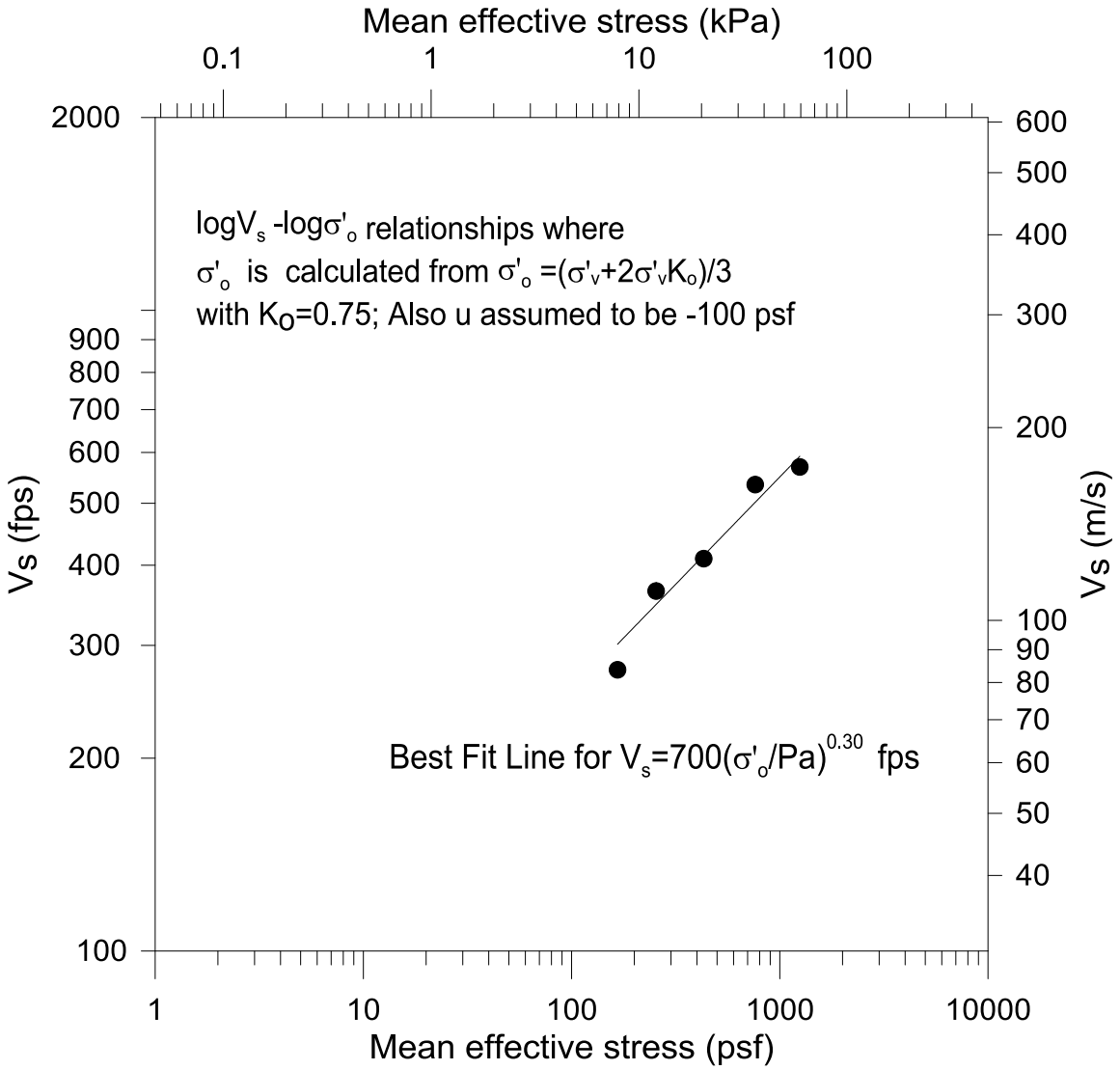

Figure 7.12: Log V_s-log σ‘$_o$ relationships for the Hornsby test site obtained from the average SASW testing results near the 1.5-ft (0.46-m) diameter footing

$$V_s = 663 \text{ ft/s} \cdot \left(\frac{\sigma_0'}{P_a}\right)^{0.23} \quad (7.1)$$

$$V_s = 700 \text{ ft/s} \cdot \left(\frac{\sigma_0'}{P_a}\right)^{0.30} \quad (7.2)$$

In Equations 7.1 and 7.2, 663 fps (202 m/s) and 700 fps (213 m/s) are the shear wave velocity values at one atmosphere of confining pressure. Comparison of the V_s profiles obtained using Equations 7.1 and 7.2 and the average V_s profiles from SASW tests near each footing are shown in Figure 7.13 and Figure 7.14 for the 3.0-ft (0.91-m) diameter and 1.5-ft (0.46-m) diameter footings, respectively. As seen in the figures, the measurements and field results are in good agreement. Hence, the formulations in Equations 7.1 and 7.2 are used in the settlement prediction analyses.

As explained in Section 6.5, the small-strain shear modulus at one atmosphere of pressure, G_{max_1atm} , can be expressed as a function of V_{s_1atm} and ρ . Moreover, the small-strain shear modulus, G_{max}, can be expressed as a function of G_{max_1atm} and σ_0' as shown in Equation 6.5. Using ρ= 3.29 slug/ft^3 (1.70 g/cm^3) and V_{s_1atm}=663 fps (202 m/s) and V_{s_1atm}=700 fps (213 m/s) and; G_{max_1atm} values are calculated as 1448 ksf and 1614 ksf (69.3 MPa and 77.3 MPa) for the soils under the 3.0-ft (0.91-m) and 1.5-ft (0.46-m) diameter footings, respectively.

7.5 $G/G_{max} - \log\gamma$ RELATIONSHIPS FOR HORNSBY BEND SITE

The soil model developed and explained in Chapter 4, combines G_{max} and $G/G_{max} - \log\gamma$ relationships obtained from field seismic and laboratory dynamic tests, respectively. In case there are no in-situ tests at larger strains to evaluate the $G/G_{max} - \log\gamma$ relationships, models such as Darendeli (2001) and Menq (2003) can be

used to estimate these relationships. Both the Darendeli (2001) and Menq (2003) relationships are modified hyperbolic models developed at the University of Texas at Austin with the form:

$$G/G_{max} = \frac{1}{1 + \left(\frac{\gamma}{\gamma_r}\right)^a} \tag{7.3}$$

where γ_r is the reference strain and "a" is the curvature coefficient. Figure 7.15 shows the $G/G_{max} - \log\gamma$ relationships at various confining pressures based on the Darendeli (2001) and Menq (2003) models. In this study, the Menq (2003) model is used to evaluate the $G/G_{max} - \log\gamma$ relationships for the Hornsby Bend site because it contains more specific parameters for granular soils.

7.6 LOAD-SETTLEMENT TESTS AT THE HORNSBY BEND SITE

Two, circular, reinforced concrete footings with diameters of 3.0 ft (0.91 m) and 1.5 ft (0.46 m) were constructed at the site. Each footing was 1.0 ft (0.3 m) thick and was embedded into the ground 10 in. (0.25 m). The upper 10 in. (0.25 m) of the soil was removed prior to construction. Both foundations were reinforced with prefabricated steel rebar cages. To determine soil settlements at different depths below the 3.0-ft (0.91-m) diameter footing, tell-tales were installed. The settlements measured at different depths beneath the footing were then used to calculate the strain distribution beneath the footing. The cross-sectional views of both footings are presented in Figure 7.16. The surface settlements of the footings were measured with linear potentiometers which were attached to reference frames. Loads were applied with a hydraulic jack reacting against the weight of a vibroseis truck, “T-Rex”. The load-transfer mechanisms and the

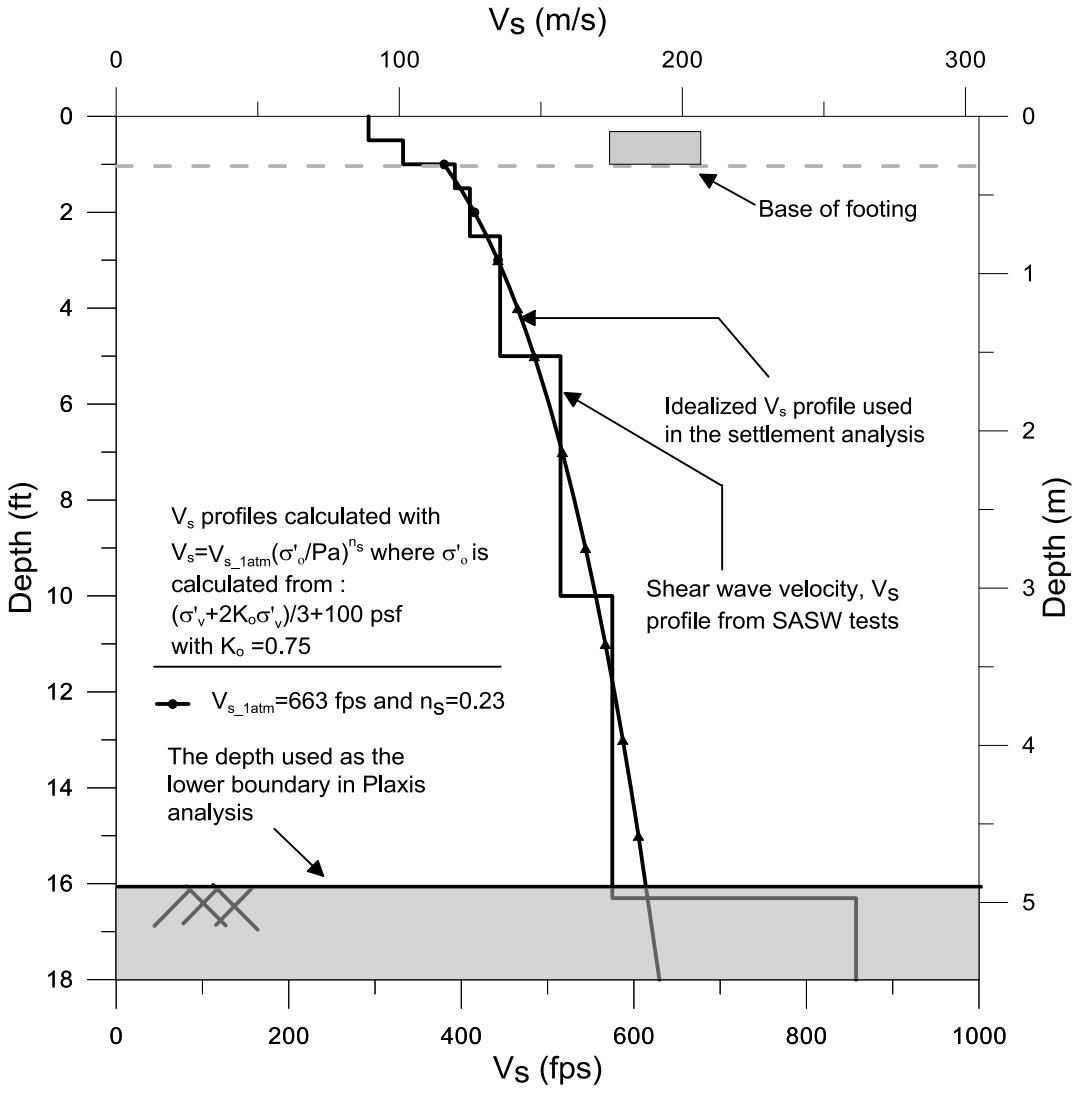

Figure 7.13: Representative V_s profiles obtained from log V_s-log σ‘$_o$ relationships compared with the average V_s profiles obtained from SASW testing beneath the 1.5-ft (0.46-m). diameter footing

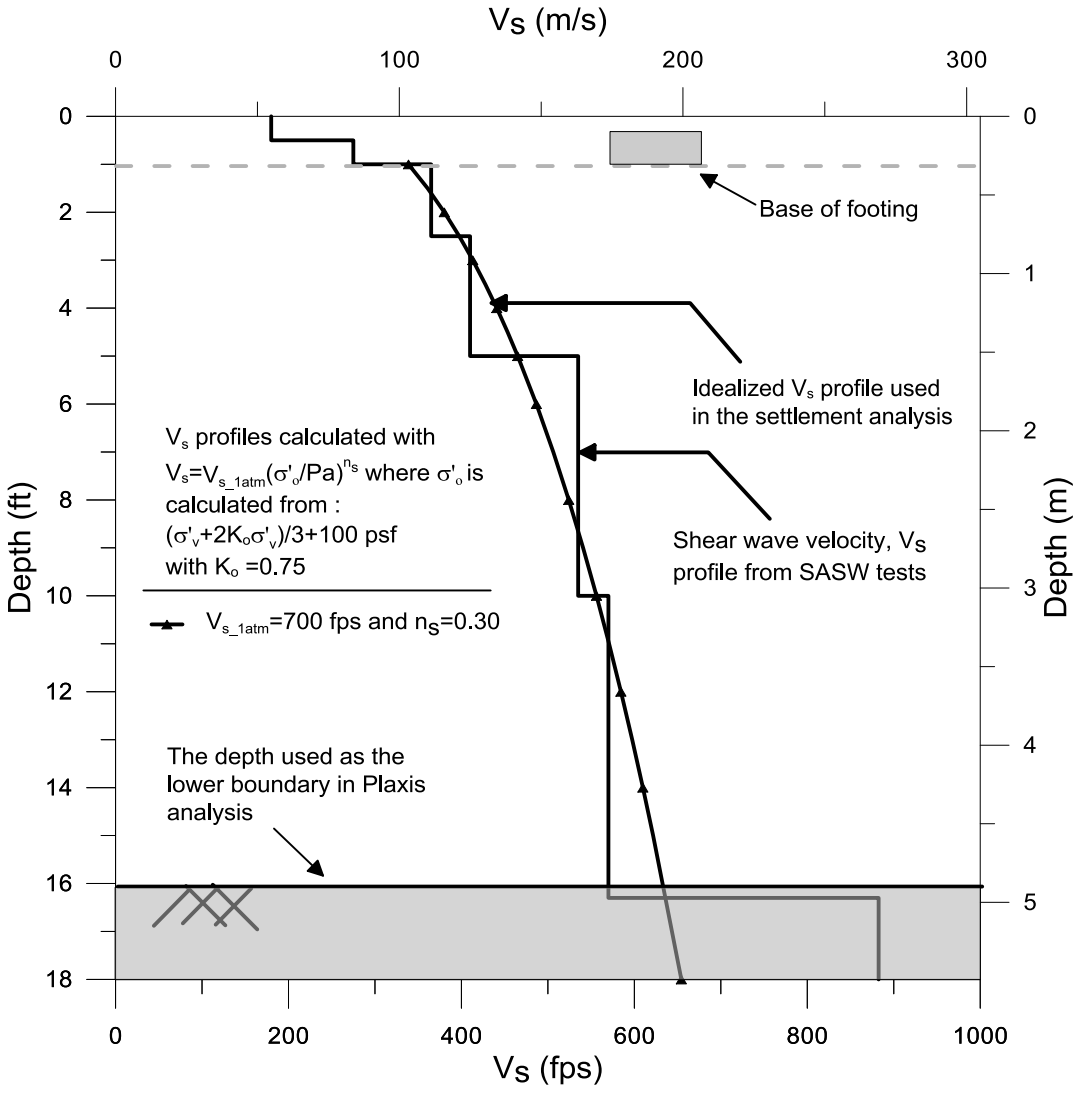

Figure 7.14: Representative V_s profiles obtained from log V_s-log σ‘$_o$ relationships compared with the average V_s profiles obtained from SASW testing beneath the 3.0-ft (0.91-m) diameter footing

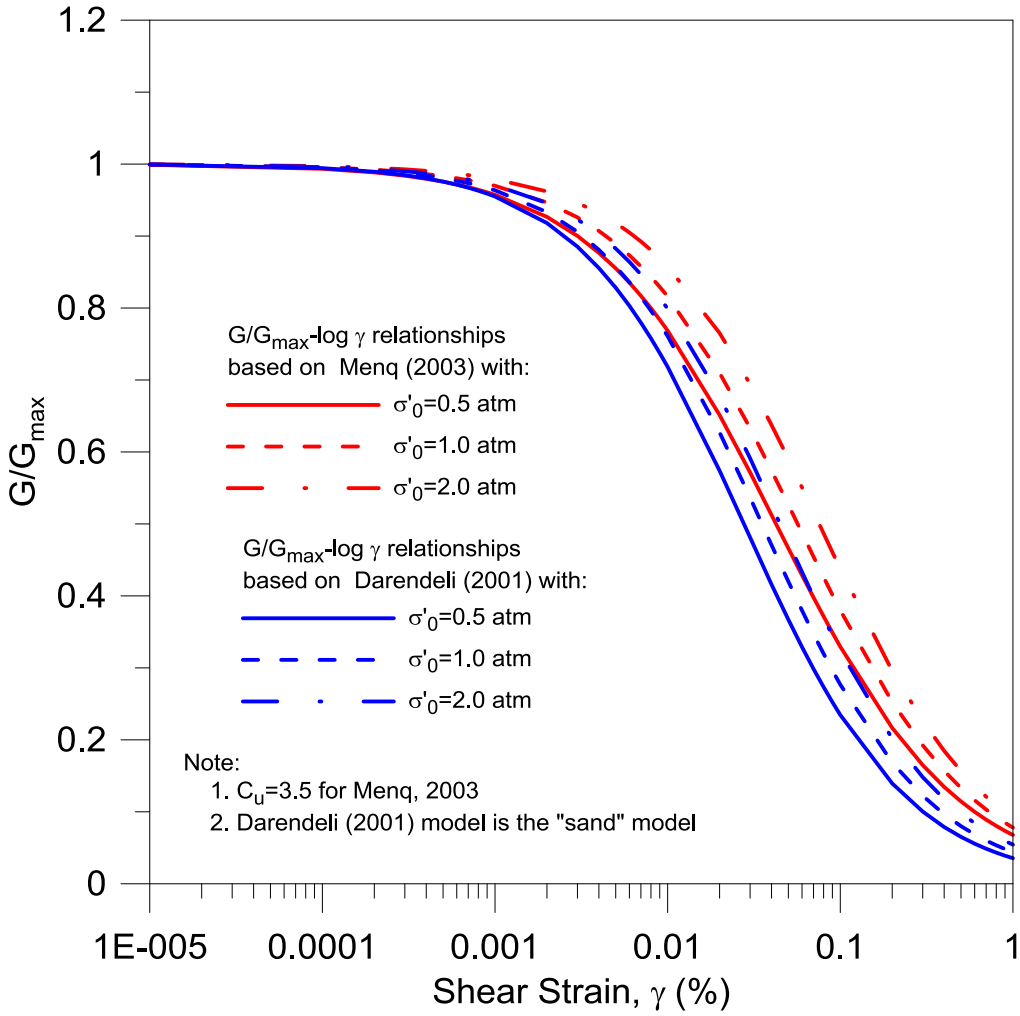

Figure 7.15: $G/G_{max} - \log\gamma$ relationships based on Darendeli (2001) and Menq (2003) relationships evaluated for the Hornsby Bend site

lay-out of the linear potentiometers are presented in Figure 7.17 for both footings. The load transfer mechanism differed slightly for each footing. For the 3.0-ft (0.91-m) diameter footing, the reaction force from T-Rex was transferred first to a 50-kip load cell. From the load cell, the load was directed to a T-shaped steel loading frame. The load was then applied to the footing through pads at each end of the steel frame. The steel frame was used to distribute the applied load over a larger area of the footing, thus the bearing pressure applied to the soil from the footing would be more uniform. For the 1.5-ft (0.46-m) diameter footing, the load from T-Rex was transferred first to the load cell through three steel plates. The load was then directed to the footing by a solid steel plate (Van Pelt, 2010).

Figure 7.18 shows T-Rex in position during loading of one footing while the operator monitors the applied pressure.

The loading and unloading of the footings was achieved by increasing and decreasing the reaction force from T-Rex by adjusting the hydraulic ram. When an incremental load was applied, the load level was held constant until the settlement or rebound, respectively, was completed. Completion of the settlement was defined as when the change in measured footing settlement was less than 0.06 in. in 6 minutes. The completion of rebound was defined as when the change in measured settlement was less than 0.001 in. in 6 minutes (Van Pelt, 2010). The measured load-settlement curves are presented in Figure 7.19. The settlements were measured using the linear potentiometers up to 2 inches which is the maximum stroke length of the linear potentiometers. The ultimate settlements at the end of loading and unloading stages were measured by surveying using a total station. The settlement values between 2 inches and the ultimate settlement were interpolated using the known data points.

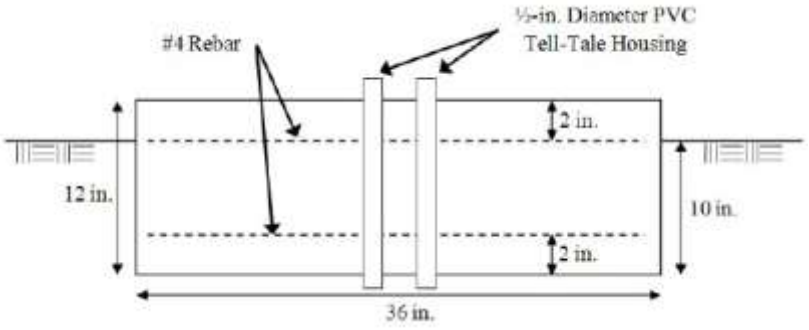

(a)

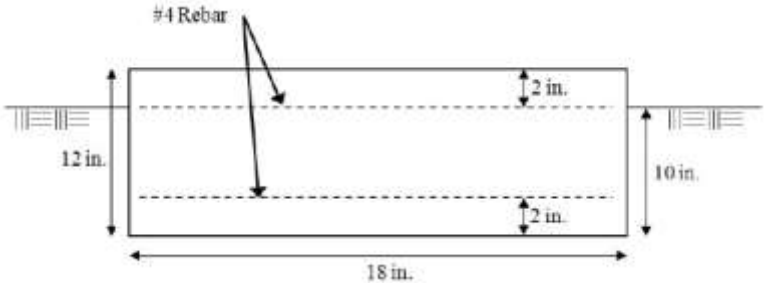

(b)

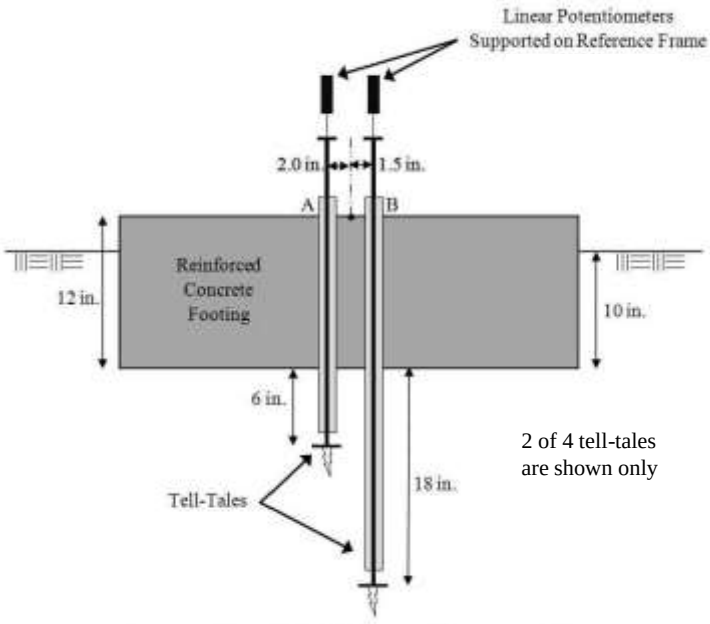

(c)

Figure 7.16: Cross-sectional view of (a) the 3.0-ft (0.91-m) diameter footing, and (b) the 1.5-ft (0.46-m) diameter footing and (c) tell-tales beneath the 3.0-ft (0.91-m) diameter footing (from Van Pelt, 2010)

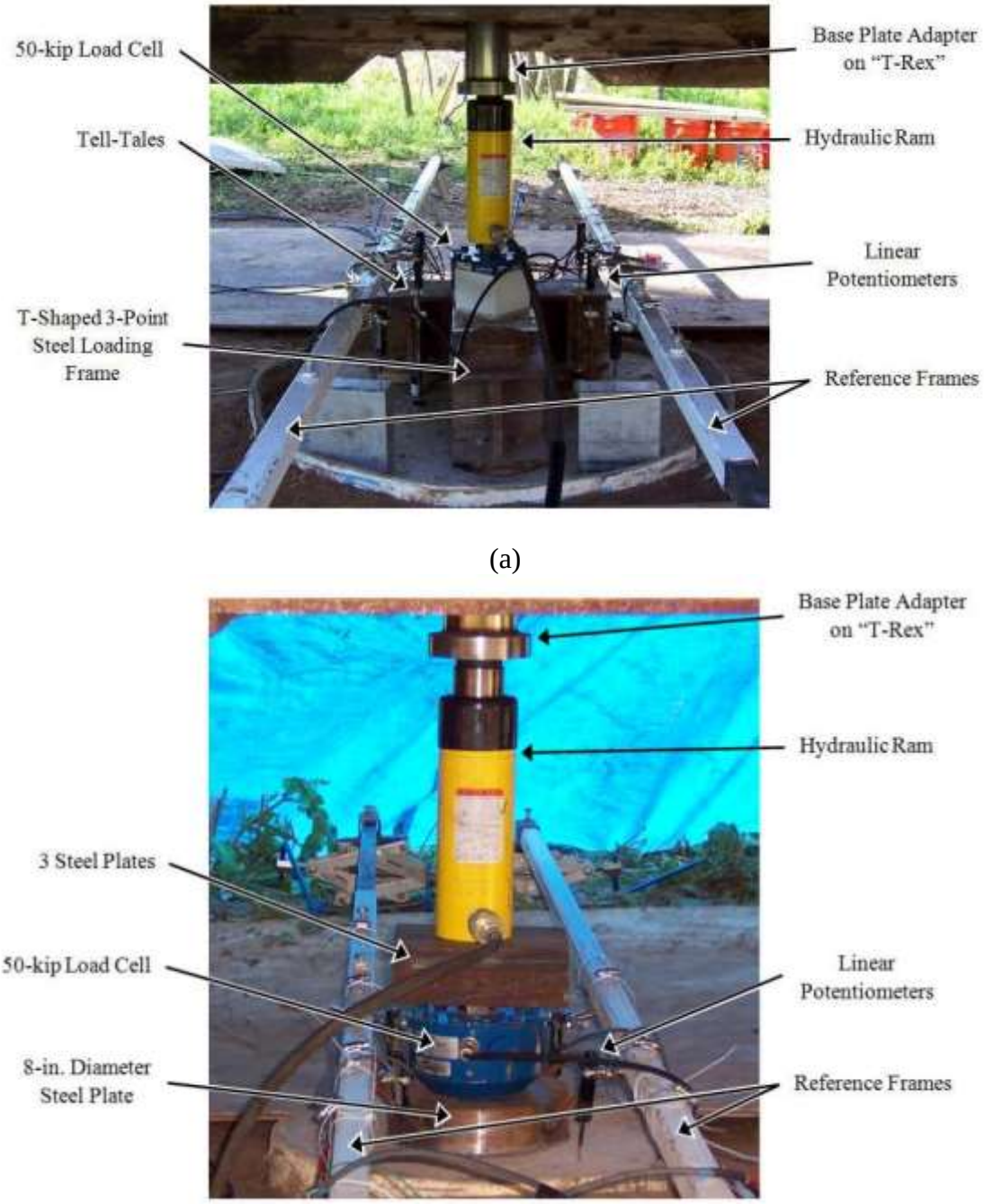

Figure 7.17: Load-transfer system and the lay-out of the linear potentiometers for the (a) 3.0-ft (0.91-m) diameter and (b) for the 1.5-ft (0.46-m) diameter footings (from Van Pelt, 2010)

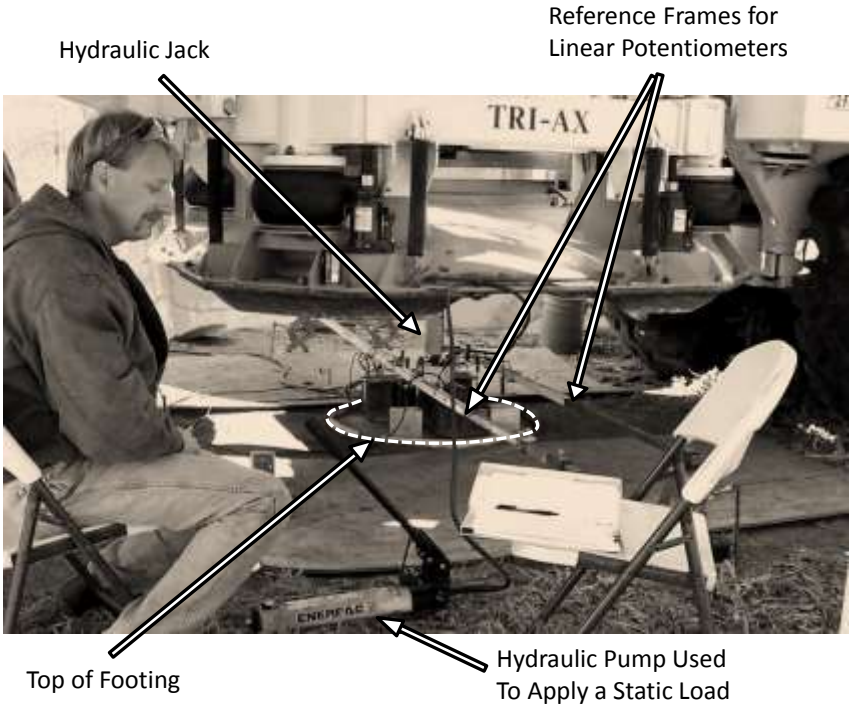

Figure 7.18: T-Rex in position during loading, with the operator constantly monitoring the applied load (after Van Pelt, 2010)

7.7 LOAD-SETTLEMENT PREDICTIONS

In this section, load-settlement curves of the two small-scale footings at the Hornsby Bend site predicted using MoDaMP are presented. Moreover, two very widely-used methods, Schmertmann et al. (1978) and Burland and Burbidge (1985), are also used to predict the settlements of two footings for comparison purposes.

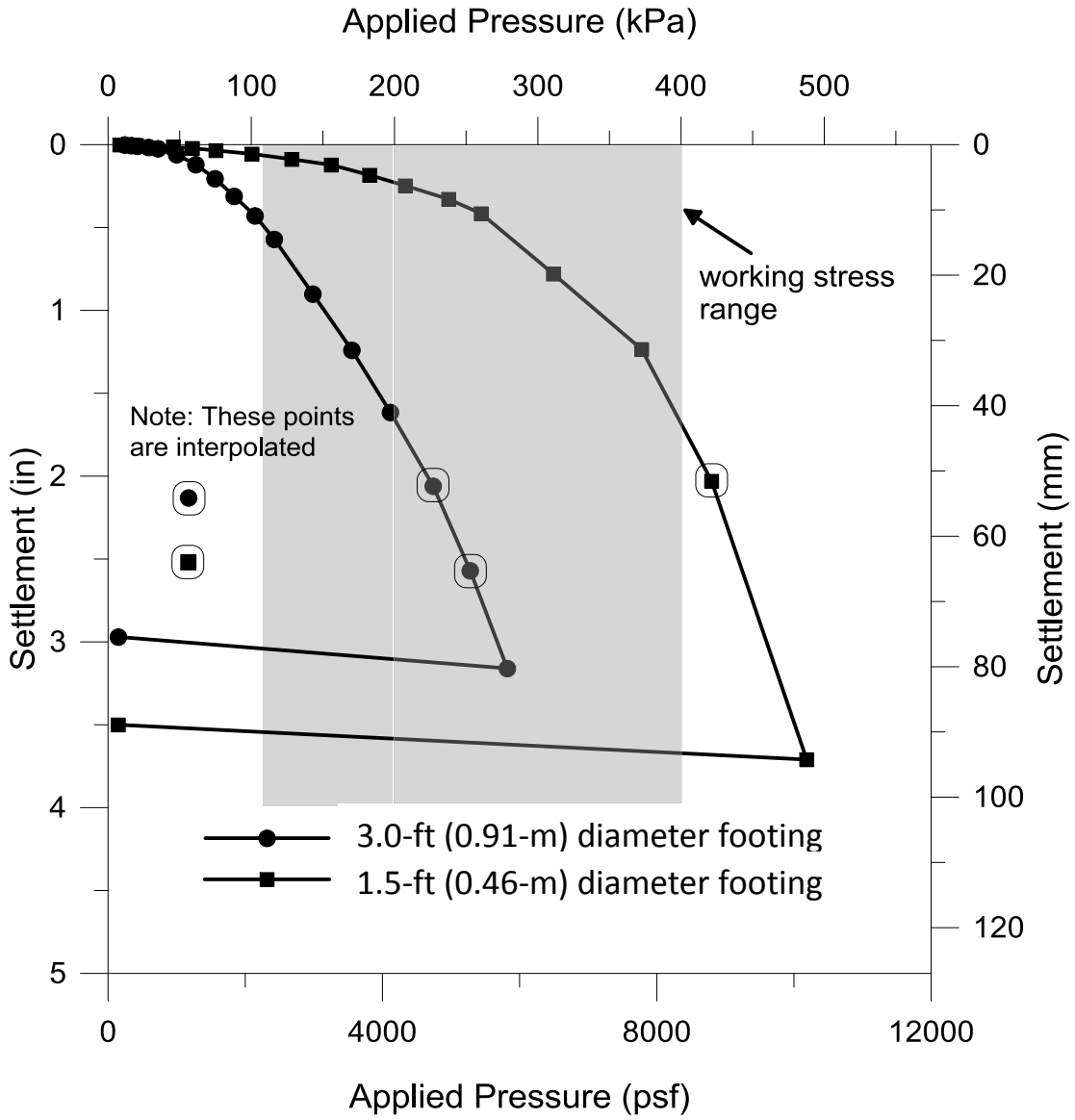

Figure 7.19: Measured settlements for the 3.0-ft (0.91-m) and 1.5-ft (0.46-m) diameter footings at the Hornsby Bend site (after Van Pelt, 2010)

7.7.1 Load-Settlement Predictions with MoDaMP

The user-defined soil model, MoDaMP, is implemented in PLAXIS as explained in Chapter 4. A finite element analysis was carried out to predict the settlements of the small-scale footings. Table 7.1 presents the values of the input parameters that were obtained in Section 7.4 and used in the finite element analysis. Please note that γ_r and "a"

are stress-dependent parameters and therefore only the equations expressing these parameters are provided. Each analysis was given a different identifier (analysis ID) to differentiate the site, footing diameter, Poisson's ratio assumption, as explained in Section 6.7.1. The first two letters indicate the site; HB stands for Hornsby Bend test site, the following number indicates the diameter of the footing in ft and the following two letters (CP,CM or CK) indicates which assumption about Poisson's ratio is made. CP indicates that the small-strain Poisson's ratio is kept constant throughout all strain ranges, whereas CK indicates that Poisson's ratio is varied by keeping K constant, and CM indicates that Poisson's ratio is varied by keeping M constant. If a modification is made to $G/G_{max} - \log\gamma$ relationships, then "mdf" is added at the end of the identifier. For example, HB-3.0-CK-mdf1 is the analysis for the 3.0-ft diameter footing at the Hornsby Bend test site where the Poisson's ratio is evaluated based on a constant K assumption and modified $G/G_{max} - \log\gamma$ relationships (MoDaMP -1) are used.

Table 7.1: Input parameters used in the settlement analysis with MoDaMP for the Hornsby Bend site

	36-in. Diameter	18-in. Diameter
G_{max_1atm}	1448 ksf	1614 ksf
ν_0	0.3	0.3
a	Equation 3.13	Equation 3.13
γ_r (%)	Equation 3.12	Equation 3.12

7.7.1.1 PLAXIS model for the Footings

The subroutine MoDaMP is implemented into PLAXIS and finite element analyses of settlements of footings are carried out using these subroutines. The soil-

footing system was modeled as axisymmetric and symmetrical, therefore only half of the footing was modeled. To eliminate the boundary effects, the thickness of the soil beneath the footing is assumed as 15 ft (5 times the diameter of the larger footing) as proposed by Brinkgreve et al, 2011. The reinforced concrete footings are modeled as flexible plate members.

PLAXIS automatically generates the mesh for the model but the size and type of the mesh can be altered by the user. The mesh used in the analyses consisted of 922, 15-node triangular elements. The mesh is refined beneath the footings since most of the deformations are expected to occur in this region. The undeformed mesh is shown in Figure 7.20. The soil up to the depth of embedment of the footings is modeled as a surcharge because the deformations due to loading are occurring beneath the footings.

G_{max} values are calculated with Equation 6.5 based on the initial stress states. Values of G are calculated using the G_{max} values and Equations 3.11, 3.12, and 3.13. Next, values of G and ν are used to establish the nonlinear elastic stiffness matrix. New stresses are calculated based on the nonlinear elastic stiffness matrix and new G_{max} values are calculated with these stresses.

To illustrate this procedure, three reference points at different depths beneath the 3.0-ft diameter footing are used (Figure 7.21a). The octahedral shear strain and shear modulus at each reference point are determined under five, increasing load levels applied to the footing (Figure 7.21b). Five $G - \log\gamma_{oct}$ relationships determined for the five load levels identified in Figure 7.21b are plotted as solid lines in Figures 7.21c, 7.21d and 7.21e for Reference Points X, Y, and Z, respectively. The sets of (G, γ_{oct}) coordinates that correspond to each of the five load levels on the load-settlement curve are identified on the appropriate $G - \log\gamma_{oct}$ relationship by the solid circles and associated load-level numbers. The increase in G_{max} and general upward shifting of the $G - \log\gamma_{oct}$ curves

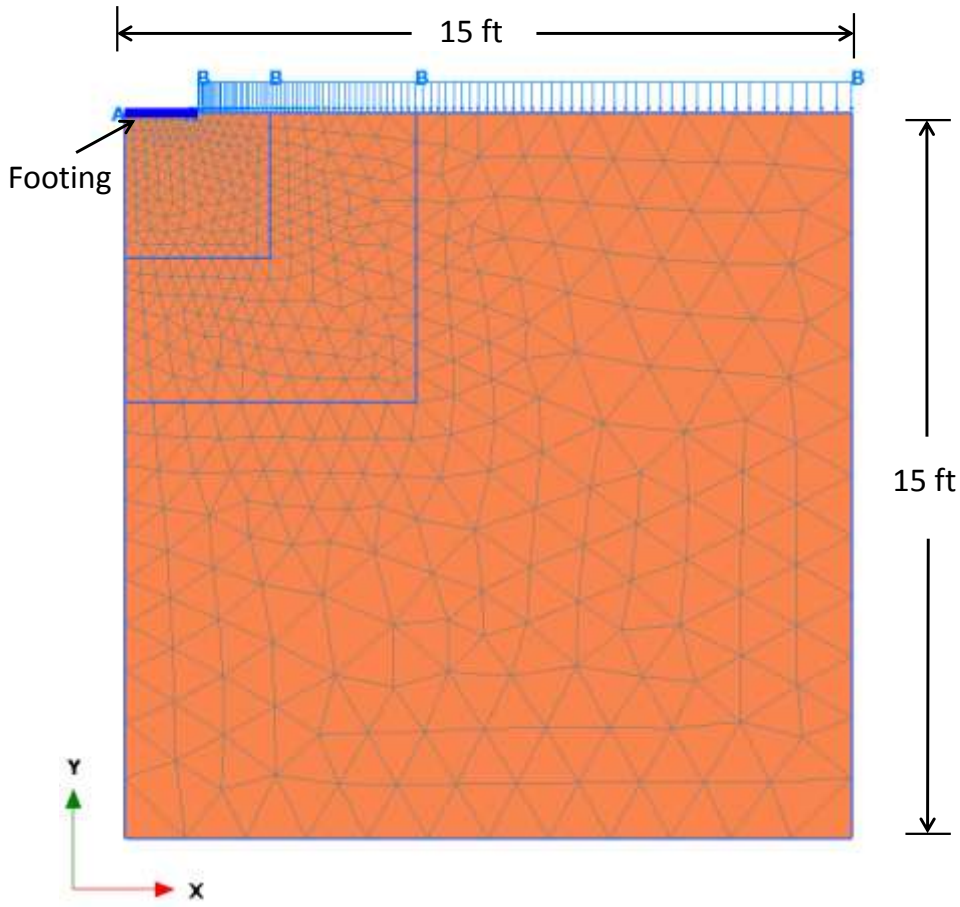

Figure 7.20: PLAXIS model geometry and mesh used in the settlement analysis with MoDaMP

(solid lines) with increasing load level is seen in Figures 7.21c, 7.21d, and 7.21e. As loading increases, the net effect is G decreasing as γ_{oct} increases at each reference point. This effect diminishes with increasing depth because the incremental stress change decreases with depth.

7.7.1.2 Predicted Settlements

Predictions with the PLAXIS model using MoDaMP are presented in this section. As explained previously, every analysis is given an identification name to distinguish between different footing sizes and different assumptions. The first analysis, HB-3.0-CP,

is the analysis for the 3.0-ft (0.91-m) diameter footing on Hornsby Bend site with a constant Poisson's ratio using MoDaMP as the soil model, whereas HB-1.5-CP is the same analysis for the 1.5-ft (0.46-m) diameter footing. The results of these analyses are shown in Figures 7.22a and 7.22b for HB-3.0-CP and HB-1.5-CP, respectively.

As seen in Figure 7.22, the predicted settlements closely match the measured settlements up to applied pressures of 2000 psf and 1000 psf, for the 3.0-ft diameter and for the 1.5-ft diameter footings, respectively. However, in the working stress range, which is defined as 2000-8000 psf, the predicted settlements are considerably larger than the measured settlements. The reason is that the soil softens more rapidly at larger strains when modeled with MoDaMP and a constant Poisson's ratio.

The $G/G_{max} - \log\gamma$ relationships described in Chapter 3 have been primarily developed by torsional resonant column testing over small-to-moderate values of strains, typically shear strains less than 0.2 %. The relationships need to be modified to use them in MoDaMP at larger strains which occur in problems such as shallow foundation settlements.

7.7.2 Modification of $G/G_{max} - \log\gamma$ Relationships in MoDaMP

Figure 7.23 presents the $\tau - \gamma$ results from the CD triaxial test conducted on reconstituted samples from the Hornsby Bend site (Van Pelt, 2010). The $\tau - \gamma$ relationships obtained by converting the $G/G_{max} - \log\gamma$ relationships to $\tau - \gamma$ relationships are also shown in the same figure for comparison purposes. As seen in Figure 7.23, the $\tau - \gamma$ responses from the $G/G_{max} - \log\gamma$ relationships are stiffer at strains less than 0.5% compared to the triaxial results. However, as the confining pressure increases, the $\tau - \gamma$ responses from the $G/G_{max} - \log\gamma$ relationships at strains above about 1 to 2% are softer. Therefore, the $G/G_{max} - \log\gamma$ relationships need to be modified in the larger strain range. This modification is achieved by adjusting the "a" parameter

only in the larger strain range of the $G/G_{max} - \log\gamma$ relationships to match the triaxial results. The effect of the modified "a" parameter on the $G/G_{max} - \log\gamma$ relationships is shown in Figure 7.24. This adjustment of the "a" parameter consists of two parts:

(1) for $G/G_{max} \geq 0.4; a = 0.86 + 0.1\log\left(\frac{\sigma_0'}{P_a}\right)$ (7.4)

(2) for $G/G_{max} < 0.4; a = 0.773 - 0.0622\log\left(\frac{\sigma_0'}{P_a}\right)$ (7.5)

To avoid the discontinuity in the $G/G_{max} - \log\gamma$ relationships at $G/G_{max} = 0.4$, the "a" parameter is changed gradually from the original value to the modified value between $G/G_{max} = 0.4$ and $G/G_{max} = 0.3$. The $\tau - \gamma$ results from the CD triaxial tests and from the modified $G/G_{max} - \log\gamma$ relationships are presented in Figure 7.25. The modified $G/G_{max} - \log\gamma$ relationships are implemented into MoDaMP, which is now denoted as MoDaMP-1and the model with the modified relationships is used to predict the settlements of the footings to see the effect of the adjustment on footing settlements.

7.7.2.1 Settlement Predictions with modified $G/G_{max} - \log\gamma$ Relationships implemented in MoDaMP

The settlements predicted using the modified $G/G_{max} - \log\gamma$ relationships are shown in Figure 7.26. As seen in the figure, the predicted settlements for the 3-ft (0.91-m) diameter footing match the measured settlements quite well for all stress ranges considered. For the 1.5-ft (0.46-m) footing, the predicted settlements are higher than the measured settlements for all applied pressure ranges.

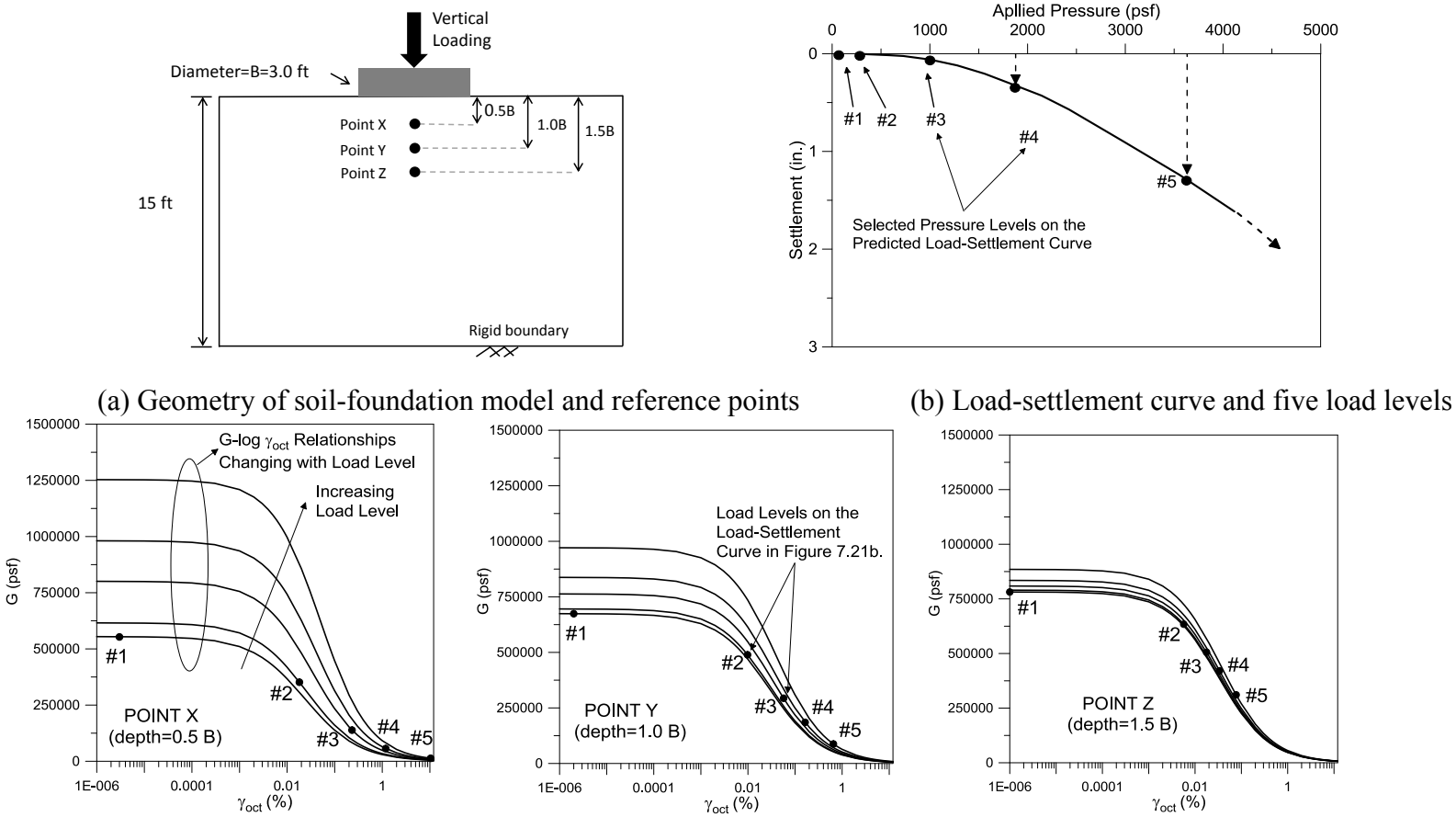

(a) Geometry of soil-foundation model and reference points

(b) Load-settlement curve and five load levels

(c) Secant Shear Modulus at Five Load Levels at Point X

(d) Secant Shear Modulus at Five Load Levels at Point Y

(e) Secant Shear Modulus at Five Load Levels at Point Z

Figure 7.21: Illustration showing how the modulus-strain relationships and secant shear moduli change in the numerical model during loading at three reference points beneath the 3.0-ft diameter footing at the Hornsby Bend site for HB-3.0-CP-mdf1

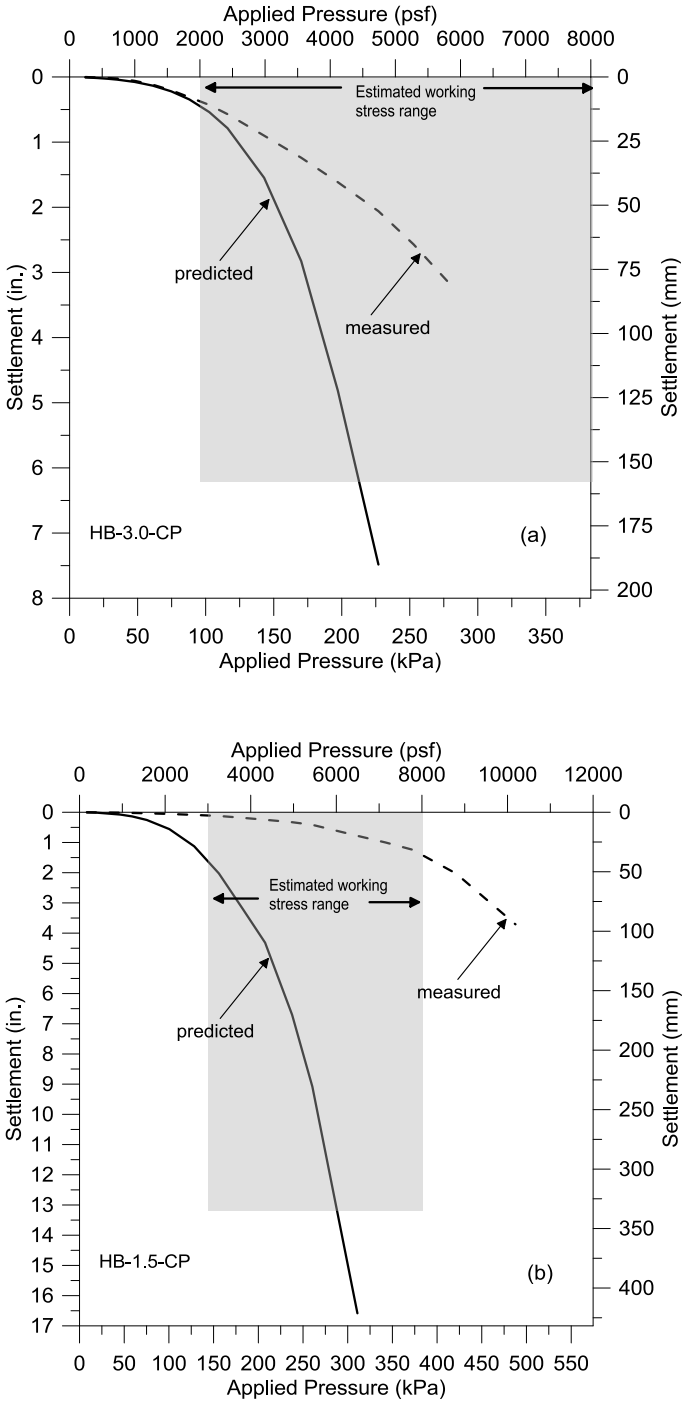

Figure 7.22: Predicted footing settlements using MoDaMP with an assumption of constant Poisson's ratio for (a) 3.0-ft (0.91-m) diameter footing and (b) 1.5-ft (0.46-m) diameter footing at the Hornsby Bend Site

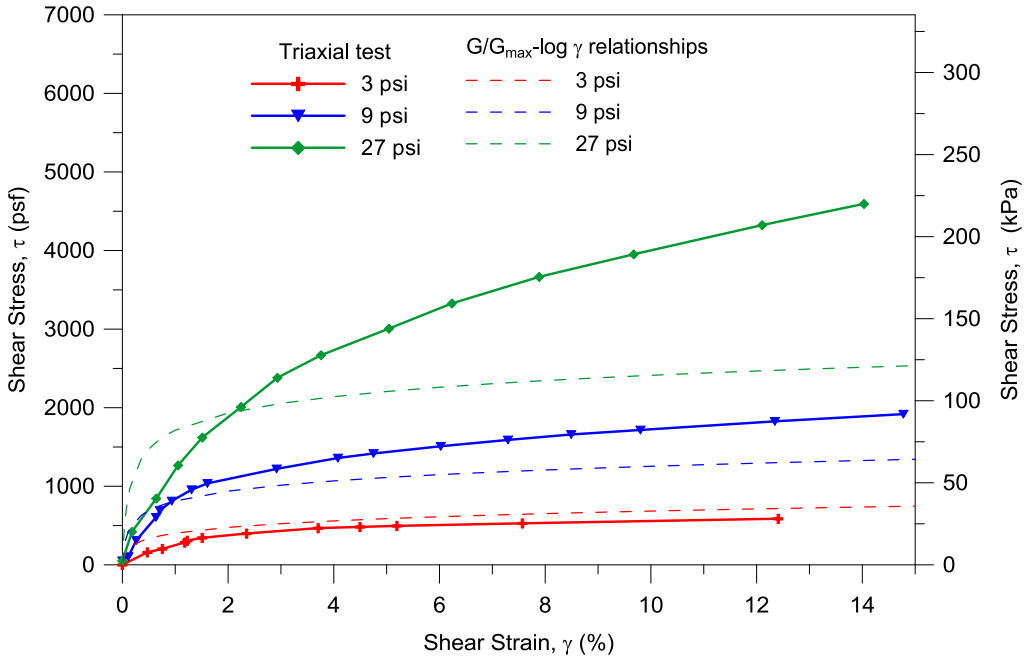

Figure 7.23: Comparison of shear stress-shear strain responses from the triaxial tests and from the $G/G_{max} - \log\gamma$ relationships

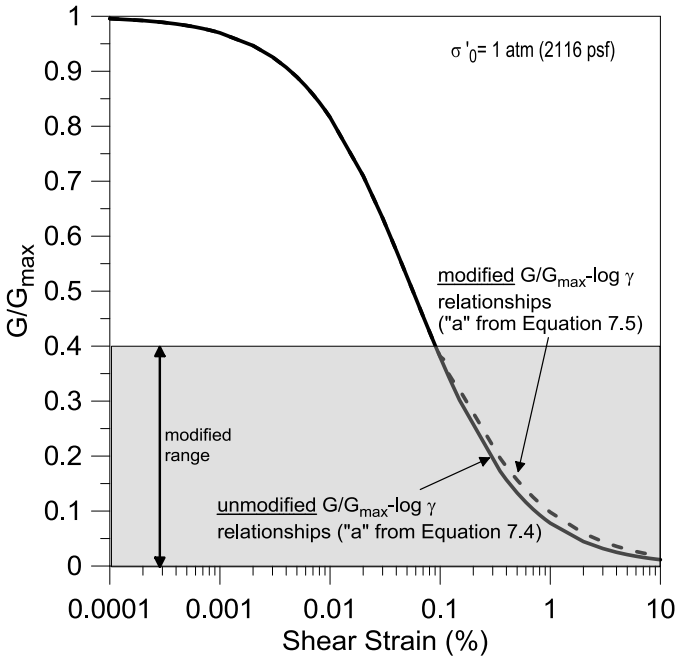

Figure 7.24: Comparison of unmodified and modified $G/G_{max} - \log\gamma$ relationships

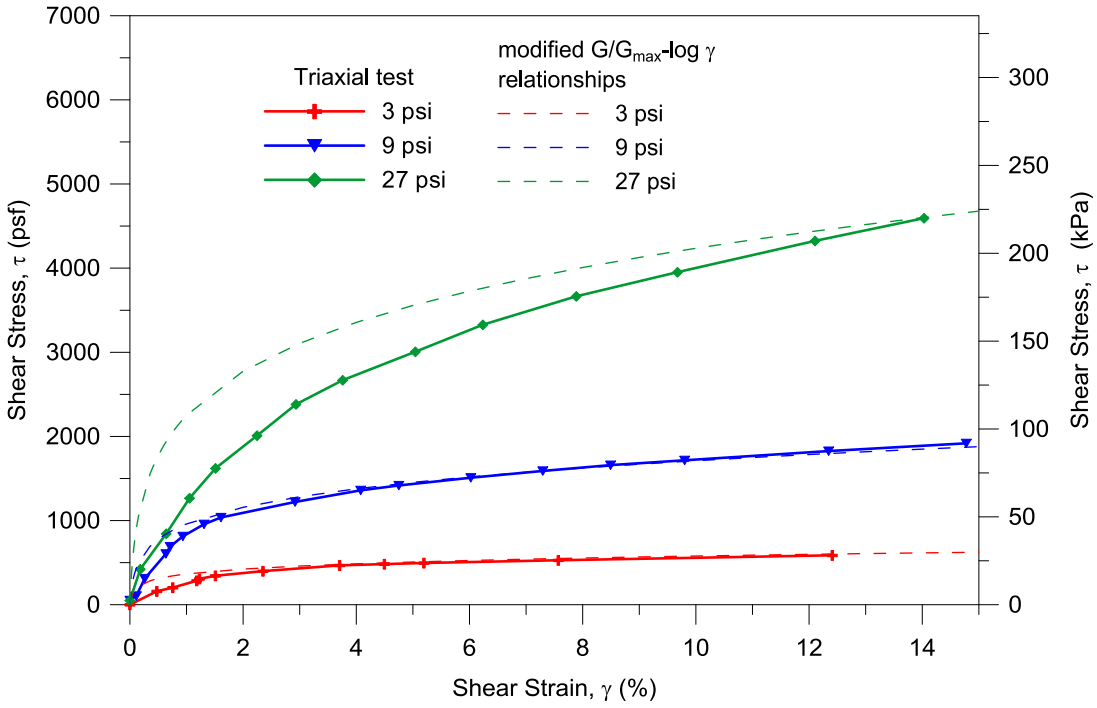

Figure 7.25: Comparison of shear stress-shear strain responses from the triaxial tests and from the modified $G/G_{max} - \log\gamma$ relationships

7.7.2.2 Vertical Strains beneath the 3-ft Diameter Footing

During footing construction at the Hornsby Bend site, tell-tales were installed at various depths to measure the displacements in the soil beneath the 3-ft (0.91-m) diameter footing. The measured vertical strains are compared with the predicted vertical strain profiles obtained using the modified $G/G_{max} - \log\gamma$ relationships. The predicted and measured vertical strains are presented in Figure 7.27. As seen in the figure, the general trend of the vertical strains matches well. However, the predicted maximum vertical strains are slightly smaller than the measured vertical strains.

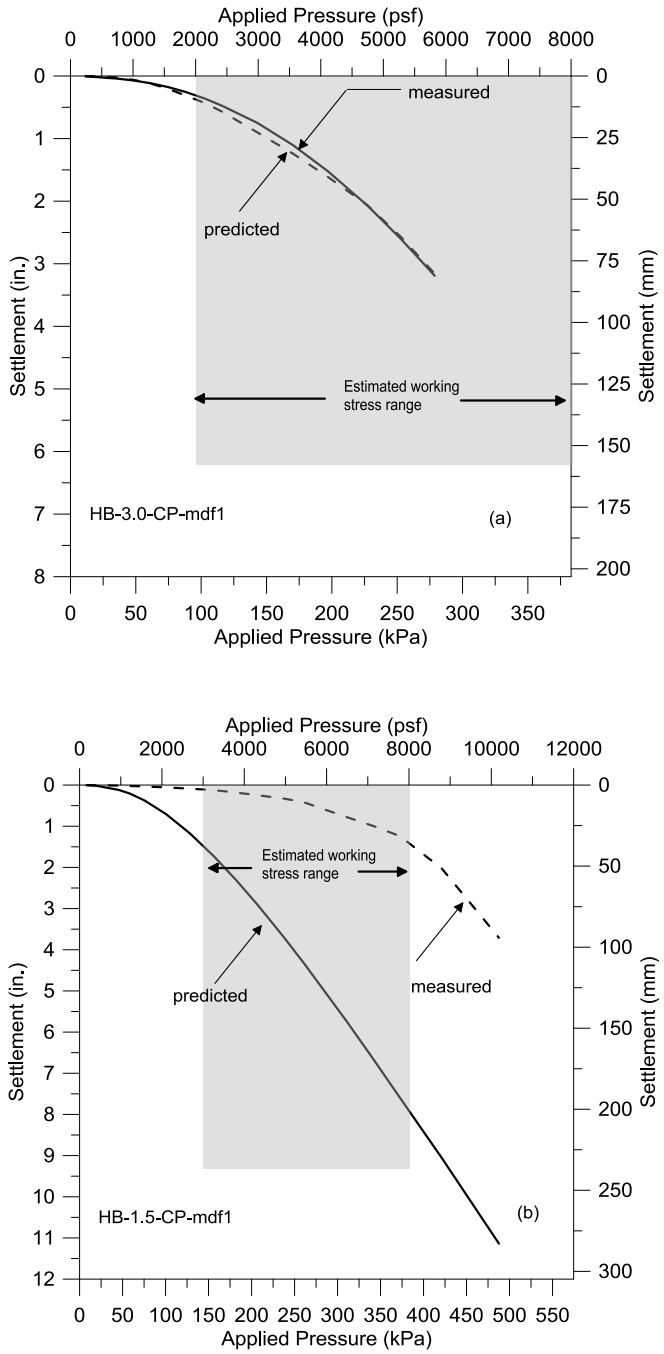

Figure 7.26: Predicted footing settlements using modified $G/G_{max} - \log\gamma$ relationships (MoDaMP-1) with a constant Poisson's ratio for (a) the 3.0-ft (0.91-m) diameter footing and (b) the 1.5-ft (0.46-m) diameter footing at the Hornsby Bend Site

7.7.3 Load-Settlement Predictions with CPT and SPT Based Methods

Schmertmann et al. (1978) and Burland and Burbidge (1985) methods presented in Chapter 2, are very commonly used in predicting the settlements of shallow footings. These methods are also used to predict the settlements of the small-scale footings at the Hornsby Bend site.

For the Schmertmann et al. (1978) method, the elastic modulus is calculated with $E = 2.5q_c$. The average tip resistance of the soil is assumed as 16 tsf (1.53 MPa) based on the CPT results presented in Figure 7.7. The upper 6 ft (1.83m) of the soil beneath the footings is divided into 5 layers and using Equations 2.6, 2.7 and 2.9, the settlements are predicted. Predicted settlements are compared with the measured settlements in Figure 7.28.

The Burland and Burbidge (1985) method utilizes SPT test results in the settlement predictions. Since no SPT tests were performed at the site, the SPT blow counts (N_{60}) were estimated from the correlation proposed by Robertson et al. (1983). In this correlation, the CPT results are used to find an estimate for the SPT blow count, N_{60}. The average CPT tip resistance and the mean grain size of the soil over the depth of influence, which is about 3 ft (0.91-m) for a 3-ft diameter footing, results in a SPT blow count of $N_{60} = 5$. Using Equation 2.10, the settlements are predicted and compared with the measure settlements in Figure 7.28 .It should be noted that in both methods there is a correction for the creep. However, the load-settlement tests were not continued long enough to investigate the creep. Therefore, creep is neglected in these predictions.

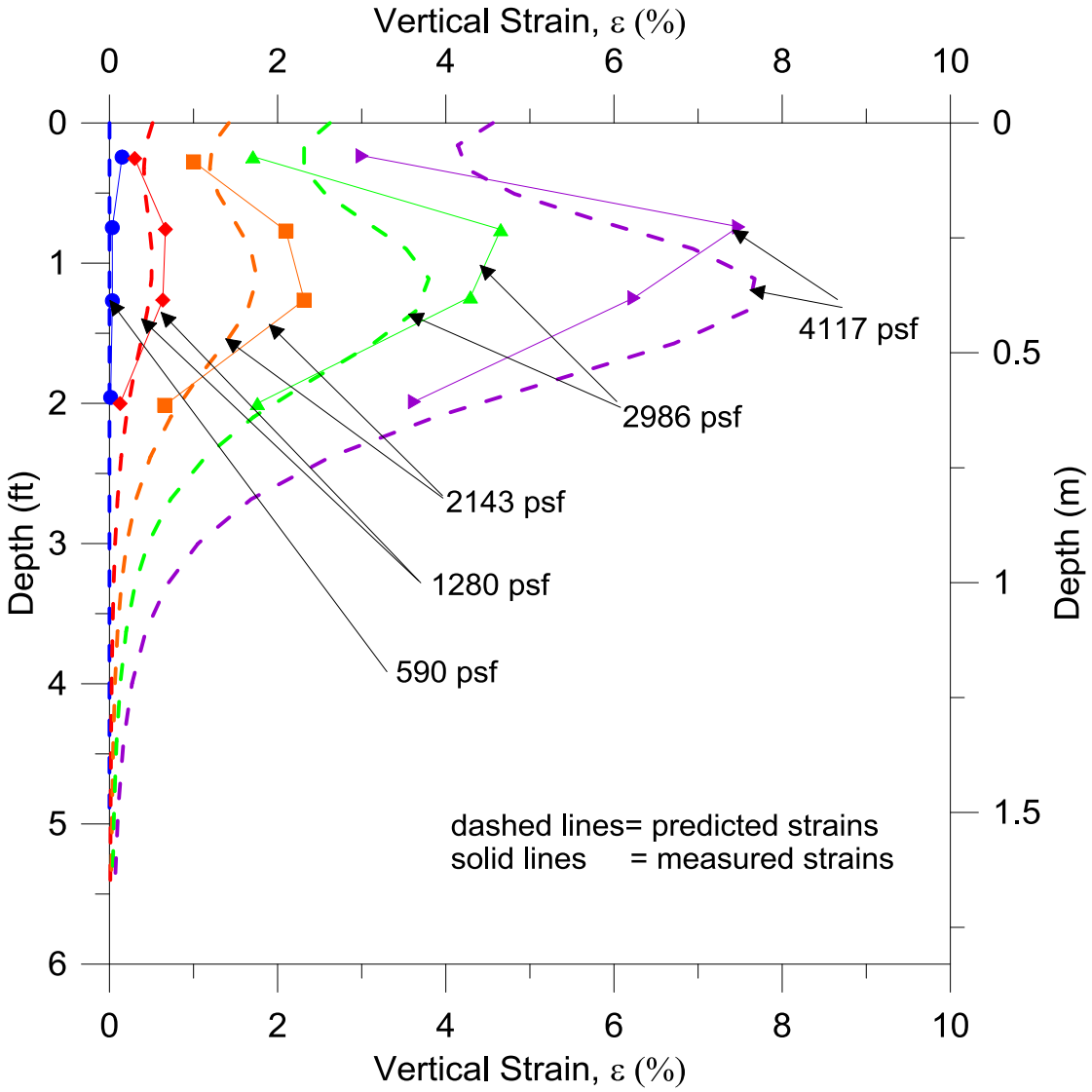

Figure 7.27: Predicted and measured vertical strains beneath the 3.0-ft diameter footing at the Hornsby Bend site

.

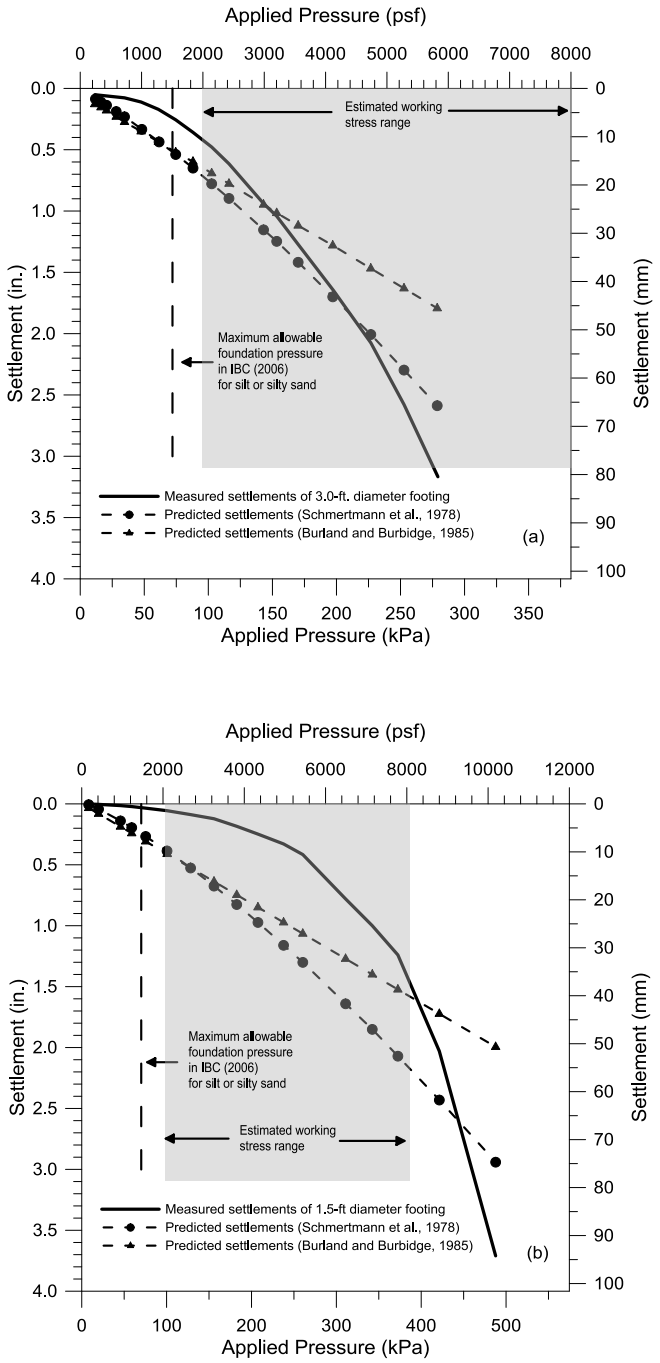

Figure 7.28: Settlements predicted using the Schmertmann et al. (1978) and Burland and Burbidge (1985) methods and their comparison with the measured settlements for (a) the 3.0-ft (0.91-m) diameter footing and, (b)1.5-ft (0.46-m) diameter footing at the Hornsby Bend site

7.7.4 Load-Settlement Predictions with varying Poisson's Ratio

In the previous settlement predictions, the Poisson's ratio was assumed constant for all strain ranges. On the other hand, the value of Poisson's ratio most likely increases with increasing shear strain levels as discussed in Chapter 4. In this section, the effect of the varying Poisson's ratio on the settlement prediction of the footings is investigated. The values of the Poisson's ratio are determined by following the procedures explained in Section 4.4. The settlements of the small-scale footings predicted by assuming a constant constrained compression modulus, M, are presented in Figure 7.29. The settlements predicted by assuming a constant bulk modulus, K, are shown in Figure 7.30.

As seen in the figures, the predicted settlements with the varying Poisson's ratio assumption are smaller than the predicted settlements with a constant Poisson's ratio assumption. This result can be attributed to the smaller volumetric strains occurring with the varying Poisson's ratio assumption.

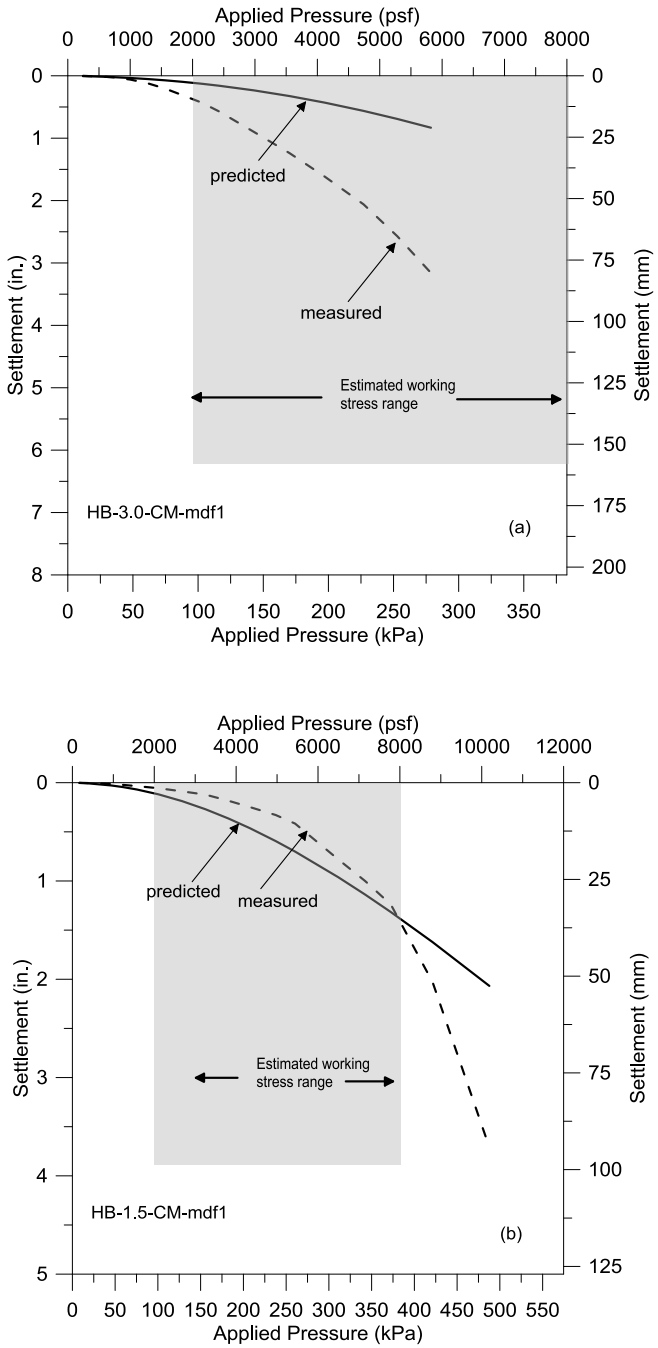

Figure 7.29: Predicted footing settlements with modified $G/G_{max} - \log\gamma$ relationships (MoDaMP-1) and a varying Poisson's ratio (M = constant) for (a) the 3.0-ft (0.91-m) diameter footing and (b) the 1.5-ft (0.46-m) diameter footing at the Hornsby Bend Site

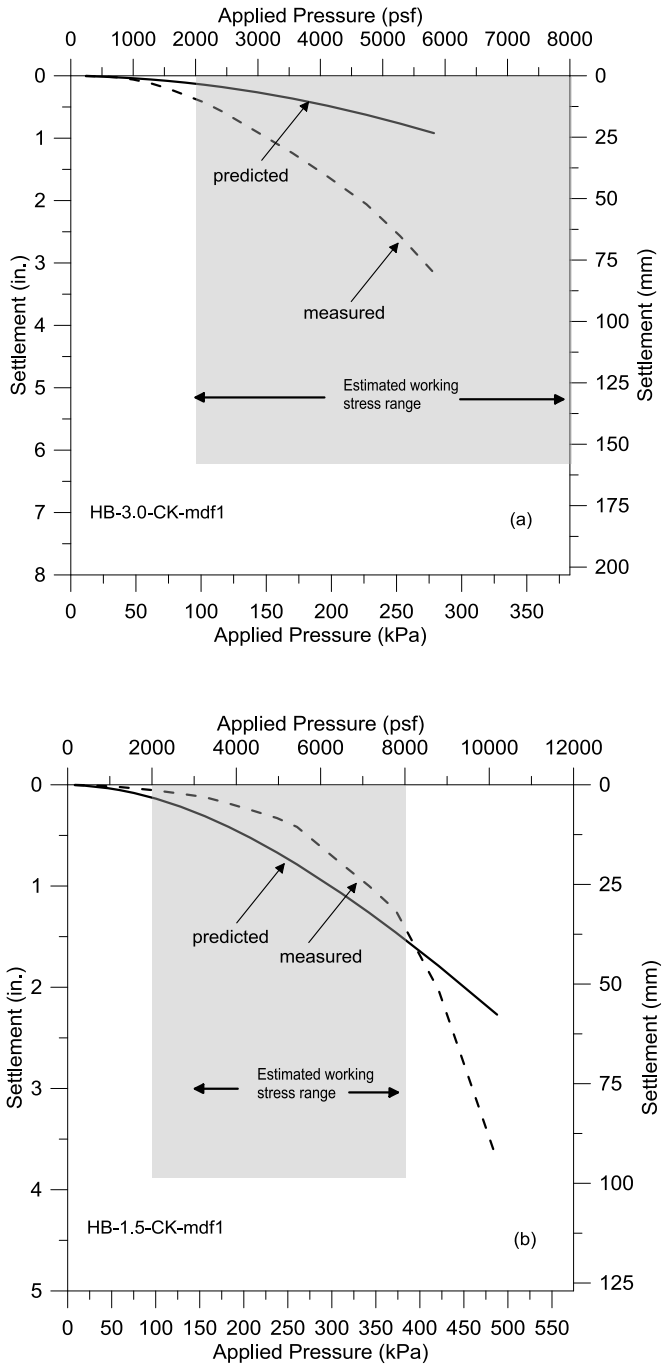

Figure 7.30: Predicted footing settlements with modified $G/G_{max} - \log\gamma$ relationships (MoDaMP-1) and a varying Poisson's ratio (K = constant) for (a) the 3.0-ft (0.91-m) diameter footing and (b) the 1.5-ft (0.46-m) diameter footing at the Hornsby Bend Site

7.8 SUMMARY

The load-settlement tests of two, small-scale footings at the Hornsby Bend site in Austin, Texas are discussed in this chapter. Laboratory tests were conducted in a study by Jeff Van Pelt (2010) to identify the general soil properties of the sandy silt at the site and strength parameters of the soil. Field testing at the site included CPT and SASW testing. SASW measurements were used then in the settlement prediction procedure to create representative shear wave velocity profiles. These profiles were obtained by developing $\log V_s - \log \sigma_0'$ relationships based on the average V_s profile and estimated mean effective confining pressures. Using the $\log V_s - \log \sigma_0'$ relationship, V_s at one atmosphere ($V_{s\,1atm}$) and the slope of the $\log V_s - \log \sigma_0'$ relationship were determined. Then $V_{s\,1atm}$ was converted to $G_{\max 1atm}$ and then used in the settlement analyses with MoDaMP.

The settlement predictions using the $G/G_{max} - \log \gamma$ relationships proposed by Menq (2003) result in higher values of the settlement at large strains compared to the measured settlements. Therefore, the $G/G_{max} - \log \gamma$ relationships were modified at large strains based on triaxial test results. The predictions using these modified relationships give a better match with the measured settlements, especially for the 3.0-ft (0.91-m) diameter footing.

The effect of the Poisson's ratio on the settlement predictions was investigated by varying the value of Poisson's ratio with increasing shear strain assuming that either: (1) the constrained compression modulus was constant or (2) the bulk modulus was constant. The effect of this assumption on Poisson's ratio is discussed in Chapter 4. The predictions with these assumptions are smaller compared to the constant Poisson's ratio assumption. The reason for this difference is the smaller volumetric strains due to the increased Poisson's ratio with the constant constrained compression modulus and bulk

modulus assumption. The predicted settlements give a better match for the 1.5-ft (0.46-m) diameter footing, however for the 3.0-ft (0.91-m) diameter footing; the predicted settlements are smaller than the measured values.

Chapter 8: Loading Tests at the Yucca Mountain Test Site

8.1 INTRODUCTION

The Department of Energy (DOE) selected Yucca Mountain in Nevada as the location of the long-term nuclear waste repository because of the geological formation, location and arid climate. Yucca Mountain is located on federal lands about 100 miles north west from Las Vegas, Nevada in a remote area, on the western edge of the Nevada Test site (Park, 2010). The location of Yucca Mountain is shown in Figure 8.1. The proposed geological repository is about 1,000 ft below the crest of the mountain. As part of extensive geological and geotechnical investigations at Yucca Mountain, dynamic field testing was conducted by Park et al. (2010) to evaluate the linear and nonlinear shear moduli of cemented alluvium at three locations. The studies conducted by Park (2010) were done in support of the design of surface facilities at Yucca Mountain Test Site (YMTS). As part of Park's studies, load-settlement tests were also performed which are analyzed in this chapter.

The geology and general soil properties at Park's test sites are discussed in Section 8.2.The dynamic field tests in the linear and nonlinear ranges include small-scale downhole and crosshole tests and SASW tests. These tests are presented in Section 8.3 and Section 8.4. Determination of representative $\log V_s - \log \sigma_o'$ relationships is also presented in Section 8.3. The static-load settlement tests conducted by Park (2010) and the resulting load-settlement curves are introduced in Section 8.5. Settlement predictions with MoDaMP for the small-scale footings at the YMTS are presented in Section 8.6. In Section, 8.7 a brief summary of the findings is given.

Figure 8.1: Location of Yucca Mountain, Nevada (from Park, 2010)

8.2 SOIL PROPERTIES AT THE YUCCA MOUNTAIN TEST SITE

The geologic formation of Yucca Mountain consists of layers of different types of volcanic rocks. The surface deposit in the north portal area where the small-scale footing test sites are located is naturally cemented alluvial materials. The thickness of the alluvium at the footing locations varies between about 150 ft (45.7 m) to 200 ft (61.0 m). To investigate the characteristics of the shallow cemented alluvium, three test pits, named Test Pit 5, Test Pit 6 and Test Pit 7, were excavated in the north portal area. Each pit was square in plan view with a side length of about 75 ft. Visual inspection of the exposed alluvium in the test pits showed that the alluvium consists mainly of coarse grained

particles, ranging from poorly graded sand to gravel with varying amounts of cobbles and boulders. The cementation of the soil is spatially variable based on the visual inspection. From sieve analyses of disturbed samples, it was found that the mean grain size (D_{50}) varies between 0.4-24.8 mm and the uniformity coefficient (C_u) varies between 16 and 86 (Park, 2010).

Due to the cementation and the inhomogeneity of the alluvium at Yucca Mountain, the soil behavior in the linear and nonlinear range is quite complex. The study conducted by Park et al. (2010) is important as it is only in-situ study on the nonlinear dynamic properties of cemented alluvium, to the best of the writer's knowledge.

8.3 Linear Seismic and Dynamic Tests at the Yucca Mountain Test Site

Field linear and nonlinear dynamic tests were conducted at three sites at YMTS in May through August, 2007 by Park et al. (2010). These tests were part of the soil characterization of the subsurface soil at the proposed locations of the surface facilities of the proposed permanent repository.

For the linear and nonlinear dynamic tests, small-scale concrete footings were constructed at Test Pit 6 (TP6), Test Pit 7 (TP7) and Lower Muck Yard (LMY). At each site, two footings were constructed; a 3-ft (0.91-m) and a 1.5-ft (0.46-m) diameter footing. Only the results for the 3-ft diameter footings are discussed herein. Also, only the 3.0-ft (0.91-m) diameter footings at TP6 and TP7 are studied. The 3.0-ft (0.91-m) diameter footing at LMY is not investigated since no test pit was dug at this site and it is more than 1000 ft (305 m) for Test Pits 6 and 7. Figure 8.2 shows the plan view and locations of the footings and the SASW tests at Test Pit 6 as an example. Small-scale downhole and crosshole tests were conducted at these three sites. The results of the crosshole tests are not discussed in Park (2010). The shear moduli in the linear range at

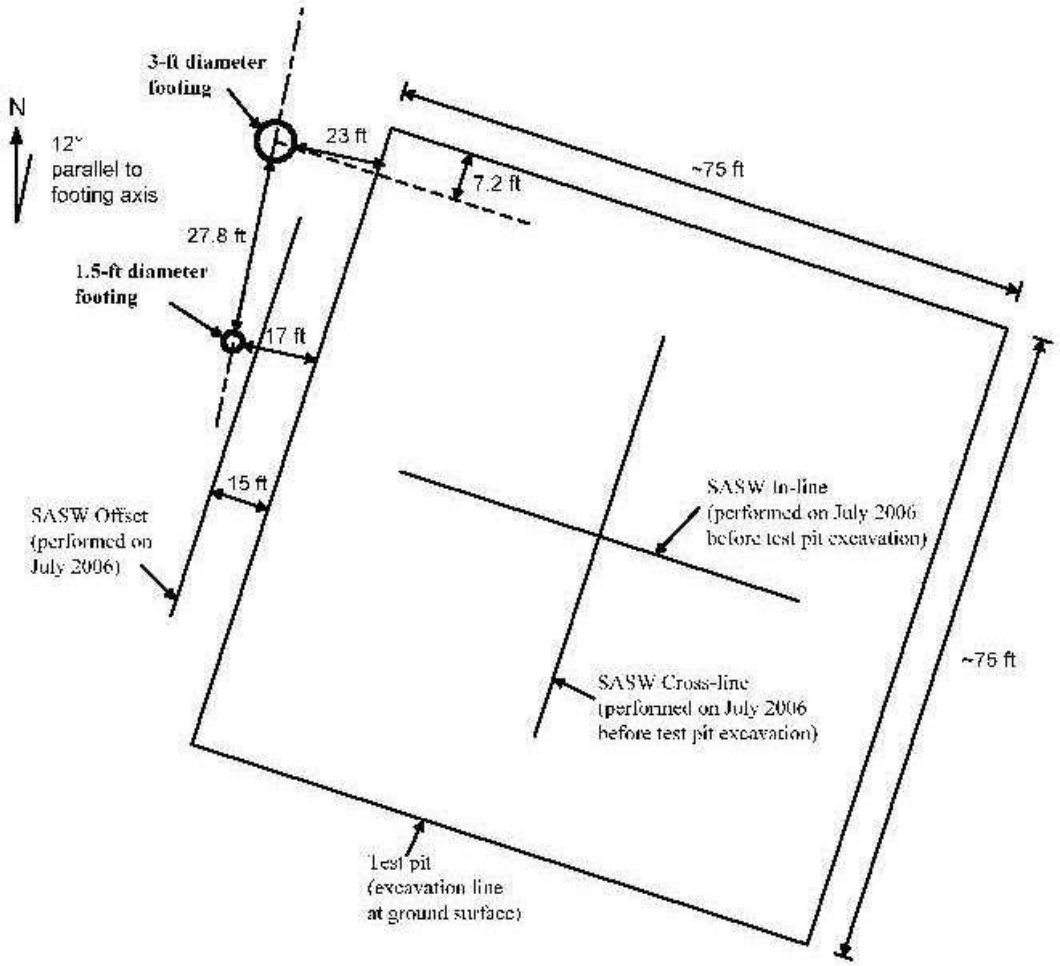

Figure 8.2: Plan view of Test Pit 6 (not to scale) (from Park, 2010)

Yucca Mountain are based on the downhole tests results presented by Park (2010). These results are also compared with the SASW test results.

8.3.1 Downhole Test Results

Shear and compression wave velocities were measured under varying static load levels applied to the concrete footings using geophones embedded beneath the footings at

various depths (6, 12, 18 and 24 in.) (15, 30, 46 and 61 cm). Details of the testing and data reducing procedure can be found in Park (2010).

The measured V_s and V_p values can be expressed as $\log V_s - \log \sigma_o'$ relationships to see the effect of confining pressure on V_s and V_p. Park calculated the vertical stresses beneath the footings by using the Boussinesq's stress distribution method and he expressed the effect of the pressure on V_s and V_p in terms of vertical stresses. In this study, a linear elastic material model was used to model the stress distribution beneath the foundations via PLAXIS. The stress distribution beneath the footings for a linear elastic medium is not stiffness dependent. Poisson's ratio (ν) is assumed to be 0.4. It should be noted that after determining the $\log V_s - \log \sigma_0$ and $\log V_p - \log \sigma_0$ relationships based on the horizontal and vertical stress distribution beneath the footings, the Poisson's ratio at small-strains range was calculated from V_s and V_p. The average values of ν for the footings at TP6, TP7 and LMY are 0.42, 0.40 and 0.30, respectively. To simplify the stress distribution analysis, the value of 0.4 was chosen.

The $\log V_s - \log \sigma_0$ and $\log V_p - \log \sigma_0$ relationships for Test Pit 6 are shown in Figures 8.3 and 8.4, respectively. As seen in the figures, two layers are identified for both and $\log V_s - \log \sigma_0$ and $\log V_p - \log \sigma_0$ relationships. For both layers, the n_s value is determined as 0.12 which indicates that the alluvium is cemented. The V_{s_1atm} value for the depths of 3 in. (8 cm) and 21 in. (53 cm) is 1950 fps (594 m/s) and for the depths of 9 in. (23 cm) and 15 in. (38 cm) is 1200 fps (366 m/s). This variation in V_{s_1atm} shows that the settlement prediction analyses with MoDaMP should be carried out with layers of soil extending from 0 in. to 6 in. (0 cm to 15 cm), from 6 in. to 12 in. (15 cm to 30 cm), from 12 in. to 18 in. (30 cm to 46 cm) and from 18 in. (46 cm) to the rigid boundary. The $\log V_s - \log \sigma_0$ and $\log V_p - \log \sigma_0$ relationships for Test Pit 7 are shown in Figures 8.5 and

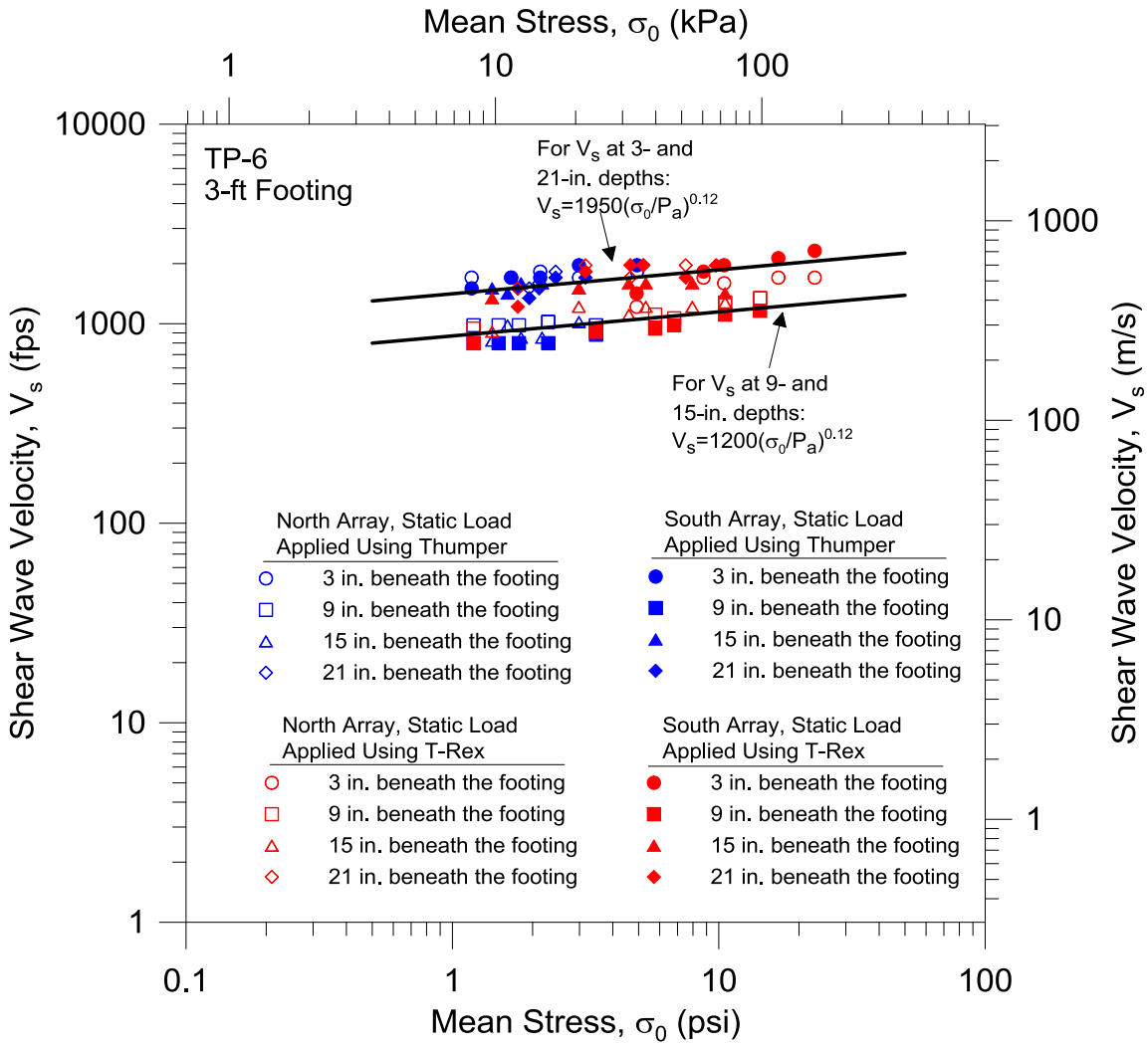

Figure 8.3: $\text{Log}\, V_s - \log \sigma_0$ relationships for Test Pit 6 obtained from small-scale downhole tests (after Park, 2010)

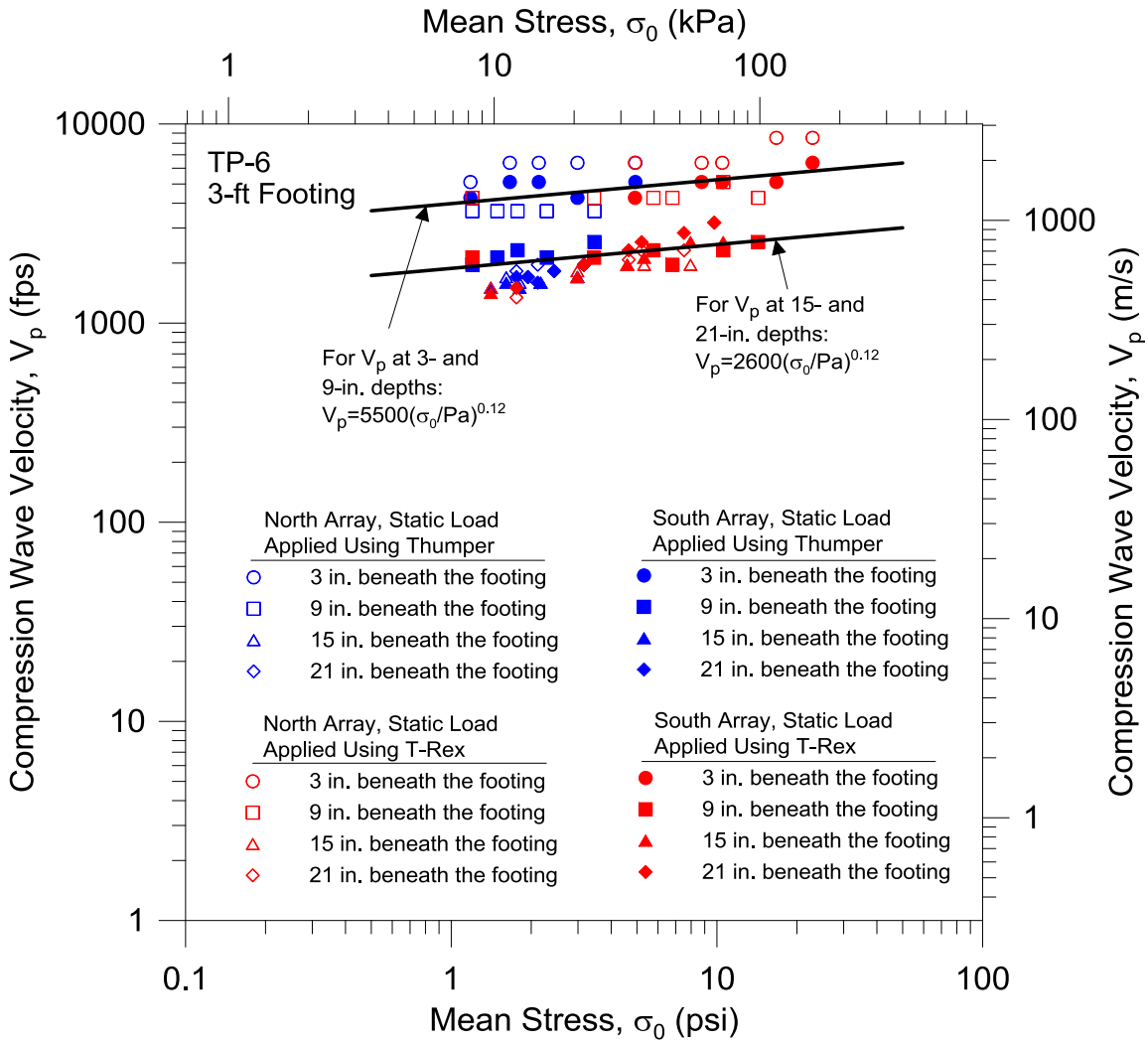

Figure 8.4: $\text{Log}\, V_p - \log \sigma_0$ relationships for Test Pit 6 obtained from small-scale downhole tests (after Park, 2010)

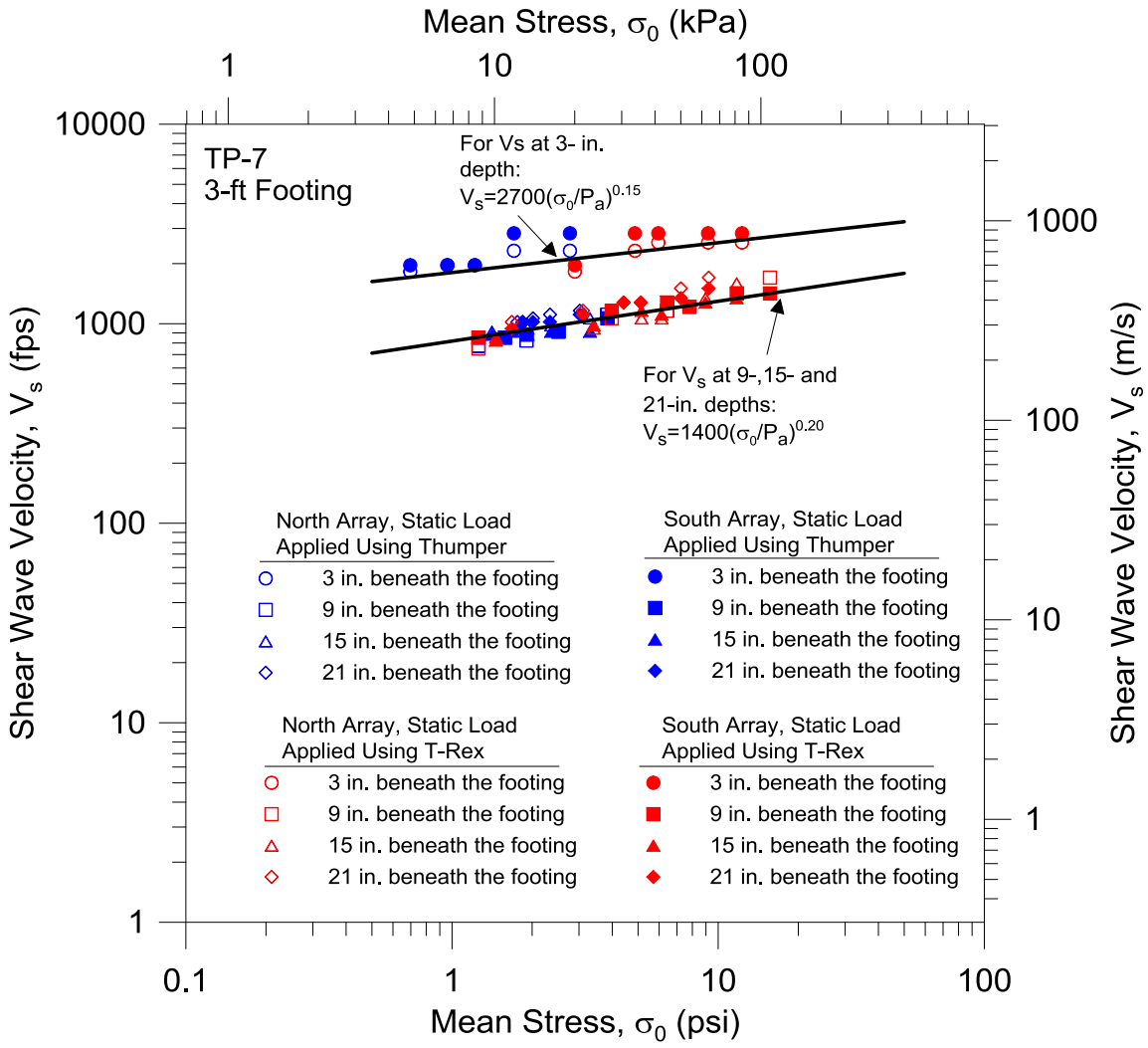

Figure 8.5: Log V_s – log σ_0 relationships for Test Pit 7 obtained from small-scale downhole tests (after Park, 2010)

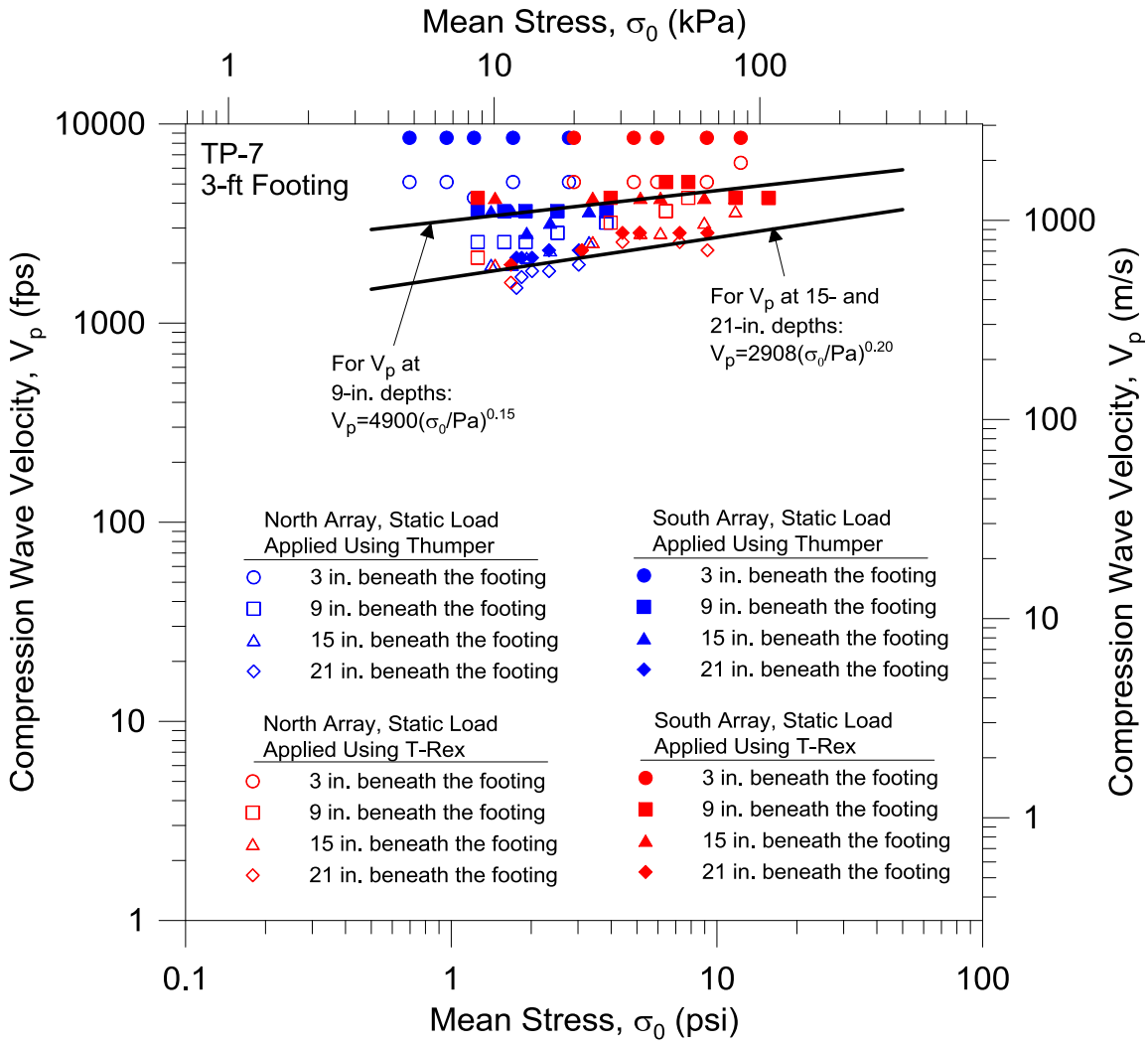

Figure 8.6: $\text{Log}\, V_p - \log \sigma_0$ relationships for Test Pit 7 obtained from small-scale downhole tests (after Park, 2010)

8.6, respectively. As seen in these figures, the $\log V_s - \log \sigma_0$ relationships indicate a two-layer system, where V_{s_1atm} for the first layer is 2700 fps (823 m/s) and for the second layer V_{s_1atm} is 1400 fps (427 m/s). This variation in V_{s_1atm} also shows that the soil near the surface is stiffer, likely due to higher cementation. It should also be noted that the $\log V_p - \log \sigma_0$ relationship for the first layer is omitted since the V_p measurements for this layer are affected by the concrete footing and the measurements are too high and the slope of the $\log V_p - \log \sigma_0$ relationship is too low to be cemented alluvium. Instead a value for Poisson's ratio of 0.46 was assumed.

For each layer, the small-strain Poisson's ratio was calculated by using Equation 4.7 using the V_s and V_p measurements. It should be noted that in order to determine the Poisson's ratio from V_s and V_p measurements, the slope of the $\log V_s - \log \sigma_0$ and $\log V_p - \log \sigma_0$ relationships (n_s) should be equal.

As discussed above, the mean stresses beneath the footings were calculated by using a linear elastic finite element analysis. Park (2010) presented the effect of the pressures at which the V_s and V_p measurements were made in terms of vertical stresses rather than mean stresses. To compare these two different ways of presenting the pressure dependency of V_s and V_p, $\log V_s - \log \sigma_v$ and $\log V_p - \log \sigma_v$ relationships presented by Park (2010) for Test Pit 7 are given in Figures 8.7 and 8.8, respectively. By using σ_v , V_{s_1atm} for the first layer is 2612 fps (796 m/s) but is 2700 fps (823 m/s) for σ_0, and V_{s_1atm} for the second layer is 1298 fps (395 m/s) but is 1400 fps (427 m/s) for σ_0. Moreover, n_s values are close as expected, 0.15 for the first layer for both σ_0 and σ_v cases, and 0.20 and 0.15 for the second layer, for σ_0 case and σ_v case , respectively.

In addition to the small-scale downhole tests, 11 fixed- free resonant column (RC) tests were conducted at the University of Texas to characterize the cemented alluvium at

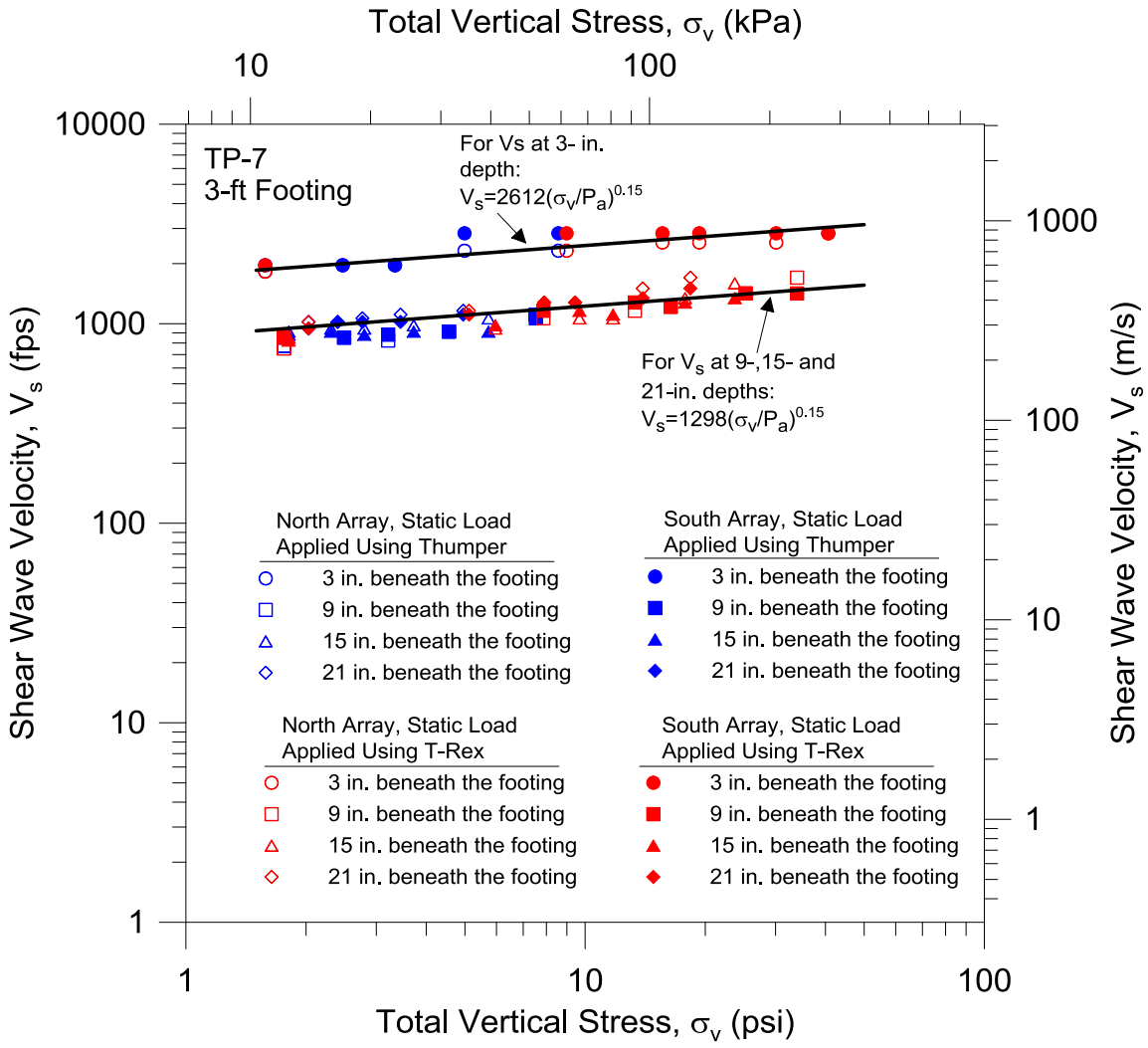

Figure 8.7: Log V_s – log σ_v relationships for Test Pit 7 obtained from small-scale downhole tests (after Park, 2010)

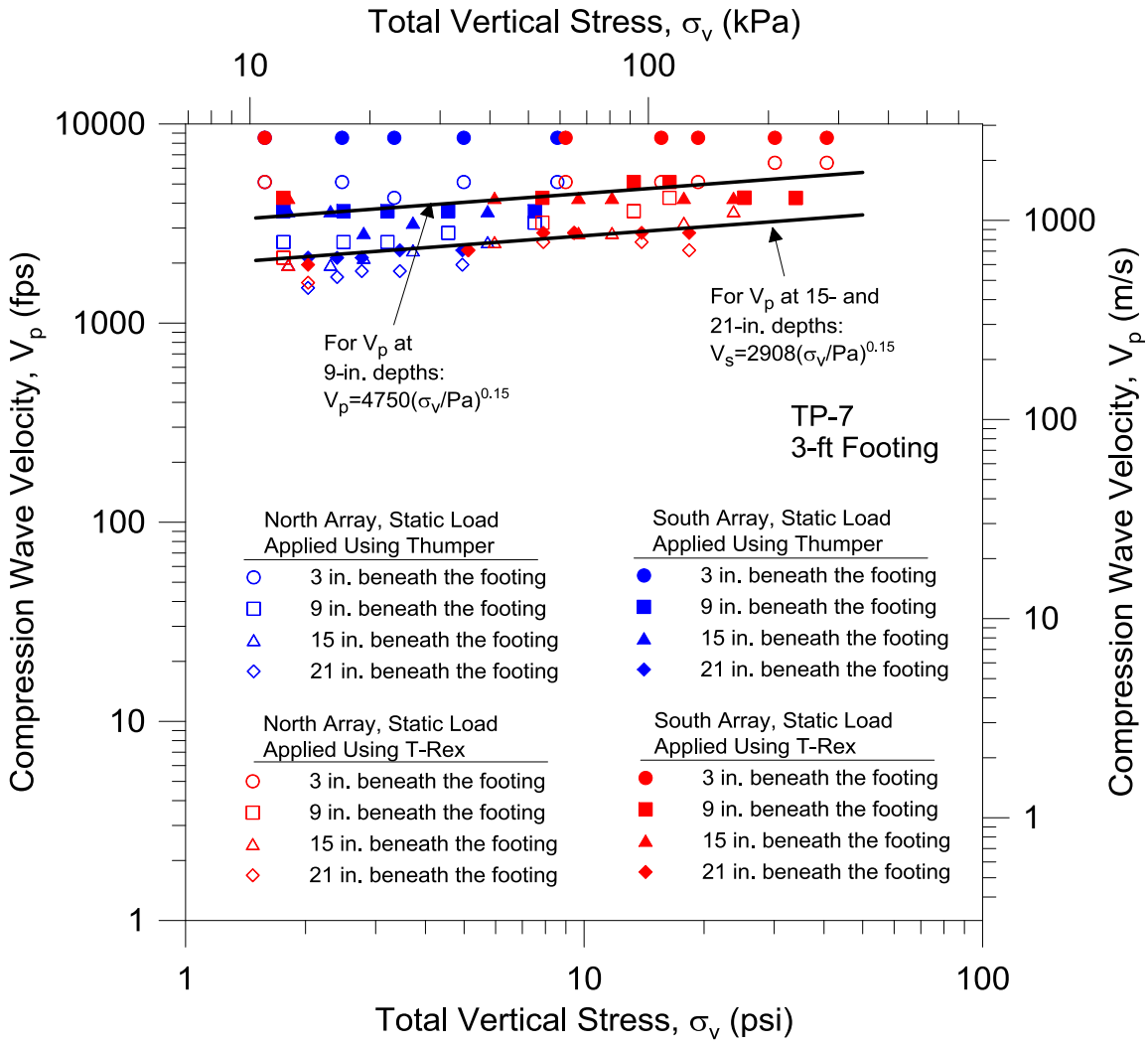

Figure 8.8: Log V_p – log σ_v relationships for Test Pit 7 obtained from small-scale downhole tests (after Park, 2010)

small-strain ranges. The sampling process to obtain undisturbed samples was extremely difficult and this process was achieved at a great cost (Schuhen, 2009). The V_s measurements of the cemented intact samples from the RC tests in the small-strain range are presented in Figure 8.9. The $\log V_s - \log \sigma_v$ relationships obtained from these tests are grouped into three categories: Group 1 is the stiffest alluvium, Group 2 is the slightly less stiff alluvium and Group 3 is the softest alluvium. As seen in the Figure 8.9, Group 1 has the smallest slope (n_s), 0.09, indicating stronger effect of cementation. Group 3 has $n_s = 0.16$ which is in the range of the n_s values obtained from small-scale downhole tests.

8.3.2 SASW Test Results

Spectral-Analysis-of-Surface-Waves (SASW) tests were also conducted at the proposed test-pit locations before they were excavated to investigate the small-strain shear wave velocity profile of the cemented alluvium in the test pits. Figure 8.10 presents the results of the SASW tests for TP 6 and TP 7. The shear wave velocities at both sites range between approximately 300 and 1600 fps (91 and 488 m/s). The shear wave velocity (V_s) profile at Test Pit 6 based on the $\log V_s - \log \sigma_v$ relationships obtained from the small-scale downhole tests are presented in Figure 8.11. Based on the $\log V_s - \log \sigma_v$ relationships shown in Figures 8.3, the V_s profile from the small-scale downhole tests is divided into three layers. The shear wave velocity (V_s) profile at Test Pit 7 based on the $\log V_s - \log \sigma_v$ relationships obtained from the small-scale downhole tests are presented in Figure 8.12. Similar to Test Pit 6, the V_s profile from the small-scale downhole tests is divided into two layers, based on the $\log V_s - \log \sigma_v$ relationships shown in Figures 8.5. As seen in Figure 8.11, V_s profile compare reasonably at depths up to 4 ft (1.2 m), but at greater depths than 4 ft (1.2 m), V_s values are higher from the small-scale downhole tests.

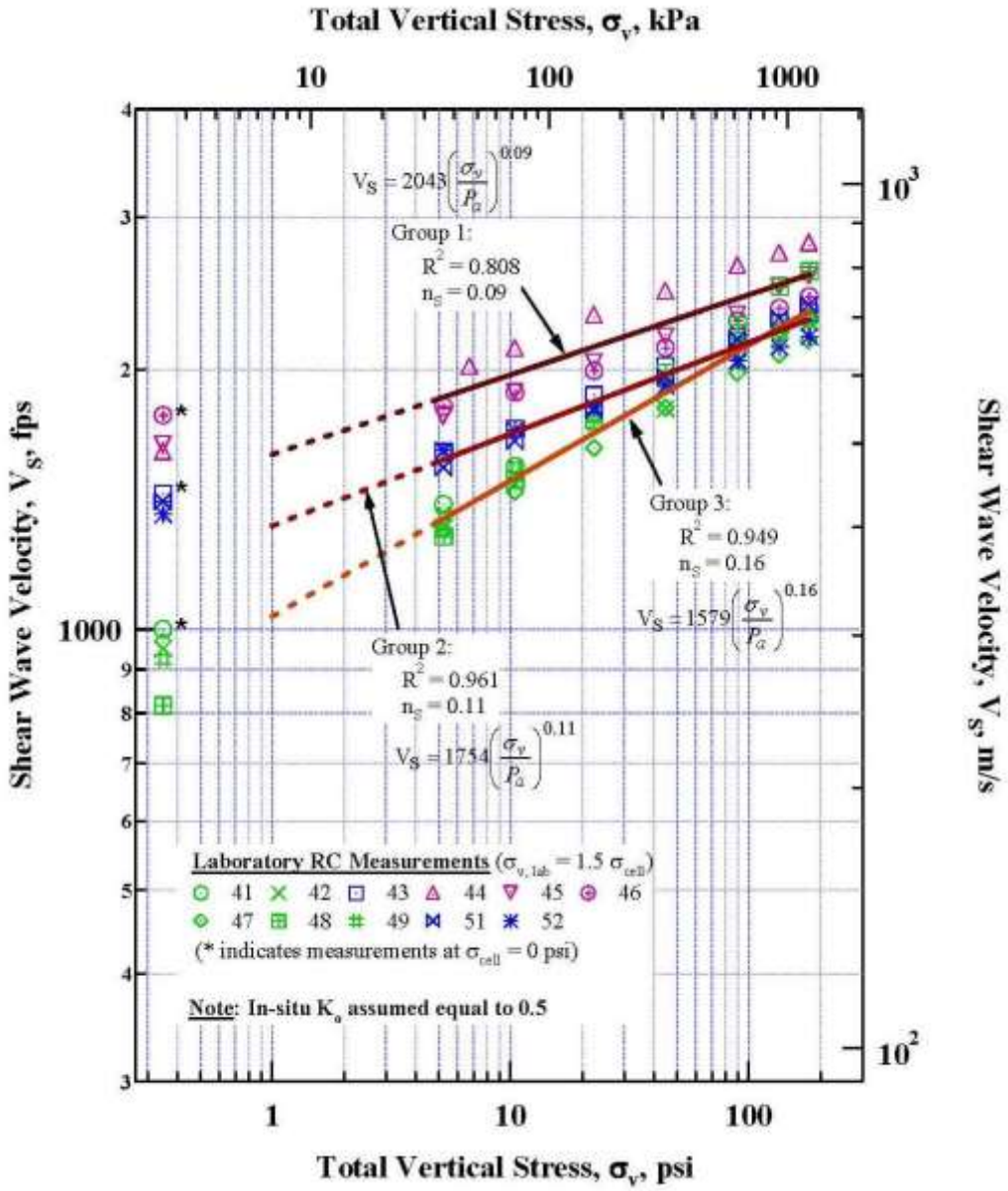

Figure 8.9: $\text{Log}\, V_s - \log \sigma_v$ relationships measured with the RC tests on 11 intact alluvium specimens (from Park, 2010, modified from Schuhen, 2009)

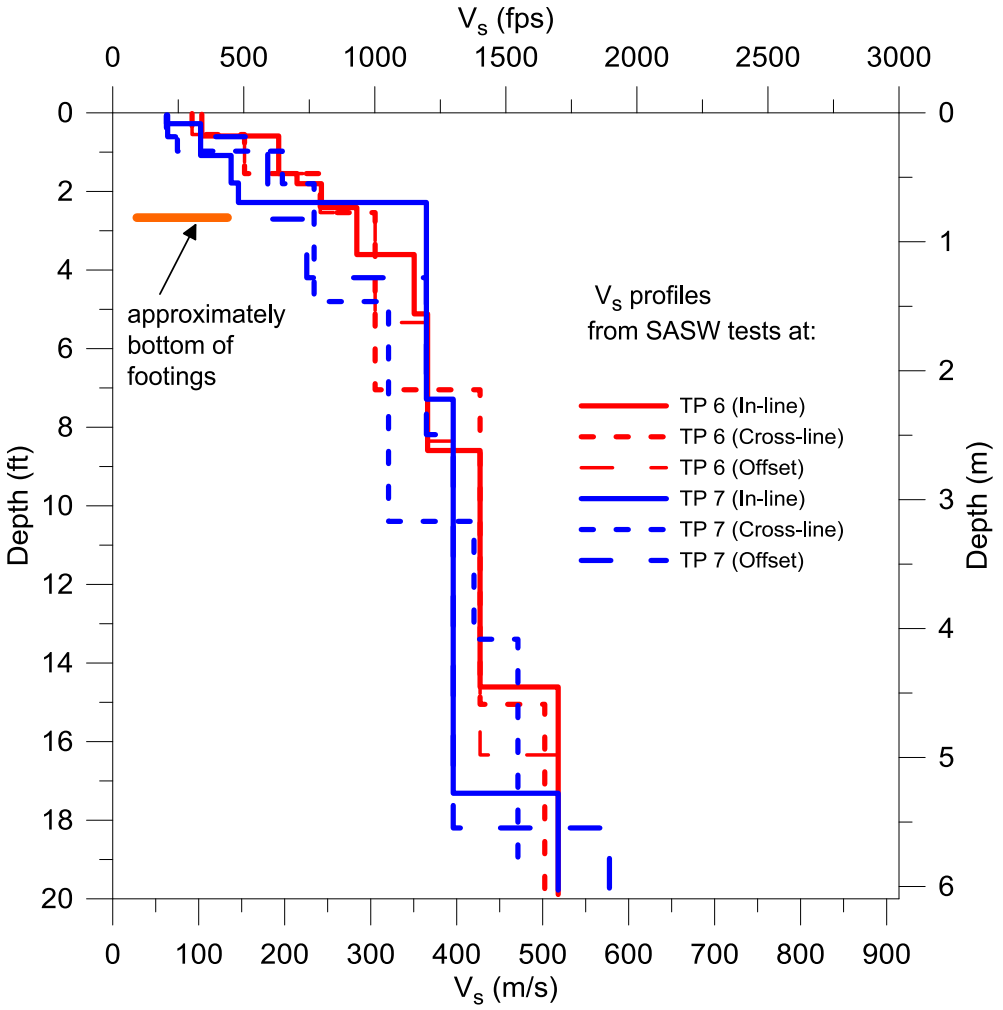

Figure 8.10: V_s profiles determined from SASW measurements at TP 6 and TP 7 sites (after Park, 2010)

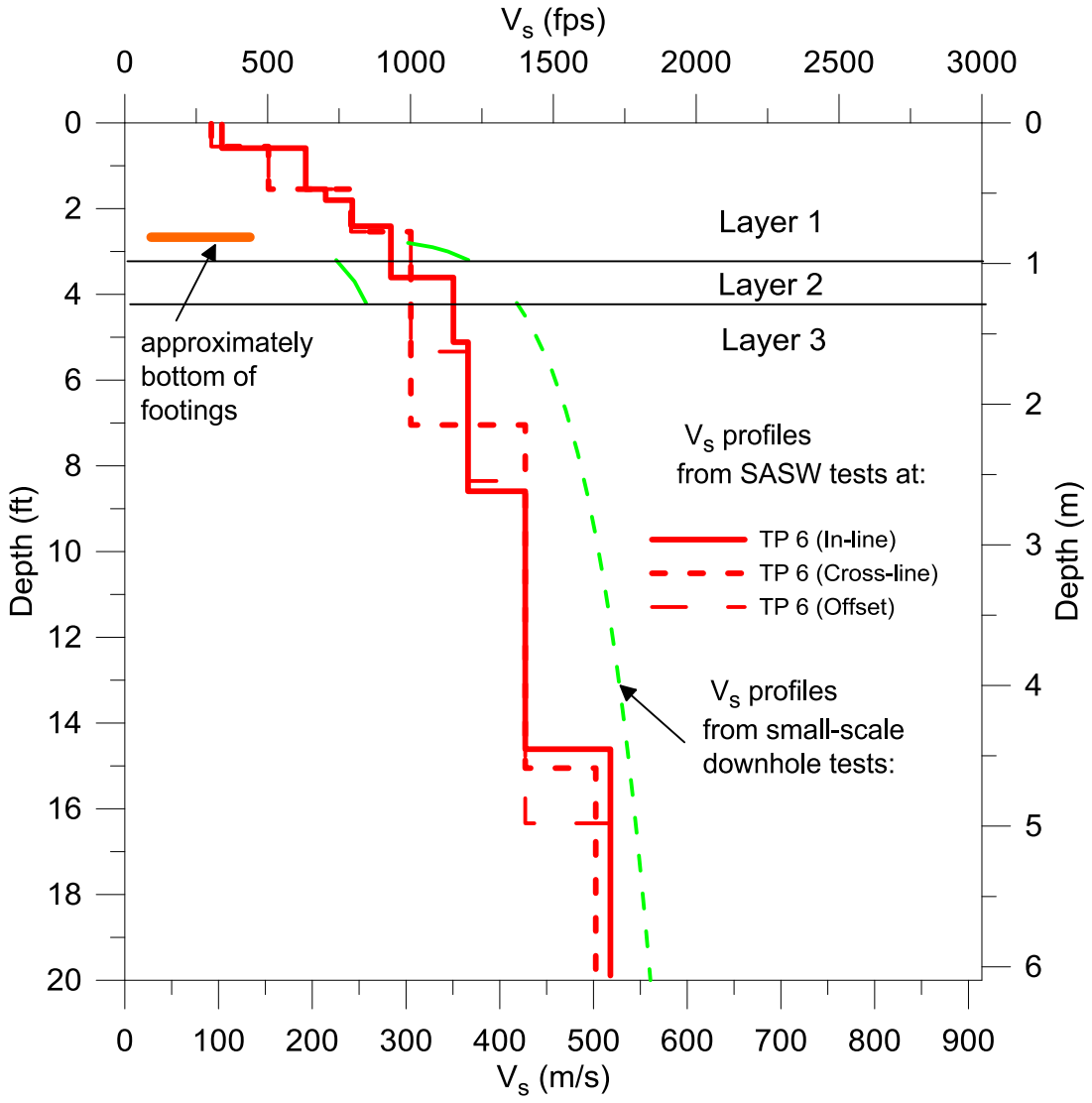

Figure 8.11: Comparison of V_s profiles determined from SASW measurements at TP 6 and with V_s profiles determined from the small-scale downhole measurements beneath the 3.0-ft (0.91-m) diameter footing

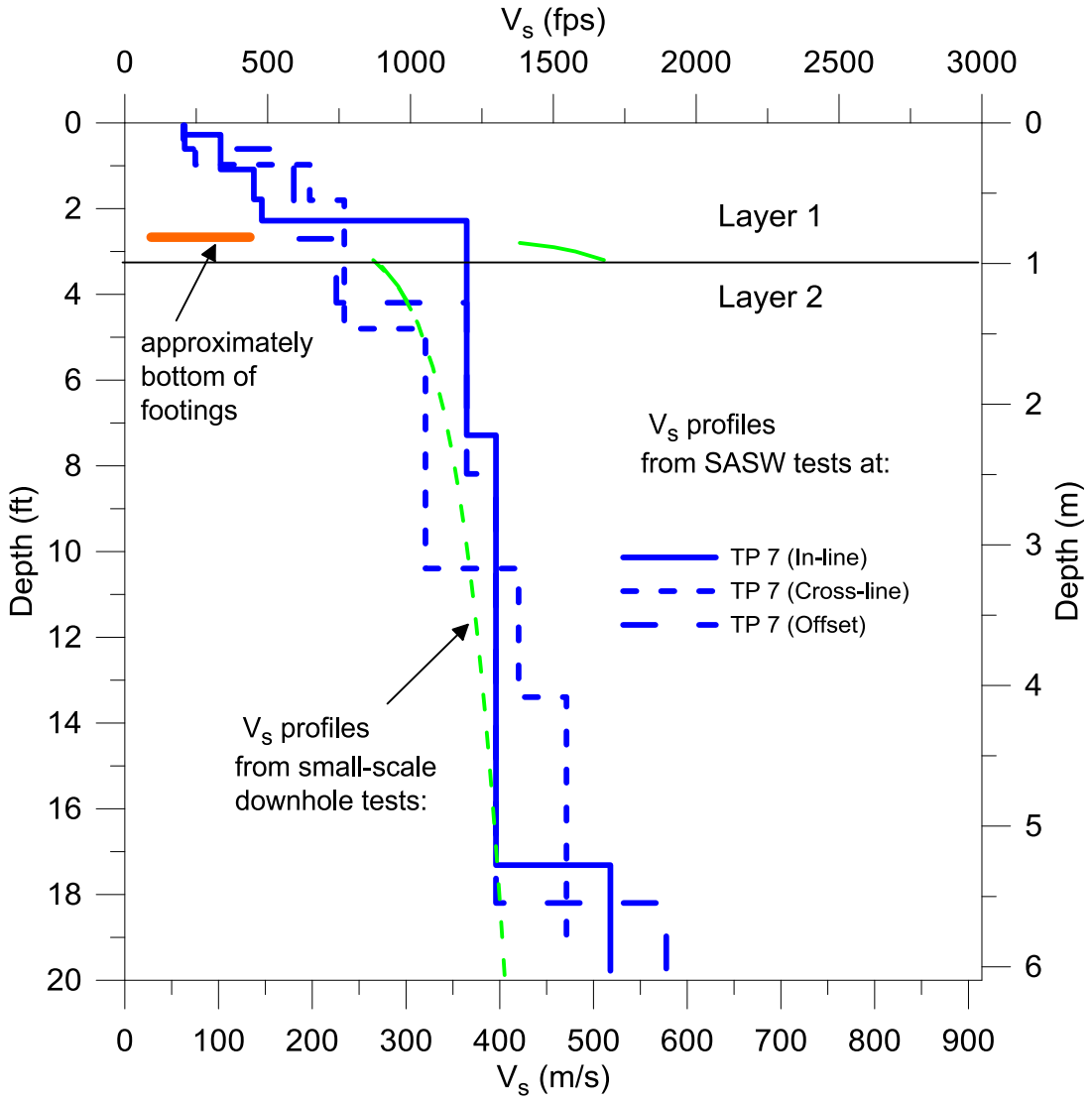

Figure 8.12: Comparison of V_s profiles determined from SASW measurements at TP 7 and with V_s profiles determined from the small-scale downhole measurements beneath the 3.0-ft (0.91-m) diameter footing

It should be noted that the downhole tests are conducted up to a depth of 21 in. (53 cm) beneath the footings, and the values at greater depths are extrapolated based on the V_s values at this depth. For Test Pit 7, V_s profile from downhole tests at the upper 0.5 ft. beneath the footing are higher, however below 0.5 ft, V_s values from the small-scale downhole tests and SASW tests are similar.

The V_s profiles from the small-scale downhole tests are used in the settlement prediction analyses of the 3-ft (0.91-m) diameter footings at TP 6 and TP 7. The reason for choosing the small-scale downhole test measurements for the settlement prediction analyses is that the downhole measurements have a higher resolution compared to SASW tests since the SASW measurements average the V_s.

8.4 NONLINEAR SEISMIC AND DYNAMIC TESTS AT THE YUCCA MOUNTAIN TEST SITE

8.4.1 Steady-State Dynamic Tests

The results of the steady-state dynamic tests at Lower Muck Yard and Test Pit (TP 7) conducted by Park (2010) are presented in Figures 8.13. The details of the testing and data reducing processes can be found in Park (2010). The dynamic tests are conducted at two different static load levels, ~ 4000 lbs (2 tons) and ~ 8000 lbs (4 tons), at the Lower Muck Yard. At Test Pit 7, only a static load level of ~ 4000 lbs was used. The results of the steady-state nonlinear dynamic tests show that the $G/G_{max} - \log\gamma$ curves are slightly more nonlinear for the static load level of ~ 8000 lbs. The reason or reasons for this difference are not known but could be the result of breakage of cementation bonds with increased load levels, general scatter in these tests in such difficult to test materials or other causes.

The $G/G_{max} - \log\gamma$ model proposed by Darendeli (2001) was fitted to the data. The fitted curves are shown in Figure 8.13 along with the data. The values of parameters obtained with the Darendeli (2001) model also indicate that the cemented alluvium is more nonlinear than uncemented sand; that is γ_r at $\sigma_v =$ 5 psi (34.5 kPa) averages about 0.012% for TP7 and Lower Muck Yard while the Darendeli curve for sand at $\sigma_v =$ 5 psi and $K_o = 0.5$ is 0.022%.

High-amplitude resonant column (RC) tests were performed on intact specimens recovered from the test pits at three different confining pressures, σ_0 ($\sigma_0 = 15$, 30 and 90 psi) ($\sigma_0 = 103$, 207 and 620 kPa). The highest strain levels that could be excited in the specimen varied from ~ 0.002 to ~0.01 %, depending on the confining pressure and the stiffness of the specimen. The results of these tests are shown in Figure 8.14. As seen in the figure, the $G/G_{max} - \log\gamma$ curves in the RC tests are more linear compared to those from steady-state dynamic tests in the field. The reason for this difference is thought to be that the intact specimens tested in the RC tests do not represent the whole soil body because they are stiffer than the alluvium in the field. The Darendeli (2001) model was also fit to the data from the RC tests and the resulting γ_r and a values are also presented in Figure 8.14.

The $G/G_{max} - \log\gamma$ curves from RC tests show that γ_r is confining pressure dependent. Best-estimate $G/G_{max} - \log\gamma$ curves which take the pressure dependency into account that is shown in the RC tests and also take the higher nonlinearity into account based on the field tests, are shown in Figure 8.15. The reference strain, γ_r, versus the confining pressure, σ_0, relationship from these best estimate curves are shown in Figure 8.16. This relationship is given by:

$$\gamma_r = 0.00166\left(\frac{\sigma_0}{P_a}\right) + 0.0101\ \% \tag{8.1}$$

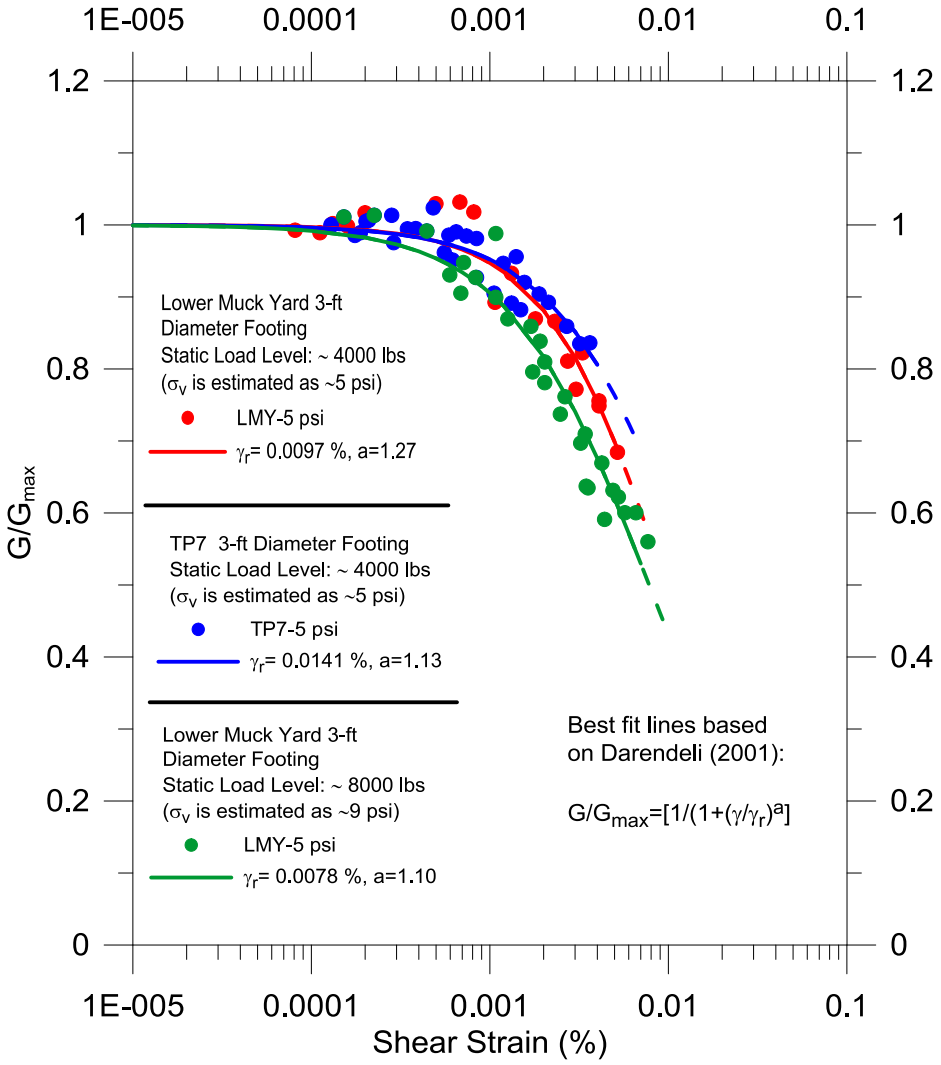

Figure 8.13: $G/G_{max} - \log\gamma$ relationships obtained from steady-state dynamic tests at Lower Muck Yard and Test Pit 7 and the best fit curves to the data with Darendeli (2001) model (from Schuhen, 2009)

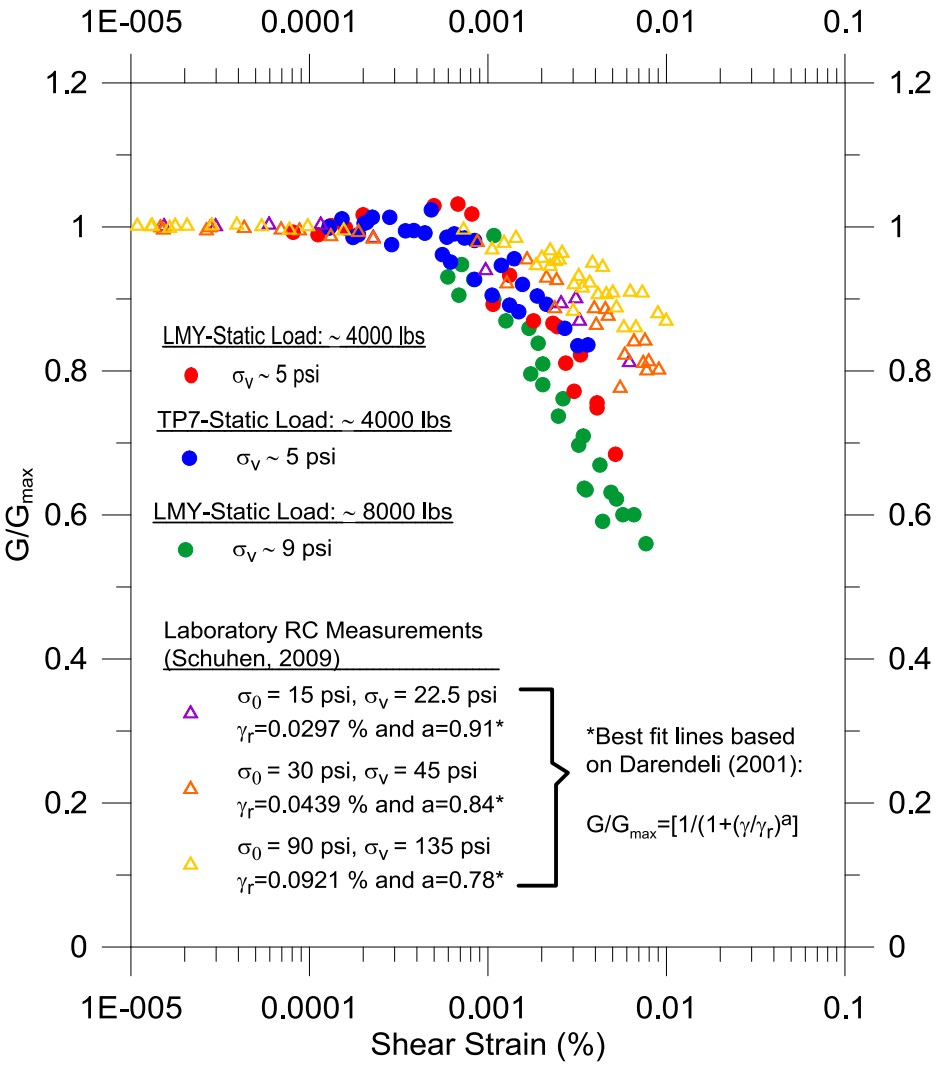

Figure 8.14: $G/G_{max} - \log\gamma$ relationships obtained from steady-state dynamic tests at Lower Muck Yard and Test Pit 7 and from RC tests (Park, 2010 and Schuhen, 2009)

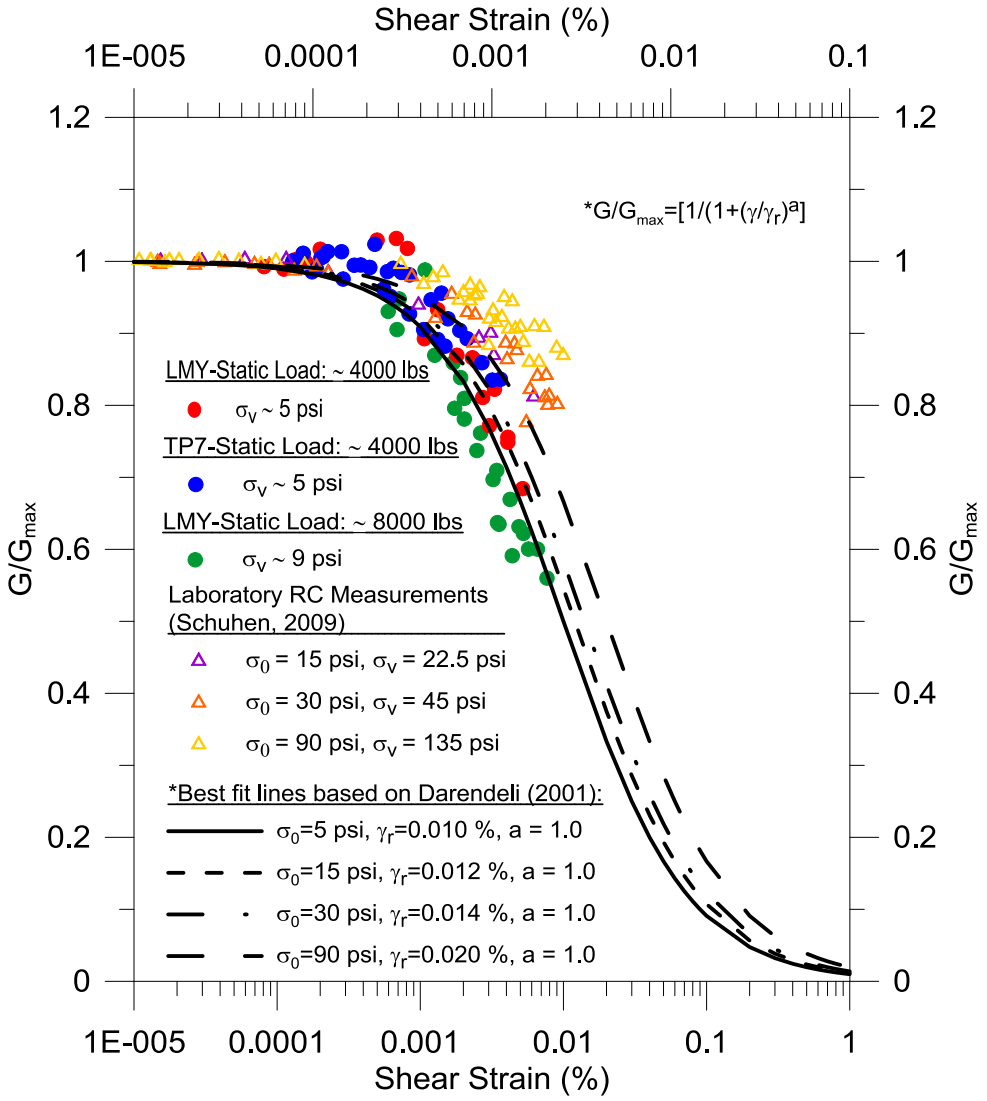

Figure 8.15: Best-estimate $G/G_{max} - \log\gamma$ curves determined by combining the steady-state dynamic tests in the field at Lower Muck Yard and Test Pit 7 with the results from laboratory RC tests on intact alluvial specimens

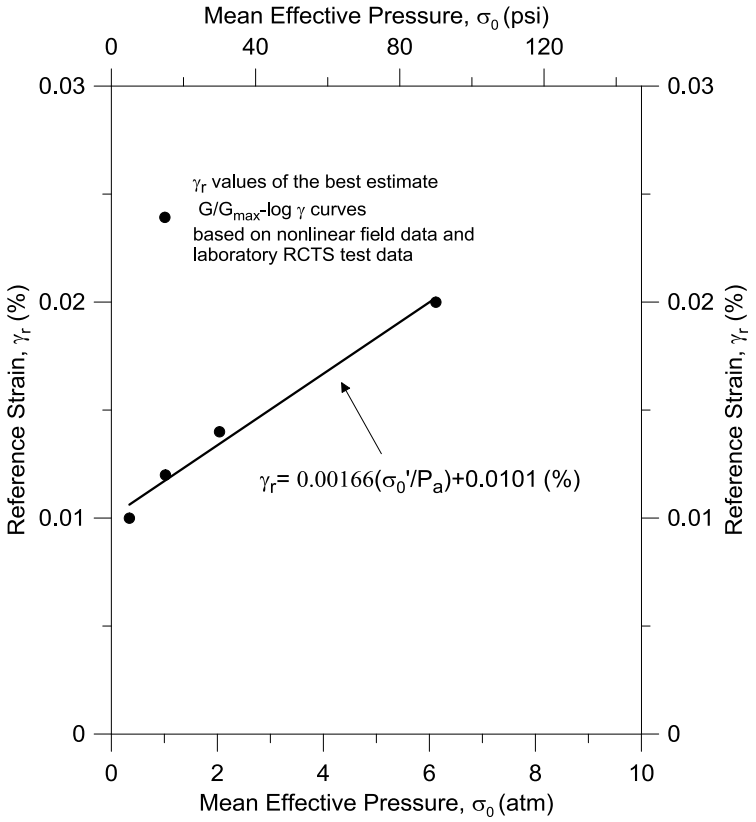

Figure 8.16: Reference strain-log confining pressure relationship based on the best-estimate $G/G_{max} - \log\gamma$ curves shown in Figure 8.15

These curves were used in the settlement prediction analyses with MoDaMP. The average value of $a = 1.0$ that is obtained from the best-estimate $G/G_{max} - \log\gamma$ curves is modified at larger strains based on laboratory triaxial test data on intact alluvial specimens discussed in Section 8.6.2.

8.5 LOAD-SETTLEMENT TESTS

A circular, reinforced concrete footings with a diameter of 3.0 ft (0.91 m) was constructed at both Test Pit 6 and Test Pit 7. The load-settlement tests were conducted by Dr. Kwangsoo Park. Each footing had a thickness of 1.5 ft (0.30 m). Prior to footing construction, a thickness of about 2.5 ft (0.75 m) of soil was carefully removed from the

surface and 1.0 ft (0.30 m) backfill was placed around the footing after it was constructed (see Figure 8.17). The load was applied on top of each footing in two load-unload cycles. A backbone curve was added to the load-unload cycles to obtain a continuous load-settlement curve (Figure 8.18). As seen in the figure, the settlements for both sites are very similar and the measured settlements are less than 0.1 in. in both load-settlement tests. The load-settlement curve in Test Pit 6 is slightly more nonlinear compared to the load-settlement curve in Test Pit 7.

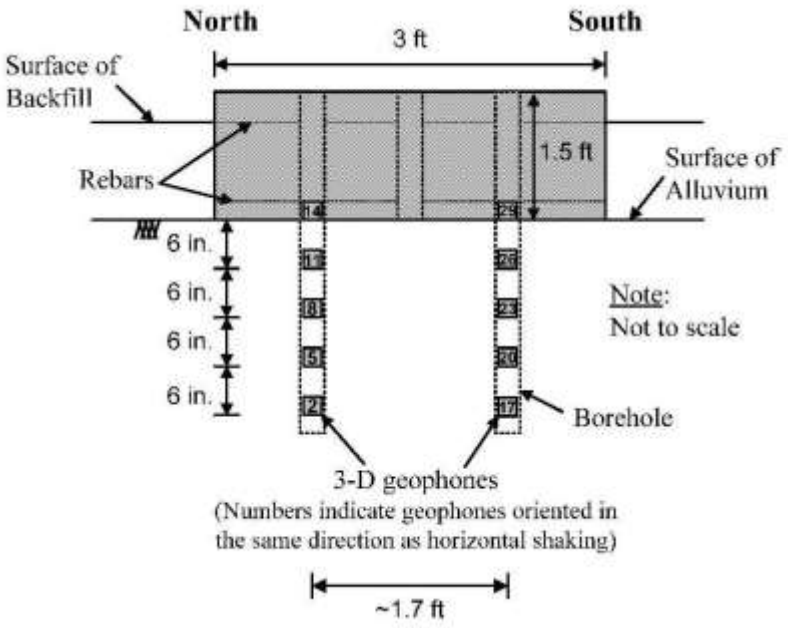

Figure 8.17: Cross-sectional view of the 3-ft diameter footing at the TP 7 and TP 6 sites (from Park, 2010)

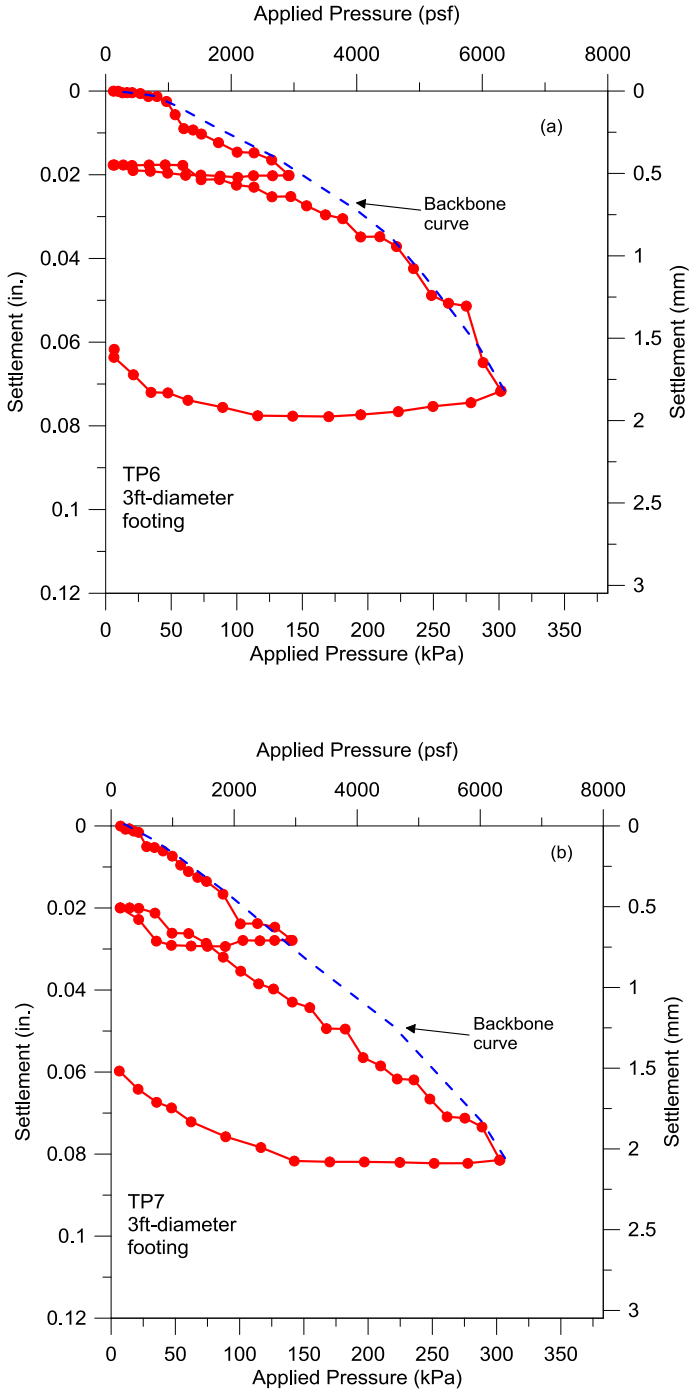

Figure 8.18: Load-unload-reload settlement results for the 3.0-ft (0.91-m) diameter footings with backbone curves fitted to approximate simple continuous loading at: (a) Test Pit 6 and (b) at Test Pit 7

8.6 LOAD-SETTLEMENT PREDICTIONS

In this section, the load-settlement curves of the two, 3.0-ft (0.91-m) diameter footings at the Yucca Mountain Test Site predicted using MoDaMP are presented and compared with the measured settlements.

8.6.1 Load-Settlement Predictions with MoDaMP

A finite element analysis was carried out to predict the settlements of the small-scale footings at Test Pit 6 and Test Pit 7. The input parameters were obtained from the $\log V_s - \log \sigma_0$, $\log V_p - \log \sigma_0$ and $G/G_{max} - \log \gamma$ relationships described in Section 8.3. The input parameters for both test sites are given in Table 8.1. Similar to the settlement analyses discussed in Chapter 6 and Chapter 7, each analysis is given a different identifier (analysis ID) to differentiate the site, footing diameter, Poisson's ratio assumption and the soil model. For example, TP6-3.0-CP stands for the analysis of 3.0-ft (0.91-m) diameter footing at Test Pit 6 using MoDaMP.

Table 8.1: Input parameters used in MoDaMP analyses for: (a) TP6 and (b) TP 7

(a)	Layer 1 (0-6 in.)	Layer 2 (6-12 in.)	Layer 3 (12-18 in.)	Layer 4 (> 18 in.)
G_{max_1atm}	13357 ksf	5060 ksf	5060 ksf	13357 ksf
ν_0	0.43	0.48	0.36	0.43
a	1.00	1.00	1.00	1.00
γ_r (%)	Equation 8.1	Equation 8.1	Equation 8.1	Equation 8.1

(b)	Layer 1 (0-6 in.)	Layer 2 (> 6 in.)
G_{max_1atm}	25607 ksf	6885 ksf
ν_0	0.46	0.35
a	1.00	1.00
γ_r (%)	Equation 8.1	Equation 8.1

8.6.1.1 PLAXIS Model for the Footings

The subroutine MoDaMP is implemented into PLAXIS and finite element analyses of settlements of footings are carried out using this subroutine. The soil-footing system was modeled as axisymmetric and symmetrical as explained in Section 6.7.1.1

All boundaries except the top boundary are restrained from horizontal movement and the bottom boundary is restrained from both horizontal and vertical movements. PLAXIS automatically generates the mesh for the model but the size and the type of the mesh can be altered by the user. The mesh used in the analyses consisted of 970, 15-node triangular elements which is slightly different than the mesh used in Chapter 6 and 7 due to layering of the soil. The backfill soil is modeled as a surcharge of 113 psf (5.7 kPa) because the deformations due to loading are occurring beneath the footings. The soil-footing geometry and the undeformed mesh of Test Pit 7 are shown in Figure 8.19 as an example.

The calculation process to evaluate the G_{max} values based on the current stress state and the associated $G - \log\gamma_{oct}$ relationships according to both stress and strain states is the same with the procedure explained in Section 6.7.1.1.

8.6.1.2 Predicted Settlements

Settlement analyses with the PLAXIS model using MoDaMP are presented in this section. In Figure 8.20, the predicted settlements are shown for TP6-3.0-CP and TP7-3.0-CP, respectively. Measured settlements for TP 6 and TP 7 compared with the predictions in these figures. As seen, the predicted settlements match the measured settlements reasonably well of around 2500 psf. Beyond this level, the predicted settlements increase rapidly, becoming much larger than the measured settlements and exhibiting a much softer system. The reason for this softer response can be seen in the $\tau - \gamma$ relationships

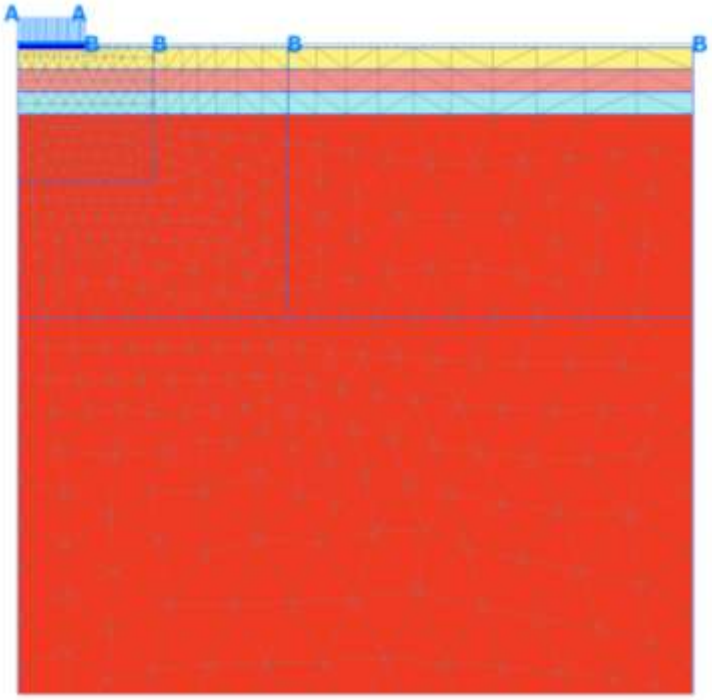

Figure 8.19: Geometry of the soil-footing model and the undeformed mesh for Test Pit 7

obtained by converting the $G/G_{max} - \log\gamma$ relationships to $\tau - \gamma$ relationships. It should be noted that soil layers beneath the footings have different $G_{\max\_1atm}$ values. Therefore, lower and upper boundaries of the $\tau - \gamma$ relationships were considered where the lower and upper boundaries refer to the softest and stiffest soil layers, respectively. The comparison of these $\tau - \gamma$ relationships with the $\tau - \gamma$ relationships obtained from quasi-static triaxial tests is shown in Figure 8.21. The $\tau - \gamma$ relationships obtained from quasi-static triaxial tests of intact specimens of undisturbed alluvium soils were performed at the Sandia National Laboratories (Schuhen, 2009). As seen in the figure, the $\tau - \gamma$ curves from the $G/G_{max} - \log\gamma$ relationships are much below the $\tau - \gamma$ relationships from the quasi-static tests at $\gamma > \sim 0.03\%$. Therefore, the $G/G_{max} - \log\gamma$ relationships have to be modified at larger strains. This modification process is explained in the following section.

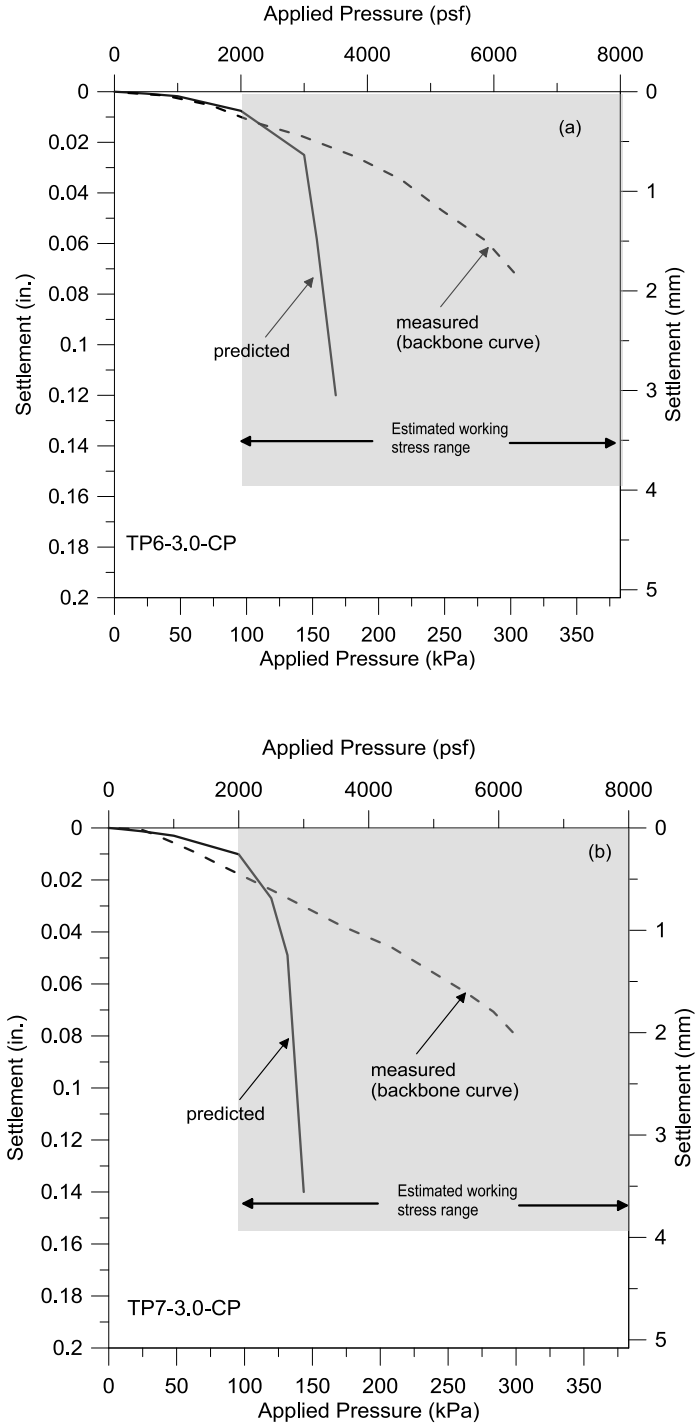

Figure 8.20: Predicted footing settlements using MoDaMP with a constant value of Poisson's ratio (see Table 8.1) for: (a) TP 6 and (b) TP 7

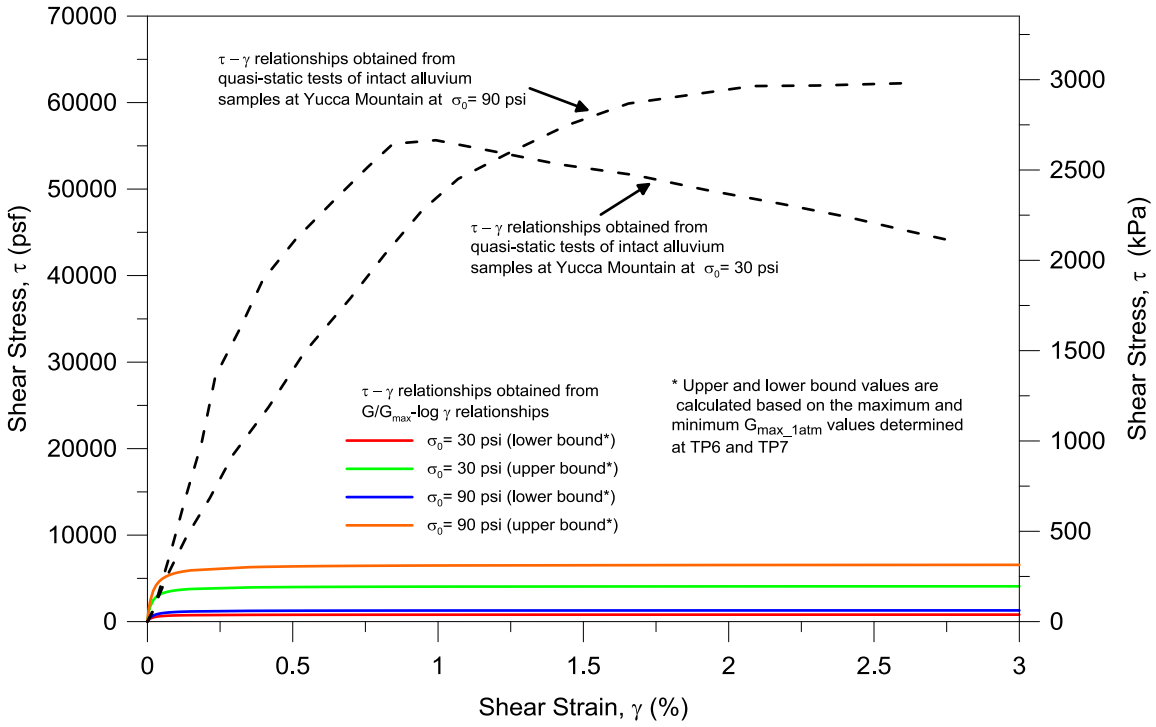

Figure 8.21: Comparison of shear stress-shear strain responses from quasi-static tests and from the $G/G_{max} - \log\gamma$ relationships (quasi-static test results are from Schuhen, 2009)

8.6.2 Modification of $G/G_{max} - \log\gamma$ Relationships in MoDaMP

As explained in the previous section, the $G/G_{max} - \log\gamma$ relationships need to be modified in the larger strain range just as was done in Chapter 6 and 7. This modification is achieved by adjusting the "a" parameter (only) in the larger strain range of the $G/G_{max} - \log\gamma$ relationships to match the quasi-static test results. However, the intact specimens used in the quasi-static tests are assumed to be stiffer than the field conditions. This assumption is based on the condition found by comparing field and laboratory V_s values shown in Figure 8.9. Therefore, the $\tau - \gamma$ curves from $G/G_{max} - \log\gamma$ relationships

are not exactly "matched" with the $\tau - \gamma$ curves from the quasi-static triaxial test results. Rather, the $G/G_{max} - \log\gamma$ relationships are adjusted in a way so that a softer response was obtained. This adjustment of the "a" parameter consists of two parts:

(1) for $G/G_{max} \geq 0.4$; $a = 1.0$ (8.2)

(2) for $G/G_{max} < 0.4$; $a = 0.80$ (8.3)

The comparison of the unmodified and modified $G/G_{max} - \log\gamma$ relationships is presented in Figure 8.22. The $\tau - \gamma$ responses obtained using the $G/G_{max} - \log\gamma$ relationships with the modified "a" parameter are presented in Figure 8.23. The modified

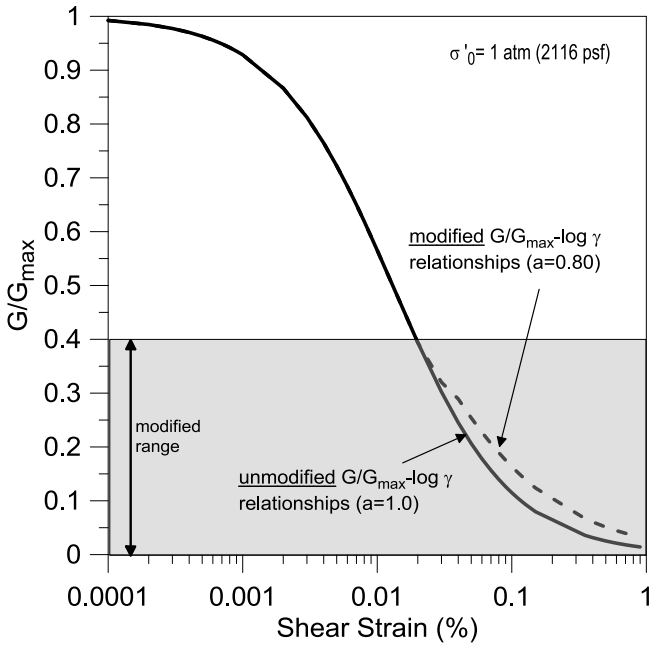

Figure 8.22: Comparison of unmodified (MoDaMP) and modified (MoDaMP-1) $G/G_{max} - \log\gamma$ relationships

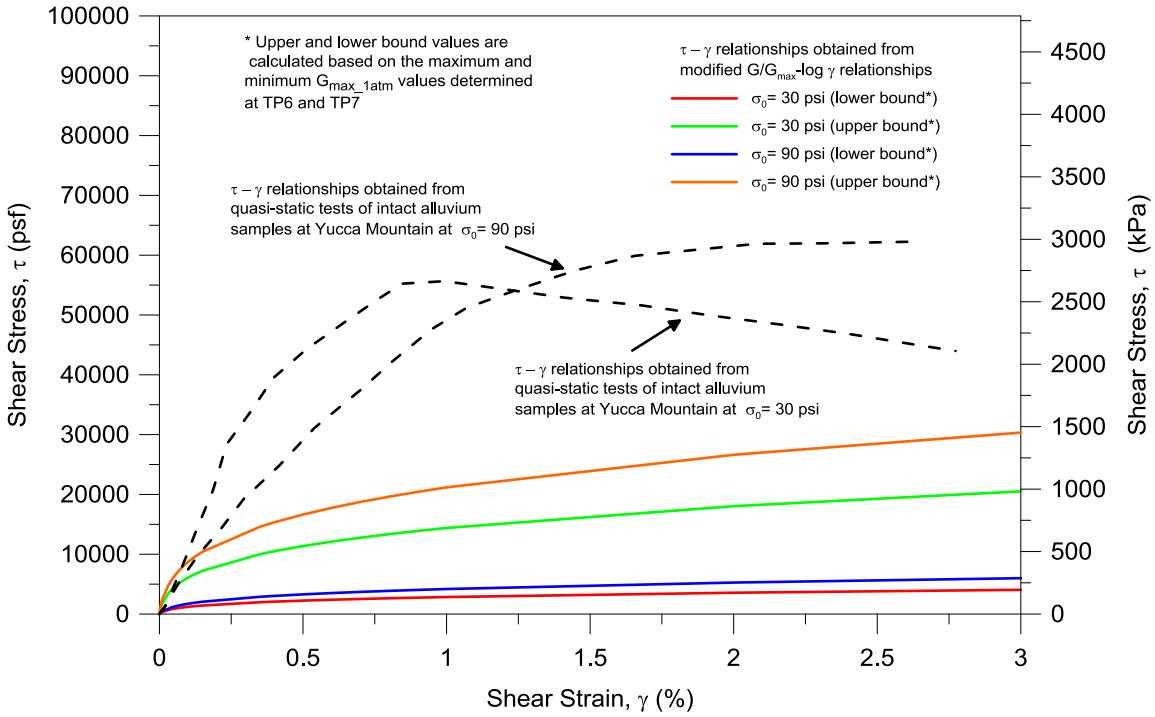

Figure 8.23: Comparison of shear stress-shear strain responses from quasi-static tests and from modified $G/G_{max} - \log\gamma$ relationships (used in MoDaMP-1)

$G/G_{max} - \log\gamma$ relationships are implemented into MoDaMP and the model with the modified relationships is used to predict the settlements of the footings to see the effect of the adjustment on footing settlements.

8.6.2.1 Settlement Predictions with modified $G/G_{max} - \log\gamma$ Relationships

The modified $G/G_{max} - \log\gamma$ relationships are implemented in MoDaMP and this model with the modification is designated as "MoDaMP-1". The settlements predicted using the modified $G/G_{max} - \log\gamma$ relationships are shown in Figure 8.24. As seen in the figure, the predicted settlements for footing at TP6 match the measured settlements well over much of the test-pressure range. The footing at TP7 showed a softer behavior and the predicted settlements are smaller than the measured settlements. It is important to

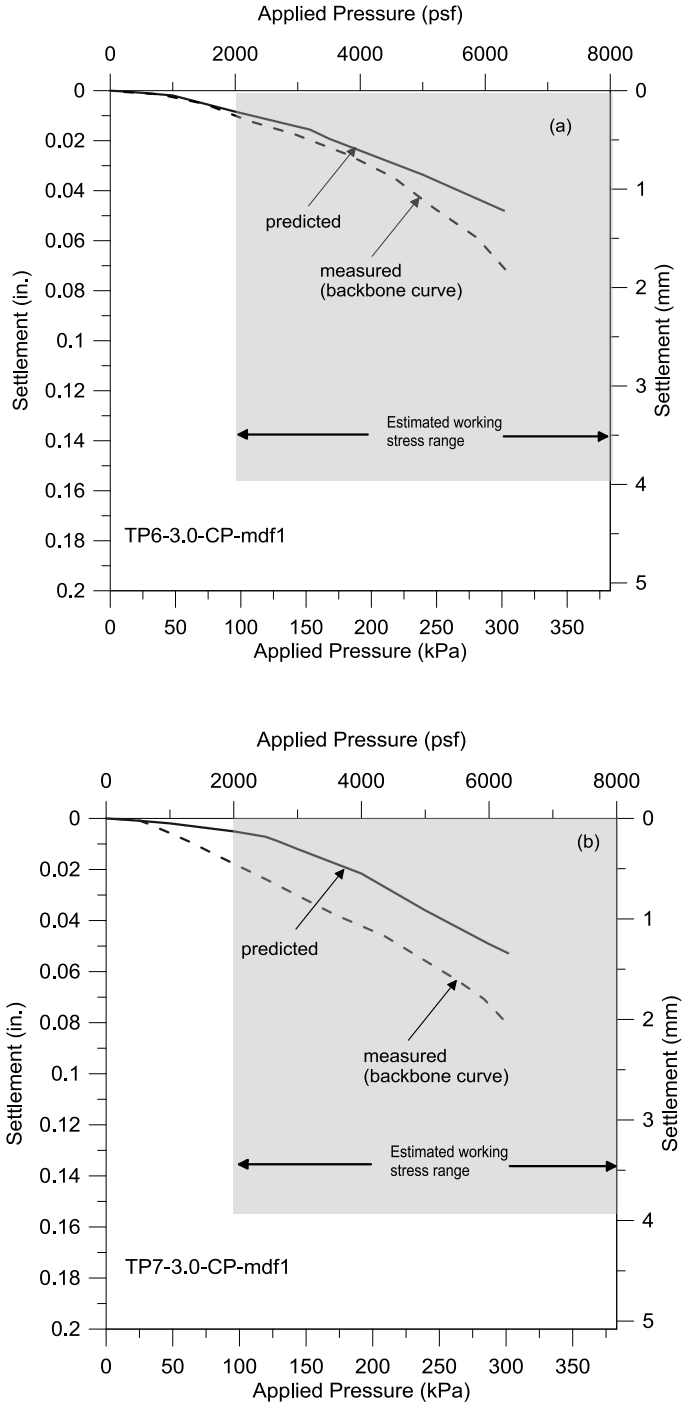

Figure 8.24: Comparison of predicted footing settlements using MoDaMP-1 with a constant Poisson's ratio value assumption and measured settlements for the 3.0-ft (0.91-m) diameter footing at: (a) TP6 and (b) TP7

note that the measured settlements are relatively small and the difference between the measured and predicted settlements are not more than 0.02 in.

8.6.3 Load-Settlement Predictions with varying Poisson's Ratio

In the previous settlement predictions, the value of Poisson's ratio is assumed constant for the complete loading range. On the other hand, the value of Poisson's ratio likely changes with increasing shear strain levels as discussed in Chapter 4 for uncemented to lightly cemented granular soil. In this section, the effect of the varying Poisson's ratio with strain level on the settlement prediction of the footings is investigated. The value of Poisson's ratio is determined by following the procedures explained in Section 4.4. The results of the settlement analyses with MoDaMP-1 and a constant constrained compression modulus, M, assumption, are given in Figure 8.25a and 8.25b for the footings at TP6 and TP7, respectively. As seen in the figures, the predicted settlements with MoDaMP-1 and constant M are smaller than the measured settlements. The results of the settlement analyses with MoDaMP-1 using a constant constrained compression modulus, K, assumption, are given in Figure 8.26a and 8.26b for the footings at TP6 and TP7, respectively. Similar to the constant M assumption case, the settlements for the constant K assumption are also smaller than the measured settlements. This result can be attributed to the smaller volumetric strains occurring with the varying Poisson's ratio assumption since the Poisson's ratio is increasing with strain for a constant M or K assumption.

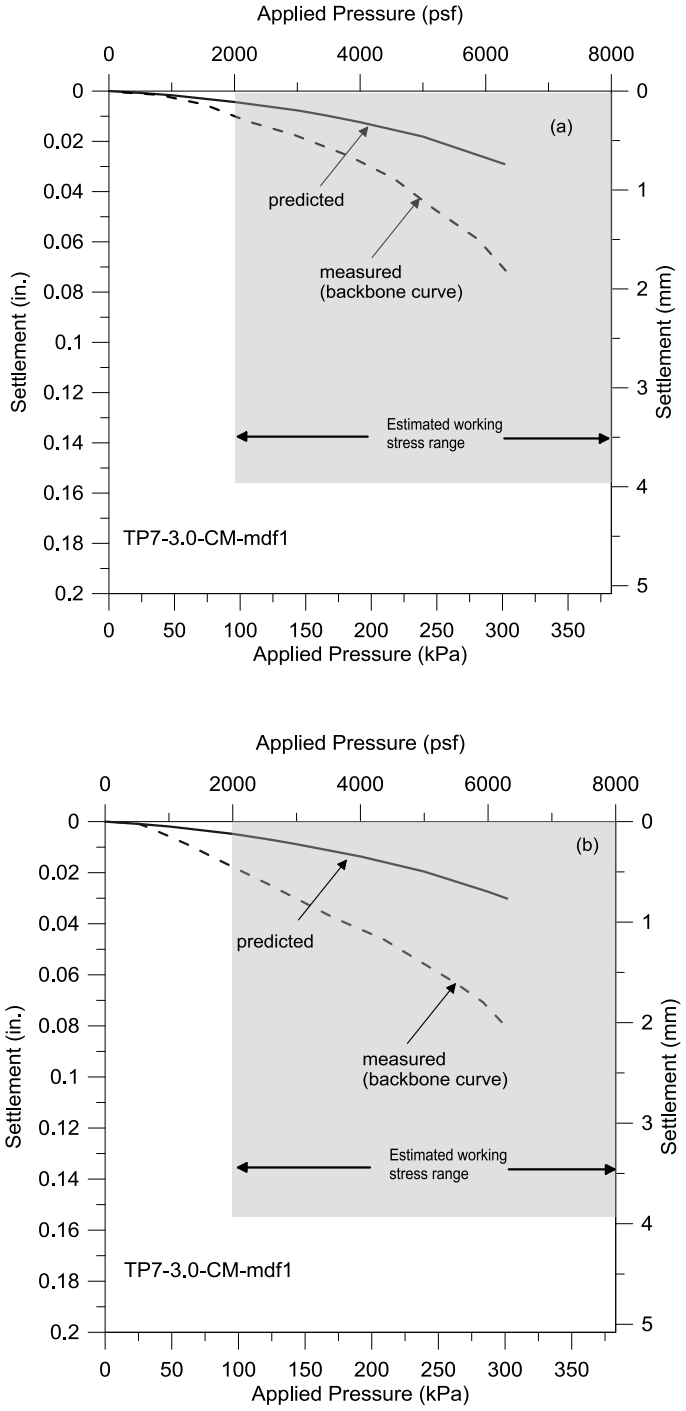

Figure 8.25: Comparison of predicted footing settlements using MoDaMP-1 with a constant compression modulus (M) assumption and measured settlements for the 3.0-ft (0.91-m) diameter footing at: (a) TP6 and (b) TP7

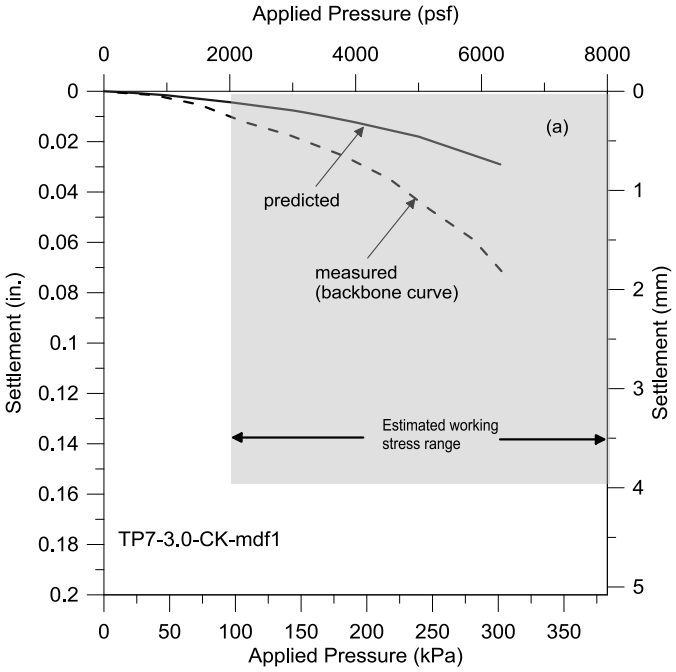

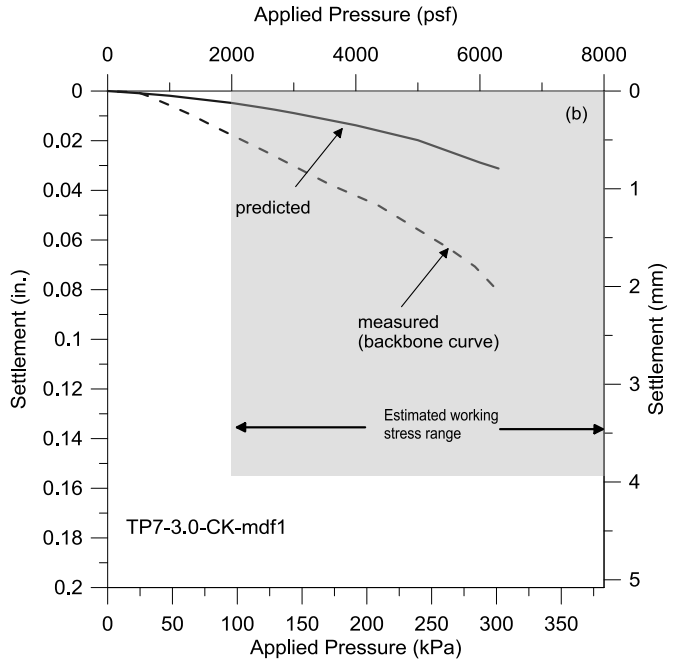

Figure 8.26: Comparison of predicted footing settlements using MoDaMP-1 with a constant bulk modulus (K) assumption and measured settlements for the 3.0-ft (0.91-m) diameter footing at: (a) TP6 and (b) TP7

8.7 SUMMARY

The load-settlement tests of two, small-scale footings, each 3-ft (0.91-m) in diameter, at the Yucca Mountain Test Site, Nevada are discussed in this chapter. One footing was constructed near Test Pit 6 and one footing was constructed near Test Pit 7.In both cases, the footings were founded on a thick deposit of cemented alluvium. The test pits were excavated to investigate the alluvium.

The load-settlement tests were performed as a part of the geotechnical investigations for the proposed nuclear repository at Yucca Mountain. Several field seismic tests including small-scale downhole, and crosshole, and SASW tests were conducted at the footing locations. Steady-state dynamic tests were conducted at on each footing. The geotechnical material at footing locations, a naturally cemented alluvium, is very difficult and expensive to sample. Researchers at the University of Texas at Austin were given the rare opportunity to have undisturbed samples from this site and test them in the laboratory in RCTS equipment. The results from the field downhole tests, field steady-state, dynamic tests, and RCTS tests were used to characterize the cemented alluvium in the linear and nonlinear ranges in terms of shear moduli. Representative $\log V_s - \log \sigma_0'$ relationships for the soil behavior beneath the footings were determined and these relationships were used to model the stress dependency of the small-strain shear modulus (G_{max}) of the cemented alluvium.

The nonlinear shear modulus of the cemented alluvium is determined using the measurements from the steady-state dynamic tests. By comparing them with the results from RCTS tests, $G/G_{max} - \log \gamma$ relationships were determined.

The stress dependency of G_{max} and stress and strain dependency of $G/G_{max} - \log \gamma$ relationships were implemented into MoDaMP. The settlements of the 3.0-ft (0.91-

m) diameter footings at Test Pit 6 and Test Pit 7 were then predicted using MoDaMP. The $\tau - \gamma$ relationships determined from the $G/G_{max} - \log\gamma$ relationships obtained from the field steady-state dynamic tests and laboratory RCTS tests were combined and studied. It was found that the $G/G_{max} - \log\gamma$ relationships needed to be modified. This modification was achieved by adjusting the $G/G_{max} - \log\gamma$ relationships for $G/G_{max} < 0.4$. Beyond this point, the $\tau - \gamma$ relationships were determined from modified $G/G_{max} - \log\gamma$ relationships with the modification guided by larger-strain, quasi-static, triaxial test data performed at Sandia National Laboratories.

The effect of the Poisson's ratio on the settlement predictions was also investigated by varying the Poisson's ratio with increasing shear strain assuming that: (1) the constrained compression modulus (M) was constant or (2) the bulk modulus (K) was constant. Settlements predicted with these two assumptions are smaller than those predicted assuming a constant value for Poisson's ratio. The reason for this difference is the smaller volumetric strains due to the increased Poisson's ratio which results with the assumption of either a constant constrained compression modulus or a constant bulk modulus.

Chapter 9: Summary, Conclusions, and Recommendations

9.1 SUMMARY

The governing factor in design of shallow foundations on granular soil is generally the settlement. Due to difficulties in obtaining undisturbed soil samples of granular soil, settlement predictions of shallow foundations have been traditionally made using empirical correlations. Soil penetration tests such as the Standard Penetration Test (SPT) and Cone Penetration Test (CPT) are used to correlate the penetration data with foundation settlements. These methods usually include some correction factors for embedment depth, foundation shape, foundation rigidity and time (Schmertmann, 1970; Burland and Burbidge, 1985; Briaud, 2007). In all conventional settlement prediction methods, the soil stiffness is taken as constant at all strain levels. Moreover, the effects of increasing stresses and strains during loading on soil stiffness are not considered in any of these methods.

It has been widely known in geotechnical engineering for more than 40 years that soil stiffness, and therefore the shear stress (τ) - shear strain (γ) response is highly strain and stress dependent (Hardin and Drnevich, 1972). There are some more-recent methods in the literature that account for the strain dependency of the soil in predicting the settlements (Berardi and Lancelotta, 1991; Mayne, 2000; Lehane and Fahey, 2002; Elhakim 2005). However, none of these methods incorporate field seismic measurements of shear wave velocity (V_s) to evaluate the small-strain shear modulus (G_{max}) profile and then combine the profile with nonlinear $G/G_{max} - \log\gamma$ relationships to calculate linear and nonlinear strains. In addition, the following effects are not explicitly considered in the methods: (1) the effects of gradation on the nonlinear stress-strain behavior of granular soil, and (2) the combined effects on soil stiffness of changing levels of stress

state and shear strain. Therefore, a new method that is deformation based and incorporates all effects described above is needed.

In this study, a framework is being developed to predict the settlements of shallow foundations on granular soil using dynamically measured soil properties. The framework consists of: (1) determining the small-strain (linear) and larger-strain (nonlinear) properties of granular soil based on field seismic and laboratory dynamic measurements and (2) implementing these relationships in a user-defined soil model for use in FEM-based numerical analyses.

9.1.1 Development of Soil Model using Dynamically Measured Properties (MoDaMP)

The proposed framework utilizes the field seismic measurements of V_s from small-scale crosshole, downhole test or from Spectral-Analysis-of-Surface-Waves tests. The measured V_s profiles represent the soil beneath the shallow foundations before loading and are used to determine the $\log V_s - \log \sigma_0'$ relationships of the granular soil. In this case, σ_0' represents the initial state of the geostatic stresses before loading the footing. The initial $\log V_s - \log \sigma_0'$ relationships are then converted to $\log G_{max} - \log \sigma_0'$ relationships which are used to determine G_{max} just before the start of loading. The next step is to determine the normalized shear modulus- log shear strain ($G/G_{\max} - \log \gamma$) relationships. These relationships are typically evaluated from laboratory tests such as combined Resonant Column and Torsional Shear (RCTS) tests. These tests are conducted under different confining pressures; hence, a relationship between the $G/G_{\max} - \log \gamma$ curves and the confining pressures is established. In this study, $G/G_{\max} - \log \gamma$ relationships are expressed by the modified hyperbolic model proposed by Darendeli (2001). If V_s measurements in the nonlinear range are conducted in the field, as in the case

of Yucca Mountain presented in Chapter 8, the field data are used in determining the $G/G_{\max} - \log\gamma$ relationships. In case of lack of any laboratory or field measurements in the nonlinear range, the $G/G_{\max} - \log\gamma$ relationships are estimated from empirical models. In Chapter 7, the $G/G_{\max} - \log\gamma$ relationships for the Hornsby Bend site are determined from the model proposed by Menq (2003). In this model, soil gradation and confining pressure are taken into account. It should be noted that $G/G_{\max} - \log\gamma$ relationships are also stress dependent and increased stresses beneath the foundation during loading make the $G/G_{\max} - \log\gamma$ relationships less nonlinear. The next step in the method is to combine G_{max} and $G/G_{\max} - \log\gamma$ relationships to calculate G at each stress and strain state.

The $G/G_{\max} - \log\gamma$ relationships are based on laboratory and field measurements which usually do not include measurements at strains that corresponds to $G/G_{\max}$ less than about 0.4. Also, empirical $G/G_{\max} - \log\gamma$ relationships are established based on data that do not extend to larger strains. In many geotechnical applications, such as settlements of shallow foundations, the strain values are well beyond the strain values observed in field and laboratory dynamic measurements. Comparison of $\tau - \gamma$ relationships obtained using $G/G_{\max} - \log\gamma$ relationships with those obtained from tests that extend to larger strains, such as triaxial or direct shear test data, shows that the $\tau - \gamma$ relationships from $G/G_{\max} - \log\gamma$ relationships are softer at larger strains. Therefore, the $G/G_{\max} - \log\gamma$ relationships are modified at larger strains. To this end, the "a" parameter in the Darendeli (2001) model is modified using the $\tau - \gamma$ relationships at larger strains as a guide.

All dynamic properties and relationships at small-strain and larger-strain ranges and the modification of the $G/G_{\max} - \log\gamma$ relationships need to be combined in a subroutine that can be used in numerical analysis.

9.1.2 Implementation of Soil Model using Dynamically Measured Properties (MoDaMP) into PLAXIS

The proposed model (MoDaMP) described in the previous section is implemented as a user defined soil model via a subroutine in the finite element program, PLAXIS. The key point in implementing MoDaMP in PLAXIS is defining the stiffness matrix that follows the relationships between $\log G_{max} - \log\sigma_0'$ and $G/G_{\max} - \log\gamma$ curves. The stiffness matrix consists of G and Poisson's ratio (ν). To determine G accurately, a tangent stiffness matrix approach is adopted in the subroutine. To determine the tangent shear modulus, the derivative of the $\tau - \gamma$ curve is taken and it is integrated over the strain increment that is provided by the calculation kernel of PLAXIS. Thus, the tangent shear modulus, G_t, is obtained. Based on the stress state, G_{max} is updated and based on both stress and strain states, $G/G_{\max} - \log\gamma$ relationships are updated and G_t in the next calculation step is determined based on the updated values. Since the soil is assumed isotropic, it is concluded that the shear modulus reduction takes place in every direction. To this end, the shear strain (γ) is replaced with a scalar measure of shear strain, the octahedral shear strain (γ_{oct}), to represent the shear strain in 3D space. The small-strain Poisson's ratio (ν) is calculated from small-strain field seismic V_s and V_p measurements and is used in the stiffness matrix at the start of loading. The effect of Poisson's ratio (ν) on settlement predictions is also investigated by assuming that either: (1) the constrained compression modulus (M) is constant or (2) the bulk modulus (K) is constant.

9.1.3 Load-Settlement Predictions

The user-defined soil model developed in this study, MoDaMP is used to predict the settlements of small-scale concrete footings at three different test sites where load-settlement tests have been performed. The load-settlement tests were parts of other studies but were performed in an attempt to create a database of load-settlement tests which include comprehensive dynamic soil property measurements. Field seismic and laboratory dynamic tests are conducted at these sites by researchers from the University of Texas at Austin.

The first site that is considered in this study is the National Geotechnical Experimentation Site in College Station, TX. The load-settlement tests were conducted by Park et al. (2009). Two, small-scale concrete footings with diameters of 3.0 and 1.5 ft (0.91 and 0.46 m) were tested. The $\log G_{max} - \log \sigma_0'$ relationships were determined by SASW testing. The $G/G_{\max} - \log \gamma$ curves were determined by RCTS testing with intact specimens. The predicted settlements with MoDaMP are larger than the measured settlements at applied pressures that are larger than about ~ 600 psf (28.7 kPa) the. The larger predicted settlements are not surprising since the $\tau - \gamma$ curves based on the $G/G_{\max} - \log \gamma$ relationships are below $\tau - \gamma$ curves from triaxial tests. As a result, the $G/G_{\max} - \log \gamma$ curves were modified at larger strains. The settlement predictions with the modified model, MoDaMP-1, were still larger than the measured settlements for both footings. The soil behavior predicted with MoDaMP-1 is still softer than the real behavior. This behavior is attributed to the effect of horizontal stresses beneath the footing that is not captured in triaxial tests at larger strains. Therefore, a second modification was applied to the $G/G_{\max} - \log \gamma$ curves to have a stiffer behavior of the soil. The model with the second modification, MoDaMP-2, was then used to predict the

settlements. Settlements predicted with MoDaMP-2 are in quite reasonable agreement with the measured settlements. The approach where the Poisson's ratio is varying based on either constant M and K assumption is implemented in MoDaMP-2 to investigate the effects of Poisson's ratio on settlements. It was found that the settlements predicted with constant M or K assumptions are similar to each other. Predicted settlements are smaller compared to those found with constant Poisson's ratio.

The second site that is considered in this study is the Hornsby Bend test site in Austin, TX. The load-settlement tests were conducted by Van Pelt (2010). Two, small-scale concrete footings with diameters of 3.0 ft (0.91-m) and 1.5 ft (0.46-m) were tested. Vertical movements at various depths beneath the footings were also measured with tell-tales. The $\log G_{max} - \log \sigma_0'$ relationships were determined from SASW tests. The $G/G_{\max} - \log \gamma$ curves are determined from empirical relationships proposed by Menq (2003). The predicted settlements with MoDaMP are larger than the measured settlements at larger applied pressures. The reason for this softer behavior predicted with MoDaMP is that the $\tau - \gamma$ curves based on the $G/G_{\max} - \log \gamma$ relationships are exhibiting a softer behavior compared to those curves from triaxial tests at larger strains. Therefore, the $G/G_{\max} - \log \gamma$ curves are modified based on triaxial test data at larger strain on reconstituted samples. The settlement predictions with the modified model, MoDaMP-1, agree reasonably with the measured settlements for 3.0-ft (0.91-m) diameter footing and the predicted settlements are higher for the 1.5-ft (0.46-m) diameter footing. The effect of Poisson's ratio on predicted settlements are shown by using constant constrained compression modulus (M) and bulk modulus (K). The predicted settlements with these constant M and K assumptions are in good agreement for the 1.5-ft (0.46-m) diameter

footing whereas the predictions for the 3.0-ft (0.91-m) diameter footings are smaller than the measured settlements.

The third site investigated in this study is the Yucca Mountain Test Site in Nevada. Load-settlement tests at two locations, called Test Pit 6 and Test Pit 7, in Yucca Mountain are studied. The load-settlement tests were conducted by Park (2010). The small-scale concrete footings are 3.0 ft (0.91 m) in diameter and 1.5 ft (0.46 m) in thickness. The $\log G_{max} - \log \sigma_0'$ relationships were determined from small-scale downhole tests using embedded arrays beneath the footings. The $G/G_{\max} - \log \gamma$ curves were determined from steady-state dynamic tests and from RCTS tests with intact specimens. The predicted settlements with MoDaMP agree well with the measured settlements up to a level of applied pressure of ~ 3000 psf. At larger applied pressures; the predicted settlements are higher than the measured settlements since the $\tau - \gamma$ curves based on the $G/G_{\max} - \log \gamma$ relationships are softer than the $\tau - \gamma$ curves from quasi-static triaxial tests at larger strain. Therefore, the $G/G_{\max} - \log \gamma$ curves were modified based quasi-static test data at larger strain on intact samples. The settlement predictions with the modified model, MoDaMP-1, agree reasonably well with the measured settlements for both tests sites. The predicted settlements at Test Pit 6 are slightly smaller than the measured settlements. The effect of Poisson's ratio on predicted settlements are shown by using constant constrained compression modulus (M) and bulk modulus (K). The predicted settlements with these constant M and K assumptions are smaller than the measured settlements at both sites.

It should be noted that assuming a constant value M and K is a first attempt in defining the change in these moduli with increasing strain and this assumption will be studied further.

9.2 CONCLUSIONS

The research presented in this dissertation is composed of two parts. The first part is the initial development of a soil model that incorporates dynamically measured soil properties from field seismic and laboratory dynamic tests to represent the nonlinear response of granular soil over shear strains from the elastic range, 0.0001%, to the highly nonlinear range, 1 to 3% for use in deformational analyses. The second part is to investigate and to improve the developed model with load-settlement tests where field seismic and/or laboratory dynamic tests are available. The following conclusions concerning the developed method and its applicability can be drawn.

1) A soil model that combines linear and nonlinear dynamic measurements of granular soil can be used in evaluating the stress-strain response of the soil under static loading conditions.

2) The developed model, MoDaMP, is implemented into a finite element program and it is verified with element tests that the developed model is working correctly by comparing the numerical solutions with analytical solutions.

3) Field seismic tests must be used to determine G_{max} at the start of the load-settlement curve.

4) G_{max} and $\log G_{max} - \log \sigma_0'$ relationship must be determined from field seismic tests and then combined with $G/G_{\max} - \log \gamma$ relationships obtained from field seismic and/or laboratory dynamic tests to predict the settlements in the nonlinear elastic and moderately nonlinear ranges.

5) The settlements corresponding to the highly nonlinear range can be predicted with modified $G/G_{\max} - \log \gamma$ relationships where the modification is guided by larger-strain laboratory data such as triaxial test data.

6) The effect of using a varying Poisson's ratio with constant M or K assumptions is less pronounced in stiffer soil.

7) Settlements of larger (3.0-ft diameter) footings are generally more closely predicted than the settlements of smaller (1.5-ft diameter) footings

9.3 RECOMMENDATIONS FOR FUTURE RESEARCH

The research presented in this dissertation has concentrated on building the framework for a deformation-based method of predicting the settlements of shallow foundations on granular soil. The following recommendations are made to improve the quality of this method.

1) More load-settlement tests with comprehensive field seismic, laboratory dynamic and triaxial testing are needed to create a robust dataset. The proposed predictions need to be compared and refined.

2) Laboratory methods to investigate the $G/G_{\max} - \log\gamma$ relationships at strains larger than 0.1-0.2% should be explored. The $\tau - \gamma$ relationships at larger strains are very important in predicting the settlements of shallow foundations since the strains observed in such problems are above the maximum strain range that can be measured in most dynamic laboratory tests.

3) The effect of the increased horizontal stresses beneath the footings on the stiffness of the soil should be investigated. And if possible, laboratory tests that can simulate the increases in both vertical and horizontal stresses should be explored.

4) The "a" parameter in Darendeli (2001) model to express the $G/G_{\max} - \log\gamma$ relationships should be investigated further. This parameter is most likely a function of additional/different parameters at larger strain ranges (compared to the smaller strain ranges where it has been developed). It should be also noted that the trend of change in

"a" with increasing confining pressures is different at different strain ranges. This understanding is also important in geotechnical earthquake engineering where Darendeli (2001) and Menq (2003) models are widely used at shear strains well above 0.1-0.2% .

5) In this study, relationships between shear modulus, constrained compression modulus and Poisson's ratio based on the research completed by Le Blanc (2013) are investigated. It is found that these relationships which result in varying Poisson's ratio, have a great effect on the settlement predictions. The effect of relaxing the constrained boundary, hence reducing constrained modulus at larger strains and how this affects the relationships between shear and constrained modulus and Poisson's ratio needs studying.

6) The proposed framework presented in this dissertation utilizes a nonlinear elastic soil response. The effect of the plastic deformations on the predicted settlements should be investigated. To this end, the additional soil model described in Chapter 5, MoDaMP-P, which is a soil model that combines nonlinear elastic and perfectly plastic soil behavior, can be used. MoDaMP-P is still under verification process but it promises a great benefit in understanding the compressive and dilative behavior of granular soil.

References

Ahlvin R.G. and Ulery H.H. (1962). Tabulated values for determining the complete pattern of stresses, strains and deflections beneath a circular uniform load on a homogenous half space, *Highway Research Board Bulletin 342, Stress Distribution in Earth Masses:* 1-13.

Axtell, P.J., Stokoe K.H.II. and Rathje E.M. (2002). *Development of methods to measure nonlinear properties and liquefaction characteristics of near-surface soils*, Report No. GR02-4, Civil Engineering Department, University of Texas at Austin.

Benz, T. (2006). *Small-strain stiffness of soils and its numerical consequences*. Institute für Geotechnik der Universitaet Stuttgart, Germany, pp. 193.

Berardi, R. and Lancellotta, R. (1991). Stiffness of granular soil from field performance. *Geotechnique*, 41 (1), 149-157.

Briaud, J. and Gibbens. R. M., (1994). Predicted and measured behavior of five spread footings on sand. *Proceedings of a Prediction Symposium Sponsored by the Federal Highway Administration at the occasion of the Settlement'94 ASCE Conference* Geotechnical Special Publication No.41, College Station, Texas.

Brinkgreve, R.B.J., Swolfs W.M. and Engin E., (2011). *Plaxis 2D 2011 User Manual*, Plaxis bv., Delft, The Netherlands.

Burland, J.B. and Burbidge M.C., (1985). Settlement of foundations on sand and gravel. *Proceedings of Institution of Civil Engineers* 78 (1), 1325-1381.

Chang, N.Y. and Ko, H.Y. (1982). *Effect of grain size distribution on dynamic properties and liquefaction potential of granular soils*, Research Report R82-103, University of Colorado at Denver, 145 pp.

Chen, W. F. and Mizuno, E. (1990). *Nonlinear analysis in soil mechanics, theory and implementation*, Elsevier, Amsterdam, The Netherlands, 661 pp.

Chitas P.C. (2008). Site-effect assessment using acceleration time series application to Sao Sebastiao volcanic crater, Universidade Nova de Lisboa, Lisboa, Portugal, pp. 265.

Darendeli, M.B. (2001). *Development of a new family of normalized modulus reduction and material damping curves*, Ph.D. Dissertation, The University of Texas at Austin, U.S.A., 362 pp.

Das, B.M. and Sivakugan, N. (2007). Settlements of shallow foundations on granular soils-an overview, *International Journal of Geotechnical Engineering*, 1(1), 19-29.

Elhakim A. F. (2005). *Evaluation of shallow foundation displacements using soil small-strain stiffness*, Ph.D. Dissertation, Georgia Institute of Technology, U.S.A, 396 pp.

Fahey, M. and Carter, J. P. (1993). A finite element study of the pressuremeter test in sand using a nonlinear elastic plastic model. *Canadian Geotechnical Journal*, *30*(2), 348-362.

Hardin, B.O. (1973). *Shear modulus of gravel*, Report-TR74-73-CE19, Civil Engineering Department, The University of Kentucky.

Hardin, B. O. (1978). The nature of stress-strain behavior for soils, *Proceedings of the ASCE Geotechnical Engineering Division Specialty Conference on Earthquake Engineering and Soil Dynamics*, Pasadena, California, Vol. 1, 3-90.

Hardin, B. O. and Black, W.L. (1968). Vibration modulus of normally consolidated clay, *Journal of the Soil Mechanics and Foundations Division,* ASCE, 94(SM2), 353-369.

Hardin, B.O. and Drnevich, V.P. (1972). Shear modulus and damping in soils: design equations and curves, *Journal of the Soil Mechanics and Foundation Engineering Division*, ASCE 98 (7), 667-692

Hardin, B. O. and Kalinski, M. E. (2005). Estimating the shear modulus of gravelly soils, *Journal of Geotechnical and Geoenvironmental Engineering*, *131*(7), 867-875.

Henke, R. and Henke, W. (2002). In situ nonlinear inelastic shearing deformation characteristics of soil deposits inferred using the torsional cylindrical impulse shear test, *Bull. Seism. Soc. Am.*, 92(5), 1970-1983.

Ishihara, K. (1986). *Soil behavior in earthquake geotechnics*, Oxford University Press, Walton Street, Oxford, 350 pp.

Iwasaki, T. and Tatsuoka, F. (1977). Effects of grain size and grading on dynamic shear moduli of sands." *Soils and Foundations* , 17(3), 19-35.

Janbu, N. (1963). Soil compressibility as determined by oedometer and triaxial tests, *Proceedings of 3rd European Conference on Soil Mechanics and Foundation Engineering*, Wiesbaden, Germany, 1, 19-25.

Kokusho, T. (1980). Cyclic triaxial test of dynamic soil properties for wide strain range, *Soils and Foundations,* 20(2), 45-60.

Kokusho, T. (1987). In-situ dynamic properties and their evaluations. *Proceedings of the 8th Asian Regional Conference on soil Mechanics and Foundation Engineering*, Kyoto, Japan, Vol. 2, 215-240.

Kokusho, T., Yoshida Y and Tanaka Y. (1995). Shear wave velocity in gravelly soils with different particle grading, *Static and Dynamic Properties of Gravelly Soils, Geotech. Spec. Pub.* (56), ASCE, 92-105.

Kramer, S.L. (1996). *Geotechnical earthquake engineering*, Prentice Hall, Upper Saddle River, New Jersey, 653 pp.

Kurtulus, A. (2006). *Field measurement of the linear and nonlinear shear moduli of soils using drilled shafts as dynamic cylindrical sources*, Ph.D. Dissertation, The University of Texas at Austin, U.S.A., 492 pp.

Kurtulus, A. and Stokoe, K. H. (2008). In situ measurement of nonlinear shear modulus of silty soil, *Journal of Geotechnical and Geoenvironmental Engineering, 134*(10), 1531-1540.

LeBlanc, M.T. (2013). *Field measurement of the linear and nonlinear constrained moduli of granular soil,* Ph.D. Dissertation, The University of Texas at Austin, U.S.A., 338 pp.

Mayne, P.W. (2000). Enhanced geotechnical site characterization by seismic piezocone penetration tests, *Invited lecture, 4th International Geotechnical Conference*, Cairo, Egypt, 95-120.

Mayne, P. W. (2001). Stress-strain-strength-flow parameters from enhanced in-situ tests, *Proceedings of International Conference on In Situ Measurement of Soil Properties and Case Histories,* Bali, Indonesia, 27-47.

Mayne, P.W. and Poulos, H.G. (1999). Approximate displacement influence factors for elastic shallow foundations, *Journal of Geotechnical and Geoenvironmental Engineering,* ASCE,125 (6), 453-460.

Menq, F. (2003). *Dynamic properties of sandy and gravelly soils,* Ph.D. Dissertation, The University of Texas at Austin, U.S.A., 364 pp.

Meyerhof, G.G. (1965). Shallow foundations, *Journal of the Soil Mechanics and Foundations Division,* ASCE, 91 (SM2), 21-31.

LeBlanc, M.T. (2013). *Field measurement of the linear and nonlinear constrained moduli of granular soil*, Ph.D. Dissertation, The University of Texas at Austin, U.S.A., 340 pp.

Lehane, B. and Cosgrove, E. (2000). Applying triaxial compression stiffness data to settlement prediction of shallow foundations on cohesionless soil, *Proceedings of the ICE-Geotechnical Engineering*, 143(4), 191-200.

Lehane, B. and Fahey, M. (2002). A simplified nonlinear settlement prediction model for foundations on sand, *Canadian Geotechnical Journal*, 39 (2), 293-303.

Lee, J. and Salgado, R. (2001). Estimation of footing settlement in sand, *International Journal of Geomechanics*, 2(1), 1-28.

LoPresti, D.C.F., Pallara, O. and Puci, I. (1995). A modified commercial triaxial testing system for small-strain measurement, *ASTM Geotechnical Testing Journal*, 18(1), 15-31.

Park, K. (2010). *Field measurements of the linear and nonlinear shear moduli of cemented alluvium using dynamically loaded surface footings*, Ph.D. Dissertation, The University of Texas at Austin, U.S.A., 350 pp.

Park, K., Stokoe, K.H. II, Olson, R.E. and Seo, W. (2009). Settlement of footings in sand using dynamic soil properties, *Proceedings of International Workshop on Soil-Foundation-Structure Interaction (SFSI 09)*, Auckland, New Zealand.

Puzrin, A. M. and Burland, J. B. (1998). Non-linear model of small-strain behavior of soils, *Geotechnique, 48*(2), 217-213.

Rathje, E. M., Phillips, R. D., Chang, W. J. and Stokoe, K. H. (2001). Evaluating nonlinear soil response in situ, *Proceedings of 4th International Conference. on Recent Advances in Geotechnical Earthquake Engineering and Soil Dynamics*, San Diego, California.

Richart, F.E., Jr., Hall, J.R., and Woods, R.D. (1970). *Vibration of Soils and Foundations*, Prentice-Hall, Inc., Englewood Cliffs, New Jersey.

Robertson, P. K., Campanella, R. G. and Wightman, A. (1983). SPT-CPT correlations, *Journal of Geotechnical Engineering, 109*(11), 1449-1459.

Salgado, R., Drnevich, V. P., Ashmawy, A., Grant, W. P. and Vallenas, P. (1997). Interpretation of large-strain seismic cross-hole tests. *Journal of Geotechnical and Geoenvironmental Engineering, 123*(4), 382-388.

Schuhen, M. (2009). *Technical Report: Geotechnical data from 2007 and 2008 for a geologic repository at Yucca Mountain, Nevada*, TDR-MGR-GE-000011 REV 00, Sandia National Laboratories, Las Vegas, Nevada.

Schmertmann, J.H. (1970). Static cone to compute static settlement over sand, *Journal of the Soil Mechanics and Foundations Division,* ASCE, 96(3), 1011-1043.

Schmertmann, J.H., Hartman, J.P. and Brown P.R. (1978). Improved strain influence factor diagrams, *Journal of the Geotechnical Engineering Division,* ASCE, 104 (8), 1131-1135.

Seed, H. B. and Idriss, I.M. (1970). *Soil modulus and damping factors for dynamic response analysis*, Report No. EERC 70-10, Earthquake Engng. Res. Ctr., University of California at Berkeley, California.

Seed, H. B., Wong, R. T., Idriss, I. M. and Tokimatsu, K. (1986). Moduli and damping factors for dynamic analyses of cohesionless soils. *Journal of Geotechnical Engineering*, *112*(11), 1016-1032.

Skempton A. and MacDonald D. (1956). The allowable settlements of buildings, *Proceedings of Institute of Civil Engineers,* 5(3), 727-784

Smith, R. (2005). *Predicting static deformations with dynamic soil properties: a review of case histories*, M.S. Research Report, the University of Texas at Austin, U.S.A., 196 pp.

Stokoe, K. H. II, and Santamarina,C. (2000). Seismic-wave-based testing in geotechnical engineering, *International Conference on Geotechnical and Geological Engineering,* GeoEng, Melbourne, Australia, 1490-1536.

Stokoe, K. H., Axtell, P. J. and Rathje, E. M. (2001). Development of an in situ method to measure nonlinear soil behavior, *Earthquake Resistant Engineering Structures* Malaga, Spain, pp. 561-570.

Tatsuoka, F., Teachavorasinskun, S., Dong, J., Kohata, Y. and Sato, T. (1994). Importance of measuring local strains in cyclic triaxial tests on granular materials, *In Dynamic Geotechnical Testing, II,* ASTM, STP 1213, pp. 288-302.

Terzaghi, K. and Peck, R.B. (1948). *Soil Mechanics in Engineering Practice*, John Wiley and Sons, New York.

Van Pelt, J. D. (2010). *Predicting settlements of shallow foundations on cohesionless, granular soil using dynamic soil measurements,* M.S. Thesis, the University of Texas at Austin, U.S.A., 363 pp.

Wichtmann, T. and Triantafyllidis, T. (2009). Influence of the grain-size distribution curve of quartz sand on the small strain shear modulus G_{max}, *Journal of Geotechnical and Geoenvironmental Engineering*, *135*(10), 1404-1418.